DEVELOPING A NOVEL METHOD FOR MAKING METAL OXIDE NANOCOATINGS FOR ELECTROCATALYSIS APPLICATIONS

A Dissertation

presented to

the Faculty of the Graduate School

at the University of Missouri-Columbia

In Partial Fulfillment

of the Requirements for the Degree

Doctor of Philosophy

By

Ahmed Mohammed Jasim

Dr. Yangchuan Xing, Dissertation Supervisor

December 2020

The undersigned, appointed by the dean of the Graduate School, have examined the Dissertation entitled

DEVELOPING A NOVEL METHOD FOR MAKING METAL OXIDE NANOCOATING FOR ELECTROCATALYSIS APPLICATIONS

Presented by Ahmed Mohammed Jasim,

a candidate for the degree of doctor of philosophy of Science,

and hereby certify that, in their opinion, it is worthy of acceptance.

Professor David G. Retzloff

Professor Matthew R. Maschmann

Professor Zheng Yan

Professor Yangchuan Xing

DEDICATION

To my beloved wife “Huda”

ACKNOWLEDGEMENTS

I would like to express my special appreciation and thanks to my research advisor **Professor Dr. Yangchuan Xing**, you have been a tremendous mentor for me. I would like to thank you for encouraging my research and for allowing me to grow as a research scientist. Your advices on the research as well as on my personal life have been invaluable. It was a great honor for me to work under your supervision and I hope I can take a stereotype of your supervision style in my future academic life.

I would also like to thank my committee members, **Professor David G. Retzloff**, **Professor Matthew R. Maschmann**, **Professor Zheng Yan** for serving as my committee members and for the valuable comments and suggestions. Not to forget, I am thankful to the electron microscopy center (EMC) staff, Dr. Tommi White, Dr. Xaioqing He, Deana Grant, Dr. Davide Stalla, and Dr. Martin Schauflinger for their cooperation and continuously fruitful discussions. A special thanks to **Dr. Tommi White** for her crucial help in the Cryo-TEM work.

Words cannot express how grateful I am to my mother, father, my mother-in law, and father-in-law for all of the support that you've made on my behalf. I would also like to thank to my family here in the USA, beloved wife, Huda and my four lovely kids, Rahma, Sarah, Ibrahim, and Mohammed. Thank you for supporting me for everything. Thanks to all colleagues who helped me to achieve this work. This work was not possible without the financial support from Dr. Xing and the University of Missouri.

TABLE OF CONTENTS

LIST OF ILLUSTRATIONS

List of Figures

Schemes

Chapter Two

Chapter Three

Tables

Chapter Two

Chapter Six

Chapter Eight

LIST OF ABBREVIATIONS

Techniques

ALD: Atomic Layer Deposition

CVD: Chemical Vapor Deposition

CLD: Condensed Layer Deposition

Materials

CNTs: Carbon Nanotubes

CB: Carbon Black

IOPs: Iron Oxide Nanoparticles

Pt NPs: Platinum Nanoparticles

Characterizations Tools

GC-MS: Gas Chromatography Mass Spectrum

FT-IR: Fourier Transform Infrared spectroscopy

TGA: Thermogravimetric Analyzer

SAED: Selected Area Electron Diffraction

TEM: Transmission Electron Microscopy

EF-TEM: Energy Filtered Transmission Electron Microscopy

EELS: Electron Energy Loss Spectroscopy

STEM-HAADF: Scanning Transmission Electron Microscopy

TEM-EDS: Transmission Electron Microscopy-Energy Dispersive Spectroscopy

XRD: X-ray Diffraction

XPS: X-ray Photo Spectroscopy

CV: Cyclic Voltammetry

BET: Brunauer-Emmett-Teller

Notations

N: Mass Transfer Flux ($g/cm^2 \cdot s$) *eq (2.1)*

K_{ls}: Mass Transfer Coefficient (cm/s) *eq (2.1)*

A: Interfacial Area of Water and CNTs surface *(1/m) eq (2.1)*

Cl: Water Concentration in Heptane (mole/L*) eq (2.1)*

Cs: Water Concentration on the Nanosubstrates (mole /L) *eq (2.1)*

D_A: Diffusion Coefficient (cm^2/s) *eq(2.3)(2.5)(7.1)(7.2)*

dp: Substrate Diameter (nm) *eq (2.3)*

ρ: Density (Kg/m^3), or (gm/cm^3) *eq (2.4), (2.5)(4.2)*

u: Velocity (linear velocity m/s), or Angular Velocity (S^{-1}) *eq (2.4)*

μ: Viscosity ($N \cdot s/m^2$) *eq (2.4)*

Sh: Sherwood Number *eq (2.3)*

Re: Reynold Number *eq (2.4)*

Sc: Schmitt Number *eq (2.5)*

Vm: Water Molar Volume (m^3/mole) *eq (2.7)*

r: Water Film Thickness (nm) *eq (2.7)*

R: Gas Universal Constant *eq (2.7)*

T: Temperature (ºC or K) *eq (2.7)*

γ : Interfacial Tension *eq (2.7)*

D: Mean Diameter of Platinum Nanoparticles (nm) *eq (4.2)*

K: Shape Factor in XRD *eq (4.1) (5.2)*

λ: X-ray Wavelength *eq (4.1)* (5.2)

β: Full Peak Width at Half Maximum *eq (4.1) (5.2)*

θ: Diffraction Angle *eq (4.1) (5.2)*

I_k: Kinetic Current (mA) *eq (7.1)*

I_d: Diffusion Limited Current (mA) *eq (7.1)*

n: Number of Electrons Transferred *eq (7.1)*

F: Faraday's constant (96,485 C mol^{-1}) *eq (7.1)*

A: Area of the Rotating Disk Electrode (0.196 cm^2) *eq (7.1)*

C: Concentration of Molecular Oxygen in 0.5M H_2SO_4 Solution *eq (7.1)*

ω: Angular Frequency of Rotation *eq (7.1)*

Chemicals

TEO: Titanium Ethoxide

NEO: Niobium Ethoxide

TTiP: Titanium tetra-isopropoxide

TMA: Trimethylaluminum

Oil: Heptane

Experimental Tests

ORR: Oxygen Reduction Reaction,

MOR and EOR: Methanol and Ethanol Oxidation Reaction

ABSTRACT

In this dissertation, a new and novel technique to synthesize conformal films of metal oxides on top of nanoscale substrates in different geometries such as carbon nanotubes, carbon black particles, and iron oxide nanoparticles was developed. The coating technique is based on principles of condensing water molecules from an organic solvent, heptane, onto nanoscale substrates after oversaturating the heptane above its water saturation limit. When metal oxide precursors are introduced into the heptane dispersed with the nanoscale substrates, they diffuse to the surface of the substrates and react with the water film on their surface to form metal oxide nanocoatings. Due to the high surface tension between the water film and the heptane, the condensed water film takes a conformal shape on the substrates with minimum roughness, which also leads to producing uniform metal oxide coatings. This new coating technique is termed condensed layer deposition, or CLD. Various metal oxides were successfully made, such as TiO_2, Nb_2O_5, and Al_2O_3 on various substrates, such as carbon black (CB), carbon nanotubes (CNTs), carbon nanofibers (CNFs), iron oxide particles (IOPs), and TiO_2. By removing the carbon supports (CB, CNTs, CNFs), Nb_2O_5 nanoshells, TiO_2 nanotubes and Al_2O_3 porous nanotubes have been obtained. It was found that the CLD technique can produce fluffy coatings with a high specific surface area of ~310 m^2/g, when a large molecule size of organic precursor such as titanium terta-isopropoxide is used. The surface hydrophilicity was observed to increase by increasing the water ratio. Subsequently, a fluffy TiO_2 coating on CNTs was made with tin oxide and used as a support for platinum nanoparticles for ethanol electrooxidation and for oxygen

reduction reaction (ORR). The catalyst has shown a much higher ethanol mass activity peak of 560 $mA/mg_{(Pt)}$ than Pt/C (Pt on CB) which showed 296 $mA/mg_{(Pt)}$. In addition, the catalyst has a current density by over 2.2 times of that in Pt/C at 600 mV after 0.5 hours in durability test. In ORR, a remarkable improvement in ORR onset potential was achieved at 930 mV vs. RHE in 0.5 M sulfuric acid electrolyte. The mass activity was 2.66 times that of Pt/C at 900 mV. The same fluffy TiO_2/CNTs was used to support platinum and iridium for methanol electrooxidation. Pt-Ir/C-TiO_2/CNTs has shown a significant improvement in the anodic to the cathodic current ratio with a 5.6-fold increase. The *i-t* curve showed a high stability at 0.5 V after 3600 seconds by 12.5 times. On the other hand, Nb_2O_5 coating of 5 nm on CB was used for the oxygen reduction reaction. Electrochemical tests showed only a 1.7% activity loss after 5000 cycles, demonstrating an excellent durability of the electrocatalyst. Compared to the electrocatalyst without niobium oxide coating, it shows a 25 mV improvement in half-wave potentials, indicative of a better kinetics. The 5 nm Nb_2O_5 on CB was coupled with tin oxide supporting platinum toward methanol electrooxidation. Pt-TNb/C (tin and niobium oxide support) showed 2.7 $A/mg_{(Pt)}$ in mass activity at 0.8 V vs. Ag/AgCl which is better than most studies reported in the literature. Moreover, the Pt-TNb/C showed 0.0% loss after 1000 cycles in electrolyte containing 1.0 M CH_3OH, whereas, Pt-Nb/C (niobium oxide support) and Pt/C suffered 21% and 30% loss, respectively. The chronoamperometry results showed the catalyst has a high CO tolerance after testing for 2 hours with a remarkable stability.

Chapter 1. Background and Literature Review

1.1 Work Motivation

The coating on nano-substrates, defined as nanocoating, has shown a breakthrough in all modern technologies such as nano-membranes, nano-chips, nano-catalysis, nano-batteries, and beyond. In energy related applications such as polymer exchange membrane fuel cells (PEMFCs), the most active catalyst used usually is platinum nanoparticles (Pt NPs). To reduce the loading of such expensive metal, Pt NPs are usually loaded on conductive supports such as carbon materials. However, two main issues associated with the carbon materials supports are the weak interaction with Pt NPs and the high vulnerability to corrosion which make the metal oxides nanocoating a vital role in their uses. Carbon supported catalysts are subjected to a significant improvement if the carbon supports are coated by metal oxides. However, some developed coating techniques are limited due to a couple of reasons. Such reasons are pace of the coating process and complexity, coating efficiency, and operative cost. Some of these reasons make the coating technique fall in the expectation for scaling up purpose.

Based on such urgent need, we have developed a new, novel, cost effective coating technique of metals oxides on nanosubstrates *via* an organic solvent. This developed technique has a fast coating rate by making nanolayers instead of atomic layer and less cost by recycling the organic solvent, the process has been named “Condense Layer Deposition” (CLD). Additionally, this technique allows us to make porous and dense

metal oxide nanocoating based on the used precursors. In addition, this technique can produce metals oxides nanostructure based on the substrate's dimension such as TiO_2 and Al_2O_3 nanotubes in case carbon nanotubes (CNTs) were used and Nb_2O_5 nanoshells in case carbon black (CB) was used.

1.2 Background

1.2.1 Metals Oxides Applications

1.2.1.1 Titanium Dioxide (TiO_2)

Since early twentieth century, TiO_2 (M^{+4} group) has been used in pigments manufacturing [1], sunscreen [2] and ointments [3], paints and toothpastes [4], and beyond. After a while, it was found that TiO_2 is an efficient material for water splitting in photocatalytic as reported first time by Fujishima and Honda [5]. TiO_2 behavior is different from bulk to nano size as the physical and chemical properties are different. For example, the specific surface area increases from the bulk size to the nano-size from 9.5 m^2/g to 185.5 m^2/g , respectively. Therefore, the applications have seen an exponential increase particularly when the nanotechnology was adapted [6, 7]. In next subsections, a couple of selected application for TiO_2 was concisely demonstrated.

1.2.1.1.1 Photo-active material

TiO_2 has been extensively studied and applied as a photocatalyst [8] since it is cheap in price, active and stable in performance, and nontoxic material [9]. It has multi-phases with different band gaps such as brookite (3.2 eV), anatase (3.2 eV), and rutile (3.0 eV) [10]. The first use of TiO_2 in environmental remedy is dated in 1977 as reported by Frank and Bard [11]. In anatase phase, electrons in the valence band can be excited to the conduction band at a wavelength of $\leq$387 nm that generates positive holes in the

valence band. Inside the TiO_2 lattice, the charge carriers are either Ti^{3+} or O^- defects sites that migrate to the surface. After water oxidation on such defects, OH radicals are produced. Consequently, these radicals oxidize organic species producing CO_2 and H_2O [12].

Approximately 40% of the solar photons are visible light which makes the use of pure TiO_2 difficult. Asahi et al. [13] has synthesized nitrogen-doped TiO_2 in a form of $TiO_{2-x}N_x$ to overcome the sluggishness of the visible light. In their results, the band gap was significantly narrowed; therefore, the photocatalytic activity has increased. Another study was reported by Pore et al. [14] on using atomic layer deposition by using $TiCl_4$, NH_3, and water as precursors to engineer $TiO_{2-x}N_x$. They found the films can be excited by the visible light, but it suffers from a recombination. Unlike other non-metal dopants [15-17], the incorporation of transition metals (i.e., Fe, Cu, Co, Ni, Cr, V, Mn, Mo, Nb) in TiO_2 crystal lattice creates a new energy level between the valence and conduction bands resulting in a shift in the visible light absorption [9]. The visible light absorption is also used for environmental remedies such as water and air purification. Nitrogen doped-TiO_2 photocatalyst was used to degrade the organochlorine pesticide (lindane) as reported by Senthilnatan and Philip [18]. By using solvothermal method, Wang and Lim have reported using carbon and nitrogen doped-TiO_2 for the degradation of bisphenol-A under the visible light-emitting diodes [19]. On the other hand, a bifunctional TiO_2 based photocatalyst was doped by nitrogen and was coupled with platinum. This photocatalyst was used toward air purification as an effective material for decomposition of benzene [20]. Another study reported a high activity of N-

TiO_2/zeolite to oxidize toluene performed in an integrated system consists of a photocatalyst and a biofilter [21].

In water disinfection, Matsunaga et al. [22] was the first in using TiO_2 for the inactivation of bacteria in 1985. Yu et al. [23] has reported using sulfur-doped titanium dioxide after exposing to 100 W of tungsten halogen lamp to exclude the wavelength less than 420 nm. The sulfur-doped titanium dioxide was prepared by the sol–gel method and based on their results, a 96.7% reduction in viable organisms was observed. Mitoraj et al.[24] has demonstrated carbon-doped TiO_2 and TiO_2 modified with platinum toward the inactivation of a range of organisms such as Gram negative, Gram positive bacteria, and fungi. Nitrogen-doped TiO_2 supported palladium (TiON/PdO) photocatalyst was used to disinfect and treat Coliphage MS2 under visible light [25]. They reported a significant virus adsorption of (95.4–96.7%) under dark conditions and an additional (94.5–98.2%) after 1 hour under visible light.

1.2.1.1.2 Catalytic material

As a catalytic material, TiO_2 has been widely applied in both electrocatalysis and thermal catalysts approaches. In polymer exchange membrane fuel cells catalysis approach, TiO_2 has extensively been used in a form of a catalyst's support [26] and a catalyst by itself [27] due to its activity, structure stability, and durability. In oxygen reduction reaction (cathode side in fuel cell) [28-31] where the kinetics suffers from the sluggishness, rutile TiO_2 plays a vital role due to the structure oxygen vacancies [32, 33]. Those vacancies are believed to have tendency toward water splitting that enhances

the protons supply to reduce the oxygen atoms from platinum surfaces. In the direct methanol oxidation reaction (MOR)(anode side in a fuel cell), the poisoning species such as carbon monoxide (CO-ads) evolved from the methanol lower the catalyst performance. It was found that incorporating Pt NPs with TiO_2 has enhanced the activity and the durability for MOR. Abida et al. [34] has reported the active sites on TiO_2 can initiate water on the electrode 's surface to produce the (OH) adsorbates that reduce the CO-ads from PtNPs active sites. In our previous work, TiO_2 with tin oxide as a support for Pt NPs have significantly enhanced the methanol oxidation reaction [35]. The aspects that make TiO_2 widely applicable in the electrochemical reactions are its unique structure stability, ability to change the stoichiometry, and strong bonding with the host catalyst (usually precious elements catalyst). Moreover, its potential window is not in the fuel cell voltage range (0-1.0 V) that makes it a practical support. In thermal catalysts, TiO_2 has also been applied in the extractive and catalytic oxidative desulfurization in an ionic solvent in desulphurization of dibenzothiophene [36]. This study reported a sulfur removal of DBT reached up to 99.1% under normal reaction conditions when TiO_2 was calcined at 150 °C. In biodiesel production, TiO_2 shows a remarkable activity in the transesterification reaction as a catalyst [37]. Yu et al. [38] has reported using cobalt-based Fischer-Tropsch loaded on TiO_2 nanotubes for CO hydrogenation. They reported a higher selectivity and activity on Co/TiO_2 nanotubes than Co on bulk TiO_2. Shinde et al.[39] reported Ni/TiO_2 as a catalyst for natural gas production. The remarkable performance in CO methanation and a high coke resistance were attributed to the vacancies created because of partial substitution of Ni with TiO_2.

1.2.1.1.3 Sensing applications

In various nanostructures and compositions, TiO_2 has been used in many sensors types such as gas sensors for detection gases (oxidative gases such as O_2 and NO_2 and reductive gases such as H_2, CO, NH_3, H_2S) [40], for other chemicals [41], in chemical oxygen demand (COD) for detecting soluble organics in water quality assessment [42], and biosensors for detecting biological substance [43]. Jun et al.[44] have fabricated TiO_2 sensor for H_2 gas by thermal oxidation for Ti plate. In their results, when porous morphology of TiO_2 with a high specific surface area is used, a better performance was observed as the H_2 molecules can be easily absorbed. TiO_2 tubular structure showed a remarkable activity in H_2 gas detection due to two parameters the surface area and the low resistance for electrons transport [45, 46].

As an oxygen sensor, TiO_2 based sensor has been reported as a good candidate[47, 48]. TiO_2 is one of earliest sensors used for detecting oxygen concentration as used by Ford Motor Co. as a first used in industry [49]. In the opposite to H_2, the O_2 detection mechanism is based on the increase in TiO_2 resistance due to oxygen vacancies and interstitial oxygen ions forming anionic oxygen. This monolayer of oxygen ion change the n-type doping density to p-type causing a depletion region which is defined the resistance [47]. Lu et al.[50] used aluminum oxide anodic as an etching mask in which TiO_2 film was deposited on microporous silicon wafer. In their study, microporous TiO_2 sensor was found to enhance the detection by 33% relative to the nonporous sensor. TiO_2 has also been reported to be an effective sensor for carbon monoxide detection even under a level of ppm [51-53]. Seeley et al.[54] have found the anatase and the

amorphous phase to be more robust and active toward sensing CO than the rutile phase. They assigned that to the available surface area and particles size. Other people have reported using TiO_2 as an efficient sensor for detection NH_3 [41], H_2S [55], and NO_2 [56].

1.2.1.2 Niobium Oxide (Nb_2O_5)

Nb_2O_5 (M^{+5} group) mainly exists in a form of stoichiometric oxides such as NbO, Nb_2O_3, NbO_2 and Nb_2O_5 [57]; in addition, many crystal phases such as pseudo-hexagonal, orthorhombic, tetragonal and monoclinic [58]. It has shown a notable performance in providing a strong surface acidity and stability in an aqueous medium for various acid-catalyzed reactions especially in catalysis [59]. Nb_2O_5 is a dielectric material applicable in capacitor technology [60], waveguides [61], gases sensors [62], corrosion-resistant [63], batteries [58], and solar cells [64]. In next subsections, we demonstrate a couple of niobium oxide uses.

1.2.1.2.1 Catalytic material

Like TiO_2, niobium oxide is applied in both electrocatalysis and thermal catalysts. In electrocatalysis approach, NbO_2 [65] and Nb_2O_5 phases have been used as a catalyst [66] or an electrocatalyst support such as in oxygen reduction reaction [59], alcohols electrooxidation [67], and hydrogen oxidation [68]. Nb_2O_5 based catalysts can be applied in the dehydration reactions due to the high activity and stability in aqueous reactions. In many contributions, Nb_2O_5 as a support or alloyed with platinum have shown an outstanding activity and durability in oxygen reduction reaction (ORR) [59, 69, 70]. In thermal catalysts [71], Nb_2O_5-based catalysts in biphasic processes have increased furfural yields with toluene, THF, and xylene by 14% [72]. In hydrogen

evolution approach, niobium oxide in a form of niobates containing alkali element ($K_4Nb_6O_{17}$) was found as a first metal oxide that serves as a catalyst in hydrogen production without addition of a co-catalyst. However, it performs even better by an order of magnitude when it supports NiO [73]. Another study has reported using Nb_2O_5 supporting Rh for hydrocarbon formation from CO and H_2 as a hydrogenation process with a CO conversion of 76% which is better than other metals oxides by far [74]. Nb_2O_5 shows excellent performance in both approaches due to a couple of reasons. It is highly stable in acidic electrolyte even under a high voltage conditions such as 1.2 V. Its catalytic behavior in thermal catalysts is due to its electronegativity and its ionic radius [71].

1.2.1.2.2 Corrosion resistance

Nb_2O_5 coating has been applied in corrosion resistant technology such as for dental implants, stainless steel, and beyond. The corrosion resistance of Nb_2O_5 films on stainless-steel was determined using potential-dynamic anodic in a solution of 8.9 g/l of NaCl at pH of 7.4 [75]. The biological evaluation in the last study showed the biocompatibility and the corrosion resistant was significantly improved upon the Nb_2O_5 coating. In ceramic manufacturing, the thermal conductivity of Al_2O_3 was increased by adding 3-6% of Nb [76]. In a relevant matter, Nb_2O_5 has shown a considerable performance in self-healing in ceramics especially when it is combined with other metals oxides [77]. Marcondes et al. [78] reported that adding applied significantly modifies the thermal, structural and optical properties of alkali germinate glasses.

1.2.1.2.3 Gas sensors

At the early 1980s, the first work using Nb_2O_5 as a gas sensor was reported [79]. With it's a band-gap n-type metal oxide, Nb_2O_5 is used as an oxygen sensor at a high temperature conditions of 400-800 °C providing the temperature and oxygen partial pressure data at the same time [80]. Another study reported nanoporous Nb_2O_5 films were effectively applied in hydrogen gas sensing [81]. It was used also as a humidity sensor as it was found that electrical resistivity decreases by 10 times as water vapor adsorbed [82]. Nb_2O_5 performs very well in gas sensing due to the electron voids that exist in Nb 4d level as most of Nb 4d electrons are shared with O 2p band [83].

1.2.1.3 Aluminum Oxide (Al_2O_3)

Aluminum oxide (Al_2O_3) is known with its versatility in various applications such as catalysts, filters, adsorbents, ceramics, dental crowns, electronics industry, and beyond. It has outstanding properties such as hardness and bio-inertness (for medical purposes), strength and lightweight (for body armors), excellent thermal resistive (furnace insulations), and a high specific surface area in nano size (for catalyst supporting). In next subsections, we will discuss in more details some selective applications for Al_2O_3.

1.2.1.3.1 Catalytic material

As a co-catalyst, $CoMo/Al_2O_3$ was incorporated with zeolite as a catalyst for hydrodesulfurization (HDS) for 4,6-dimethyldibenzothiophene (4,6-DMDBT). This catalyst composite showed a remarkable activity in term of the removal of the sulfur content; in addition, it was found a durable against the acidic sites [84]. Another study reported using Al_2O_3 as a catalyst support for Ni-Pd for production of COx-free hydrogen methane thermal catalytic decomposition [85]. In methane production, γ-

Al_2O_3 was used as a catalyst support for Rh in CO_2 methanation at a low temperature of (100-200 °C) [86]. In solar cell approach, a study was reported on using Al_2O_3 as a passivation stabilizer for p-type silicon. After exposing Al_2O_3 boron-doped surfaces to a firing process between 700 °C to 825 °C, the Al_2O_3 passivation is shown to be stable [87]. A previous study has found using amorphous AlOx film over anatase phase of TiO_2 affect the Dye-sensitized solar cells performance through tunnel barrier mechanism [88].

1.2.1.3.2 Membranes and adsorbents

In membranes, γ-Al_2O_3 was used as ultrafiltration membranes for nitrates removal from aqueous solution. The study reported an optimal rejection rate of NO^{3-} when the solution PH matches the PH_{pzc} [89]. The same γ-Al_2O_3 was used but in a hollow structural microsphere into interlayers for helping water permeability [90]. The results show that the γ-Al_2O_3 composite NF membrane has a high pure water permeability of 26.4 L m^{-2} h^{-1} bar^{-1}. Aluminum oxide nanoparticles on ceramic membrane have been used in the asphaltene separation from the crude oil [91]. As adsorbents, a recent study has reported a composite of the nanofibers of Al_2O_3/Fe_2O_3 for Cr (VI) removal [92]. The Al_2O_3/Fe_2O_3 composite nanofibers were synthesized via electrospinning and it showed increasing in the surface area as Al_2O_3 increasing leading to a remarkable adsorption capacity up to 169.5 mg/g. Several studies have been carried out to use γ-Al_2O_3 as adsorbents to remove some cariogenic contaminates such as Congo red (CR). A previous study has reported an enhancement in CR removal by using nanorod-like mesoporous γ-Al_2O_3 [93].

1.2.1.3.3 Protection material

Several studies have reported that aluminum oxide nanocoating on lithium ion battery electrodes improves structure stability and chemical durability [94, 95]. Hoskins et al.[96] has reported a thin film of 2 nm of Al_2O_3 on lithium nickel manganese cobalt oxide cathode. They found a thin and nonuniform film of Al_2O_3 have improved the cathode stability at the presence of the electrolyte protecting the lithium from side interactions. Yan et al.[95] studied using Al_2O_3 coating on $Li_{1.2}Ni_{0.2}Mn_{0.6}O_2$ cathode. Based on their study, three aspects have been found. Firstly, Al_2O_3 coating hinders the side reaction between the cathode and the electrolyte during the cycling. Secondly, manganese reduction was remarkably reduced which prevents the Mn dissolution in the electrolyte. Thirdly, they found the coating suppress phase transformation layers to spinal. Other people have found coupling Al_2O_3 with Ga_2O_3 as coating agents on $Li[Ni_{0.5}Mn_{0.3}Co_{0.2}]O_2$ improve the rate performance in lithium ion battery [97].

1.2.2 Coating Techniques

Owing to the numerous uses of the metal oxides, people have developed many fabrications/coating methods whether to synthesize metals oxides as nanoparticles or as nanocoating films. The unit size at a range of (1-100 nm) is designated as a ‘nano’ in various dimensions such as spherical, sheets, and tubes. They have become more attractive if they are synthesized in a form of nanocoating layer offering exceptional interfacial properties. Various coating techniques such as atomic layer deposition (ALD), chemical vapor deposition (CVD), sol-gel, spin coating, dip coating, and more have become a crucial tool to achieve such objectives. In next subsections, we describe

the coating techniques and their mechanisms, advantages, and limitations, particularly of ALD, CVD, and sol-gel technique.

1.2.2.1 Atomic Layer Deposition (ALD)

In making nanocoatings, the most known technique developed recently and attracted extreme attention in the recent decade is the ALD [98]. This technique uses a chemical precursor that can be vaporized into a carrier gas and reacts with the surface water on a substrate to form an atomic thick layer of coatings [99]. By introducing the chemical precursor vapor and a purge gas with water vapor alternatively, the chemical precursor can react with the surface water newly adsorbed each time and thus form a coating in a layer by layer fashion. Nowadays, ALD technique has been widely used today in a various elements as in Figure 1.1 [100]. However, a gas phase chemical precursor often has limitations in their availability and deposition efficiency. The substrates, especially those nanoscale objects, are difficult, if not impossible, to be dispersed in a gas phase, leading to either non-uniform coatings or nucleated on certain original active sites. The deposition time in ALD process can be extremely long if thick coatings of even a few tens of nanometers are to be made because hundreds or thousands of deposition cycles are needed to accomplish it. Furthermore, the ALD process often involves quite expensive equipment.

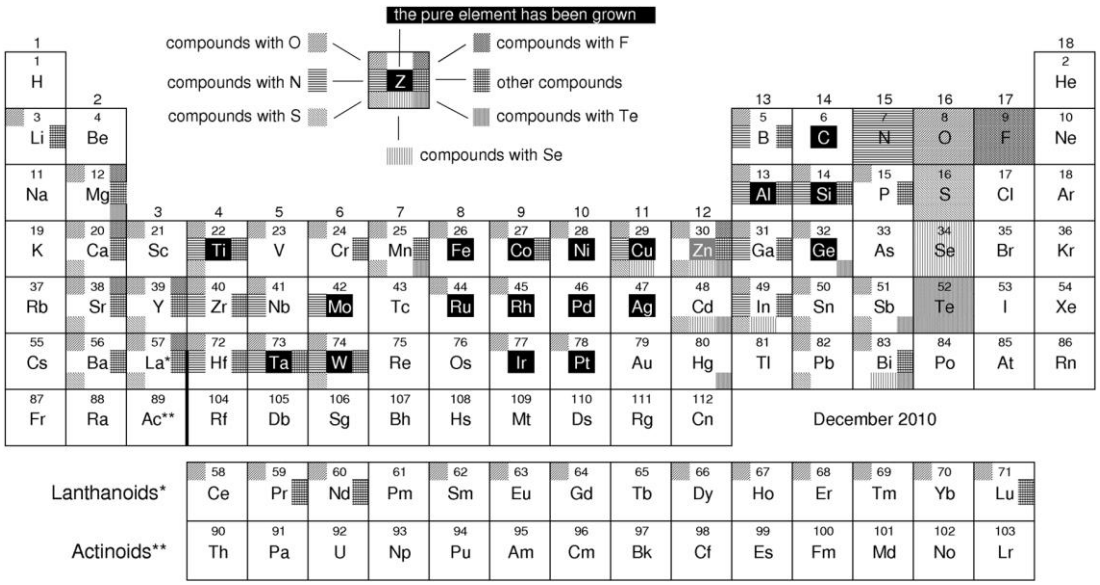

Figure 1.1. An overview of the materials grown by ALD based on (The International Union of Pure and Applied Chemistry (IUPAC, ated 21 January 2011).

Additionally, ALD has some other technical limitations. Firstly, the required vapor pressure is above 0.1 Torr at a low temperature for the precursors to meet the coating conditions meaning not all chemistries are applied. Secondly, ALD suffers from the coating agent nucleation and precursors thermal decomposition. For example, titanium ethoxide and niobium ethoxide are decomposed at a range of (325 – 350 °C) [101], [102]. Working at a low temperature may solve the precursor decomposition issue but can generate hydrogen contamination (known as precursor condensation) to the films comes from injected water and that causes some problems during the purging.

1.2.2.2 Chemical Vapor Deposition (CVD)

Another coating technique is called CVD. CVD is a process in which the substrate is exposed to one or more of volatile agents in a same time that reacts or decomposes on the substrate surface to produce the desired films [103]. CVD is widely used technique to make solid thin-film coatings to surfaces, but it also could produce a high-purity bulk

materials and powder. The chemistry used in CVD is broader as shown in shaded boxes in figure 1.2.

PERIODIC TABLE

IA	IIA	IIIA	IVA	VA	VIA	VIIA	VIII			IB	IIB	IIIB	IV	VA	VIB	VIIB	O
1 H 1.008																	2 He 4.003
3 Li 6.941	4 Be 9.012											5 B 10.81	6 C 12.01	7 N 14.01	8 O 16.00	9 F 19.00	10 Ne 20.179
11 Na 22.990	12 Mg 24.305											13 Al 26.98	14 Si 28.09	15 P 30.97	16 S 32.07	17 Cl 35.45	18 Ar 39.948
19 K 39.098	20 Ca 40.08	21 Sc 44.956	22 Ti 47.90	23 V 50.942	24 Cr 51.996	25 Mn 54.938	26 Fe 55.847	27 Co 58.933	28 Ni 58.70	29 Cu 63.546	30 Zn 65.39	31 Ga 69.72	32 Ge 72.61	33 As 74.92	34 Se 78.96	35 Br 79.90	36 Kr 83.80
37 Rb 85.468	38 Sr 87.62	39 Y 88.906	40 Zr 91.22	41 Nb 92.906	42 Mo 95.94	43 Tc (99)	44 Ru 101.07	45 Rh 102.905	46 Pd 106.4	47 Ag 107.868	48 Cd 112.4	49 In 114.8	50 Sn 118.7	51 Sb 121.8	52 Te 127.6	53 I 126.9	54 Xe 131.30
55 Cs 132.905	56 Ba 137.33	57 La 138.9	72 Hf 178.49	73 Ta 180.948	74 W 183.85	75 Re 186.2	76 Os 190.2	77 Ir 192.22	78 Pt 195.09	79 Au 196.966	80 Hg 200.59	81 Tl 204.37	82 Pb 207.2	83 Bi 209.0	84 Po (210)	85 At (210)	86 Rn (222)
87 Fr (223)	88 Ra (226)	89 Ac 227.0															

LANTHANIDES	57 La 138.9	58 Ce 140.115	59 Pr 140.1	60 Nd 144.2	61 Pm (145)	62 Sm 150.4	63 Eu 152.0	64 Gd 157.2	65 Tb 158.9	66 Dy 162.5	67 Ho 164.9	68 Er 167.3	69 Tm 168.9	70 Yb 173.0	71 Lu 174.96
ACTINIDES	89 Ac 227.0	90 Th 232.0	91 Pa 231.0	92 U 238.0	93 Np 237.0	94 Pu (244)	95 Am (243)	96 Cm (247)	97 Bk (247)	98 Cf (251)	99 Es (252)	100 Fm (257)	101 Md (256)	102 No (259)	103 Lr (257)

Fig. 1: Periodic table, where shaded boxes indicate elements that have been deposited using CVD.

Figure 1.2. Periodic table where the shaded boxes refer to the material used in CVD [104].

It has a similar protocol of ALD; however, the mechanism is based on a binary reaction such , A+B → Product, and the two reactants should be present at the same time to form the film on the substrates [105]. CVD has several advantages as a technique for making thin films. One of the distinguished advantages is that CVD films are often conformal. That said, CVD also suffers from a couple of drawbacks particularly the properties of used precursors. Firstly, precursors need to be volatilized at the room temperature which is not a common property for several elements in the periodic table since such precursors are expensive. Secondly, some used precursors could be highly toxic as $Ni(CO)_4$, explosive as B_2H_6, and corrosive as $SiCl_4$. In addition, the produced by-product of those precursors is hazardous which is usually comprised of CO, H_2, HF.

Finally, an elevated temperature is usually used to deposit the thin films leading to restricting the versatility for used substrates. This high temperature causes a distortion in the substrate's properties due to the thermal expansion [104].

1.2.2.3 Sol-gel

Sol-gel is a process involves the use of a liquid solution as a mixture for the raw materials [106]. This technique has a long history back to mid-1800s belonged to Ebelman [107] and Graham's work [108]. They observed the hydrolysis reaction for tetraethyl orthosilicate (TEOS) $Si(OC_2H_6)_4$ under low pH conditions to produce SiO_2 gel. However, their work required a long time drying up to one year to avoid the silica gels fracturing into a fine powder. People showed an interest in gel fabrication as first reported by Stöber's early studies [109]. Stöber's group used ammonia as a catalyst to control the morphology and the powder size producing a spherical powder which is called later Stöber silica powder. The final particles size depends on water and ammonia ratio, precursor ligands, and the reaction temperature.

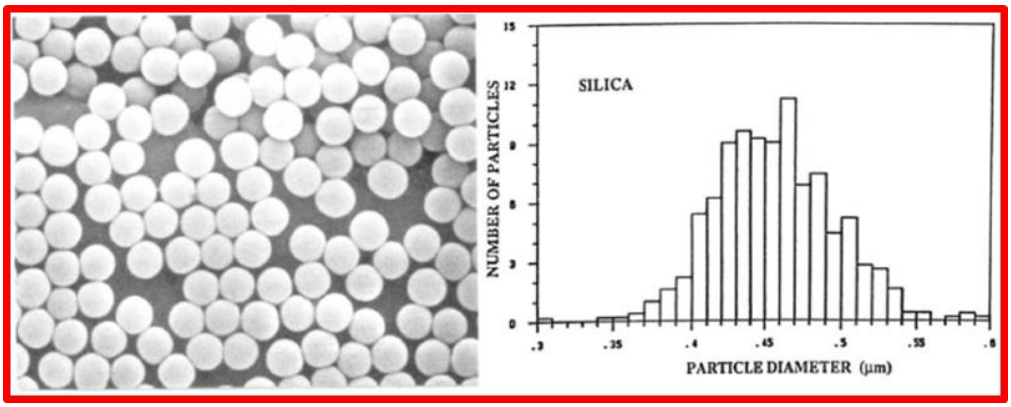

Figure 1.3. (left) Stöber spherical silica powders, (right) Histogram for particles size [110].

The process has three unique characteristics steps, making sols in a solution of colloidal powders. This step includes sub-steps like hydrolysis and polycondensation of the

alkoxide precursor [111]. Second step is called casting in which the sols (a low-viscous material) adhesion phenomenon must be avoided. Finally, the 3-dimensions network viscosity increases in gelation step where the solid material is produced. These principles for sol-gel have paved a way for the community to apply it in vast applications. Sol-gel technique has some advantages and disadvantages and the most significant ones are briefly illustrated here. One distinct property is that sol-gel can achieve well-mixed solution at a molecular level at a short time due to low viscosity and high homogeneity of the sols [112]. It also produces thick coatings to provide corrosion protection layers. It provides a low temperature sintering capability, usually at 200-600°C [113]. On the other hand, sol-gel process does possess series of drawbacks like other techniques. The major one is the impactable shrinkage that is associated with the gelation step. The presence of the high concentration of the pores, removal the undesired materials (organic ligands), and long process time are all issues existing in sol-gel processes. Other people have reported a weak bonding, high permeability, and difficulty in controlling porosity [114].

1.2.3 Research Objectives and Structure of the Dissertation

1.2.3.1. Objectives

The objective of this graduate study is to develop a coating technique for making metal oxide nanocoatings on different substrates as a support for electrocatalysts. Consequently, we developed the CLD process. This new CLD technology is expected to close the gap of lacking a fast coating technique in making a thick nanocoating and provide low-cost nanocoating process. It allows a wide range of metalorganic

precursors to be applied. In the course of studying the coating technique, we also tried to understand how the organic ligands attached to the metal precursors (e.g., ethoxide, isopropoxide, and butoxide) influence the metal oxide coating morphology and property. Moreover, we have applied the synthesized metal oxide nanocoatings in electrocatalysis studies, including electrooxidation of alcohols (methanol and ethanol) and oxygen electroreduction.

1.2.3.2 Structure of Dissertation

This dissertation is structured to have nine chapters. Chapter 1 is a literature review and introduction of the dissertation. Chapter 2 describes the CLD process. In this new coating process, we utilized an organic solvent (heptane in this work) to disperse the substrates and to make a particle dispersion. Afterward, we added water to the dispersion while it is under a sonication and stirring. Since heptane has an ultra-low water solubility (ca, 61 ppm v/v), the added water would oversaturate the heptane leading water to condense on the substrates. Once water film is formed, an organic precursor is added to diffuse and to react with a water film forming metal oxide layer.

the main idea of the work and the experimental section are extensively illustrated. The existence of the water film prior the metal oxide precursors injections is provided in term of Cryo-EM transmission electron microscopy TEM image of the ice layers on carbon nanotubes and iron oxides. The experimental part also describes in detail on how to make the three metals oxides on the nanosubstrates and how to control the metals oxide thickness. Subsequently, nanostructures of metal oxides were synthesized

by removing the carbon supports (carbon nanotubes and carbon black) to produce either metal oxide nanotubes or nanoshells.

Chapter 3 discusses applying the CLD principles but using big molecule precursors such as titanium isopropoxides (TTiP), which gives a fluffy-porous TiO_2 layer on the carbon nanofibers. The study has demonstrated there is a left-over organic ligand come from the precursor mother molecules. Those ligands decrease with increasing the water ratio during the coating process. The results have been confirmed by three techniques, FT-IR, GC-MS, and slow scan TGA. By increasing the water ratio with fixed TTiP, the FT-IR detect less -CH_x in the layer whereas the GC-MS has detected more isopropoxide desorbed into heptane. The slow scan TGA has further confirmed the depletion of the -CH_x with increasing the water mole ratio. This study demonstrated the big organic precursor molecules suffer from incomplete hydrolysis reaction on the nanosubstrates. The latter statement has been further confirmed by using the titanium ethoxide (small molecules) which gives a smooth and dense layer. The next following chapters are illustrating some applications for the CLD method.

Chapters 4 and 5 are focused on a catalyst that was synthesized using a high surface area TiO_2 on carbon nanotubes to support platinum nanoparticles coupled with tin oxide and it was used for ethanol electrooxidation and oxygen reduction reaction, the catalyst was denoted as Pt@ST/CNTs. The electrochemical results showed a remarkable activity in both approaches. The prepared catalyst exhibited a considerable electro-catalytic activity for ethanol oxidation (EOR) with 350 mV negative onset potential relative to Pt/C (E-TEK). In addition, it showed an enhancement in the durability based

on i-t curve at 705 mV by ~2.2 times. Transmission electron microscopy (TEM) revealed a rough- porous surface of TiO_2 as well as the crystalline states of SnO_2, TiO_2, and Pt NPs after they were annealed. X-ray photoelectrons (XPS) revealed a 0.9 eV positive shift in SnO_x binding energy. Cyclic voltammetry (CV) and the polarization test (ORR), showed a remarkable improvement in the onset potential of this catalyst. The half-wave potential of the prepared catalyst recorded a positive shift by 38 mV, as compared to a Pt on carbon catalyst. The fluffy-TiO_2 layer showed very high specific surface areas of 310 m^2/g. X-ray diffraction (XRD) revealed a rutile phase formation R (110) after incorporating SnO_2 in which a second annealing was carried out. Furthermore, X-ray photoelectron spectroscopy showed a shift in Sn 3d, Ti 2p, and Pt 4f binding energies indicating a flow of electrons among the catalyst elements.

Chapter 6 introduces a catalyst consisting of platinum and iridium nanoparticles decorated onto a fluffy 10-nm doped -titanium dioxide layer on carbon nanotubes. This catalyst, denoted Pt-Ir/C-TiO_2/CNTs, was used for methanol electro-oxidation (MOR). Fluffy TiO_2 coating layer was utilized with a high surface area support to host the metals nanoparticles with small nanoparticles size. Having them incorporated on doped TiO_2 with small size particles secures a decent number of the active sites toward methanol molecules; therefore, the catalyst activity is enhanced. Based on electrochemical results of MOR, Pt-Ir/C-TiO_2/CNTs has shown a significant improving regarding the anodic to the cathodic current ratio 5.6-fold magnitude and a negative shift in scan onset by 0.12 V relative to Pt/C (a commercial catalyst of Pt supported on CB from E-TEK). A positive shift in Pt and Ir binding energies was revealed by XPS indicating the metals

shared electrons as a back donation with TiO_2. We impute the high forward / backward ratio and the high current after 3600 seconds to hydrated iridium oxide phase incorporated on reduced Ti_xO_{2-x} where a layer of surface hydroxyl is formed on the hydrous oxide supplying protons to Pt-CO_{ads}. All other characterizations such as X-ray diffraction (XRD), X-ray photoelectron spectroscopy (XPS), transmission electron microscopy (TEM), and electron energy loss spectroscopy (EELS) were carried out to get deep insights for the prepared catalyst.

In Chapter 7, another catalyst was synthesized for oxygen reduction reaction approach. The catalyst is comprised of 3-5nm thickness of niobium oxide layer on carbon black to host platinum nanoparticles (Pt NPs). The catalyst, which was denoted Pt/c-Nb_2O_5/CB, was used toward oxygen reduction reaction (ORR). X-ray Photoelectron spectroscopy (XPS) results revealed a positive shift in Pt binding energy indicating electrons delocalization between Pt NPs and the oxide layer. Whereas a negative shift in Nb 3d was observed and this is because of the carbon doping at 700 °C. This is also associated with a partial phase transformation in Nb_2O_5 to reduced and conductive form. The experimental results for the activity and the durability were both enhanced relative to Pt/C (E-TEK). The kinetics region showed a 25-mV positive shift in the half-wave and a 1.7% loss after 5000 cycles. We attribute this improvement to a well-designed Nb_2O_5 layer underneath the Pt NPs leading to sharing a strong bond with Pt NPs and to resisting the carbon corrosion. Elemental mapping (EELS), transmission electron microscopy (TEM), X-ray diffraction (XRD), X-ray photon spectroscopy

(XPS), and thermogravimetric analysis (TGA) were conducted to get more information about the catalysts composite.

In Chapter 8, combining different valences in metal oxides, we used niobium pentoxide (Nb^{5+}) as a coating agent on carbon black and tin oxide (Sn^{2+}) as a promoter with platinum nanoparticles (Pt NPs) in methanol oxidation (MOR), the catalysts are denoted Pt-TNb/C (with tin oxide) and Pt-Nb/C (no tin oxide). XRD revealed a change in NbO_x phase from partially orthorhombic to fully orthorhombic upon tin oxide loading which is followed by annealing at 600 ºC under nitrogen gas. XPS analysis displays and further confirms there is a synergistic effect between carbon doped-NbO_x and SnO_2. After the carbon doping, oxygen defects are created leading to have sub-stoichiometric of niobium oxide. This has produced a stable SnO_2 and has reversed c-NbO_x to a highly oxidized form which both are required in MOR anode reaction as oxygen surface sources. After 1000 cycles in 1.0 M CH_3OH, Pt-TNb/C has shown (0%) loss in the mass activity compared to (20%) and (31%) in Pt-Nb/C and Pt/C, respectively. Moreover, the Pt-TNb/C shows a remarkable mass activity of 2.7 A/mg_{pt} which is superior compared with a list of papers. We highlight that tin oxide with niobium oxide have the key role on the catalyst activity and stability; however, niobium oxide alone failed.

Finally, Chapter 9 summarizes the conclusions of the dissertation and points out some potential work for the future.

Chapter 2. Nano-Layer Deposition in Liquid Hydrocarbons using Condensed Water Film

- Published in communication material-nature articles DOI: 10.1038/s43246-020-0010-9

Abstract

Traditionally, nanocoatings have been made through various processes, such as the sol-gel and atomic layer deposition techniques. Here we report a new, versatile, and fundamentally different technique, the condensed layer deposition (CLD) technique, in depositing conformal metal oxide nanocoatings on nanoparticles and nanofibers dispersed in liquid hydrocarbons. The CLD technique takes the advantage of the ultralow solubility of water in liquid hydrocarbons in condensing a water film on the substrate surface. The interfacial tension between polar water and nonpolar liquid hydrocarbons creates a uniform nanoscale water film on the nanomaterial substrates, as visualized in CryoEM. Chemical precursors subsequently introduced then react with the condensed water film to form a metal oxide nanocoating (including titania, alumina, or niobia) deposited on various nanomaterial substrates (carbon nanotubes, iron oxide particles, or carbon black). Our results show that the CLD technique can deposit conformal metal oxide nanocoatings on a variety of substrates with tunable thicknesses, in one pass, at room temperature. Furthermore, metal oxide nanostructures were made after thermally-oxidized the carbon substrates, CNTs and CB, producing titanium oxide nanotubes, alumina nanotubes, and niobia nanoshells.

2.1. Introduction

Nanocoatings are coatings or thin films on a solid surface. They play an important role in altering surface properties, such as hydrophobicity, durability and reactivity [115].

Nanocoatings can be applied to a surface using a variety of techniques, in both gas and liquid phases. Coatings made in liquid phase processes do not require sophisticated and expensive tools comparing with the gas phase techniques. One widely used process is the sol-gel technique, in which sols are formed often in an aqueous solution and gel when deposited onto a surface to form a thin film [116, 117]. However, the wet-chemistry coating route can be affected by several factors, such as substrate concentrations, functional groups, surfactants and solvents. Despite that nanoscale coatings have been made through sol-gel methods [26, 118], it is often difficult to control the thickness to a few nanometers and often produces coatings in the sub-micron scales [119, 120].

Chemical vapor deposition (CVD) is a well-known method to deposit atomic and nanoscale coatings on a surface [121, 122]. This method and its variations normally involve a reactive chemical precursor that can react on a solid surface to form a coating. While it requires vapor precursors and often high temperatures to prevent the condensation, the coatings formed are mostly dense. Another commonly used vapor process is the atomic layer deposition (ALD)[123-125]. The ALD technique uses various oxygen sources such as water vapor, molecular O_2, ozone O_3, and O_2 from plasma to react with chemical precursors that can be vaporized [126]. By flowing consecutively, a chemical precursor vapor in a carrier gas, a purge gas, and a gas with water vapor in a cyclic manner, a nanocoating can be deposited on a substrate surface in a layer-by-layer fashion at the atomic scale. Solution ALD was reported most recently, in which chemical precursors were dissolved in a liquid and flown passed the substrate surface for a layer-by-layer deposition [127].

Another method using gas infiltration, combined with ALD or CVD, has been reported to make coatings, especially on internal surfaces or pores [128-130]. The gas phase

infiltration method takes the advantage of gaseous condensates inside pores, transforming them into coatings on the inside walls of nano- or micro-channels, as demonstrated for transforming porous alumina membranes to silica nanotubes [130]. The coatings made in such ways are conformal to the inside walls of channels or pores. The gas infiltration processes still need gas phase precursors. In microemulsions[131] there exist two immiscible liquid phases, water and oil, and if oil is the continuous phase, water droplets can be formed in oil. When a surfactant is added, it can adsorb onto the water droplet surface and make a stable water in oil emulsion, in which the surfactant layer can be viewed as a coating on water droplets [132, 133]. Such water in oil emulsion systems have been used to make nanoparticles and coatings on them [134, 135].

Built on the aforementioned work, we report a fundamentally different process for making nanocoatings on the outer surface of nanoscale solid substrates. We have developed a condensed layer deposition (CLD) technique, which employs a liquid hydrocarbon as oil phase to disperse particles to prevent their aggregation. Uniquely, the CLD technique utilizes nanoscale condensed water films to react with chemical precursors in creating metal oxide nanocoatings. The ultralow solubility of water in oil makes it possible to condense it on solid substrates. The high interfacial tension makes the condensed water film conformal on the outer surfaces on the substrates. In theory, a wide range of metal oxide nanocoatings can be deposited if metalorganic precursors can be dissolved in liquid hydrocarbons. Nanocoating thickness can be controlled as desired and is a function of the water film thickness. The new CLD technique can make conformal metal oxide nanocoatings on various nanoscale surfaces in one pass at room temperature.

The experiments were conducted under an inert atmosphere (N_2 gas H_2O content <10 ppm) trying to create a dry atmosphere. This could eliminate the effect of the water vapor in the air to the coating reaction due to the moisture sensitivity of the used metal alkoxides precursors [136]. We were able also to make a porous-dense metal oxide nanostructures such as Nb_2O_5 nanoshells, TiO_2 nanotubes, and Al_2O_3 nanotubes. A computer modeling was performed by using math lab to know how the water condensation is taken place on the substrate (CNTs was used in the model). The physics part in the modeling is by using the mass transfer equation. *Sherwood*, *Reynold*, and *Schmitt* numbers were used to figure out the mass transfer coefficient (K). In addition, the curvature and the surface tension were considered as a part of *Kelvin equation*. The modeling results indicated a higher water mole flux into the CNTs surface with increasing the added water which is reasonable as the mass transfer law indicates. To prove the water film formation, the mixture of H_2Oads-CNTs-heptane was exposed to a sudden freezing at 93 K in liquified ethane surrounded by liquid nitrogen jacket. The process has led to freeze the water layer on the CNTs and IOPs resulting in a dense ice layer. The latter layer was proven by performing a Cryogenic TEM. In such complicated system, knowing the film identity is a crucial since heptane might freeze as well.

To eliminate such ambiguity, the layer was exposed to a slow *online-temperature* ramping from (-170 °C to -130 °C) inside the high resolution TEM scope in a cryo-holder. At -135 C, the ice layer phase transformed from vitreous phase to cubic ice as confirmed by the FFT diffraction pattern. For further confirmation, electron energy loss spectrum (EELS) has confirmed the characteristic ice characteristics peaks.

2.2. Experimental Section

2.2.1 Materials and Chemicals

Titanium ethoxide (TEO) (99.9 % metal basis), niobium ethoxide (NEO) (99.9 % metal basis), and trimethylaluminum (TMA) (2.0 M in heptane) were obtained from Alfa Aesar. Heptane (HPLC grade) was purchased from Fisher Scientific. Nitrogen gas (99.99% UHP) was obtained from Airgas. Carbon nanotubes (CNTs) from Pyrograf Products, 60–150 nm in diameter and 30–100 μm in length) were used. Carbon black (CB) (XC-72 Vulcan) used was. Iron oxide particles (IOPs) (average primary particle size ~ 50 nm) was purchased from Sigma-Aldrich.

2.2.2 Syntheses

2.2.2.1 Reactor and Procedures for Making Nanocoatings

The reactor for making the nanocoatings is a regular polypropylene bottle (100 mL) for lab use. This bottle was chosen for the purpose of having a hydrophobic surface to avoid adsorption of water on its walls. Ultrahigh purity nitrogen gas was used to purge moisture in the reactor for 30 minutes to ensure there is minimum water vapor (<10 ppm) in it. The bottle is then filled with certain amount of heptane as the solvent, or the oil phase, which is protected on top with nitrogen gas blanket from any room moisture contamination. The bottle was capped, but with tubing inlets and a vent hole on the cap. The tubing inlets are for injection of water and chemical precursors during experiments. A vertical sonication probe installed through the cap was used for stirring.

2.2.2.2 Substrate Surface Functionalization

The substrates used in this study, CNTs, IOPs, and CB, were surface functionalized before use. The purpose of this procedure was to create hydrophilic surfaces so that water can be easily condensed on them. CNTs have mostly graphitic surfaces that are hydrophobic, and therefore they were treated in a mixture of concentrated acid (6.0-8.0

M), which consists of 3:1 (v/v) H_2SO_4:HNO_3 [137]. The treatment was conducted in an ultra-sonication bath at 60 °C for 2 hours. They were then washed with deionized water thoroughly to remove any residual anions that would affect the substrate dispersion in the oil phase. They were further dried in a vacuum furnace at 65 °C for 4 hours. Similarly, IOPs and CB were also surface functionalized in acids. Because these substrates should already have mostly hydrophilic surfaces, the acids used are diluted. For IOPs, 0.1 M sulfuric acid was used and it was treated under sonication at 60 ˚C for 1 hour. For CB, the acid concentration was a mixture of 3.0 M sulfuric acid and 0.1 M nitric acid, respectively. They were also thoroughly washed with deionized water and dried in a vacuum furnace before use.

2.2.2.3 Titania, Alumina, and Niobia Nanocoatings on CNTs

A 100 mg of functionalized CNTs was put in the reactor in 50 mL heptane. The sonication probe was inserted to disperse the CNTs under slow flow of N_2 gas as blanket on top of the heptane. The amount of water added to the dispersion was calculated, depending on a desired nanocoating thickness to make (see Table 1.1). For each experiment, the dispersion was vigorously sonicated for 20 minutes after water addition. The sonication probe created strong vortex that enhanced convective mass transfer for the water to reach the substrate surfaces, where it can condense. A nitrogen-flushed glass vial (20 mL) was used to prepare the chemical precursor solution in heptane. In the case of TiO_2, TEO was dissolved in heptane in the vial under inert atmosphere. It was then pipetted into the reactor with the CNT dispersion. It was allowed for 10 minutes as a total reaction time under sonication. After the reaction was completed, the TiO_2 coated-CNTs were centrifuged and dried. To make Al_2O_3 nanocoatings on CNTs, the procedures are similar, except that the precursor was changed to trimethylaluminum (TMA) dissolved in heptane. The water amount was

calculated based on its reaction with TMA for different coating thicknesses desired (see Table 1.2). To make Nb_2O_5 nanocoatings on CNTs, NEO precursor was used, and the procedure is similar to the case of the TiO_2 coating procedure.

2.2.2.4 Titania, Alumina, and Niobia on IOPs

After surface functionalization, the iron oxide particles (IOPs) must be washed thoroughly to remove any residual of SO_4^{2-} anions. Flushing the reactor by ultrahigh purity nitrogen gas for 30 minutes to ensure there is minimum water vapor. A 100 mg of functionalized IOPs was put in the reactor, and a 30 mL heptane was poured in. The sonication probe was used to disperse the IOPs, also under a slow flow of N_2 gas. To increase dispersibility of the IOPs, a 1.0 mL of ethanol was added and left for 15 minutes to disperse. The amount of water added depends also on desired coating thicknesses. TEO, NEO or TMA precursors in heptane was injected to the dispersion to obtain the corresponding nanocoatings, following similar procedures as in the case of CNTs described above.

2.2.2.5 Titania, Alumina, and Niobia on Carbon Black

The same procedure for the case of coating CNTs was followed in coating carbon black, except that functionalized carbon black is the substrate.

2.2.2.6 Ice Layer Formation

The water film vitrification was conducted as follows: 100 mg CNTs or IOPs was dispersed in heptane and 75 micro-liters of water was added via a pipette. The dispersion was sonicated for 30 minutes. The sample was secured carefully by parafilm to reduce contact with ambient air. MultiA grids (200 mesh, Quantifoil Micro Tools GmbH, Großlöbichau Germany) were glow discharged (Pelco Easiglow, Ted Pella, Redding CA USA) for 45 sec at 0.38 mbar 15 mAmp. Water-coated CNT or IOP dispersions in heptane (10 uL) was sonicated again and immediately was added to a

freshly glow discharged MultiA grid, loaded into a Mark IV Vitrobot (FEI Co, Hillsboro OR USA) with a chamber set at 10 ℃ and 100% humidity and plunge frozen into an ethane slush. Vitrified specimens were transferred to liquid nitrogen and stored until visualization by cryogenic transmission electron microscopy (cryoEM).

2.2.2.7 Synthesis of Al_2O_3 and TiO_2 Nanotubes, and Nb_2O_5 Nanoshells

A 10 mg of alumina-coated CNTs, titania-coated CNTs, or niobia-coated carbon black was placed in a ceramic boat, which was put in a quartz tube furnace. Under air flow, the oxidation process was conducted at 500℃ for 24 hours. Samples were collected from the ceramic boat for further characterizations.

2.2.2.8 Transmission Electron Microscopy (TEM) / Elementals mapping

Two types of transmission microscopes were used. For sample pre-check and preliminary analysis, the JEOL JEM-1400 equipped with Lanthanum-hexaboride (LaB6) filament was operated at an acceleration voltage 120 kV and data were collected on the Gatan Ultrascan 1000 CCD camera. For further investigation, we used a FEI Tecnai F30 Twin TEM equipped with analytical spectrometers (Bruker Quantax 400 Silicon Drift Detector or Quantum 963 Gatan Image filter (GIF)). Brightfield images were acquired on a Gatan Ultrascan 4000 charge coupled device at 300 kV and energy filtered-TEM (EFTEM) maps were acquired at 300 kV with the Quantum GIF in EFTEM imaging mode. A suitable objective aperture (40 micron in diameter) centered on the directed beam in the diffraction pattern was used to increase the sharpness and spatial resolution of the EFTEM maps. The scanning TEM (STEM)-electron energy loss spectroscopy (EELS) spectrum image was taken at 300 kV in the high angle annular dark field image mode with a collection semi-angle of 11 mrad defined by a 2.5 mm entrance aperture of the GIF and a camera length of 100 mm.

2.2.2.9 Cryogenic Transmission Electron Microscopy Imaging (CryoEM)

The vitrified specimen was loaded into a side-entry cryoholder (Gatan 626, Gatan Inc Pleasanton CA USA) at -180 ^{o}C which was transferred to the FEI Tecnai F30 Twin TEM (FEI Co, Hillsboro OR USA). Images were acquired at -170 ^{o}C using low dose conditions (0.2 sec exposure, ~20 $e^{-}/Å^{2}$) at a nominal magnification of 39,000X on a Gatan Ultrascan 4000 CCD (U-type pixels, Gatan Inc, Pleasanton CA USA) at 200 keV, gun lens 1, extraction voltage of 3900 microAmps, with 100 and 40 micrometer apertures for C2 and objective lenses, respectively. The plunge-frozen samples were visualized using the cryoEM with a low irradiation fluence (20 electrons/$Å^{2}$).

2.3 Results and Discussion

2.3.1 Three Substrates Coating by TiO_2, Al_2O_3, and Nb_2O_5

The process for depositing nanocoatings using CLD is illustrated in figure 2.1 (a). Nanoparticle substrates are first dispersed in a liquid hydrocarbon as the oil phase (e.g., heptane in this work). A small, measured amount of water is then added and fully dispersed in the oil phase. When the water is above its saturation point figure 2.2 [138], it condenses out on the nanoparticle surface. A nanoscale water film is thus conformally formed on the surface of the nanoparticles due to interfacial tension between polar water and nonpolar oil. When a chemical precursor is injected into the nanoparticle dispersion, it reacts with the condensed water film to form a metal oxide nanocoating. After separating out the solid substrates, the oil phase can be recycled by vacuum filtration and distillation and reused.

Titania nanocoatings were made in the CLD process on carbon nanotubes (CNTs). Figure 2.1 (b-e) shows a low magnification transmission electron microscopy (TEM) image of bare CNTs, TiO_2/CNTs, E-FTEM of TiO_2/CNTs, and elementals mapping, respectively. To render the CNTs surface hydrophilic, they were sonochemically

functionalized [137] before use. Titanium ethoxide (TEO) was used as a chemical precursor to titania nanocoatings. After the water condensation process, a measured amount of TEO was injected into the CNTs dispersion.

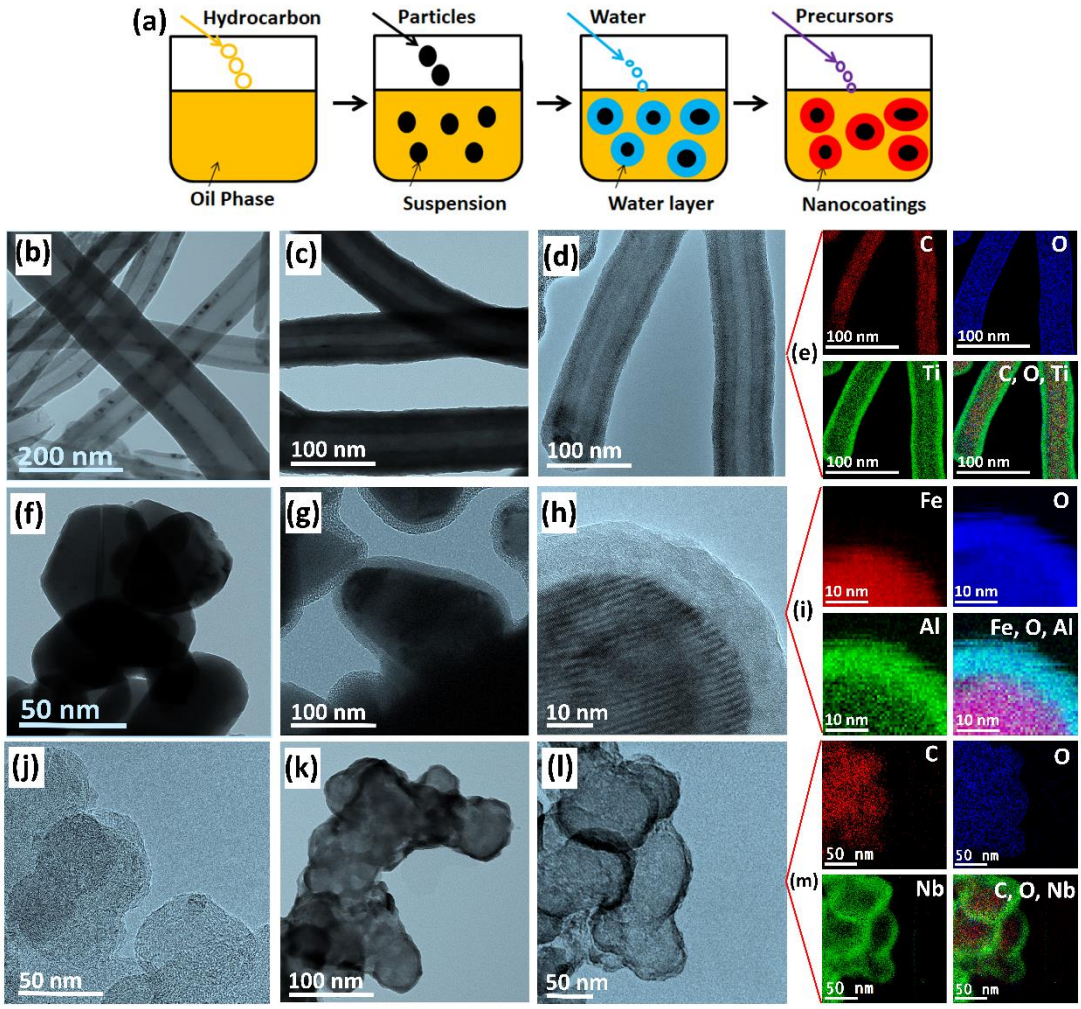

Figure 2.1. (a) Cartoon shows the coating steps, (b) A low resolution TEM for bare CNTs, (c) A low resolution TEM for TiO_2/CNTs, (d) EF-TEM for TiO_2/CNTs, (e) Elementals mapping of TiO_2/CNTs, (f) A low resolution TEM of bare IOPs, (g) A low resolution TEM of Al_2O_3/IOPs, (h) STEM image of Al_2O_3/IOPs (i) Elementals mapping of Al_2O_3/IOPs, (j) TEM image for bare CB, (k) A low resolution TEM of Nb_2O_5/CB, (l) EF-TEM for Nb_2O_5/CB, (m) Elementals mapping of Nb_2O_5/CB.

As shown in figure 2.1 (d) titania nanocoatings were clearly seen to be deposited on the CNTs. The deposition of titania nanocoatings were confirmed in figure2.1 (e) through energy filtered TEM (EFTEM) elementals mapping, which shows that the material consists of C, Ti and O, and the nanocoating consists of only Ti and O, indicative of formation of titania on the CNTs.

Using trimethylaluminum (TMA) as a chemical precursor, alumina nanocoatings were made on iron oxide particles (IOPs). The IOPs, mostly in aggregate form as in figure 2.1 (f), were surface functionalized in dilute acids. It can be seen from figure 2.1 (g-h) that uniform and conformal alumina nanocoatings were obtained on IOPs, even at sharp corners as in figure 2.1 (g). At the neck of two particles figure 2.1 (g), the nanocoatings were observed to be a little thicker, which was attributed to the meniscus formed from capillary effect during water condensation. While the surface at the neck is concave, the CLD technique may not be able to make a conformal coating inside nanopores as achieved in the gas filtration method [130]. The reaction of TMA with water is extremely exothermic, and follows the idealized reaction, $2Al(CH_3)_3 + 3H_2O \rightarrow Al_2O_3 + 6CH_4$ for a complete reaction. Elemental mapping of the nanocoatings achieved by scanning TEM-electron energy loss spectroscopy (STEM-EELS) (figure 2.1 (i)) showed that Al and O exist only in the nanocoatings.

Niobium ethoxide is another precursor has been used in CLD process to make coating layers on carbon black (CB). Like IOPs, CB suffers from the aggregation as well which could reduce the exposed surface areas for the coating as in figure 2.1 (j). Due to nanocrystalline structure, CB was surface functionalized by 3.0M of acids. It is seen in figure 2.1 (k) the layer of Nb_2O_5. The EF-TEM image in figure 2.1 (I) shows clearly the coating film and its elementals mapping depicted in figure 2.1 (m).

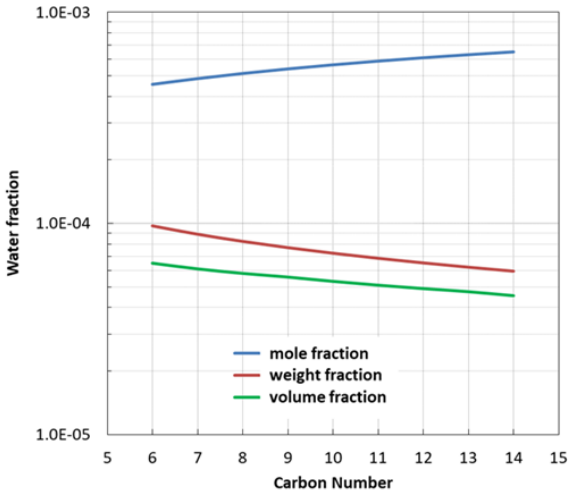

Figure 2.2. Solubility of water in mole, weight and volume fractions in relation to the carbon numbers at 20 °C. Adapted from Reference [138]. For heptane, it is about 61 ppm by volume.

2.3.1.1 Surface Chemistry

Metals precursors are chemisorbed onto the surface then they start the hydrolysis and condensation reactions [101, 139].The mechanism of the hydrolysis reaction is typically explained as a nucleophilic substitution where water acting as a Lewis base and metal atom of the alkoxide precursor acts as a Lewis acid [140]. It has been stated that one of an oxygen lone pair of a water molecule attacks the positively charged metal atom as a first step. Then, protons transfer from water molecules to negatively charged adjacent ligands-groups compelling those groups to depart the precursor molecule structure as in the scheme 2.1:

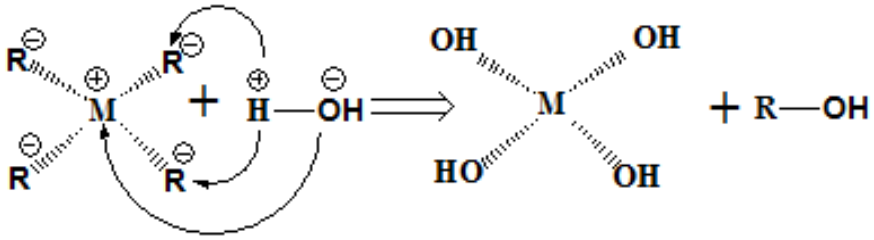

Scheme 2.1. Shows the hydrolysis mechanism.

As soon as the hydrolysis step has occurred and a metal hydroxide (monomer) has been produced, the condensation step starts; however, it is rather a complicated mechanism and it may be responsible on metal oxide layer morphology.

The condensation process yields amorphous oxides that can be crystallized at higher temperatures [141]. There are two different competitive pathways for the condensation either alkox-olation or olation to reject either alcohols or water molecules [142]. The condensation mechanism starts as a nucleophilic attack of an oxygen lone pair of a metal hydroxide to a positively charged metal atom M as in the scheme 2.2:

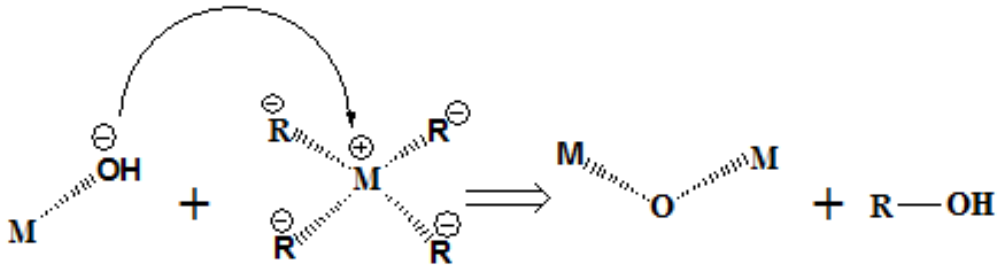

Scheme 2.2. Shows the condensation mechanism.

Sanchez and Ribot have described the reactivity of different metal alkoxides precursors. They stated the electrophilic property is not the only reason but rather is more a function of unsaturation degree [143-145]. The degree of unsaturation is defined as the difference between the metal oxidation state (Z) and the coordination number (N) of the atom in the stable oxide form. For instance, silicon oxide has Z=4 and N=4 that makes the unsaturation degree N-Z=0. The zero value explains the weak reactivity of the silicon precursors toward the moisture without any catalyst such as a base or an acid [146]. Unlike silicon, titanium and niobium ethoxides and trimethylaluminum precursors have 2 and 3 unsaturation degree, respectively [147, 148]. The precursor's reactivity decreases as the ligands attached to the metal center getting bigger [145]. From a geometric perspective, niobium ethoxide is a dimer molecule with ten ethoxide ligands. Each niobium atom is octahedrally surrounded by four terminal ligands and two bridging ethoxide ligands. During the poly-condensation, the two centered Nb-atoms increase the possibility of nucleophilic substitution because both metals are coordinately saturated forming a tetramer of niobium pentoxide. In addition, the two

Nb-atoms hold identical tendency to water since they are homogeneous without a difference in the electronegativity [139]. On the other hand, titanium ethoxide is originally tetramer with four titanium atoms (Ti) in its chemical formula. Each Ti-atom metal center has an octahedral coordination environment [149].

2.3.1.2 Thickness Control of TiO_2 and Al_2O_3 on CNTs

The nanocoating thickness is limited either by the water amount or by the precursor amount in a complete reaction. With a fixed amount of water in each experiment, the water layer thickness is dependent on the total surface areas of the nanoscale substrates as well as the temperature of the experiment. Control of the nanocoating thicknesses in the current work was achieved through control of condensed water film thicknesses. For heptane used in this study, a saturation concentration of water is 61 ppm by volume at room temperature (20 °C), see figure 2.2 [138]. Any additional water beyond this concentration would condense out on the hydrophilic substrate surfaces.

Several nanocoatings of titania and alumina with different thicknesses have been made on CNTs. Shown in figure 2.3 (a) are TEM images of three titania nanocoatings, with thicknesses ranging from ~5 to 45 nm. For the alumina nanocoatings as in figure 2.3 (b), thicknesses achieved range from ~10 to 70 nm. The specific surface area of the CNTs was measured to be 44 m^2/g by the Brunauer–Emmett–Teller (BET) method. With this surface area, water was added accordingly to achieve a desired thickness (Table 2.1 and Table 2.2). The predicted nanocoating thickness was determined by calculating the amount of oxides generated from the corresponding reaction of the precursor and the condensed water film. The actual thickness was obtained by analyzing the bright-field, high-resolution TEM images. As shown in figure 2.3 (c), the predicted titania thicknesses are in close agreement with the actual thicknesses, except for the nanocoating at 43 nm. Interestingly with alumina nanocoatings, the predicted

thicknesses are much smaller than the actual thicknesses in basically all cases as in figure 2.3 (d). Previous studies have shown that the reaction between TMA and H_2O is rather complex, involving many intermediate species in gas phase processes [150-152]. Such intermediate species could be trapped in the alumina nanocoating, which is formed starting from the outside and growing to the inside in the CLD process. A complete reaction will need two TMA molecules and three water molecules to form Al_2O_3. In a kinetically driven reaction as such, there could be a local shortage of water, leading to an incomplete reaction. Indeed, the XRD on the alumina nanocoatings shows that they consist of a γ-AlOOH phase (*see figures 2.7 and 2.8 in section 2.3.1.3 Phase structure of coating layer*), indicating an incomplete reaction, a reason for the increased nanocoating thickness in Al_2O_3. Furthermore, when the alumina nanocoatings were heat treated at 600 °C in air, they became thinner and denser as in figure 2.4, which was attributed to release of unreacted organic components trapped in the nanocoatings. In contrast, the thinner titania nanocoatings showed no obvious changes in thicknesses before and after heat treatment, but only became crystalline (*see figure 2.7 in phase structure of coating layer section*). Elemental analyses from EELS identified Ti (L-edge) and O (K-edge) in the titania nanocoatings and Al (K-edge) in the alumina nanocoatings are shown in figure 2.5. STEM-energy dispersive X-ray spectroscopy (EDS) provided additional evidence of the alumina nanocoating deposition on CNTs as in figure 2.6.

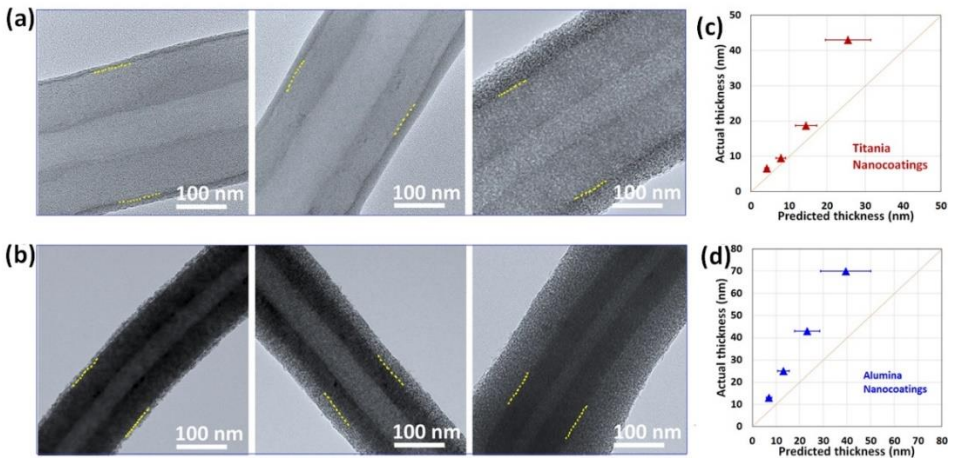

Figure 2.3. (a) TEM images of titania nanocoatings on CNTs showing three different thicknesses, with the yellow dash-dotted lines as guide for the eye, (b) TEM images of alumina on CNTs showing three different thicknesses, (c) Predicted and actual thicknesses of titania nanocoatings, with the diagonal line indicating the same thicknesses. The error bars are estimates in calculating the predicted thicknesses, see Supplementary Table 2.2, (d) Predicted and actual thicknesses of alumina nanocoatings.

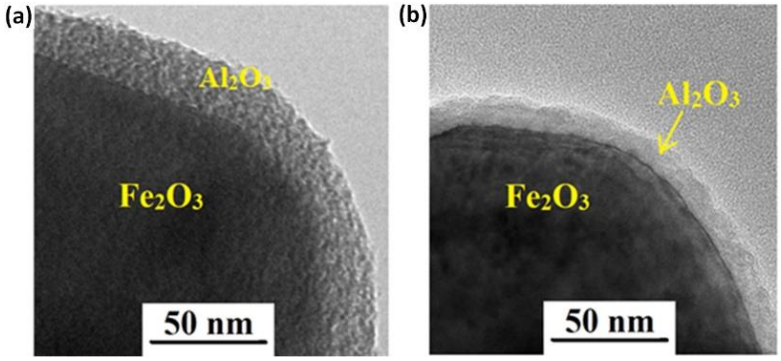

Figure 2.4. Alumina nanocoatings before and after heat treatment. (a) TEM image showing an as-deposited alumina nanocoating on iron oxide particles, (b) After heat treatment at 600 °C in air, the alumina nanocoating became thinner and denser, indicative of possible trapping of intermediate species in the nanocoating during deposition.

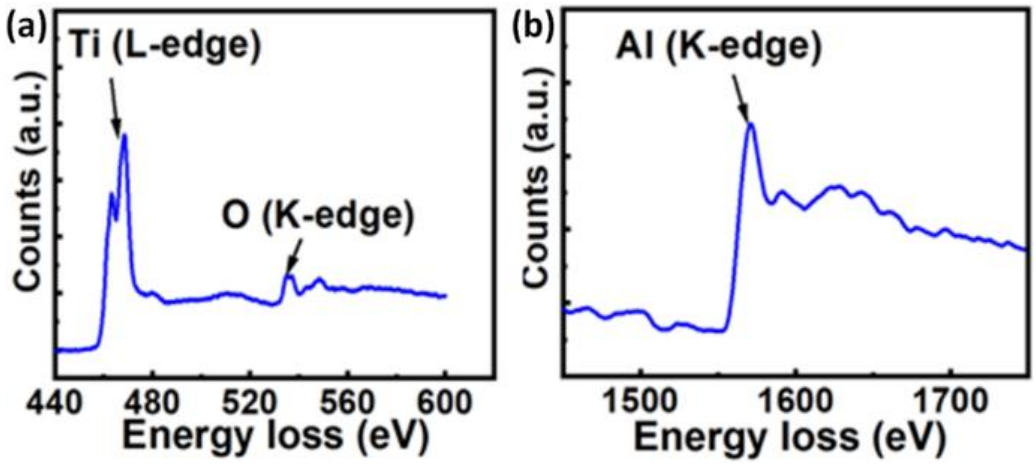

Figure 2.5. EELS spectra of the nanocoatings on CNTs (a) Titania nanocoatings showing Ti (L-edge) and O (K-edge), (b) Alumina nanocoatings showing Al (K-edge) (O K-edge is out of range).

Table 2.1. Water film and titania nanocoating thicknesses on CNTs*

Water added (μL)	Water added (mole)	Water film thickness (nm)	Stoichiometric TEO needed (mole)	Actual TEO added (mole)	Predicted thickness (nm)	Actual thickness (nm)
37	0.00205	7.6	0.00102	0.00115	4.1	6.6
74	0.00410	13.9	0.00205	0.00215	7.9	9.5
148	0.00820	24.7	0.00410	0.00430	14.5	18.7
296	0.01639	41.7	0.00820	0.00860	25.5	43.0

*Note: The water layer thickness is estimated from the added amount of water and the total surface of the CNTs that need to be covered. Thickness calculations are as follows. The total surface of substrate is: $S = 2\pi r_1 * L$, where r_1 and L are the outer radius and length of CNTs, which can be obtained from the BET specific surface area and the amount of CNTs used. The coating on the cylindrical CNTs surface has cross-section area of $A = \pi(r_2^2 - r_1^2)$ and material volume of $V = A * L$, where r_2 is the radius of the outer surface of the coating. Therefore, $r_2 = \sqrt{2r_1V/S + r_1^2}$, and the coating thickness $\Delta r = r_2 - r_1 = \sqrt{2r_1V/S + r_1^2} - r_1$. In the calculations, the water density used is 0.998 g/cm^3 (at 20 °C), titania (TiO_2) density is 4.23 g/cm^3, and alumina (Al_2O_3) density is 3.95 g/cm^3. The CNTs have a BET area of 44 m^2/g and an average radius of 34.0 ± 24.7 nm. The error bars in Fig. 3 c and d are estimated from the following derivative equation:

$$d\Delta r = \left(\frac{\frac{V}{S} + r_1}{r_2} - 1\right) dr_1 + \left(\frac{r_1}{r_2}\frac{1}{S}\right) dV + \left(-\frac{r_1}{r_2}\frac{V}{S^2}\right) dS$$

where errors in measurements in volume V and total surface area S are assumed to be 10%.

Table 2.2. Water film and alumina nanocoating thicknesses on CNTs.

Water added (μL)	Water added (mole)	Water film thickness (nm)	Stoichiometric TMA needed (mole)	Actual TMA added (mole)	Predicted thickness (nm)	Actual thickness (nm)
72	0.00399	13.6	0.00266	0.00300	7.1	13.0
144	0.00798	24.2	0.00532	0.00600	13.1	25.0
288	0.01595	40.9	0.01063	0.01200	23.2	43.0
576	0.03190	66.3	0.02127	0.02400	39.5	70.0

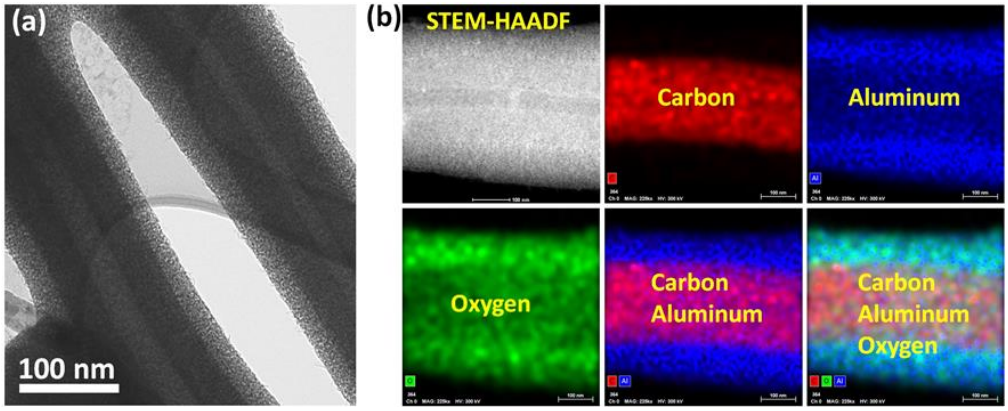

Figure 2.6. (a) TEM image of alumina coating on CNTs (b) Elementals mapping of alumina nanocoatings on carbon nanotubes STEM-HAADF image, and STEM-Energy dispersive X-ray (EDS) mapping for C, Al, O and all combined on CNTs, confirming an alumina nanocaoting with a coating thickness of ~70 nm.

2.3.1.3 Phase Structure of Coating Layer

Figure 2.7 shows the TEM images for the TiO_2 and Nb_2O_5 before and after the annealing. It is seen that before the annealing the material is in amorphous phase. This is because of two potential reasons the incomplete reaction on the substrate' surface and the coating process is carried out at room temperature [153]. A molecule of TEO reacts with water, according to $Ti(OC_2H_5)_4 + 2H_2O \rightarrow TiO_2 + 4C_2H_5OH$. Incomplete reactions could lead to amorphous titanium hydroxides, as confirmed from X-ray diffraction (XRD) before and after heat treatment as confirmed in figure 2.8. As in figure 2.8 (a), the phase of TiO_2 / CNTs (after annealing) is anatase phase as it is clear from the sharp peak at 2θ°=25.6 A (101) comparing with the peak at 2θ°= 27.8 R (110) [154]. On the other hand, figure 2.8 (b) shows a TT-Nb_2O_5 which is in good agreement with the crystallographic data [155].

The temperature effect could be conceived from the ALD process principles. In ALD, there are few parameters affecting the crystallinity such as temperature, reactants (precursors), impurities, and the film thickness [156]. These parameters are intercorrelated meaning it is hard to separate them since at a certain metal oxide it can be amorphous, or crystalline as in TiO_2 based on the deposition temperature [153]. Even

at TiO_2, the anatase phase was observed at 160-350 °C; however, a rutile phase was dominated at temperatures above 350 °C [157]. Also, TiO_2 film thickness has an impact on the crystalline degree based on the reaction of $TiCl_4$ and H_2O. It was reported that TiO_2 on RCA-cleaned Si is originally deposited in amorphous form, but when the films are made thicker, the films showed a crystalline structure [158] indicating the growth thickness has an impact as well.

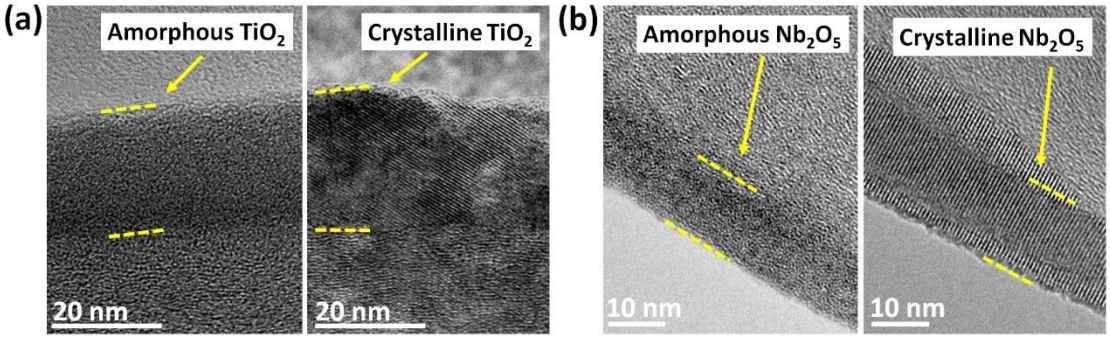

Figure 2.7. (a) TiO_2 before and after annealing at 600 °C, (b) Nb_2O_5 before and after annealing at 600 °C.

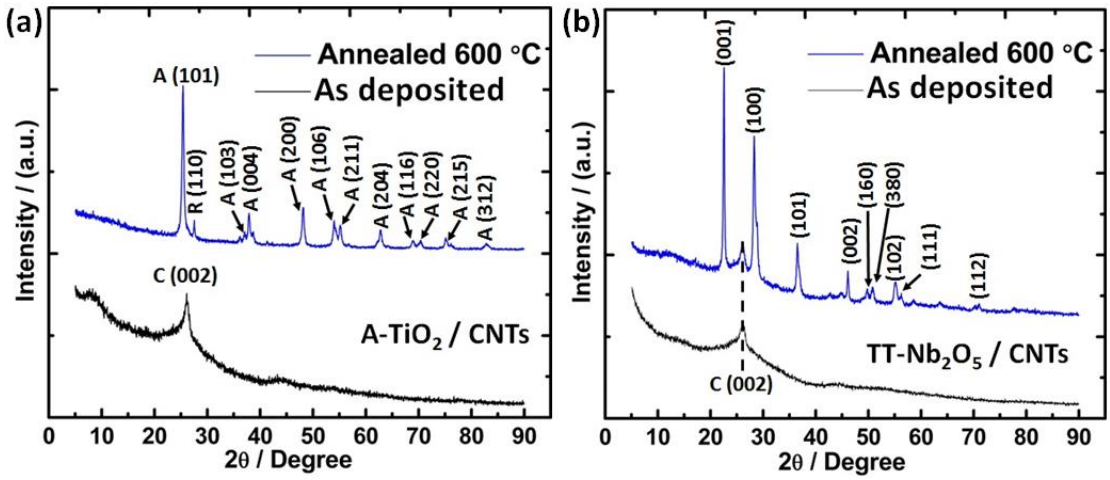

Figure 2.8. XRD pattern before and after the annealing for 1 hour (a) TiO_2 [159], (b) Nb_2O_5 [155].

Previous studies have shown that the reaction between TMA and H_2O is rather complex, involving many intermediate species in gas phase processes [150-152] nanocoatings. In Al_2O_3 and H_2O system, the amorphous film is always present up to ≤ 500 °C. The crystallization temperature is a function of the film thickness and annealing time as reported elsewhere [160]. The last study showed the 5 nm Al_2O_3 film crystallized at about 900°C in a 1-minute annealing and a 100 nm thick Al_2O_3 film

between 750 and 800 °C in 30 minutes annealing. Another study has correlated the crystallinity to the precursor original family such as halids, alkoxides, alkylamides, silylamides and aminoalkoxides. It was found ZrO_2 films that are derived from halide reactants are generally crystalline while it is amorphous film if the alkoxide was used [161]. A complete reaction will need two TMA molecules and three water molecules to form Al_2O_3. In a kinetically driven reaction as such, there could be a local shortage of water, leading to an incomplete reaction that possess some organic ligands from the precursor molecule.

Such intermediate species could be trapped in the alumina nanocoating, which is formed starting from the outside and growing to the inside in the CLD process. Figure 2.9 shows the XRD on the alumina nanocoatings shows that they consist of a γ-AlOOH phase, suggesting an incomplete reaction, a cause for the increased nanocoating thickness observed. This phase has transformed to γ-Al_2O_3 after the thermal treatment at 600 °C under the oxygen condition in which the CNTs have been oxidized producing Al_2O_3 nanotubes (figure 2.9 red line).

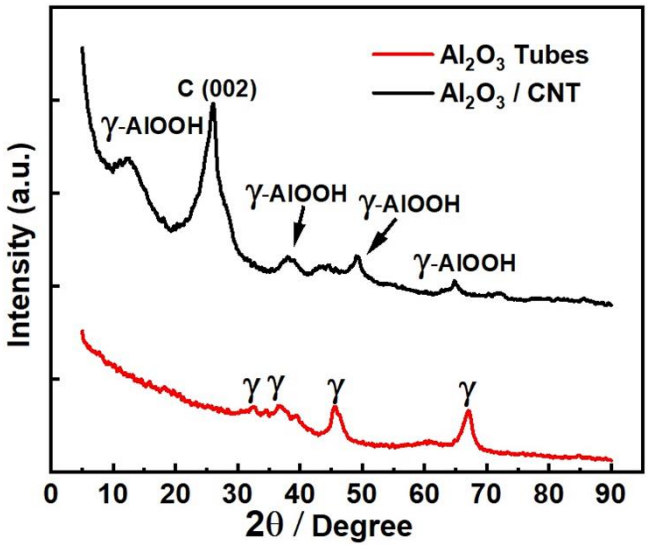

Figure 2.9. XRD patterns of alumina nanocoatings on carbon nanotubes, (a) The peaks can be indexed to γ-AlOOH phase alumina, indicative of that the alumina nanocoating has a crystalline structure but not that of Al_2O_3 for the as-deposited nanocoating, (b) The alumina nanotubes obtained from burning off carbon nanotubes inside have a γ-phase Al_2O_3 structure.

2.3.1.4 Thickness Control of Al_2O_3 on IOPs

Figure 2.10 (a) exhibits energy filtered-TEM image of a layer of Al_2O_3 /IOPs. The layer is transparent which is due to the amorphous phase. Figure 2.10 (b) displays the elementals mapping of oxygen, iron, and aluminum. Iron oxide nanoparticles are among the most used material in heavy metals removal technology from waste water due to its efficiency, low cost, easy to regenerate particularly the maghemite (γ-Fe_2O_3) [162]. The latter study has reported using maghemite nanoparticles for recovery of Cr (VI) from wastewater. However, the process is highly dependent on the pH and the lower pH the best adsorption. Nevertheless, IOPs is prone to dissolve at an acidic medium leading a loss at the adsorbent as called Fe-cation leaching. On the other hand, another study has reported a stability in IOPs after it was coated by other coating agent [163] or it is stacked as a composite with CNTs [164].

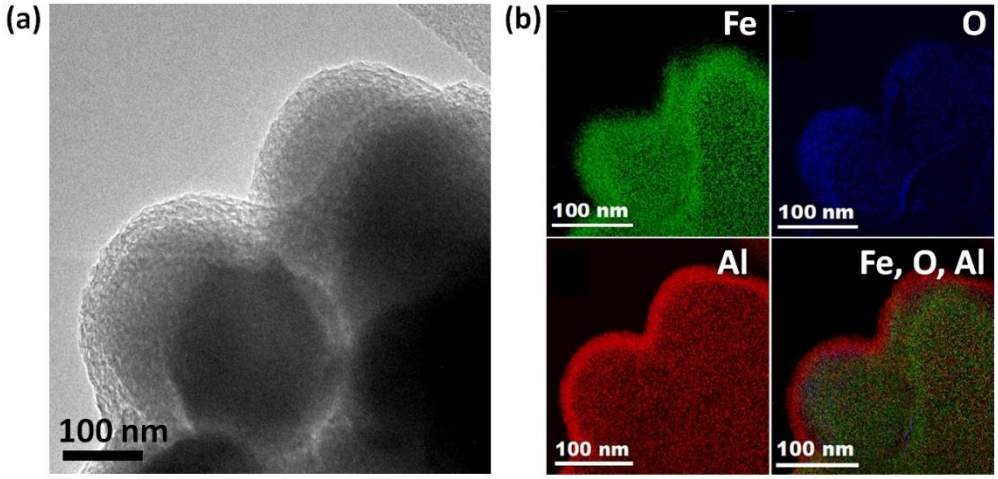

Figure 2.10. TEM images (a) Shows EF-TEM Al_2O_3 coating layer on iron oxide, (b) Elementals mapping.

Figure 2.11 (a-d) display the Al_2O_3 /IOPs coating with various thicknesses from 5 nm to ~37 nm. It is seen that the layers take a uniform shape. Uniform dispersion of solid substrates is also important and was achieved by using a sonication probe for stirring and mixing. When the nanoscale substrates are surface functionalized, their surfaces become (partially) hydrophilic. As a result, they tend to aggregate in oil, which can

become severe at high solid fractions. A small amount of alcohol can be added to alleviate this, allowing better dispersion of the substrates.

Ethanol has been used to reduce the surface tension, surface energy, and expose more surface area for the incoming precursor. It is believed that the particles would be highly hydrophilic, and they may behave like water molecules. Water molecule are strongly cohesive as each molecule may make four hydrogen bonds to other water molecules in a tetrahedral configuration [165]. Therefore, water-covered nanoparticles inside the heptane suffer from the cohesion force leading to forming clusters. Therefore, adding a surfactant becomes a must. Ethanol has hydroxyl and ethyl groups. The ethyl sides expose more on the water/ethanol layer surface where the surface energy can be reduced. Thus, ethanol becomes both a dispersant and a surfactant.

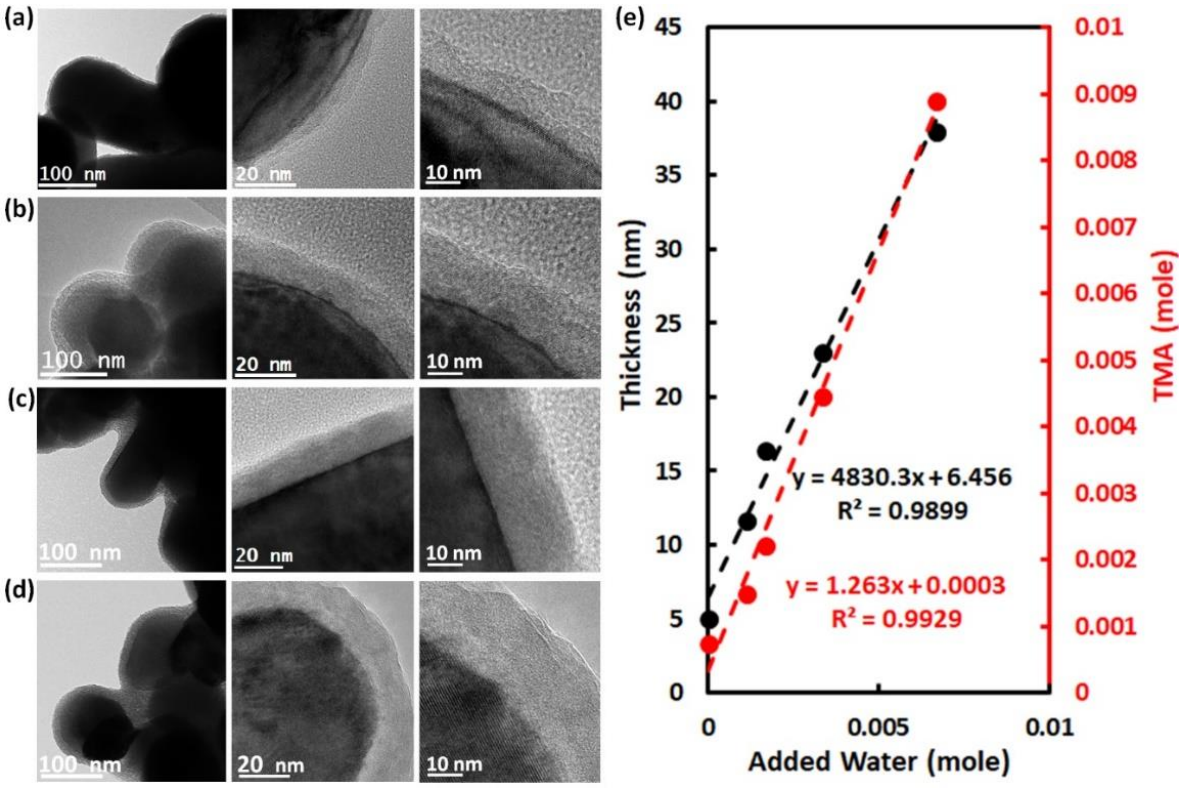

Figure 2.11. Smooth and conformal Al_2O_3 coating on iron oxide nanoparticles (IOPs), (a-d) Coating layer thickness starts at 5 nm up to 37 nm, (e) Shows the mole ratio of the water and the TMA(the used TMA concentration was 0.5 M).

Figure 2.12 (a) shows a TEM image of TiO_2 on IOPs with a uniform layer. Figure 2.12 (b) shows the elementals mapping and figure 2.12 (c) depicts the EELS spectra which

clearly displays the characteristics peaks of Ti ($L_{2,3}$ edge), O (K-edge), and Fe ($L_{3,2}$ edge).

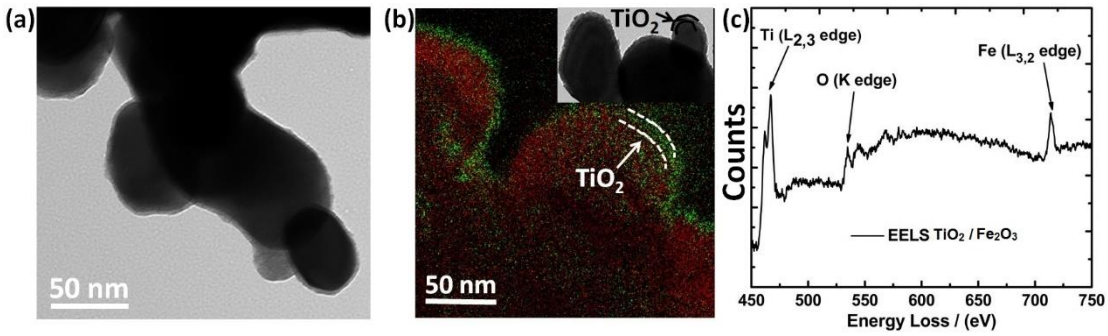

Figure 2.12. (a) A low resolution of TiO_2 on iron oxide, 20 mg of iron oxide was dispersed in 20 ml heptane. Then, it was left under sonication probe for 30 minutes than 6.74×10^{-5} mole of titanium isopropoxide was added, (b) Elementals mapping, (c) EELS spectrum.

Figure 2.13 (a) depicts a TEM image of the Nb_2O_5 coating on IOPs with the selected area (red-dotted box) displays a high resolution TEM image showing the lattice of both oxides the layer and the substrate. Figure 2.13 (b) shows the EELS for the Nb (L3, L2 edges), O (K-edge) and Fe (L3, L2 edges).

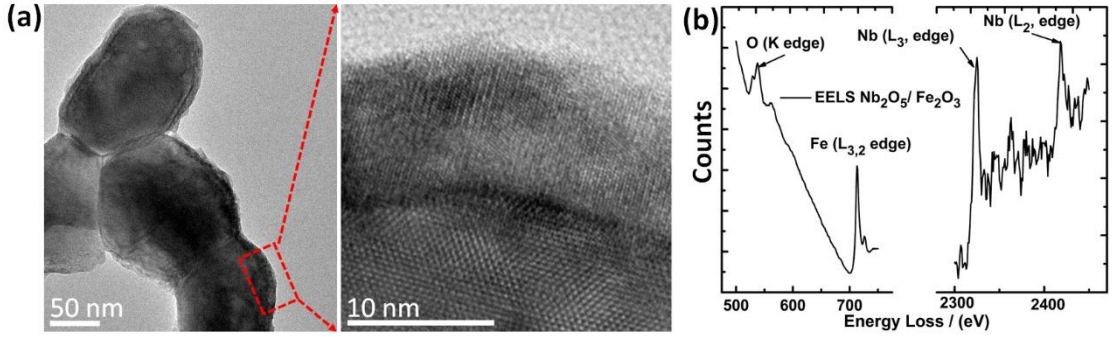

Figure 2.13. (a) A low resolution TEM of Nb_2O_5 on iron oxide, 100 mg of iron oxide dispersed in 30 ml heptane at the room temperature then 40 micro-L of water was added then 0.5 ml ethanol to improve the dispersion after 10 minutes sonication a 3 ml of 0.266 mole / L of niobium ethoxide was added. Red box refers to inset of the high magnification image (selected red dotted box), (b) EELS spectrum (divided because the Nb L2 edge is far away from zero loss peak).

2.4 Water Film on CNTs and IOPs

2.4.1 Water Condensation Mechanism on CNTs and IOPs

Uniform deposition of the nanocoatings is attributed to the formation of uniform nanoscale water film on the nanoparticles. Once water is condensed on the outer surface of nanoparticles or nanofibers, the water film would spread out on the substrate surface,

enabled by the interfacial tension between the polar water and nonpolar hydrocarbons. According to the Young-Laplace equation [166], the pressure at the interface at temperature T is $\nabla p = n\gamma(T)/R$, where γ is the interfacial tension between water and the hydrocarbon, R is the radius of curvature of the interface, and n = 2 for spherical and n = 1 for cylindrical shapes. Since the dimension of R is at the nanoscale, the interface pressure can be extremely high, [167] e.g., at ~ 0.8 MPa (or ~ 8 atm) for R = 50 nm at the water-heptane interface as in figure 2.14. Any change in the radius of curvature is suppressed, for example, from a protrusion in the water film, since a bigger change in pressure is ensued, as can be gauged from the derivative, $(\partial \nabla p/\partial R)_T = -n\gamma(T)/R^2$. As a result, the water film is always conformable to the substrate surface, resulting in a smooth metal oxide nanocoating.

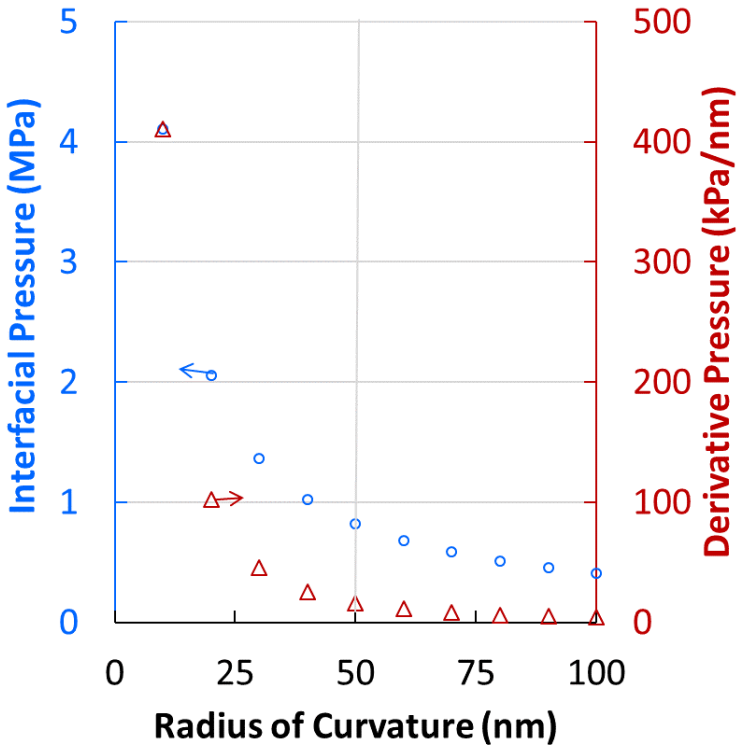

Figure 2.14. Shows the interfacial pressure vs. the radius of curvature, the interfacial pressures were calculated from the Young-Laplace equation assuming a spherical shape for the water and heptane interface. The partial derivative of the pressure relative to change in radius of curvature is also shown. The interfacial tension used is 20.53 mN/m for water-heptane at 20 °C.

To confirm that a uniform water film was indeed formed, we attempted to observe the water-coated nanomaterials using cryogenic electron microscopy (Cryo-EM) [168]. In this experiment, either CNTs or IOPs were dispersed in heptane oversaturated with water. The samples were then plunged into a cryogen (ethane slush) at 93 K with a high heat capacity (2.33 kJ/kg·K), with the expectation that the condensed water film can be vitrified instantly. As expected, vitrified ice layers were clearly observed in CryoEM on both CNTs and IOPs, as shown in figure 2.15 (a) and (b), respectively. EELS spectrum on the ice coated CNTs as in figure 2.15 (c) confirms that the layer is indeed ice with the characteristic oxygen peaks where the uncoated CNTs do not show such peaks [169, 170]. To know the exact thickness of water, further details can be found in *section 2.4.2*.

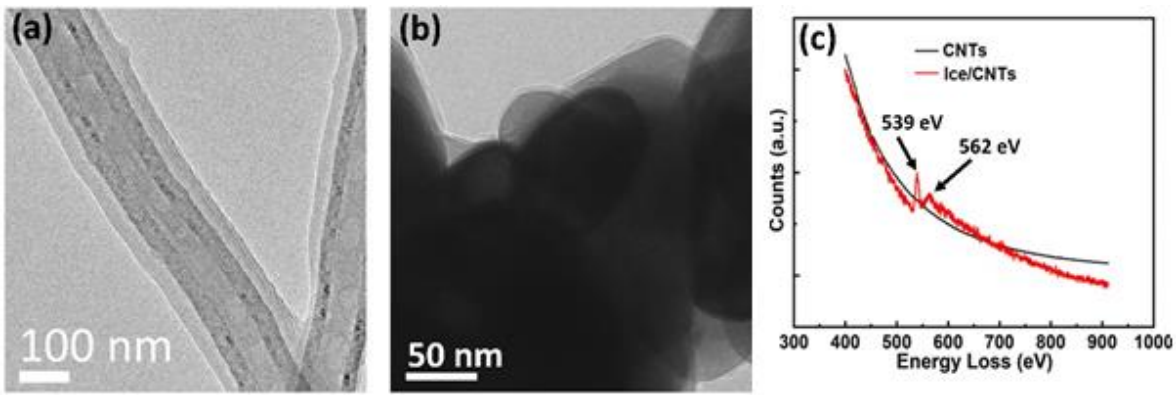

Figure 2.15. Nanoscale water film formation, (a) CryoEM image of ice layer on CNTs, (b) CryoEM image of ice layer on IOPs, (c) EELS spectrum before and after the ice formation showing oxygen peaks characteristic of ice layer in (a).

Heptane as other organic solvents has a saturation amount of water based on the solubility (82.3 ppm wt/wt, 61 ppm v/v) [171],[172]. It can be presumed that the water saturation amount in heptane has no tendency (or negligible) to be adsorbed on the dispersed CNTs. As a result, the added water amount is condensing on the substrate (CNTs or IOPs). As soon as the CNTs get water-covered, the substrate itself may be considered as a water droplet and it is getting bigger until the added water is consumed

except the saturated amount. The first molecules arrive to the surface will make cluster on the surface-active sites (COOH, C=O, OH) with certain energy (based on interaction potential) [173]. Assuming the surface has enough functional groups leads us to consider the substrate's surface as a hydrophilic or partially hydrophilic [174]. The first water layer at the interface is strongly bonded with surface groups due to the hydrogen bonds [175]. Therefore, it is expected that the condensation flux will be maximum at (r=0) then it decreases with the film radius increases. After 2-3 layers, the role of the active sites diminishes leading to a different mechanism which could be called as a water layer propagation by hydrogen bonds.

To validate this, we have applied *Kelvin's equation* [176] to check the difference in the water concentration in the bulk-heptane and on a substrate (i.e., CNTs) surface. Since the system is under a dynamic movement, the mass transfer coefficient requires the Sherwood, Reynold, and Schmitt numbers to be considered. The solid-liquid mass transfer is thought to occur between the two phases. The heptane has the water and it is in direct touch with the substrate. Thus, the process is based on the slip velocity as reported before [177].

$$N = K_{LS}A(Cl - Cs) \quad \text{.....(2.1)}$$

Where: N is the mass flux mole/s. cm^2, A is the surface area cm^2, Cl is the added water in heptane mole /L, Cs is the water condensing on the CNTs surface in mole/L.

$$Sh = A + BRe^{m}SC^{n} \quad \text{.....(2.2)}$$

$$Sh = \frac{K_{LS}d_p}{D_A} \quad \text{.....(2.3)}$$

Where: d_p is the substrate diameter, D_A is the water diffusion in heptane.

$$Re = \frac{u\, d_p \rho_L}{\mu_l} \quad \text{.....(2.4)}$$

where u is the velocity between the solids and the surrounding fluid, dp is the particle diameter, ρ_L is the liquid density and μL is the liquid viscosity.

$$SC = \frac{\mu_L}{\rho_L D_A} \quad \text{.....(2.5)}$$

Nienow and Miles (1978) [178] developed the Froessling equation based on the slip velocity principles and they found A and B values as below:

$$Sh = 2 + 0.44Re^{0.5}Sc^{0.38} \text{.....(2.6)}$$

If we use kelvin equation (2.7) and we may correlate it in terms of concentration:

$$ln\frac{p}{p_0} = \frac{2\gamma V_M}{rRT} \text{.....(2.7)} \rightarrow P = CRT \rightarrow ln\frac{CL}{CS} = \frac{2\gamma V_M}{rRT} \quad \rightarrow Cs = \frac{Cl}{EXP(\frac{2\gamma V_M}{rRT})} \text{ (2.8)}$$

Substitute eq. 2.8 in eq. 2.1:

$$N = K_{LS}A(Cl - \frac{Cl}{EXP\left(\frac{2\gamma V_M}{rKbT}\right)}) \text{.....(2.9)}$$

Where: γ is the surface tension (J/m^2), Vm is the atomic volume of water, r is the film thickness or radius (nm or cm), Kb is Boltzman constant erg/cm^2, T is temperature (K). On equation (2.9), Mathlab modeling was carried out to estimate the condensation flux with a respect to the film thickness (r). Figure 2.16 (a) shows the condensation flux proceeds into two profiles. At a radius less than 10 nm, the flux has significant values which could be due to a strong attraction force of the functional groups and the water molecules [174]. At a radius 10 nm, the flux has exponentially decreased which is consistent with what we have proposed. The slow condensation flux is due to the change of the condensation mechanism from water-functional groups interaction to hydrogen bonds propagation among the water molecules. Figure 2.16 (b) displays the flux decreases as the temperature of the heptane increase at constant concentration of 0.0205 M and a constant radius of 5 nm. This is a logical outcome as water solubility increases

as the temperature increases [171]. The curve shows a minimal decrease until ~ 190 K then starts going down at an onset 200 K. When it exceeds the room temperature, it sharply dropped. We think at a temperature higher than 298 K the heptane able to maximize the bonding with water. With a further warming, the water would starts evaporating together with heptane.

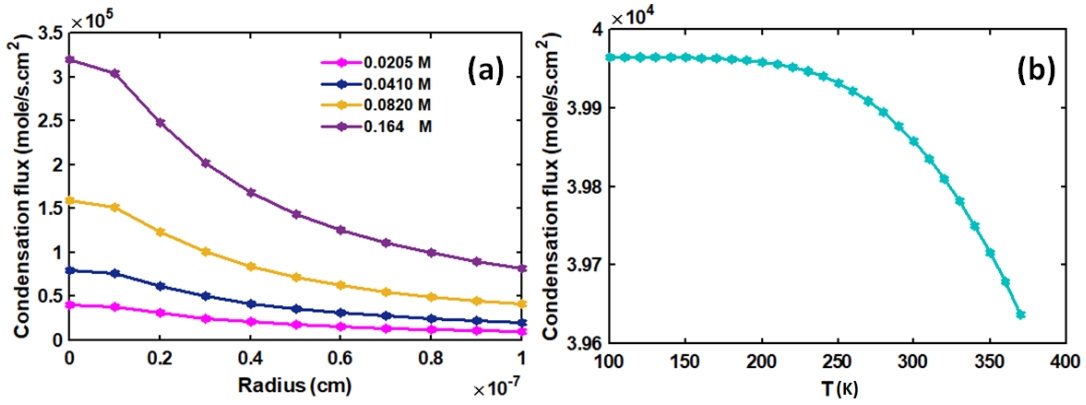

Figure 2.16. (a) Water condensation flux on CNTs calculated from equation 2.9 at different water concentrations at a constant temperature of 298 K, (b) Condensation flux decreases as temperature of the heptane increases at a constant radius of 5 nm and a constant concentration of 0.0205 M.

2.4.2 Water Thickness Detection by Temperature Ramping on Ice Film

Water vapor condenses and nucleates once it is exposed to a cold plate leading to forming ice [179]. When the ice is exposed to different the temperature and pressure , the volume changes which is associated with phase transformation [180]. Here, water condensation occurs from heptane onto the carbon nanotubes (H_2Oads-CNT) surface forming a water film. The H_2Oads-CNT film was exposed to a sudden freezing under the liquid ethane temperature of 93K producing a vitreous ice. The exact thickness can be known from the ice film after knowing the ice film density. For that, the ice layer was subjected to a temperature ramping from -170 ºC to -130 ºC. At 135°C, the ice phase transformed into a cubic-ice phase as it was confirmed by the diffraction pattern. Figure 2.17 shows the TEM images of the ice at a range of temperatures from -170 °C to 130 °C inside the scope loaded on the cryo-holder. It is seen that the ice-film

thickness has increased. This increase is explained by a phase transition which is associated with volume change [181]. Figure 2.18 (a) exhibits the ice thickness has exponentially increased from ~17 nm to 54 nm as the temperature increases until the layer deformed into particles morphology associated with a phase transformation into a cubic ice. Upon measuring the ice film in cubic phase, we can do backward calculations to see how much the ice expand. This gives us the exact thickness for the water film during the coating process.

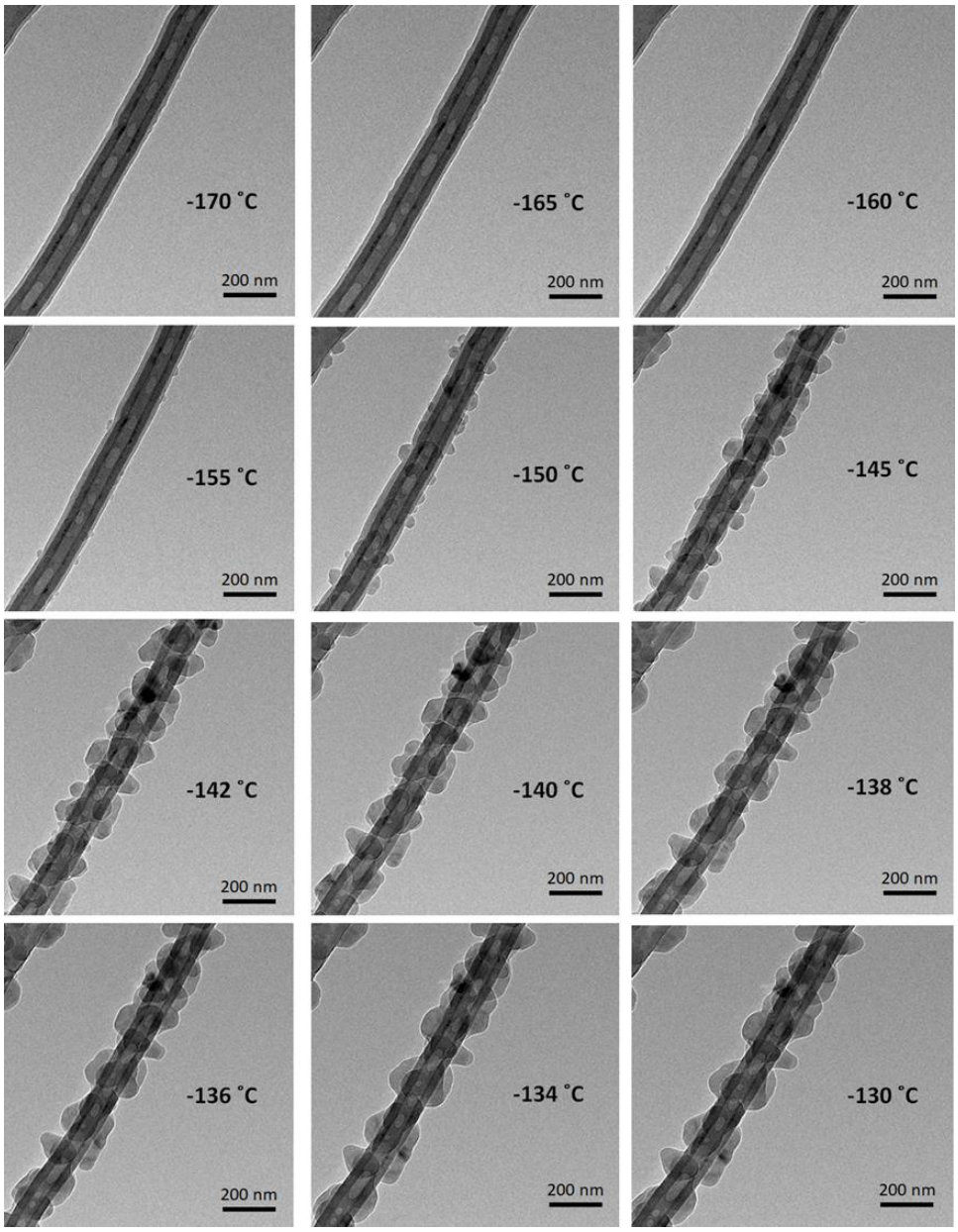

Figure 2.17. Cryo-TEM images sequences with respect to temperature for ice film after temperature ramping from -170 °C to 130 °C.

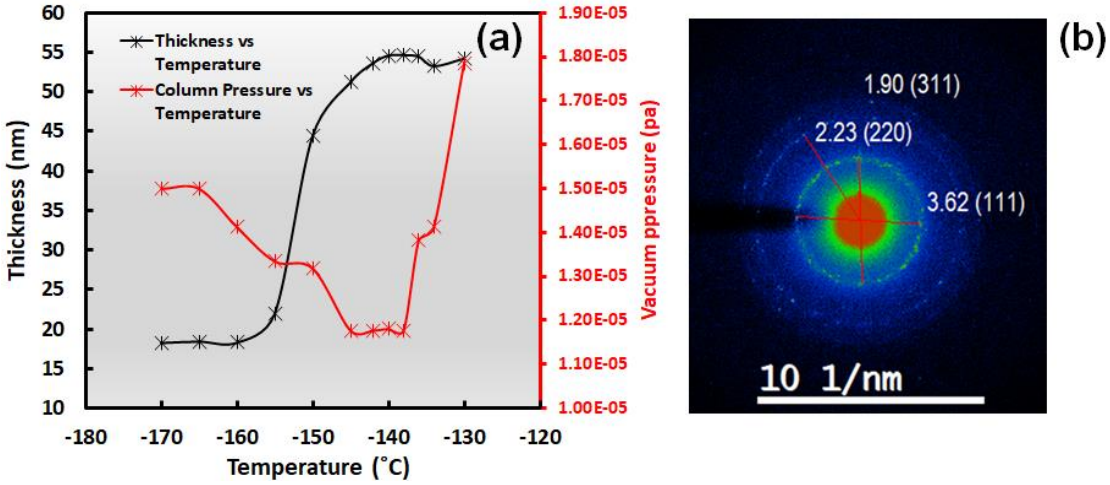

Figure 2.18. (a) Ice thickness increases with temperature,(b) Electron diffraction of the cubic ice at 136 K.

The vitrified ice has two types base on the density classified as a low-density amorphous ice (LDA) and a high-density amorphous ice (HDA) [182]. Another study reported a rout to make a glassy ice by compressing the hexagonal ice at 77 K to about 11 kbar and followed by decompressing at 120 K [183]. The HDA phase (density 1.26 g/cm^3, [184]) obtained by compressing ordinary ice and when it annealed it goes back to LDA with a change in the volume. Mishima and co-workers [183] were able to produce an amorphous ice with a density 1.17 g/cm^3 through a compression process at 15000 bar. Then, they annealed it from 77 K to 120 K they observed the LDA (density 0.94 g/cm^3 [181]) with increase in the volume by 22%. As in figure 2.17, the ice layer thickness has increased by 3-fold of magnitude in our work. In addition, we were able to determine the expansion coefficient from the thermodynamic properties volume change with respect to the temperature assuming we have a negligible change in the pressure:

$$\beta = \frac{1}{V}\left(\frac{\delta V}{\delta T}\right)_p \ldots (2.10)$$

We take a 1-nm as height, 50 nm the CNTs diameter from a TEM image since the CNTs have a cylindrical:

$V_1=\pi \times r_1^2 \times h = 3629.84$ nm^3 T_1= -170 °C$V_2= \pi \times r_2^2 \times h =8490.56$ nm^3 T_2= -130 °C

β= 0.118 C^{-1}

Since the cubic ice density is 0.94 g/cm^3[185], the initial ice phase density will be 0.94*1.118=1.050g/cm^3 this is an evidence the initial ice phase after freezing has a higher density than liquid water [186, 187]. We attribute the formation of the HDA to the water condensation due to a water molecules propagation. This propagation is enhanced by the surface tension between the water and heptane that induces the densification of the water film on the carbon nanotubes. The selected area diffraction (SAED) has confirmed a cubic ice phase as in figure 2.18 (b). Since the liquid water density is 0.998 g/cm^3, then the liquid water thickness is 17.89 nm.

2.5 Metals Oxides Nanostructure

CLD technique capable in making metals oxides nanostructure by burning the carbon supports CNTs, CB at 500 ≤T≤ 600 °C under an oxygen atmosphere. Metal oxides nanotubes (such as TiO_2 and Al_2O_3) are obtained when the CNTs are burned and metal oxide nanoshells (such as Nb_2O_5) are obtained when the CB is burned. This indicates the carbon materials work as a template to make different metals oxides nano-shapes. Metals oxides nanotubes and nanoshells have a wide range of uses such as catalysts, catalysts' supports [188], filters [189], adsorbents [190], and beyond. For instance, TiO_2 is considered as a strong heterogenous catalyst due to the high chemical and thermal stability against a low pH medium [191]. Practically, in the vapor phase hydrogenation of maleic anhydride, Ni/TiO_2 shows a remarkable activity due to the strong interaction between Ni as a metal and TiO_2 as a catalyst support [192]. Another study reported

TiO_2 applications in the organic reaction for example incorporating cobalt on TiO_2 (*ca*, Co/TiO_2) in converting carbon sources (coal, natural gas, and biomass) into long chain hydrocarbon via syngas [188].

To confirm the nonexistence of the carbon, elementals mapping and electron energy loss spectrum have been carried out. They showed neither a carbon image nor a carbon signal. Figure 2.19 (a) shows TiO_2 nanotubes after burning the CNTs and it obvious the tubes have different sizes which is assigned to the originates substrate CNTs sizes. The inset in figure 2.19 (a) shows EELS spectrum over TiO_2 nanotubes showing no carbon signal at 285-290 eV suggesting all the CNTs were removed. For further confirmation, figure 2.19 (b) shows energy filtered TEM image and elements mapping showing also only the Ti and O.

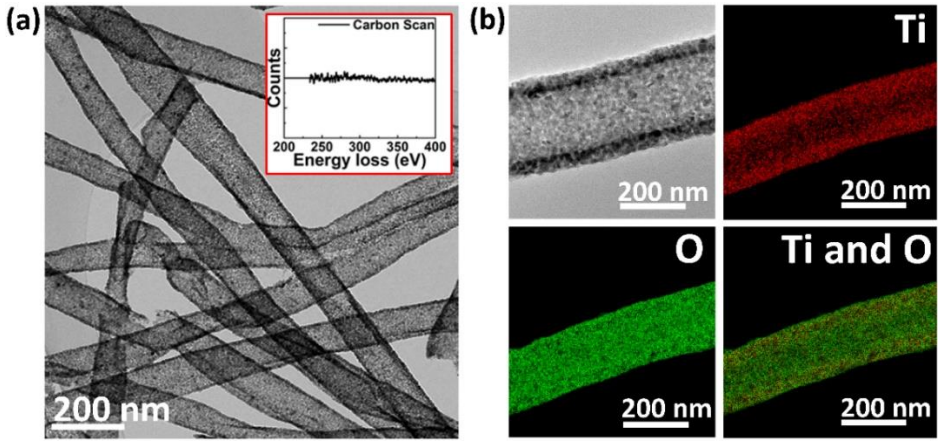

Figure 2.19. (a) A low resolution TEM image of TiO_2 nanotubes after burning (the inset is EELS spectrum scan), (b) A high magnification EF-TEM with elemental mapping showing only oxygen and titanium.

On the other hand, Al_2O_3 have also a wide spectrum of applications specially the porous one as previously reviewed in the section 1.2.1.3. A study has reported using Ni/Al_2O_3 for hydrogen production from steam reforming of glycerol [193]. The study found a glycerol conversion was 96.8% at 600 °C increasing to 99.4% at 700 °C, the largest hydrogen selectivity (99.7%) was obtained at 650 °C, and the results were assigned to well-impregnated Ni particles on the Al_2O_3 surface. In the environmental engineering,

γ-Al_2O_3 has been used as an adsorbent for heavy metal removal and other organic pollutants [194]. Al_2O_3 has been used as a catalyst or a catalyst support for a long time [195]. Porous γ-Al_2O_3 have a surface area significantly over 200 m^2/g which can be considered a good catalyst in polyethylene production and in hydrogen peroxide production [196].

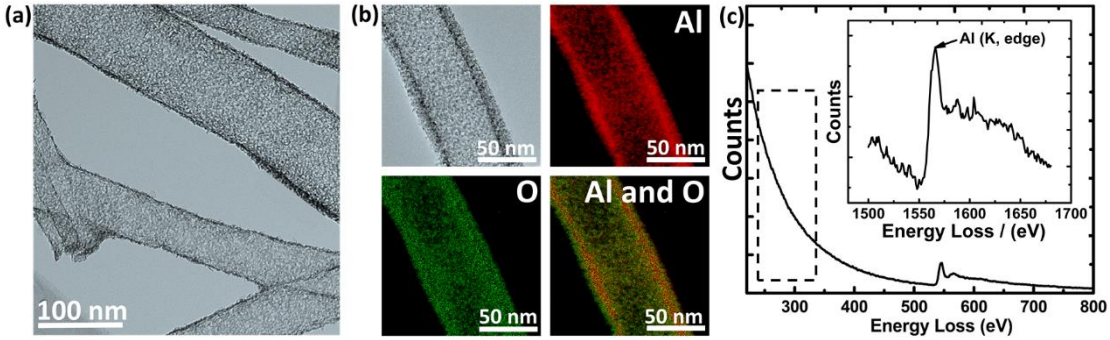

Figure 2.20. (a) A low magnification TEM image of Al_2O_3 nanotubes, (b) Elementals mapping, (c)EELS spectrums show no signal from carbon (dashed box) only oxygen and aluminum.

Figure 2.20 (a) represents a high magnification energy-filtered EF-TEM image of Al_2O_3 nanotubes. Figure 2.20 (b-c) show the electron energy loss spectrum (EELS) over the burned tubes showing no signal from C k-edge, however, only the oxygen and aluminum peaks were detected. The surface area has increased from 202.3 to 274.6 m^2/g for alumina /CNTs and Al_2O_3 nanotubes as shown in figure 2.21. It displays a type IV isotherm according to IUPAC classification, which indicates a mesoporous characteristic of the samples [197].

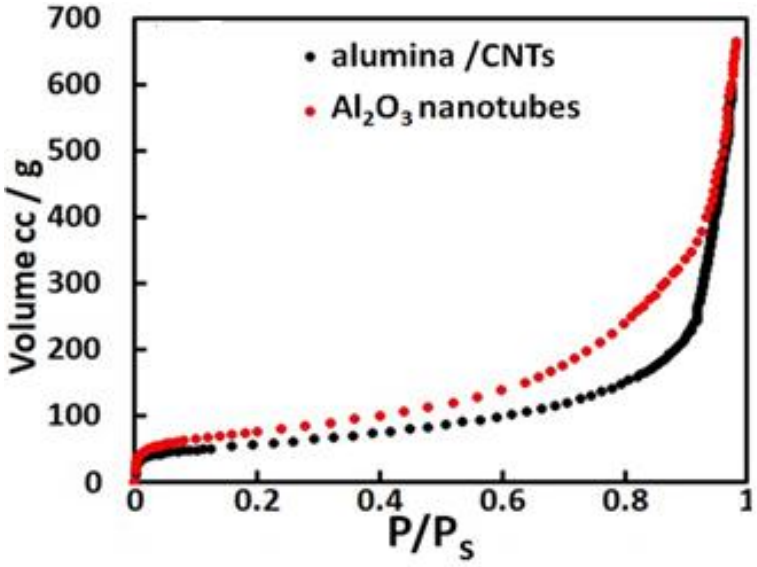

Figure 2.21. BET measurements for alumina/CNTs and Al_2O_3 nanotubes.

Niobium oxide particles are another crucial material which is mainly used as a catalyst or a catalyst support in both fuel cells catalysis [59] and thermal catalysts [71] and beyond as discussed in the section 1.2.1.2. A study has reported the effect of NbO_x particles on the activity of magnesium and vanadium toward conversion of C_2H_6 to olefins such as ethylene and propylene. The study has found the overall conversion reached 100 %. Nb_2O_5 particles are available through many vendors with particles size <500 nm which is considered a micro-size. However, here we synthesized a smaller size which is expected to offer a high surface area. In the electrochemical chemistry, Nb_2O_5 nanoparticles play a central role, especially in the polymer exchange membrane fuel cells (PEMFCs)[59, 198]. The robust interaction between precious metals such as (Pt, Pd, Ir) and Nb_2O_5 makes such catalysts to be active and durable especially after being thermally activated [70].

Figure 2.22 (a-b) show low and high magnification of TEM images of the Nb_2O_5 coating before the carbon burning on carbon black with a uniform layer at a thickness of 5 nm. Figure 2.22 (c) confirms the nonexistence of the carbon signal at a range of 280-300 eV via the EELS. Figure 2.22 (d-e) show low and high magnification of TEM images of Nb_2O_5 nanoshells after the burning of CB. Figure 2.22 (f) shows EDS

spectrum on figure 2.22 (e) suggesting no carbon signal. In this method, we were able to make Nb_2O_5 nanoshells at a nano-size of less than 100 nm. This size has shown a specific surface area of 47.22 m^2/g as shown in figure 2.23. The BET curve shape indicate a type IV isotherm according to IUPAC classification, which indicates a mesoporous characteristic of the samples [197].

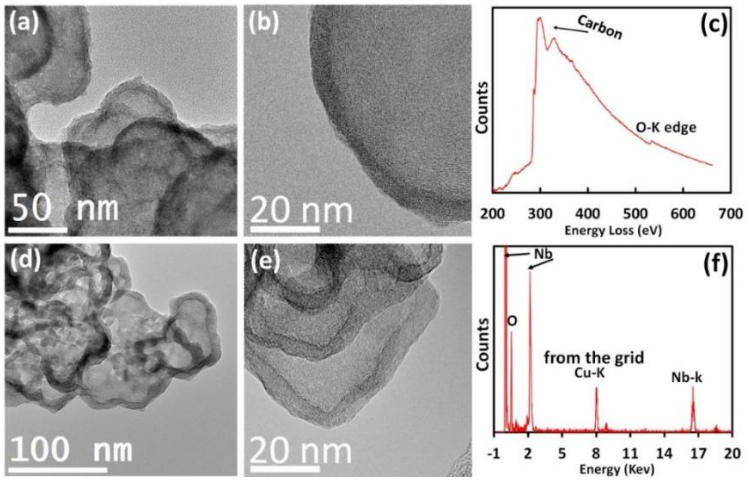

Figure 2.22. (a-b) Low and high TEM resolution of Nb_2O_5/CB, (c) EELS spectrum shows the carbon signal, (d-e) Low and high TEM resolution of Nb_2O_5 shells after carbon burning, (f) EDS scan on Nb_2O_5 shells showing no signal from the carbon.

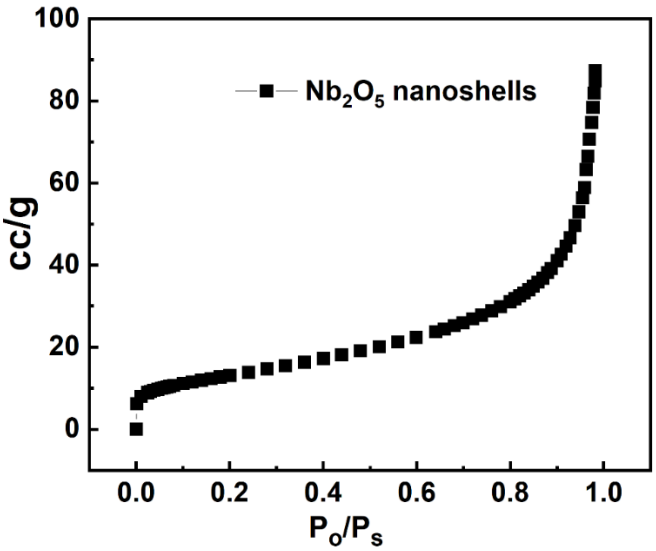

Figure 2.23. BET adsorption profile for Nb_2O_5 nanoshells.

2.6 Conclusion

In this chapter, we presented a new and versatile condensed layer deposition (CLD) technique, for depositing metal oxide nanocoatings on the outer surface of nanoscale

substrates. The CLD technique is a liquid phase process that utilizes liquid hydrocarbons, providing unique advantages in depositing nanocoatings. It was demonstrated that the CLD can deposit titania, alumina, and niobia nanocoatings on CNTs, IOPs and carbon black. The nanocoating thicknesses can be controlled as a function of the condensed water film thickness from a few nanometers up to a hundred nanometers. The results show that the CLD has the potential to deposit various metals oxides nanocoatings on a wide range of nanoscale materials with advanced applications. Due to the low coating temperature, the made oxide layers are in amorphous phase which was converted to crystalline phase after the annealing at 600 °C. The main idea of the coating is forming a water film on those substrates. The water film was studied theoretically and experimentally. The MATLAB modeling has predicted a reasonable model for the water condensation flux. Cryogenic transmission microscopy has confirmed an ice layer after freezing the water film on the nanoobjects under liquid nitrogen temperature -170 °C. In situ temperature ramping in the cryo-holder further validated the layer identity. After the temperature was changed from -170 to -130 °C, the layer thickness has grown from 17 nm to 78 nm associated with a phase transition from amorphous to cubic phase. The cubic phase has been validated by indexing the ED pattern and scanning the electron energy loss spectrum has also confirmed the OH peak at 539 eV binding energy. In addition, nanostructures of the metals oxides in various shapes (e.g., nanotubes, nanoshells) can be derived from the metal oxide nanocoatings on carbon substrates. Porous γ-Al_2O_3 nanotubes were synthesized after burning the carbon. The γ-Al_2O_3 nanotubes surface area was calculated to be 202 m^2/g and 274 m^2/g for Al_2O_3/CNTs and porous Al_2O_3, respectively.

Chapter 3. Study Organic Residues in Fluffy-Nano Titanium Dioxide Layers on Carbon Nanofibers

- This chapter is written in a manuscript in preparation

Abstract

A comprehensive study was conducted to study the residues of organic ligands in a fluffy-TiO_2 layer on carbon nanofibers (CNFs) that were made in a condensed layer deposition(CLD). The partial hydrolysis of titanium tetra-isopropoxide (TTiP) on the CNFs surface is considered to be the main reason for having a high-fluffy morphology due to retained alkyls ligands inside the metal hydroxide matrix, leading to a cross-linking structure. For nano-confined ligands, we showed, via fourier-transform infrared (FTIR), that the ligands CHx (x=2,3) content in TiO_2 network decreases as the water mole ratio increases, indicating an additional supply of protons that reduce the i-CH_3 ligands. On the other hand, the released isopropoxide content was analyzed through the gas chromatography-mass spectroscopy (GC-MS) by making an analogy with isopropanol alcohol as standard. The GC-MS results revealed that some of those ligands desorbed into the solvent and their concentration increased as the water mole ratio was increasing. A slow scan of TGA/DTG analysis further confirmed a reduction in the organic residues with an increase in the water ratio. The transmission electron microscopy images show a different growth in TiO_2 with a change in the water ratio at a constant TTIiP amount. Unlike TTiP, titanium ethoxide (TEO) was used to make the coating and it showed a dense-conformal layer which confirmed the precursor molecule size effect.

3.1 Introduction

Nanocoating of metal oxides such as Al_2O_3 [199], TiO_2 [200], ZrO_2 [201], SiO_2 [202], and ZnO_2 [203] has a wide range of applications, including electro-catalysis [204],[35] electro-photo catalysis [205], lithium-ion batteries [206], sensors [207], biological uses [208], and environmental engineering [209]. Nanocoating of titanium dioxide (TiO_2) has received extensive scientific and industrial attention. Several coating techniques have been used in making TiO_2 coating, such as atomic layer deposition (ALD) [126], Sol-gel [106], and co-precipitation [210]. The optical and physical properties of TiO_2 are affected by conditions of the synthesis. For instance, the phase and conductivity of ALD-made TiO_2 is correlated to the deposition temperature [211]. Regarding the sol-gel process, many scientists have studied TiO_2 in order to identify phase transformation, to detect impurities, and to determine particle size [212], and to evaluate the thermal stability [213]. According to numerous studies, many factors affect the sol-gel process, including the reactivity of metal alkoxides, the water/alkoxide ratio, and the reaction temperature. The microstructure and the chemistry of the surface can be vastly altered by varying these parameters. The coating in liquid phase at a low temperature usually results in some unreacted species from the precursor's mother molecule.

The left-over impurities in the TiO_2 matrix structure have been widely studied due to the significant impact on oxide's performance. A study has been conducted on TiO_2 using the TTiP as an alkoxide precursor with free water to study the gel properties in aqueous solutions [214]. One study reported on the photocatalytic activity of TiO_2 made in the sol–gel. It converts into nanocrystalline powders by supercritical drying [215]. The authors reported an enhancement in activity after burning the organic residue at 450 °C. In a related study, Toshikazu et al, [20] examined the effect of organic ligands on the crystal structures and the optical properties of TiO_2. The latter study found the

ligands aggregate grains of $TiO_2$and induce crystallinity which enhances the optical performance. In all reported studies, thermal oxidation for such species is linked to a high temperature that may reduce the surface area [216], an important property for any approach. A limited number of papers have studied the organic residue in TiO_2 as a film form on a nano substrate.

In this work, we examine the organic residue in TiO_2 film made by CLD on the surface of carbon nanofibers (CNFs) by changing TTiP:H_2O ratio to 1:2, 1:4, and 1:8. The samples were made using the CLD technique. Taking advantage of the ultralow water content in heptane, the organic species on the CNFs surface were examined on an assumption that the TTiP hydrolysis reaction took place exclusively on the surface. To the best of our knowledge, no previous studies have reported such type of precursor behavior in the organic solvents. The long ligands of isopropoxides are difficult to reduce by the supplied protons coming from the water molecules at a stoichiometric ratio. As a result, a part of them remain confined inside the metal hydroxide structure, forming a polymeric oxide-alkoxides complex $[MO_x(OR)_{4-2x}]_n$ [217], [218]. The FT-IR and slow-scan TGA analysis revealed a reduction in the organic species with an increasing the water ratio. In addition, GC-MS was applied to detect the released ligands in heptane during the coating process. The GC-MS results showed the opposite of the FT-IR and the TGA results, findings that were logically expected. Moreover, those results were supported via three characterizations of transmission electron microscopy (TEM) and Brunauer–Emmett–Teller (BET). It was also observed with more water ratio the coated CNFs can easily be dispersed in water while the least water is easily dispersed in heptane.

3.2 Material and Methods

3.2.1 Fluffy-TiO_2 Coating

The coating process was conducted using our newly developed technique, oxide layer deposition CLD [219]. In brief, carbon nanofibers (from Pyrografs company, 50-120 nm) were surface-functionalized first by 6.0 M of (3:1 Vol.) H_2SO_4: HNO_3 under a sonication force at 60 ˚C for 2 hours. Titanium isopropoxide (TTiP) (from Alfa Aesor) was used as a TiO_2 precursor. Heptane (HPLC- grade Fisher scientific) was used as a solvent and dispersant. We flushed the system (dry-set up) by nitrogen gas (99.99% UHP-Air Gas) for 30 minutes to ensure there was no water vapor, not even on the container wall. A 100 mg of CNFs was dispersed in 50 ml heptane under sonication forces with simultaneous stirring. The coating process was performed as follows: the sonication probe was used to disperse the 100 mg of CNFs under N_2 gas flow. From the stoichiometry, we measured water concentration (CB_0=0.129, 0.259, and 0.518 mole/L) and a constant amount of the TTiP as a (CA_0=0.062 mole/L) to make (1:2, 1:4, 1:8) allowing 20 minutes for reaction time. Finally, the organic solution was centrifuged to remove all the liquid to check the isopropanol concentration in the supernatant by GC-Ms. The TiO_2/CNFs was left in the oven at 140 °C to get rid of the solvent.

3.2.1.1 Thermal Analyses

Thermal analyses were carried out by Thermogravimetric analyzer (TGA), in a Q500-TA Instruments. The samples were analyzed using a temperature range from 20-900 ˚C at a scan rate of 2 °C/min. Air as a gas was used.

3.2.1.2 Fourier-transform infrared spectroscopy Analysis (FT-IR)

The surface chemistry was analyzed by the Fourier transformed infrared spectroscopy (FTIR) in a Cary 660 spectrometer (Agilent Technologies, Santa Clara, CA, USA). The samples were mixed with KBR and prepared into pellets before the transmission measurements were made. The spectra were collected using wavelengths at a range between 4000–400 cm^{-1}.

3.2.1.3 Gas Chromatography Analysis (GC-MS)

The concentration of the samples was analyzed using Agilent 6890 Gas Chromatograph coupled with an Agilent 5973 Mass-Selective Detector (GC-MS) (Agilent Technologies, Santa Clara, CA). A 60-m long fused silica capillary column DB-5MS (0.25 µm film thickness, 0.25 mm internal diameter) was used for the separation.

3.3 Results and Discussion

3.3.1 Characterizations Results

Figure 3.1 shows TEM images of CNFs coated with a fluffy layer of TiO_2. The coating thickness is obviously about 10 nm as further confirmed by HR-TEM. Electron energy Loss spectrum (EELS) was recorded via a FEI Tecnai F30 G2 Twin Transmission Electron Microscope as shown in figure 6.2 (*Chapter Six*). Although the metal oxide layer is in a fluffy shape, the area nearest to the surface is a dense layer. This is a highly important result since it does confirm that the substrate was entirely covered by TiO_2.

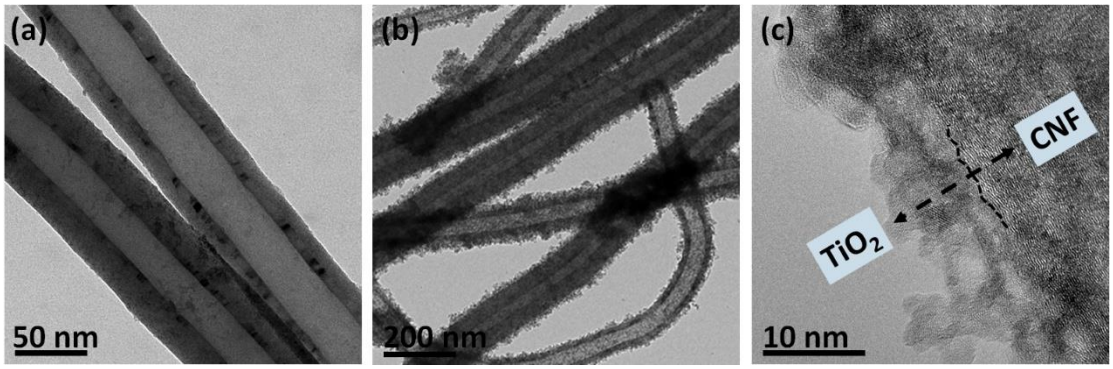

Figure 3.1. (a) TEM image of bare CNFs, (b-c) Show the TiO_2-fluffy coating low and high magnification TEM images.

The added water was initially trapped at hydrophilic centers known as "organic oxygen groups" such as (COOH, C=O, OH) and the water molecules shared a hydrogen bond to form a water film called water-bridging [220]. The water film was observed by the Cryo-EM (*see section 2.4.1, chapter 2*). Figure 3.2 shows the TiO_2 coating on the CNFs correlated to different water/TTiP ratios. It can be seen that the 1:2 has a well-distributed coating film covering the CNFs surface.

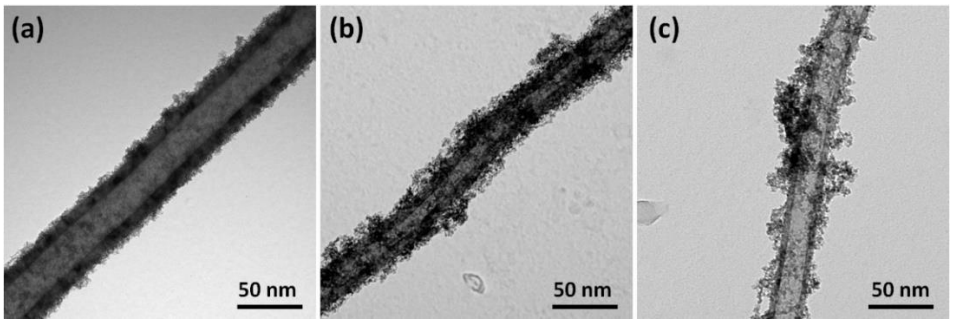

Figure 3.2. TEM images for different TTiP:H_2O (a) 1:2, (b) 1:4, (c)1:8.

The TiO_2 growth reveals a different pattern. When the water ratio increased from 1:2 to 1:4 and 1:8, the TiO_2 film was distorted. The explicit reason for having such a morphology change is not entirely clear and will be briefly discussed in here. In literature related to this subject, one study has reported the effect of using various water amounts on the synthesis of TiO_2 using the sol-gel process [212]. The study stated that by increasing the water amounts in the TiO_2 phase, crystallization is induced. Since each single phase has unique lattice parameters, the crystalline-cell volume will be

highly affected. This phenomenon directly influences the density and the volume. In our case, it is believed that 1:2-TiO_2 initially grows in a small monomer size ($TiOH_4$). This monomer increases with an increase in the water content, producing this particular morphology [213].

3.3.2 Slow scan TGA and FT-IR Results

The organic ligands groups are theoretically retained inside the structure as we believe. It has been previously reported, the degree of retention depends on the water ratio as the hydrolysis reaches completion [221]. In our system, heptane contains 61-ppm (by volume) water (at 25 °C, 1 atm) which could be considered a dry medium [222]. In addition, the reaction is a surface reaction where the condensed water on CNFs induces the hydrolysis reaction . Figure 3.3 (a) shows the slow scan TGA/DTA at a scan rate of 2 °C/min. The DTA shows five regions at ≤150 °C, 185 °C, 270 °C, 375 °C, and 580 °C. Region 1 shows an endothermic plateau which is attributed to the desorption of adsorbed water which was expected to increase as more water was introduced. At 185 °C, an exothermic peak appears, indicating an oxidation process which is related to surface adsorbed organic species. Consequently, twin exothermic peaks region 3and4 appeared at 270 °C and 375 °C. Those peaks are attributed to oxidizing chemisorbed the organic species [223]. The reason for of two exothermic peaks might be related to the location where the species whether CH_x, or CH_xCH_{x-1} (mainly C_3H_6) are coordinated [224]. These peaks are mainly associated with the complicated TTiP reaction mechanism as described elsewhere [225]. There are two possible configurations of the C_3H_6: either Ti-C_3H_6 or O- C_3H_6. Each possesses a different bond energy [226]. It is worth noting that those peaks decrease with an increasing H_2O/TTiP ratio. This indicates that the more supplied protons during the coating reaction the more organic ligands depart the coating layer on the CNFs surface. At the region 5, the large

peak is related to the CNFs thermal oxidization. Figure 3.3 (b) shows two bands that appeared at the range of 2900-3000 cm^{-1}. Those bands are related to the stretching of CH, CH_2, and CH_3 functional groups [227] which motivate our interest in having the FT-IR analysis. Additional evidence of having different i-CH_3 content is the peak intensity of the three samples. The absorbance intensity decreases by increasing the water mole ratio.

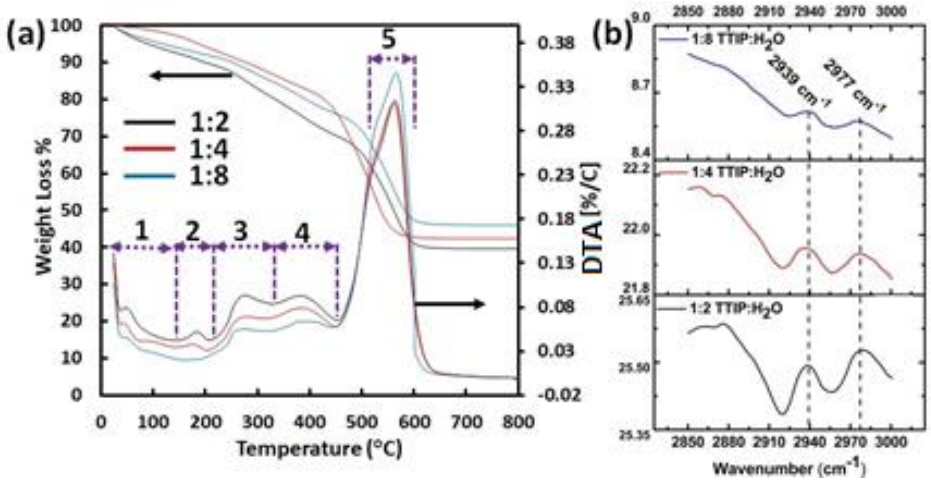

Figure 3.3. (a) Slow scan TGA/DTA analysis at 2°C/min, (b) Selected-magnified scan of FT-IR spectrum.

The FT-IR spectrum in figure 3.4 shows three samples at various TTiP/water ratios 1:2, 1:4, and 1:8. The three samples show a similar spectrum; however, at different absorbance intensity. The two bands located at 1050 and 1395 cm^{-1} are correlated to the organic moiety bending O-iCH_3inside the TiO_2 [215, 228, 229].

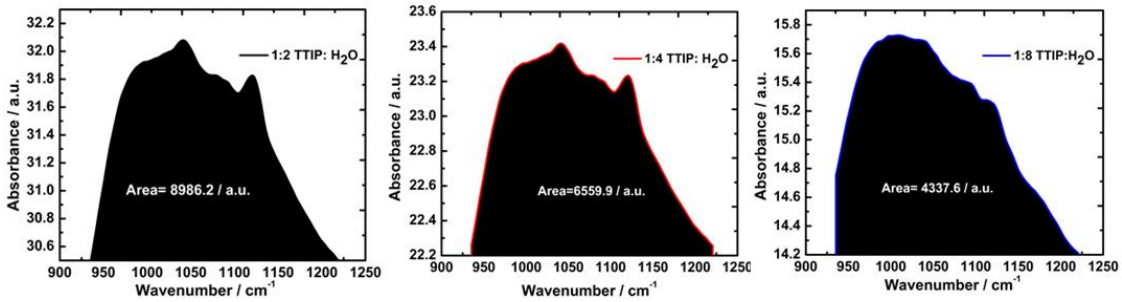

Figure 3.4. Shows the area under the peaks at a range of (935-1220 cm^{-1}).

At a wavelength of 1050 cm^{-1}, the peak is broad, beginning at 930 cm^{-1} to 1220 cm^{-1} that makes it difficult to quantify. Therefore, the quantity was relatively estimated by integrating the area under the peak, using the Origin software. In figure 3.4, the area of 1:2, 1:4, and 1:8 was 8986.2, 6559.9, and 4337.6 (a.u.), respectively. These results coincide with the results observed in figure 3.3 (b). The peaks at 1645 and 3500 cm^{-1} are assigned to the Ti-OH bending and the stretching vibration of the hydroxyl groups O-H [230]. The three samples were dispersed in two mediums: water and heptane. Figure 3.5 (a) shows a photograph of the powders dispersed in water. While figure 3.5 (b) shows the dispersion in heptane.

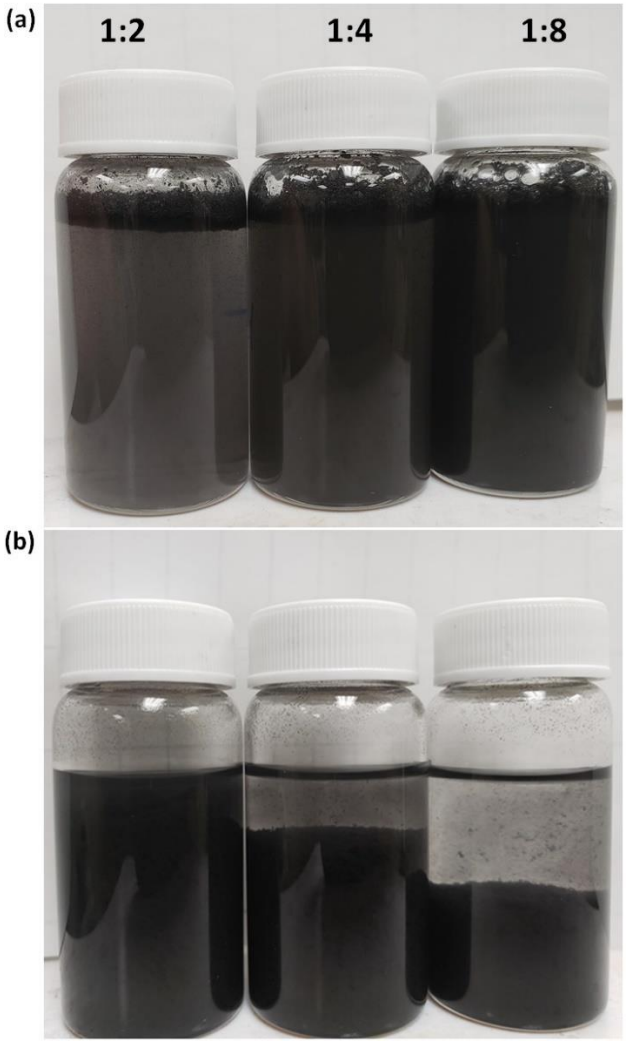

Figure 3.5. Photograph of TiO_2/CNFs dispersion (a) in water, (b) in heptane.

It can be seen that by increasing the water ratio, the powder is well-dispersed. On the other hand, the 1:8 sample shows less dispersion in pure heptane due to fewer organic ligands available. This observation might be beneficial for some environmental applications, such as the water-oil separation approach.

3.3.3 GC-MS Results

Campostrini et al. [231] has studied the pyrolysis of TiO_2-anatase powder made by the sol-gel technique by thermo-analyses (TGA, DTA) coupled with gas chromatographic (GC-MS) to identify the organic content in TiO_2 matrix and the released components. Another study was conducted by Philipp et al. [225] to investigate the kinetic mechanism for the thermal decomposition of TTiP. The last study was conducted based on an analogy between the isopropanol and TTiP due to the close similarities between isopropanol and the isopropoxide branches as they have an identical structure and bond strengths. Here, the left-over heptane was analyzed by GC-MS analysis to determine the isopropoxides concentration released from the TiO_2 matrix into the heptane medium. This is possible as the alcohol (here isopropanol) is easily diffused in the organic mediums [232, 233]. Figure 3.6 (a) depicts the three samples GC-MS spectrum with well-separated peaks of isopropanol at a retention time of 5.8 minutes. The added precursor amounts purportedly give a 0.25 mole/L as a maximum concentration of isopropoxides according to TTiP/H_2O reaction stoichiometry which corresponds to complete hydrolysis.

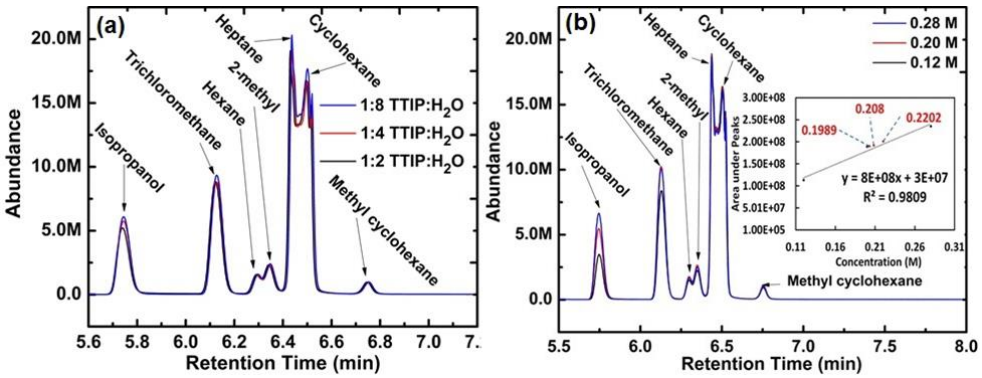

Figure 3.6. GC-MS (a) Samples spectrum,(b) Calibration data and the inset for the linear equation.

By increasing the water ratio, more isopropoxides abundance was recorded by the GC-MS. A calibration curve was prepared to analogize the released concentration. Figure 3.6 (b) shows the calibration curve of isopropanol in heptane with high linearity (R^2=0.98). The concentrations were calculated based on the calibration linear equation from the samples' abundances. The number of released ligands and the hydrolysis completion percent can be estimated as in figure 3.7. A complete hydrolysis cannot be reached even by increasing to 1:8 as a mole ratio since the released concentration did not reach the maximum 0.25 mole/L that corresponds to 4 ligands.

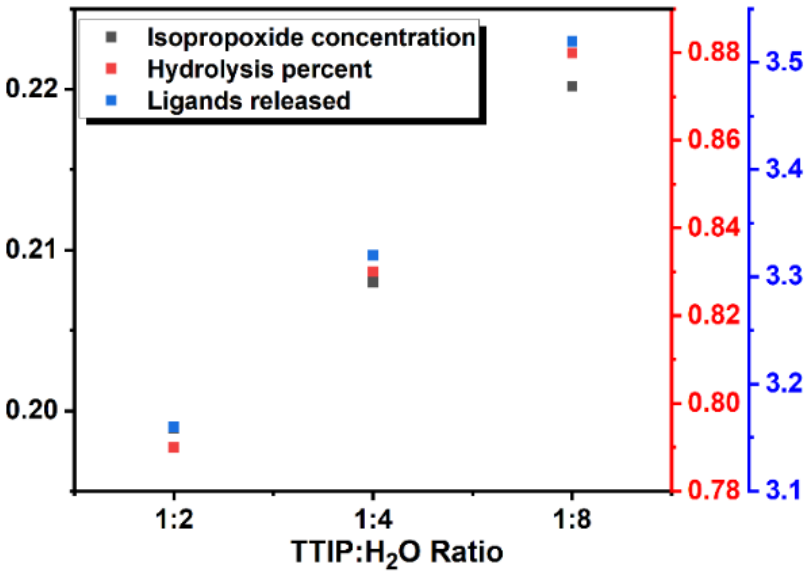

Figure 3.7. Shows the released isopropanol concentration and the hydrolysis percent.

3.3.4 Precursor's Family Effect

Typically, transition metals alkoxide precursors react vigorously with water due to the instability (polarity difference between CH_3 groups and metals centers) of the positively-charged metal inside the precursor microstructure wherein it is surrounded by highly negative-charged ligands [136],[234]. Furthermore, such a reaction depends on various parameters such as the water/alkoxide ratio, hydrolysis medium, reaction temperature, and the ligands family groups in the alkoxide structure [235]. The mechanism of TTiP hydrolysis reaction is explained as a nucleophilic substitution where water acts as a Lewis base and Ti^{+4} atom acts as a Lewis acid [236]. Due to the high electronic deficiency, the hydrolysis step is expected to occur rapidly as a lone pair of negatively charged oxygen from water attacks the positively charged $M^{\delta+}$. Then, protons transfer from water molecules to negatively charged of adjacent ligands. This will compel such ligands to depart the TTiP structure producing a metal hydroxide (M-OH) which is considered as a condensate [237] as shown in scheme 3.1 below.

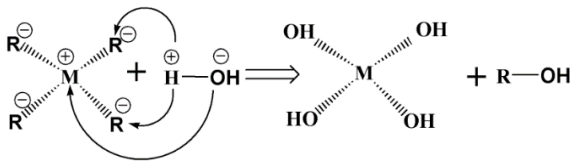

Scheme 3.1. Hydrolysis reaction step of TTiP.

Therefore, it is kinetically reasonable that more water will reduce more ligands groups leading to a high metal oxide content ratio defined as $Ti(OH)_4$/TTiP [238]. The anticipated reaction steps are depicted below [239]:

$$Ti(OR)_n + nH_2O \rightarrow Ti(OH)_n + nROH \quad \ldots\ldots\ldots\ldots\ldots\ldots\ldots\ldots\ldots\ldots \quad (3.1)$$

Equation 3.1 shows the fundamental hydrolysis reaction of the metal alkoxide with water. This reaction leads to the production of a monomer Ti $(OH)_4$ in the event we have a complete reaction with 70 % as an oxide content (TiO_2/ Ti $(OH)_4$), where R-

group is in formula (C_xH_{2x+1}). The alkoxides with higher alkyl groups such as -isopropoxide and butoxides are slow to hydrolyze and to diffuse [238] due to the steric effect.

$$Ti(OR)_X + xH_2O \rightarrow Ti(OH)_x(OR)_{4-x} + xROH \quad \ldots\ldots\ldots\ldots\ldots\ldots\ldots\ldots (3.2)$$

The reaction in equation 3.1 proceeds to produce a partially hydrolyzed result as in equation 3.2. This is considered as a starting point of the condensation step that takes places between the partially hydrolyzed species in equation 3.2 with the next precursor molecule as described in equation 3.3 below:

$$Ti(OH)_x(OR)_{4-x} + Ti(OR)_4 \rightarrow (OR)_{4-x}Ti\text{-}O_x\text{-}Ti(OR)_{4-x} + xRH \quad \ldots\ldots..(3.3)$$

Another coating experiment was conducted by using small-ligand precursor, titanium ethoxide (TEO). The heavy molecule weight precursors with long ligands produce smaller polymeric condensates (metal hydroxide). This point was confirmed by comparing the oxide coating produced by TTiP and produced from titanium ethoxide as in figure 3.8. Basically, titanium ethoxide has more oxide than TTiP as (TiO_2 Mwt/precursor Mwt) 35% and 28% of TiO_2, respectively. The condensation step proceeds through M-O as a condensation center. Thus, a high number of metal atoms such as M-O-M-O leads to the production of a larger polymer molecule than the M-O as illustrated in scheme 3.2 below:

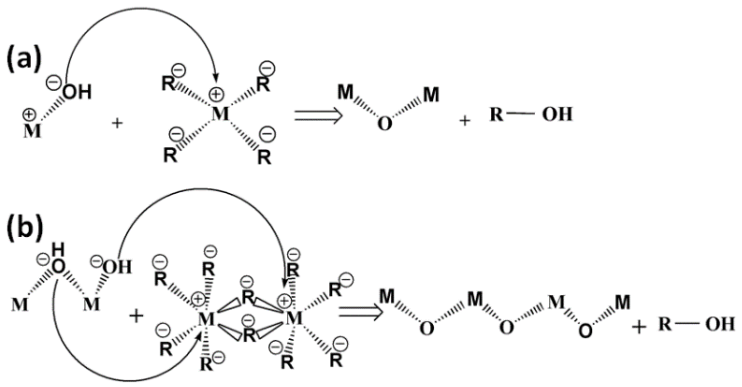

Scheme 3.2. Condensation of the produced metal hydroxide (a) One metal center, (b) Two metals center.

TTiP exists mainly as a monomer with a tetrahedral environment around the Ti center. The low degree of coordination with the metal center is assigned to the steric bulk of the isopropoxides groups versus the n-alkyl groups. This serves to prevent bridging interactions among the metal centers [240]. On the other hand, titanium ethoxide exists as a tetramer with an octahedral coordination environment around the metal centers whose role it is to form a high and uniform layer [241],[242].

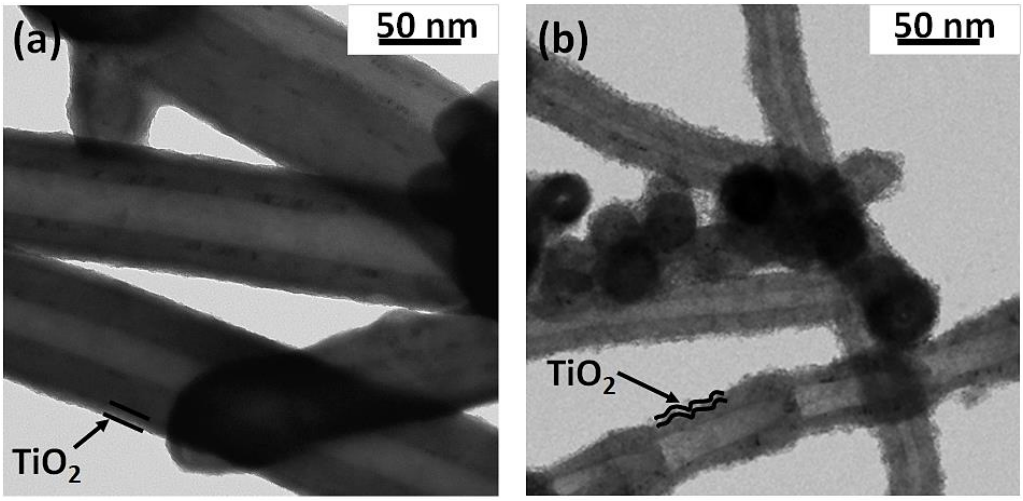

Figure 3.8. TEM images (a) TiO_2 dense-layer derived from titanium ethoxide, (b) TiO_2 fluffy-layer derived from titanium tetra-isopropoxide.

It is deduced the difference in the morphology is related to the condensation step where the metal-metal bridging interaction is hindered in TTiP. It was reported that if the condensation step begins before completion of the hydrolysis step, the ligands groups may infiltrate into the structure and sterically retard the formation of a high ordered metal oxide structure, resulting in a cross-linking structure [243]. The produced material will never have a 100% oxide content because this would require an infinite polymer with no terminal bonds [235]. The terminal groups (OH and OR) can be altered by modifying the reaction conditions such as conditions described by Cho JY et al. [27]. The hydrolytic poly-condensation equation can be written as follows:

$$nM(OR)_4 + (4n + x - y)H_2O \rightarrow M_nO_{\left[2n-\frac{x+y}{2}\right]}(OH)_x(OR)_y + (4n - y)R(OH)\ldots\ldots$$

(3.4)

where n is the number of metal ions polymerized in the condensation, and x and y are the numbers of OH and OR groups in the molecule. The polymer produced $M_nO_{\left[2n-\frac{x+y}{2}\right]}(OH)_x(OR)_y$ determines the oxide content since it will decompose to the metal oxide:

$$M_nO_{\left[2n-\frac{x+y}{2}\right]}(OH)_x(OR)_y \rightarrow nMO_2 + xH_2O + yR(OH)\ldots\ldots \quad (3.5)$$

Based on equations 3.4 and 3.5, an increase in the oxide content can be expected if we increase the number of metal polymerized cations (n) to produce titanium hydroxide which is then later converted to titanium dioxide. Furthermore, the (OR) groups decrease by increasing the water amount in the hydrolysis medium [237]. Titanium ethoxide has four Ti-atoms in their molecular structure which is expected to form more hydroxide; however, TTiP has only one Ti-atom [244]. The TiO_2 coating layer surface area was further investigated by BET. Figure 3.9 shows the BET results for the three samples in order 134.6, 129.3, and 104.2 m^2/g. It decreases as the water ratio increases. This is explained as the increase in the organic content (partial hydrolysis) which produces larger pores sizes, consistent with results reported in a previous study [231]. This might also be attributed to the growth in the particles of the TiO_2.

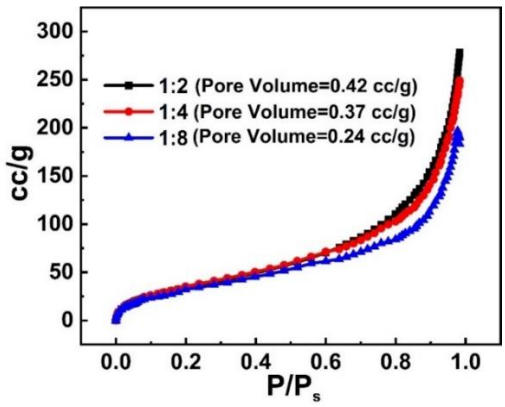

Figure 3.9. BET measurement-adsorption scan for 1:2, 1:4, and 1:8.

3.4 Conclusion

The released ligands from TTiP were studied using three techniques: TGA, FT-IR and GC-MS. By increasing the water ratio relative to TTiP, less organic content was detected by FT-IR and TGA; however, GC-MS showed that increasing the reduced ligands diffused in heptane. On the other hand, results from transmission electrons microscopy (TEM) showed a change in TiO_2 morphology with a change in the water mole ratio. These results establish a relationship between the TiO_2 morphology and the retained organic content which requires further study. TTiP has big ligands that bulk around the Ti-atom that cause titanium dioxide to retain some of the ligands, leading to the formation of the cross-linkage structure of metal hydroxides ($Ti(OH)_x(OR)_{4-x}$) defined as an incomplete hydrolysis. On the other hand, titanium ethoxide (small ligands precursor) was used, and the results showed a super uniform and conformal layer of TiO_2. This may be because of a greater number of Ti-atoms inside the titanium ethoxide structure which induces the metals to interact since each metal atom behaves as a condensation center and with a less steric effect. This study examines the organic ligands released from hydrolyzing TTiP with a water film on the surface of carbon nanofibers. More investigations are required to gain a better understanding of the kinetics of the precursor on the CNFs surface.

Chapter 4. Decoration of Tin Oxide and Platinum on Fluffy-TiO_2 on the Carbon Nanotubes for Ethanol Electro-Oxidation

- This chapter is written in a manuscript in preparation

Abstract

A fluffy titanium dioxide layer on carbon nanotubes was utilized as a support for tin oxide (bi-functional element) and platinum nanoparticles Pt NPs. TiO_2 layer was successfully synthesized by using Condensed layer deposition (CLD). The TiO_2 layer covered the carbon nanotubes in a fluffy shape showing an exceptional surface area of 310 m^2/g which is needed for Pt NPs and SnO_2 to be dispersed without agglomeration. The prepared catalyst exhibited a considerable electro-catalytic activity for ethanol oxidation (EOR) with 350 mV negative onset potential relative to Pt/C (E-TEK). In addition, it showed an enhancement in the durability based on i-t curve at 705 mV .vs RHE by ~2.2 times. Transmission electron microscopy (TEM) revealed a rough- porous surface of TiO_2 as well as the crystalline states of SnO_2, TiO_2, and Pt NPs after they were annealed. X-ray photoelectrons (XPS) revealed a 0.9 eV positive shift in SnOx binding energy. This shift was considered as a reason of having early onset and a high stability under i-t curve owing to the high presence of oxygen atoms that can initiate the water. This study demonstrates the effect of consolidating TiO_2 coating layer with SnO_2 toward the EOR.

4.1 Introduction

Polymer electrolyte fuel cells (PEMFCs) have attracted great interest as a primary stand by power source for electric vehicles or residential co-generation systems. Due to the environmental issues, working on an alternative and a clean energy sources becomes

vitally crucial. Ethanol is one of the promising fuels that could be applied to achieve future prospective energy. In PEMFCs, there are various fuels have been investigated for decades such as hydrogen, methanol and other alcohols. Compared to hydrogen and methanol, ethanol has many advantages, less toxic, easy to store and to transport [245-247]. In addition, it has high energy density due to the 12-electrons that correspond to ($8\ kWh\ kg^{-1}$) in case a complete oxidation obtained [248]. Ethanol is the smallest alcohol molecule that contains a C-C bond and can therefore serve as a model for the electro-oxidation of compounds containing C-C bonds. The C-C bonds are difficult to access electro-catalytically due to the poisoning species which are the major obstacles for a complete oxidation [249]. Acetaldehyde, acetic acid and CO_2 were determined as the main products as reported by Iwasita et al. [250].

Platinum and its alloys are the most popular electro-catalysts for the ethanol oxidation in the acidic medium. However, the high cost for sustaining platinum becomes the main impediment to produce a large-scale commercialization of (DEFCs).Therefore, incorporating other elements was found to serve better in term of the activity, durability, and the cost. Rousseau et al.[251] demonstrated that adding Sn with Pt changes the geometric and electronic characteristics of the surface resulting in enhancing the activity by initiating the C-C bond cleavage. Many researchers have devoted a great work on Pt-based alloys such as Pt-Cu [252] Pt-Sn [253] and Pt-Ru[254]. Other studies have been reported on metals oxides supporting Pt nanoparticles such Pt-SnO_2,[255] Pt-TiO_2 [256] and Pt-ZrO_2 [257]. Yunteng Qu et al. [258] found Pt/SnO_2/graphene nanocomposite showing a high durability and catalytic activity than that of the commercial Pt/C. Zhang et al.[259] have studied two types of SnO_2 supports in term of the geometry on Pt performance. They found Pt/SnO_2 flower-shaped catalyst to be active and durable due to the multidimensional active sites allowing more ethanol to

diffuse. Another study has found sulfated SnO_2 modified multi-walled carbon nanotubes supporting Pt nanoparticles to be highly active due to the synergetic interaction between Pt and S-SnO_2 [260]. Very recently, a study reported loading Pt-SnO_2 on Cr_2O_3-NPC showing high mass activity, low onset , and a descent stability [261].

In this work, TiO_2 coating on CNTs was successfully conducted by the CLD technique using titanium tetra-isopropoxide (TTiP) as a precursor [219]. The CNTs surface was uniformly coated and entirely covered by TiO_2. In addition, the coated surface took a fluffy shape that makes the support possesses a high specific surface area of 310 m^2/g based on BET measurement. To make TiO_2 conductive, we conducted a carbon doping for TiO_2/CNTs at 700 ºC as reported before [262]. The carbon doping was carried out at 450 ºC and annealed at 700 ºC to avoid TiO_2 sintering and changing to large particles size that could significantly reduce the surface area [263]. Then, tin oxide as a promotor was loaded, hereafter, the catalyst is denoted as Pt@ST/CNTs. The Pt@ST/CNTs shown a high ethanol forward mass activity peak 560 $mA/mg_{(Pt)}$ and backward peak at 560 $mA/mg_{(Pt)}$ with (I_f/I_b=1.39) which are higher than of that in Pt/C (E-TEK) values 296 $mA/mg_{(Pt)}$, 89.5 $mA/mg_{(Pt)}$ and 0.84, forward, backward peaks and their ratio, respectively. In addition, the Pt@ST/CNTs holds a current after 1800 second by over 2.2 times of that in Pt/C, this is an indication that the Pt@ST/CNTs shows high ability to generate oxyphilic species reducing the CO_x adsorbates.

4.2 Materials and Method

4.2.1 Coating and Characterizations

Organic solvent coating route was carried out to make TiO_2 nanocoating on CNTs by CLD [219] . In brief, CNTs (Nano-Lab-50 nm-diameter) surface were oxidized by 6.0M of (3:1) H_2SO_4:HNO_3 under sonication for 2 hours at 60 ˚C then washed, vacuum-

filtered and dried at 80 ˚C. 100 mg of pre-treated CNTs were dispersed in 50 ml of the pure heptane (Alfa Aesor) for 20 minutes. To make 45% TiO_2 loading, 40 micro-liter DI-water was added onto the dispersion under stirring force for 20 minutes. Finally, 303 micro-liter of titanium tetra-isopropoxide (TTiP-Alfa Aesor-99.99% metal basis) was added to make the coating (Calculations based on stoichiometry of ($TTiP + 2H_2O \rightarrow TiO2 + 4$ isopropoxides). The carbon doping was carried as follows: temperature increases at a ramp of 5 °C/min under N_2 gas until reaches a temperature of 700 °C. Acetylene was opened at 700 °C at a volume ratio of (10%Vol +90 % Vol N_2) for 20 minutes. Tin dioxide was deposited on C-TiO_2/CNTs by hydrolysis of $SnCl_2.2H_2O$ in the hot water and it was annealed at 600 °C under N_2 gas for 1 hour. Finally, Pt nanoparticles were deposited by reducing K_2PtCl_4 salt in a mixture of ethylene glycol and water solution. X-ray diffraction (XRD, Philips X-pert) equipped with Cu Kα was performed to analyze the crystalline phase of the catalyst's elements. The data was collected over an angle range of 2θ= 5° – 90˚ at a scan rate of 0.026˚ s^{-1}. X-ray photoelectron spectroscopy (XPS, Kratos Axis 165) was conducted to analyze the C 1s, Ti 2p, Sn 3d, O 1s and Pt 4f. Elements mapping ELLS were also conducted to see the oxides distribution in TEM level. In addition, thermogravimetric analysis (TGA) was carried out to know mass loading of TiO_2.

4.2.2 Electrochemical Section

All electrochemical tests were carried out by an electrochemical workstation (BAS100) to study the electrochemical performance of Pt@ST/CNTs and state-of-the art Pt/C at the same loading for the control purpose. Ag/AgCl (3.5M) electrode and platinum wire were used as the reference and counter electrodes, respectively in three electrode cells, however, the voltage values were converted to RHE as (RHE (mV)= Ag/AgCl (3.5M) +205mV). As prepared catalyst was dispersed in (1:1 v/v) mixture of ethanol and water

to prepare a catalyst ink at 1mg ml^{-1} and 20μL of the dispersion catalyst dripped onto already polished carbon glassy electrode (5mm-D) and then 5-7 μL of (0.05%) Nafion covered the ink. Cyclic voltammetry (CV) was carried out at scan rate of 50 $mV.s^{-1}$ in nitrogen purge for 20 min in a solution of 0.5M H_2SO_4 to determine the platinum electro-activity, based on oxidation and reduction peaks. The electrochemical surface area of the catalyst was determined by the integration of the cyclic voltammetry curve in the potential region of hydrogen adsorption / desorption, after double layer charge correction, considering the reference value of 210 μC cm^{-2} for a full hydrogen monolayer coverage. Then, CV was carried out in an electrolyte mixture of $0.5MH_2SO_4$ + $0.5MCH_3CH_2OH$ to assess the activity toward ethanol electrooxidation. To investigate the durability, *i-t* curve was performed as well at potential of 705 mV (RHE).

4.3 Results and Discussion

4.3.1 Characterizations Results

Figure 4.1(a) shows a TEM image of the TiO_2-coated CNTs. The CNTs were well coated without any aggregated TiO_2 out the surface. In addition, the surface shows a fluffy shape with a high specific surface area of 310 m^2/g as in figure 4.2. The efficient coating is attributed to the smart dispersant choice. Heptane has no tendency to react with titanium dioxide precursor or may consume a minimal amount. This is because heptane has ultra-low water equilibrium content [138]. Figure 4.1(b) depicts platinum nanoparticles were uniformly distributed. Figure 4.1(c) displays the high magnification image showing the Pt NPs were deposited onto metal oxides and they are clear from their lattice.

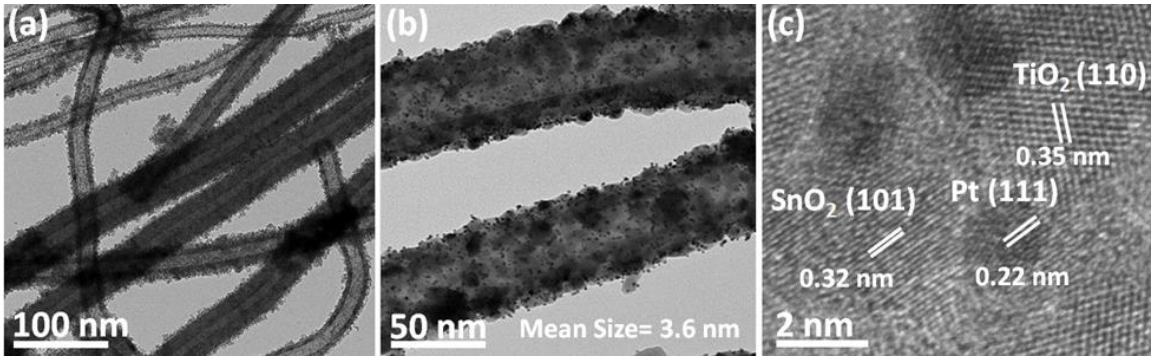

Figure 4.1. TEM images (a) TiO_2 fluffy geometry on CNTs (b) PtNPs and SnO_2 on C-TiO_2/CNTs (c) HRTEM shows the PtNPs dispersed onto oxides surface with crystalline lattice space of the catalyst elements.

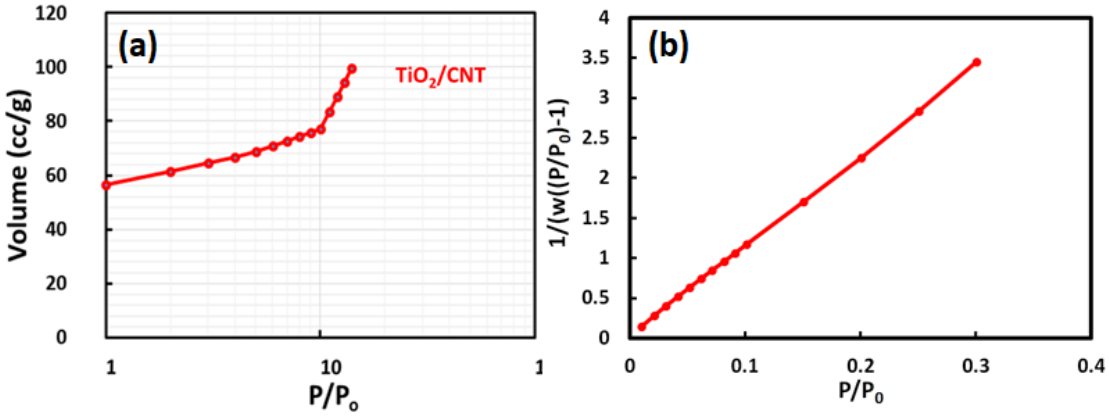

Figure 4.2. BET measurements (a) shows the isotherm, (b) shows the linearity of the adsorption pressure.

A question might be asked whether the fluffy porous morphology open to the CNTs backbone surface or not. To answer that, a high-resolution transmission electron microscopy was conducted to check such a logic inquiry. As it seen in figure 4.3, the high-resolution image for TiO_2/CNTs shows a solid layer (white dashed lines) directly attached to the CNTs surface. This layer is highly crucial since it prevents the acid to reach the CNTs surface which is the purpose of the TiO_2 coating.

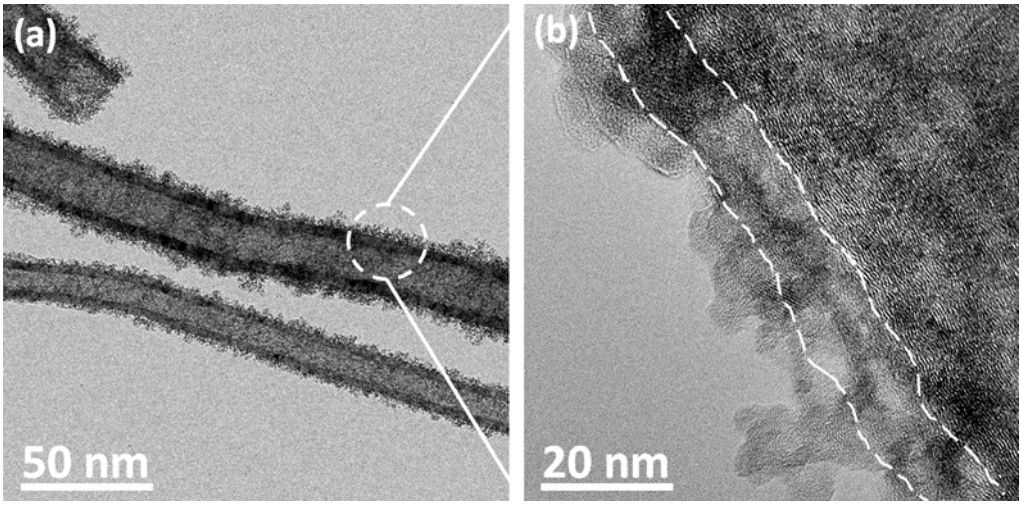

Figure 4.3. TEM images shows (a) A low magnification image, (b) HR-TEM for a dense layer directly attached on CNTs surface (in between white dotted line).

Figure 4.4 presents the XRD patterns of Pt@ST/CNTs showing all catalyst elements in crystalline phase. The XRD spectra exhibits five diffraction peaks for titanium dioxide at 2Θ°=27.5, 26.5, 54.5, 56.8, 63.5 which are assigned to 110A, 101A, 106R, 220A and 310A, respectively [263]. Tin oxide shows two peaks at 2θº=33.8 and 52.5 which are attributed to SnO_2 (101) and SnO_2 (211), respectively [264]. Platinum shows the characteristic peaks at 2θº= 39, 46.5, 68.2, 81.8 and they belong to Pt (111), Pt (200), Pt (220), and Pt (311), respectively. It is worth noting that the peaks at 2Θ°=86 to 87 for Pt (222) facet cannot be detected by the XRD. This may be assigned to the small size of Pt NPs. From XRD data, we determine the Pt NPs size by using Debye–Scherrer formula (4.1) and it was found 3.6 nm.

$$d = \frac{k\lambda}{\beta cos\theta} \qquad (4.1)$$

where d is the mean size of the crystalline domains, k is a shape factor with a value of ca. 0.9, λ is the X-ray wavelength, β is the full peak width at half maximum minus the instrumental contribution, and θ is the diffraction angle [265].

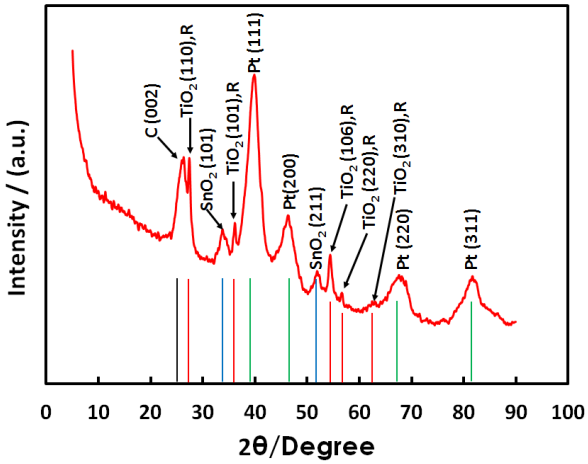

Figure 4.4. XRD pattern for the prepared catalyst.

All binding energies were calculated by referencing to the C 1s value of 284.8 eV. Figure 4.5 (a) shows the XPS spectra of Pt 4f of Pt@ST/CNTs. The BEs of Pt $4f_{7/2}$ and Pt $4f_{5/2}$ are 71.6 eV and 75 eV and they were attributed to Pt in (II) and (IV) states. Similar data were reported by authors elsewhere [266].These results point out to the strong bonding between Pt and the oxides that made Pt in negative electronic state. This is explained due to the electron delocalization between the d orbitals of Pt and the support [267]. However, as reported by Yunteng Qu study, Pt 4f 7/2 was 69.93 eV which is corresponding to Pt^0 [258]. Thus, it could be rationalized that the high binding energy of Pt with the both oxides is due to the electron sharing with metal oxides support. A great benefit of having Pt in negative states is less possibility of Pt to form strong bonds with absorbed reactants. On the other hand, it is beneficial as well to enhance the bond strength between Pt atoms [268]. Figure 4.5 (b) reveals BEs at 487.6 eV and 496.2 eV of Sn 3d which are corresponding to Sn (II) or Sn (IV) [264]. They showed no signals of any Sn metallic form. It was reported that pure SnO_2 shows BEs at 486.70 eV [269]. The 0.9 eV difference indicates electrons vacancy in 3d orbital of Sn. This vacancy has a central role for water adsorption and dissociation spilling over OH toto Pt-CO_{ads}.

Figure 4.5 (c) shows oxygen shows BE at 531.5 eV which is ascribed to oxygen-metal oxide Sn-O the 530.4 eV was most likely to be Ti-O [204].This is further confirmation that there is a high number of oxygen vacancies on the oxides surface. Figure 4.5 (d) exhibits the oxidation state of TiO_2. Per a previous report, pure TiO_2 displays BEs at 464.2 eV and 458.5 eV [270]. The BEs of Ti $2p_{1/2}$ and Ti $2p_{3/2}$ were found to be 464.7 eV and 458.8 eV which are like our previous work [35].

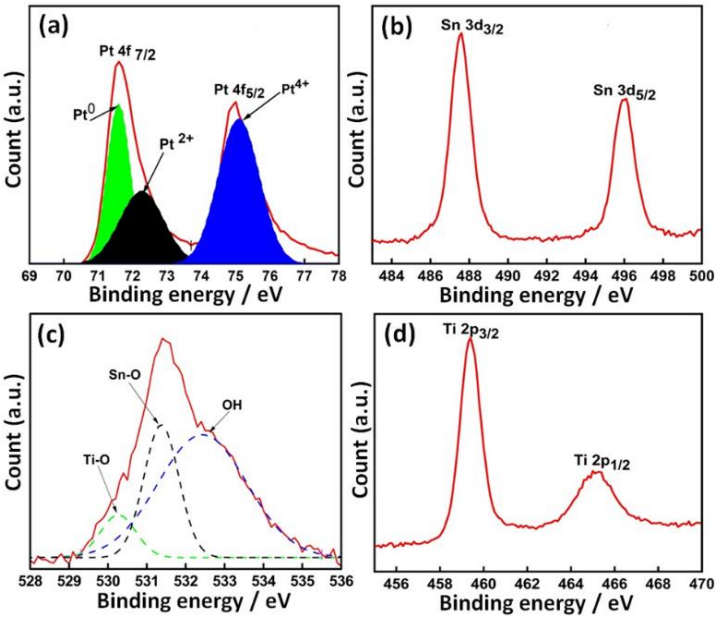

Figure 4.5. XPS analysis (a) Pt 4f, (b) Sn 3d, (c) O 1s, (d) Ti 2p.

4.3.2 Electrochemical Results

Figure 4.6 shows the electro-catalytic activity of Pt@ST/CNTs and Pt/C in a N_2-purged 0.5 M H_2SO_4 solution at a scan rate of 50 mV s^{-1}. The electrochemical surface area (ECSA) was calculated per hydrogen adsorption / desorption charges normalized with 0.210 μC/cm^2 and it was found 77.5 $m^2/g_{(pt)}$ and 41.7 $m^2/g_{(Pt)}$ for Pt@ST/CNTs and Pt/C, respectively. The geometrical specific surface areas of Pt NPs can be calculated from [271]

$$S = \frac{6}{\rho d} \qquad (4.2)$$

where ρ is the density of Pt (21.09 g/cm^3) and d is the mean diameter of the Pt nanoparticles in the catalysts [271]. A comparison between S_{act} and S_{geo} tells the active Pt atoms that contribute in electrochemical reactions. Therefore, the ratio of S_{act}/S_{geo} can be considered a scale for the catalyst activity. In Pt@ST/CNTs, the S_{geo} and S_{act} are 79.02 and 77.5 m^2/g, respectively, with a ratio of (0.98). This refers to 98% of Pt NPs in Pt@ST/CNTs are active during the electrochemical reaction.

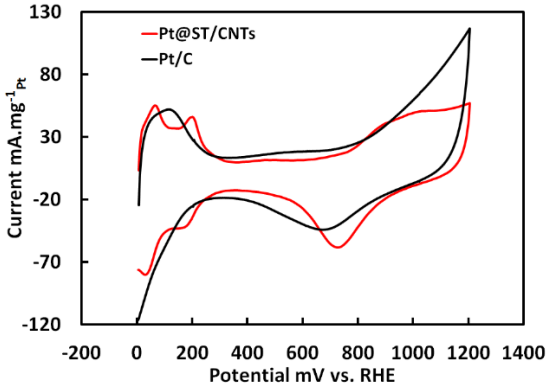

Figure 4.6. Cyclic Voltammetry (CV) in N_2-Saturated 0.5H_2SO_4 at scan rate of 50 mV/s.

The hydrogen desorption peaks of Pt@ST/CNTs with two Pt facets peaks were different from that of Pt/C indicating polycrystalline structure of Pt@ST/CNTs. At range 350 mV to 550 mV the double layer charging region of Pt/C is larger than that of Pt@ST/CNTs. This is attributed to the capacitive charges produced on the carbon support due to the carbon black surface structure which is different from CNTs [271]. At a high potential, where metal oxidation occurs, less metal surface oxidation (Pt-O_x) was observed in Pt@ST/CNTs and then it reduced at an early potential of 740 mV in the backward scan. Nevertheless, Pt/C does show a profound metal oxidation due to carbon oxidation with a late reduction potential of 709 mV [272]. The difference in the performance is attributed to the presence of the two-oxides decorated with platinum that binds with metals oxides stronger than with carbon surface [273]. It is worth noting that both SnO_2 and TiO_2 show no oxidation/reduction peaks at a potential window of 0-1200 mV.vs RHE since their characteristic potentials are below zero [274].

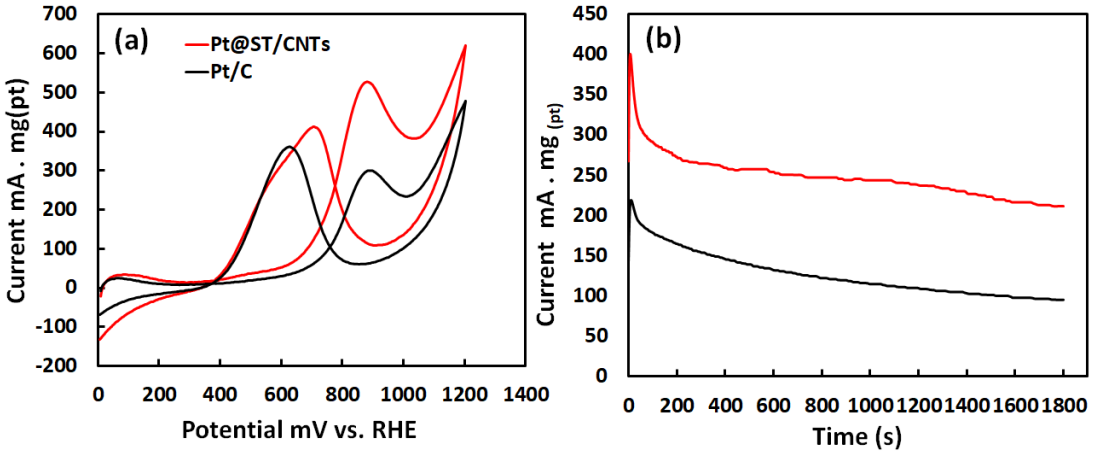

Figure 4.7. (a) Cyclic Voltammetry in $0.5MH_2SO_4$ + $0.5MCH_3CH_2OH$ at scan rate 50 mV/S (b) CA for 1800 seconds at constant potential (705 mV vs. RHE).

Figure 4.7 (a) shows the cyclic voltammetry (CV) curves in $0.5MH_2SO_4$+0.5M CH_3CH_2OH. Unambiguously, it is seen that the onset potential of the Pt@ST/CNTs is 335 mV which is lower than that of Pt/C of 550 mV. The Pt@ST/CNTs exhibits rather higher peak density of 560 $mA/mg_{(pt)}$ in forward scan than the Pt/C 296 $mA/mg_{(pt)}$. Furthermore, the EOR activity of Pt@ST/CNTs is about 1.9 times in Pt/C, which it could be assigned to more than a reason. Firstly, the high geometric surface area offered by the new coating technique makes the Pt NPs uniformly distributed on a fluffy surface that allows the ethanol molecules to be more accessible into Pt active sites. Secondly, tin oxide incorporation could serve in two aspects, changing the electronic state of Pt or by bi-functional theory mechanism, or even both aspects combined [35]. In term of electronic structure as called ligand effect, it is noteworthy to mention that Pt XPS analysis shows a positive shift in binding energy 71.6 eV elucidating a strong metal–support interaction between the Pt and double oxide which is higher than that of Pt/C 71.3 eV [275].

Ethanol oxidation has a complicated mechanism owing to the 12 electrons are released in case a complete reaction is obtained. The first path that ends up with acetic acid formation is undesired route since it ends up with 4 electrons only [276]. The second path is acetaldehyde formation which is could be oxidized to be CO_2. The acetaldehyde

evaluated by cleavage of a hydrogen atom from the hydroxyl group and the α-carbonx of ethanol [277] as ($CH_3CH_2OH \rightarrow CH_3CHO \rightarrow CHx + CO \rightarrow CO_2$) [278].The third path contains strong inactive intermediates such (CO_{ads}) requires C-C bond breaking. Pt@ST/CNTs exhibited higher forward peak than backward which probably the acetaldehyde mechanism formation and CO_2 route have occurred at a certain level. However, Pt/C exhibited higher backward peak than forward indicating to have less CO converted to CO_2 and the reaction was impeded by acetates intermediate formation. Thus, it is believed the Pt@ST/CNTs could enhance the C-C breaking and at the presence of the bi-metal oxide SnO_2 accelerates the rate of the reaction CO to CO_2. Jang et al. [279] reported a comparison between Pt-Sn alloy and Pt-SnO_x results of chronoamperometry analysis and the performance of the direct ethanol fuel cells, they found that Pt-SnO_x showed higher ethanol oxidation activity than of Pt-Sn alloy. They assigned that to unchanged Pt lattice with SnOx that makes it more favorable ethanol adsorption. At the meantime, SnO_x near Pt crystalline structure could offer oxygen species conveniently to remove the CO-like species of ethanol residues to clean Pt active sites.

Conversely, Rousseau et al. [251] demonstrated that adding Sn with Pt can change the geometric and electronic characteristics of the surface resulting in enhancing C-C bond cleavage. Pt-Sn alloy showed such a weak activity due to limited oxidation path that ends up with acetic acid which makes the C-C cleavage difficult as reported elsewhere [280]. This is because of having Pt as a skin structure that is poisoned by CO_{ads}. On the other side, Sn or SnOx (non-alloyed) as a neighbor to the Pt particles has shown a considerable performance since Sn helps formation of OH species. Another study was made by modeling the decomposition of CHCO over Pt, Pt-SnO_2 and PtSn by using density function theory (DFT) [281]. They calculated the reaction energies (E_{prod}-E

$_{react}$) and they found -1.04 eV over Pt (111), -0.19 eV over Pt-SnO_2 and +0.36 eV over PtSn alloy. This is an indication that Pt-SnO_2 performs better regarding C-C scission after Pt.

Pt NPs in Pt@ST/CNTs dispersed very well onto the oxides surface in Pt@ST/CNTs as in TEM images in figure 4.1 that shows no carbon nanotubes surface meaning the noble metal is dispersed in oxides islands. Pt@ST/CNTs shows an early ethanol oxidation at 250 mV as depicted in the inset of figure 4.7 (a). The increasing in the current indicates the ethanol is undergoing to dehydrogenation steps. The high oxide form of tin oxide shows more electronegative state of SnO_2 indicating to have more vacancies of Sn-O which could accelerate water adsorption and then enhance the formation of ligand groups OH at a low potential [282]. Consequently, the poisoning species can efficiently be removed. The dissociative chemisorption of ethanol needs the presence of several adjacent Pt ensembles [283]. That can be obtained from well dispersed of Pt onto a fluffy geometry without any aggregation.

Figure 4.7 (b) shows the i-t curve at 0.705 V vs. RHE for both catalysts Pt@ST/CNTs and Pt/C. The early decreasing is attributed to the double layer effect. After 1800 seconds the Pt@ST/CNTs has 2.2 times current density than Pt/C. Holding a high current after 1800 seconds indicating to the existence of a high number of free Pt active sites which are offered by well-designed support [284]. Furthermore, it is an indication of having an oxyphilic surface. Figure 4.8 (a and b) show the CV of both catalysts in 0.5 H_2SO_4 after 1000 cycles. The lost active area in Pt/ST/CNTs was 6% of the fresh area, from 77.5 m^2/g to 74.4 m^2/g. On the other hand, Pt/C shows a loss 13% of its fresh surface area. The coating has a direct effect on the Pt NPs durability since TiO_2 prevents the carbon corrosion.

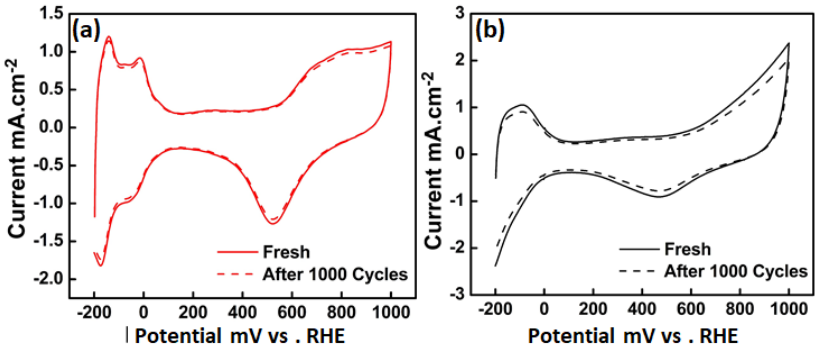

Figure 4.8. (a) Pt@ST/CNTs, (b) Pt/C before and after 1000 cycles.

4.4 Conclusion

We reported in this chapter a decoration of two metals oxides with platinum and its performance in ethanol electro-oxidation. SnO_2 is employed as a promoter and TiO_2 as a stabilizer for Pt NPs. TEM images reveal the fluffy morphology of the TiO_2 on CNTs with surface area of 310 m^2/g. In addition, the HR-TEM displays both oxides in crystalline phase. The electron mapping EELS also confirmed the co-existence of both oxides. The Pt NPs average diameter was 3.6 nm which was calculated from XRD data showing ECSA of 77.5 m^2/g. The catalyst showed a high stability after 1000 cycles in $0.5H_2SO_4$ leading to decrease the ECSA to 74.4 m^2/g. In term of ethanol electro-oxidation, the prepared catalyst exhibited a high current density with increase by ~2 times relative to Pt/C, in addition, the onset potential was negatively shifted by 200 mV. Time-base test for 1800 seconds showed the difference in the current holding by 2.2 times. We assigned the high activity and durability to the binary oxide that coats the carbon nanotubes surface which results to eliminate the support corrosion toward Pt NPs and protect SnO_2 from dissolution. Furthermore, a positive shift in SnO_2 may take a decisive role to initiate the water at a low potential which is mainly due to the electron's vacancy in the Sn 3d orbital.

Chapter 5. Platinum Decorated on Tin Oxide and Fluffy Carbon-Doped TiO_2 for Oxygen Reduction

- Published in the Journal of Electrochemical Society DOI: 10.1149/1945-7111/aba96c

Abstract

With a potential over 800 mV (vs. RHE), platinum (Pt) is not a pure metal but a mixture of Pt-OH and Pt-O. Consequently, oxygen reduction reaction (ORR) passes through a slow kinetic step that limits the feasibility of fuel cell technology. Carbon-supported catalysts perform well, but suffer weak bonding with Pt nanoparticles, and carbon corrosion leads to a release of the Pt nanoparticles from the surface. In addition, they aggregate during reactions on a substrate support with a limited surface area. In this study, we introduce a bi-metal oxide support that includes a fluffy carbon-doped titanium dioxide layer (TiO_2) coated on carbon nanotubes (CNTs), with tin oxide (SnO_2) as a bi-element with hosting Pt nanoparticles. Electrochemical results, cyclic voltammetry (CV) and the polarization test (ORR), showed a remarkable improvement in the onset potential of this catalyst. The half-wave potential of the prepared catalyst recorded a positive shift by 38 mV, as compared to a Pt on carbon catalyst. The fluffy-TiO_2 layer showed very high specific surface areas of 310 m^2/g. X-ray diffraction (XRD) and revealed a rutile phase formation R (110) after incorporating SnO_2 in which a second annealing was carried out. Furthermore, X-ray photoelectron spectroscopy showed a shift in Sn 3d, Ti 2p, and Pt 4f binding energies indicating a flow of electrons among the catalyst elements.

5.1 Introduction

Oxygen reduction reaction (ORR) typically takes place at a potential window where a catalyst works under severe conditions *ca.* 1.23 V vs. RHE. Platinum and its alloys that are supported on carbon materials are the most commonly used electrodes in ORR [285]. However, a direct deposition of Pt NPs on a bare carbon support suffers from some serious limitations. First of all, carbon support corrosion has been identified as one of the major reasons for losing Pt surface area and diminishing performance [286]. Secondly, the weak-electronic interaction between Pt NPs and carbon causes the water to bind strongly with Pt active sites resulting in a high over potential and a slow kinetic during the ORR [287]. Many research groups have devoted tremendous amounts of time and effort in the attempt to overcome these obstacles. Some have suggested replacing carbon materials with metal oxides supports [288],[204],[289],[290]. However, one of the major drawbacks of metal oxides is their low conductivity which hinders the essential flow of electrons. The conductivity issue can be resolved by either element doping [268] or carbon doping [204]. Nevertheless, both processes require a high temperature that could create another problem: metal oxide sintering which results in a significant reduction in the surface area, leading to an increase in the catalyst nanoparticles aggregation that reduces active sites [291]. Luo et al.[292] reported an enhancement of the ORR activity and durability by using SnO_2 and SiO_2 as a binary metal oxide support for Pt NPs. The latter study attributed their results to the contribution of SnO_2 as a promoter and SiO_2 as a protector against the carbon corrosion. In the study described in this chapter, a high surface area, fluffy-TiO_2 layer of 10-nm thickness on CNTs, was synthesized as support. Tin oxide (SnO_2) was used as a bi-element with platinum in order to bind with water molecules to mitigate Pt-OH formation [293]. The catalyst was denoted Pt@ST/CNTs. A binary oxide support could

accelerate the water splitting that supplies protons for adsorbed oxygen molecules on the Pt surface. As a consequence, the generated OH on metal oxides may repel the OH_{ads} on Pt sites leading to a weakening of the Pt-OH bond [294].The electrochemical results showed a reduction in overpotential of ORR and it was observed at 930 mV, compared to that of Pt/C 860 mV. Additionally, a half wave was recorded at 817 mV, 777 mV in pre-cat and Pt/C, respectively. XPS analysis showed a positive shift in SnO_2 and TiO_2 binding energies, which indicates that oxygen vacancies are present in the catalyst composite. Furthermore, a positive shift in Pt 4f. The XRD also revealed an increase in TiO_2-rutile (110) phase which plays an important role in ORR [295].

5.2 Experimental Section

The fluffy TiO_2 nanolayer on CNTs was obtained following a unique CLD nanocoating process previously reported [33, 219]. The carbon doping was carried out in a tube furnace as reported elsewhere [26]. Briefly, 10% acetylene in nitrogen was used for doping TiO_2 at 700 °C for 2 hours. Tin dioxide was deposited on TiO_2 by hydrolysis of $SnCl_2 \cdot 2H_2O$ in hot water. The metal oxides were then annealed at 600 ºC under inert N_2 gas. Pt NPs were deposited by reducing K_2PtCl_4 salt in a polyol process. The obtained catalyst is designated as Pt@ST/CNTs, hereafter. XRD (Philips, X'pert) data was obtained over an angle range of $2\theta = 5° – 90°$ at a scan rate of $0.026^{\circ}/s$. XPS (Kratos, Axis 165) data was obtained for C 1s, Ti 2p, Sn 3d, O 1s and Pt 4f. Elemental mapping from electron energy loss spectroscopy (EELS) was conducted to determine elemental distribution.

Electrochemical tests were carried out by an electrochemical workstation (BAS100). A Pt supported on carbon black (Pt/C) catalyst with the same Pt loading was used for control purpose. Ag/AgCl (3.5 M) electrode and a Pt wire were used as the reference and counter electrodes in a three-electrode cell. The catalyst was dispersed in ethanol

solution to prepare a catalyst ink at 1.0 mg/mL. A 20 μL of the dispersed catalyst was dripped onto a newly polished glassy carbon electrode disk (5 mm in diameter), and before drying a 5 μL of Nafion solution (0.05%) (DuPont) was dropped on the electrode to cover the ink and dried before tests. Cyclic voltammetry (CV) was carried out at a scan rate of 50 mV/s in a N_2-purged electrolyte solution of 0.5M H_2SO_4. ORR test was carried out in the same electrolyte but saturated by O_2 for 30 min at a scan rate of 10 mV/s.

5.3 Results and Discussion

5.3.1 Characterizations Results

Figure 5.1 (a) shows a TEM image of a TiO_2 nanocoating on CNTs. The surface of TiO_2 shows a fluffy morphology. The specific surface area was measured to be 310 m^2/g, which is much larger than that of the CNTs (~44 m^2/g) or that of carbon black (Vulcan XC 72 ~ 250 m^2/g), indicative of an ideal catalyst support of the fluffy layer.

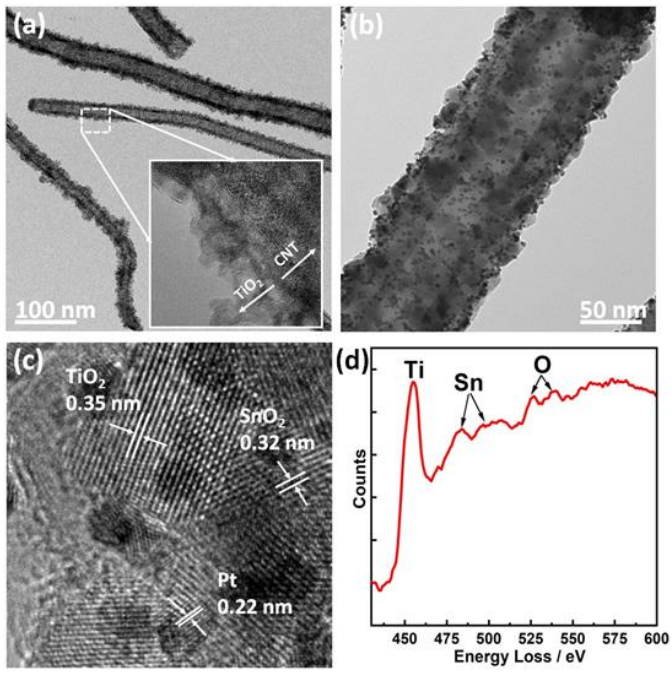

Figure 5.1. (a) TEM images (a) TiO_2 fluffy nanolayer on CNTs (with inset as higher magnification image), (b) A TEM image of the Pt@ST/CNTs catalyst: Pt NPs and SnO_2 supported on fluffy nanolayer of carbon doped TiO_2/CNTs, (c) Crystalline lattice spacing of the Pt, TiO_2 and SnO_2 in the catalyst, and (d) EELS spectra of the catalyst.

Figure 5. 1 (b) shows that the Pt NPs are uniformly dispersed on the fluffy surface. The high-resolution TEM image in the inset in figure 5.1 (c) shows interplanar spacing of major elements. EELS was carried out on the catalyst Pt@ST/CNTs and further confirmed the existence of Ti and Sn in the metal oxides, as shown in figure 5.1 (d). Figure 5.2 (a) illustrates the XRD patterns of Pt@ST/CNTs that shows all catalyst elements in crystalline phase.

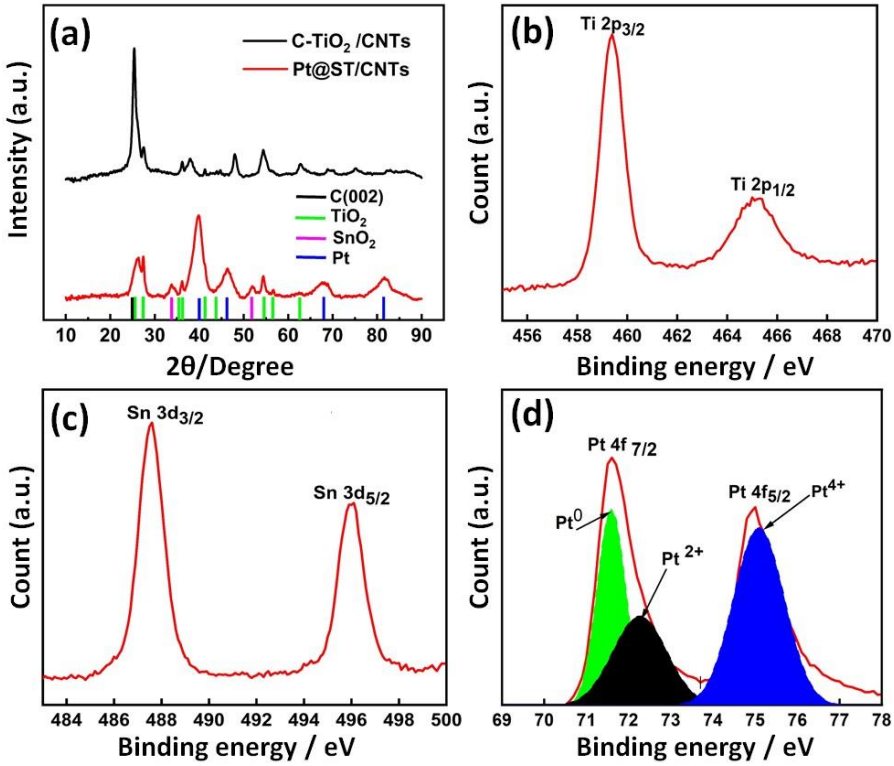

Figure 5.2. (a) XRD pattern of the doped TiO_2/CNTs and after loading platinum and tin oxide, (b-d) XPS analysis for Ti 2p, Sn 3d, and Pt 4f.

For comparison purposes, a sample of carbon doped-TiO_2 (C-TiO_2/CNTs) was examined to observe any sub-oxide formation before deposition of tin oxide and Pt NPs. The XRD spectra exhibits five diffraction peaks for titanium dioxide at $2\theta^o$=26.5, 28, 54.5, 56.8, 63.5 which are assigned to 101A, 110R, 106A, 220A and 310A, respectively[263]. Indeed, a subtle peak was observed at $2\theta^o$= 42.6 which is attributed to suboxide formation as reported elsewhere [32]. After SnO_2 incorporation and after conducting another heating step at 600 °C, the rutile phase R (110) peak shows an

increase. This is an indication that the TiO_2 in the support is in rutile phase. This phase is electrochemically active toward ORR [295]. Tin oxide shows two peaks at $2\theta^o$=33.8 and 52.5 which are attributed to SnO_2 (101) and SnO_2 (211), respectively [264]. Platinum nanoparticles show the characteristic peaks at $2\theta^o$= 39, 46.5, 68.2, 81.8 and they belong to Pt (111), Pt (200), Pt (220), and Pt (311), respectively. It is worth noting that the peak at $2\theta^o$=86 to 87 for Pt (222) facet cannot be detected by the XRD. This may be due to the small size of Pt NPs. From Pt XRD data, we determined the Pt NPs size using the Debye–Scherrer formula (5.1) and it was found to be 3.6 nm [263].

$$d = \frac{k\lambda}{\beta cos\theta} \qquad (5.1)$$

where d is the mean size of the crystalline domains, K is a shape factor with a value of ca. 0.9, λ is the X-ray wavelength, β is the full peak width at half maximum minus the instrumental contribution, and θ is the diffraction angle [265]. Where d is the mean size of the crystalline domains, K is a shape factor with a value of ca. 0.9, λ is the X-ray wavelength, β is the full peak width at half maximum minus the instrumental contribution, and θ is the diffraction angle [265].

Figure 5.2 (b) exhibits the oxidation state of TiO_2. As per a previous report, pure TiO_2 displays BEs at 464.2 eV and 458.5 eV [270]. The BEs of Ti $2p_{1/2}$ and Ti $2p_{3/2}$ were found to be 464.7.0 eV and 458.8 eV which reflect findings in our previous work [35]. Figure 5.2 (c) reveals BEs at 487.6 eV and 496.2 eV of Sn 3d which correspond to Sn (II) or Sn (IV) [264]. They showed no signs of any Sn metallic form. It was reported that pure SnO_2 shows BEs at 486.70 eV [269]. The 0.9 eV difference indicates an electron vacuum in 3d-orbital of Sn. This vacuum has a central role for water adsorption and dissociation, producing OH_{ads} close to Pt-$OH_{ads.}$ As in figure 5.2(d), the BEs of Pt $4f_{7/2}$ and Pt $4f_{5/2}$ are 71.6 eV and 75 eV and they were attributed to Pt in (II) and (IV) states; similar results were reported elsewhere by other groups [266].These findings

point to a strong bonding between Pt and the oxides that put Pt in a negative electronic state. That might also be attributed to electron delocalization between the d orbitals of Pt and the support [267]. However, as reported by Yunteng Qu study, Pt 4f 7/2 was 69.93 eV, which corresponds to Pt^0 [258]. Thus, it could be reasoned that the high binding energy of Pt with both oxides is due to the electron sharing with metal oxides.

5.3.2 Electrochemical Results

Figure 5.3 (a) shows the electro-catalytic activity of the Pt@ST/CNTs and Pt/C in a N_2-purged 0.5 M H_2SO_4 solution at a scan rate of 50 mV s^{-1}. The electrochemical surface area (ECSA) was calculated per hydrogen adsorption / desorption charges normalized with 0.210 μC/cm^2 and it was found to be 77.5 $m^2/g_{(pt)}$ and 41.7 $m^2/g_{(Pt)}$ for Pt@ST/CNTs and Pt/C, respectively. The geometrical specific surface areas of Pt NPs can be calculated from equation 5.2 [271]:

$$S = \frac{6}{\rho d} \qquad (5.2)$$

where ρ is the density of Pt (21.09 g/cm^3) and d is the mean diameter of the Pt nanoparticles in the catalysts [271]. A comparison between S_{act} and S_{geo} can determine the active Pt atoms that contribute to electrochemical reactions. Therefore, the ratio of S_{act}/S_{geo} can be considered a scale for the catalyst activity. In Pt@ST/CNTs, the S_{geo} is 79.02 m^2/g with a ratio of 0.98. This means that 98% of Pt NPs in Pt@ST/CNTs are active during the reaction. The hydrogen desorption peaks of Pt@ST/CNTs with two Pt facets peaks were distinguishable from that of Pt/C, indicating polycrystalline structure of Pt@ST/CNTs. At a range between 350 mV to 550 mV, the double layer charging region of Pt/C is larger than that of Pt@ST/CNTs. This is attributed to capacitive charges produced on the carbon support due to the carbon surface structure [271] which is different from that of CNTs. At high potential, where metal oxidation

occurs, less metal surface oxidation (Pt-O_x) was observed in Pt@ST/CNTs; it then reduced at early potential (740 mV) in the backward scan. Nevertheless, Pt/C does show a profound metal oxidation due to the high number of electrons in the d shell with a late reduction potential at (709 mV). The difference in the performance is attributed to the presence of the two-oxides coated with platinum that binds with metal oxide that is stronger than the carbon surface [273]. It is worth noting that both SnO_2 and TiO_2 show no oxidation/reduction peaks at this potential window (0-1200 mV.vs RHE) since their characteristic potentials are below zero [274].

Polarization curve (ORR) of Pt@ST/CNTs and Pt/C is shown in figure 5.3(b). The ORR performance of the catalyst with the binary oxide was significantly improved. The onset potential of Pt@ST/CNTs is positively shifted by over 40 mV of Pt/C, and the current density at 900 mV is 1.75-fold higher than that of Pt/C. At a lower over potential (+750 to +900 mV), the current approaches the mixed kinetic/diffusion regime. The half-wave potential is often used to evaluate the electrocatalytic activity for the catalysts. Pt@ST/CNTs showed a marked increase in the half wave at 817 mV and Pt/C recorded (777 mV as reported before) [262] with shift $\Delta E_{1/2}$= 38 mV relative to Pt/C. This confirms the fast kinetic of O_2 on Pt@ST/CNTs, especially in this voltage range where the kinetic is usually slow. The fast kinetic could be attributed to a high Pt specific surface area and oxygen vacancies in bi-metal oxides. It also demonstrates a weak interaction of Pt with OH.

To obtain the true kinetic currents from Pt, figure 5.3(c) shows the mass activity with respect to the potential. At 750 mV, 800 mV and 900 mV, Pt@ST/CNTs exhibits higher current at 2.8, 4.18 and 2.66 relative to Pt/C. In ORR, any catalyst depends on O_2 adsorption energy, the dissociation energy of O-O bond and binding energy of OH on the metal surface [296]. Moreover, the parameters that have an effect on these energies

are Pt electronic structure (d-band vacancy) and Pt-Pt interatomic distance, known as the strain effect [297],[298].

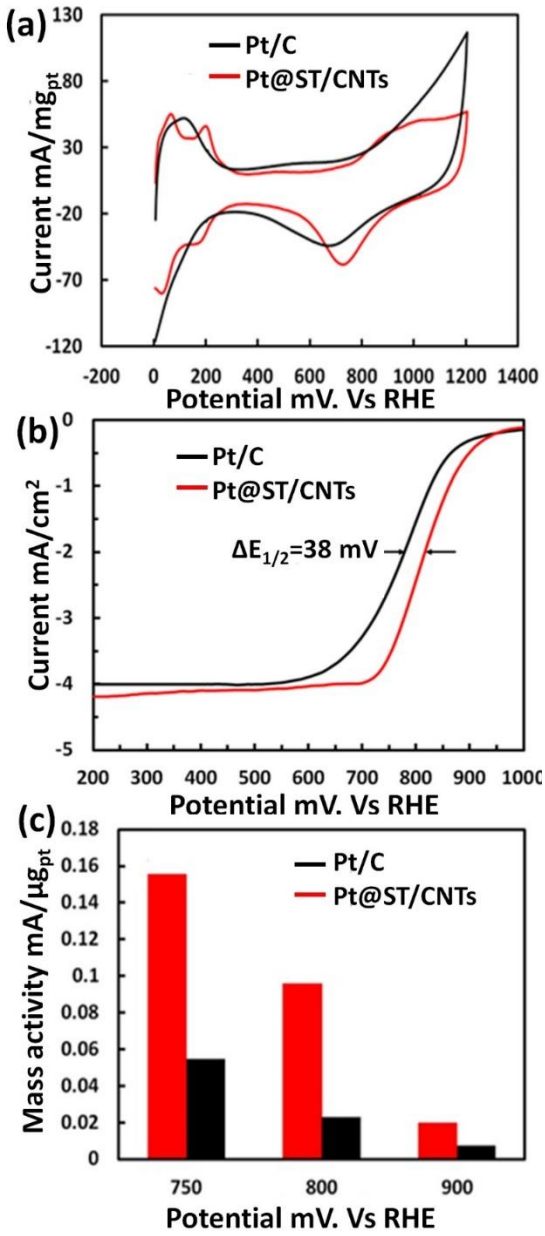

Figure 5.3. (a) CV at 50 mV/s in 0.5 MH_2SO_4 after nitrogen saturation, (b) ORR polarization test at a scan rate of 10 mV/s, (c) Mass activity at various potentials.

Thus, it was argued by others that alloying Pt with another metal such as (Pt-M) or metal oxide such as (Pt-MO_x) could cause a lattice contraction leading to a more favorable Pt-Pt distance for dissociative adsorption for O_2 [299]. Mavrikakis et al. [300] utilized (DFT) calculations to show how the strain modifies the chemical and electronic properties by changing the average energy of the d-band. If Pt atoms are under

compressive strain, the d-orbital overlaps are increased, leading to a broadening of the d-band. As a consequence, the adsorption energy of any adsorbate such as O is expected to decrease [301]. DFT was also used to study the ligand effect by showing how the presence of 3d-metal could alter the Pt surface *d* band. This change is attributed to the interaction between the *d* orbitals of the Pt surface atoms and the *d* orbitals of the substrate 3d elements [302]. Therefore, it is believed that adding metal oxides such TiO_2 [262], or SnO_2 [292] can also lower the energy of d-band, resulting in a reduction of the oxygen dissociative energy of Pt with OH [303].

Apparently, the oxygen reduction reaction does not rely only on the precious metal, but there is a significant effect that comes from the support [288]. It was reported that loading Pt on TiO_2 enhances the ORR reaction due to the surface defects in TiO_2 (110) [304]. Those researchers attributed that findings to oxygen vacancies in rutile TiO_2 (110) that may serve as active sites for water splitting since they tend to create a donor level in the upper part of the energy band gap [305]. In addition, they stated that the amount of water to be dissociated is dependent on the density of oxygen vacancies. In Pt@ST/CNTs, the co-existence of rutile-TiO_2 and SnO_2 increased the oxygen vacancies as confirmed by XPS and XRD. To recap XPS results: binding energy of SnO_2 was positively shifted with a reduced structure of TiO_2. TiO_2 reduction means more oxygen vacancies were created in rutile phase that could enhance the TiO_2 conductivity as abbreviated (Ti_nO_{2n-1}). On the other hand, SnO_2 oxidation means it is ready to adsorb water molecules mitigating Pt-OH formation. Meanwhile, Pt is oxidized as well. This is an indication that there are electrons flowing between the support and the catalyst. Having two metal oxides with PtNPs in the cathode may also generate what is called lateral repulsion between the OH on Pt surfaces and OH on metal oxides [294]. The lateral repulsion leads to a weakening of the Pt-OH bond and promotes O-O breakage

allowing H_2O formation at high potential resulting in the release of Pt active sites. It is vital to point out that SnO_2 suffers from poor stability at potentials relevant to the ORR because SnO_2 can dissolve under acidic conditions. However, SnO_2 in Pt@ST/CNTs shows a positive shift in SnO_2 binding energy as demonstrated by XPS analysis, indicating a strong interaction of SnO_2 with the catalyst composite [292]. Therefore, we added another factor that could enhance the SnO_2 stability which is the high porous surface of TiO_2/CNTs. We believe the TiO_2-fluffy topography may stabilize the SnO_2, preventing it from dissolution in the electrolyte, particularly after annealing at 600 °C. Further investigation is needed, especially regarding the information of the atomic structure of Pt NPs and the oxides.

5.4 Conclusion

Platinum nanoparticles were supported on binary metal oxides containing fluffy TiO_2 layer and SnO_2 for oxygen reduction. ORR onset was positively shifted by 40 mV; in addition, in the region where kinetic/diffusion is mixed, the half wave was shifted as well by 38 mV. The mass activity that represents the true and actual activity of Pt NPs reveals enhancement for double oxides catalyst. It showed 2.8, 4.18 and 2.66 relative to Pt/C at 750, 800, and 900 mV, respectively. The high surface area offered by fluffy TiO_2 coating enabled the Pt NPs and SnO_2 to be uniformly dispersed. The change in the electronic structure for SnO_2 (shift in BE=0.9 eV from the pure SnO_2), in addition to an increase in rutile phase (110) were considered as the main reasons for having the early onset potential. The high electron deficiency in SnO_2 valence orbitals acts as active sites for water splitting, forming SnO_2-OH. Thereupon, the OH_{ads} repulse OH_{ads} from platinum active sites. Also, the reduced form of TiO_2 induced the electron supply path by the formation of the electronic conductive Ti_xO2_{x-1} on the surface due to the carbon doping.

Chapter 6. Iridium/Iridium Oxide and Platinum Nanoparticles on Fluffy TiO_2 Layer as a Catalyst for Methanol Oxidation

- This chapter is written in a manuscript under preparation

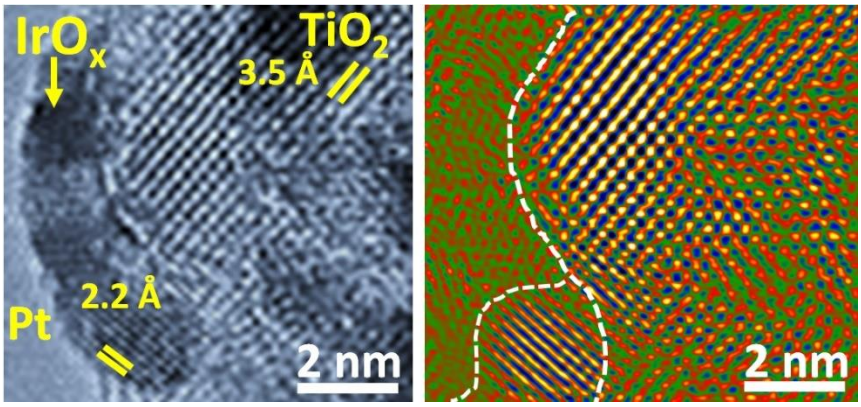

Figure 6.0. TOC

Abstract

Platinum and iridium nanoparticles were decorated onto a fluffy 10-nm doped -titanium dioxide layer on carbon nanotubes. As a prepared catalyst, denoted Pt-Ir/C-TiO_2/CNTs, was used for methanol electro-oxidation (MOR). In this study, we utilized the fluffy TiO_2 coating layer with a high surface area support to host the metals nanoparticles with small nanoparticles size. Having them incorporated on doped TiO_2 with small size particles secures a decent number of the active sites toward methanol molecules; therefore, the catalyst activity is enhanced. Based on electrochemical results of MOR, Pt-Ir/C-TiO_2/CNTs has shown a significant improving regarding the anodic to the cathodic current ratio 5.6-fold magnitude and a negative shift in scan onset by 0.12 V relative to Pt/C (E-TEK). A positive shift in Pt and Ir binding energies was revealed by XPS indicating the metals shared electrons as a back donation with TiO_2. We impute the high forward / backward ratio and the high current after 3600 seconds to the hydrated iridium oxide phase incorporated on reduced Ti_xO_{2-x} where a layer of surface hydroxyl is formed on the hydrous oxide supplying protons to Pt-CO_{ads}. All other

characterizations such as X-ray diffraction (XRD), X-ray photo spectroscopy (XPS) transmission electron microscopy (TEM), and electron spectrum (EELS) were carried out to get deep insights for the prepared catalyst.

6.1 Introduction

Direct methanol fuel cells (DMFCs) have attracted a great interest due to their potential applications. Such applications are automotive industry, co-generation system, electronic portable devices and more. However, many obstacles encounter them such as the catalysts cost, catalysts activity and stability. To make (DMFCs) feasible, it needs an intensive scientific research to address those issues. The highest promising catalyst for DMFCs is platinum based or supported on carbon material such as carbon black, graphite, and carbon nanotubes [306]. In DMFCs, the kinetic on platinum faces a sluggish mechanism due to the poisoning intermediates involved in the process [307] leading to diminishing the platinum nanoparticles actives sites after a certain number of cycles [268]. Also, incorporating the precious metals on carbon directly has several issues like carbon-corrosion in an acidic medium under a cell voltage as in equation: ($C+2H_2O \rightarrow CO_2+H^+ +4e^-$, E^o= 0.207 V vs. NHE at 25 ºC) [272] ; in addition, the weak interaction of Pt on carbon materials [262].

Reducing Pt loading by consolidating with either non-PGM metals such as Co [308], Ni [309], and Ru [310] or with less expensive PGM such as Ir [311] are considered by the community. The alloys structure has shown excellent performance in term of the activity; however, they suffer from the dissolution in the electrolyte as reported elsewhere [312]. Another way to synthesize a durable and an active catalyst is by decorating Pt on metal oxides supports or bi-metal oxides [35]. These supports offer such a high activity with a remarkable durability in acidic fuel cells. Also, they strongly bind with platinum as called the back-donation of electrons from Pt to metal oxide or

vice versa [268]. One of the downsides of metal oxides is the low electron conductivity; however, it can be improved by different electrical doping techniques [262]. Kinetically, there is similarity between oxygen evolution and methanol oxidation because both processes require water discharging on the electrode followed by forming oxygen species on the surface. Nevertheless, they have different potential windows [311]. Since formation of CO_{ads} limits the MOR, it has been stated that incorporating the bi-functional element can generate surface hydroxyl to reduce CO_{ads} to CO_2 [313-315].

Iridium has a long history dealing with water hydrolyzing process, and it is cheaper than platinum by 40%; furthermore, it is a stable element in acidic media at a certain window [316],[317]. In this research, we present a catalyst comprised of Pt-Ir/C-TiO_2/CNTs, prepared in three steps (i) CNTs coating by TiO_2 (ii) TiO_2 carbon doping (ii) Pt and Ir deposition. The prepared catalyst shows a remarkable ratio of forward to backward peak around (I_f/I_b~ 5.6) with a negative shift in the onset peak by 0.12 V in MOR. Also, the prepared catalyst exhibits 12 times increase in the current than that of Pt/C after 3600 seconds at 0.5 V (vs. 3.5 M Ag/AgCl) as tested by the i-t curve. The XPS results show a positive shift in Pt and Ir binding energies. Particularly, Ir exhibits a ~1 eV above the Ir^0 metallic state. Moreover, the metallic content is less percent comparing with IrO_x. This XPS data for Ir-oxide matches the hydrous Ir $(OH)_x$ which has a high activity toward water activation due to the oxyphilic sites among the oxygen atoms in the Ir $(OH)_x$ structure. The high performance might be attributed to couples of reasons: (1) high oxygen species are generated on the catalyst during the forward scan leaving less number of free active sites for the backward scan [318], (2) due to the fluffy surface of the oxide support led to form small particles size of the decorated metals that offer a high electrochemical surface area surface area with much less methanol

activation energy [319] (3) a strong interaction between Pt and Ir with C-TiO_2/CNTs makes the metals highly stable and tolerance towards adsorbed carbon monoxide [262].

6.2 Experimental

6.2.1 Materials

Multiwall CNTs (purity >95%, diameter 35-60 nm) were obtained from NanoLab. Potassium tetrachloroplatinate (K_2PtCl_4- 46% Pt min) was supplied from Alfa Aesar. Titanium isopropoxide ($C_{12}H_{28}O_4Ti$, 99.9% metal basis) was purchased from Sigma Aldrich. Iridium was derived from potassium hexachloroiridate (III) hydrate ($K_3IrC_{l6}H_2O$-33.4% Ir min) from Alfa Aesar.

6.2.2 TiO_2 coating, Doping, and Catalyst Deposition

Acid-functionalized carbon nanotubes were TiO_2-coated by the CLD technique with thickness ~8-10 nm [320]. To make that layer conductive, a carbon doping process [262] by acetylene decomposition at 700 ºC was performed. A certain amount of C-TiO_2/CNTs were dispersed in DI-water and ethylene glycol under sonication probe power, and 0.5 ml of NaOH was added to adjust the PH at 9. A mixed amount of platinum and iridium precursors were added onto 9-PH of C-TiO_2/CNTs dispersion under a cold stirring plate for 1 hour to allow the metals precursors to mix then the whole solution was put on a hot plate at 120 °C for 2 hours to get the precursors reduced. Then, the material was centrifuged, filtrated, and dried.

6.2.3 Characterization and Analyses

The morphology of the synthesized electrocatalysts was characterized by transmission electron microscopy (TEM, JEOL-1400 and FEI Tecnai G2 F30 TWIN) under bright–field imaging mode. X-ray diffraction (XRD, Philips X-pert) equipped with Cu Kα was performed to analyze the crystalline phase of the catalysts. The data was collected over

an angle range of 2θ= 5 ˚ – 90˚ at a scan rate of 0.026˚ s^{-1}. X-ray Photoelectron Spectroscopy (XPS, Kratos Axis 165) was conducted to analyze the C 1s, Ti 2p, O 1s, Ir 4f, and Pt 4f. Surface charge was determined by using Zeta potential. Also, the metal oxide fluffy surface area was measured under isotherm N_2 adsorption (BET).

6.2.4 Electrochemical Performance

All electrochemical tests were carried out by an electrochemical workstation (BAS100) to study the electrochemical performance of the prepared catalysts and compare with a benchmark catalyst Pt/C (E-TEK). An Ag/AgCl (3.5 M) electrode and a Pt coil wire were used as the reference and counter electrodes, respectively, in a three-electrode cell. The prepared catalysts were dispersed in ethanol and water to prepare an ink of 1 mg ml^{-1}. A 20μL of the dispersed catalyst was dripped onto a polished glassy carbon electrode (5 mm in diameter), followed by 5-7 μL of Nafion solution (0.05 wt%). Cyclic voltammetry (CV) was carried out at a scan rate of 50 mV s^{-1} in a 1.0 M H_2SO_4 electrolyte with nitrogen purge (for 30 min. Measurements were carried out in 0.5 M H_2SO_4 + 1.0 M CH_3OH to determine methanol oxidation reaction activity. To investigate the durability, *i-t* curves were obtained as well for 3600 seconds.

6.3. Results and Discussion

6.3.1. Catalyst Characterization

Figure 6.1 (a-c) show the TEM images of low, medium and the high resolution for a fluffy TiO_2 layer on CNTs. It is seen clearly that the uniform distribution of the metal oxide with fluffy topography on CNTs with a surface area 310 m^2/g as in figure 4.2. Figure 6.1 (c) shows a dense film that attaches the CNTs surface which is a crucial matter to ensure the acidic electrolyte not reach the CNTs surface preventing the carbon corrosion. Figure 6.1 (d-e) exhibit the catalysts deposited on the C-TiO_2/CNTs with an average of 2 ± 0.3 nm for the iridium/iridium oxide and platinum. The fluffy

morphology offers well-dispersion for platinum and iridium nanoparticles without aggregation and small sizes. To further confirm the metals identity, HR-TEM was performed as in figure 6.1 (f) showing the crystallite lattice for Pt, TiO_2, and IrO_x [321]. The ELLS elements spectrum was performed that revealed the light elements (O, C, Ti) distribution on the substrate as in figure 6.2.

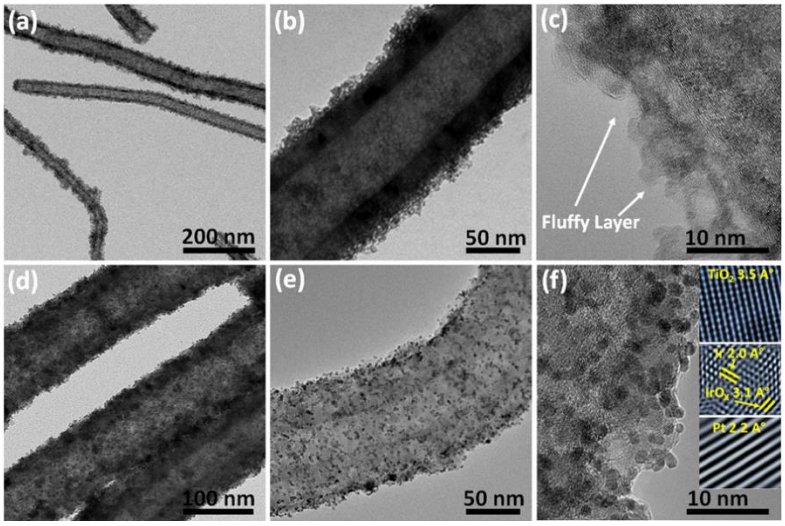

Figure 6.1. TEM images (a-c) Show the TiO_2-fluffy coating low, medium, and high magnification (d-f) Shows the catalyst deposition low, medium, and high magnification, the insets show the lattice size for the catalyst's elements.

Figure 6.3 shows the XRD pattern displaying ten characteristic peaks assigned as follows: C (002) at 2θ =25.6º ; in addition, three pronounced reflection peaks are present at 2θ = 39.8º, 47.4º,68º, and 82.5° for platinum and iridium (111), (200), (220), and (311) planes that are totally consistent with literature [322]. It is obvious that the peak at 39.8° for (111) plane is not a sharp peak. This is assigned to the small sizes Pt and Ir facets which is confirmed by the TEM images as well. Also, it was not shifted much indicating no distortion in the metal structure indicating a non-alloy catalyst. It is worth nothing that the peak at 2θ = 39.8º shows two peaks after the deconvolution (the inset in figure 6.3) that can be attributed to the plane (111) and $Ir(OH)_x$ phase [323],[324]. Titanium dioxide fcc-structures were recorded at 2θ = 44.5°, 54.8º, and 62 º, for TiO_2-

Rutile [325], and TiO_2-suboxides [262], and 2θ= 55.5°and 75° were assigned to TiO_2-anatase [326]. It is worth noting that the peak at 62º might be attributed to sub-oxides formed after carbon doping step by modifying the TiO_2 atomic stoichiometry by either replacing one oxygen atom with carbon, or embedding the carbon atom inside the titania structure to increase the conductivity [325].

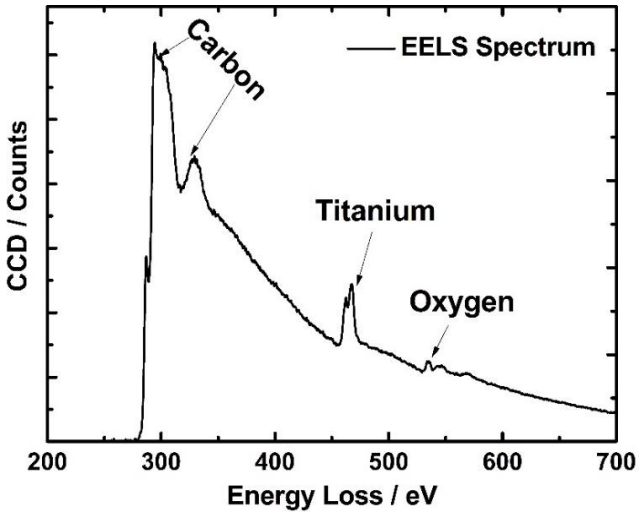

Figure 6.2. EELS spectrum of C-TiO_2/CNTs

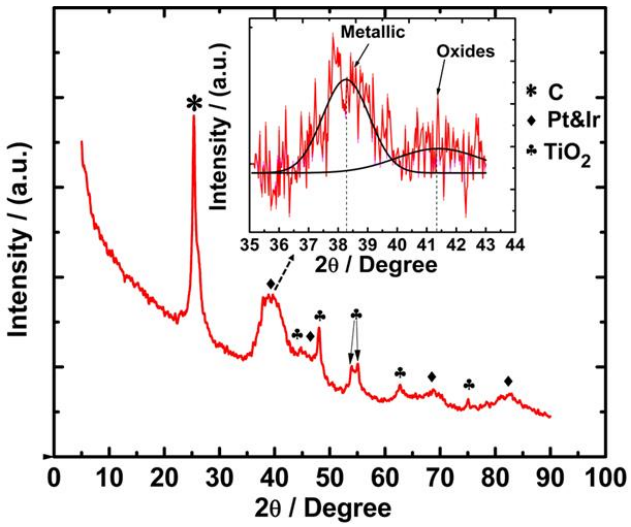

Figure 6.3. XRD pattern for the catalyst.

The chemical states of Ti, O, C, Pt, and Ir were investigated by XPS, and their results were displayed in figure 6.4. Figure 6.4 (a) shows a survey spectrum depicts all the catalyst elements. All the XPS data were calibrated based on the well-known carbon

peak at BEs of 284.9 eV as shown in figure 6.4 (b). It was reported before that the Pure TiO_2 (Degussa, P25) exhibits characteristic binding energy for Ti $2p_{1/2}$ and Ti $2p_{3/2}$ at 464.2 eV and 458.5 eV; however, the reduced form, Magneli phase Ti_4O_7, has BEs at 464.7 eV and 459.0 eV [270]. Taking that as a reference, figure 6.4 (c) shows the Ti 2p binding energy was positively shifted for Ti $2p_{1/2}$ and Ti $2p_{3/2}$ at 459.4 eV and 465.1 eV, respectively. Clearly and it is agreed with XRD data, the Ti in the catalyst composite was reduced to a form as called suboxides [327]. This is because of the probability of either carbon incorporated into the TiO_2 lattice (Ti_xO_{2x-1}) or substituted for oxygen ($TiO_{2-x}C_x$), and both formulas to enhance the conductivity [328].

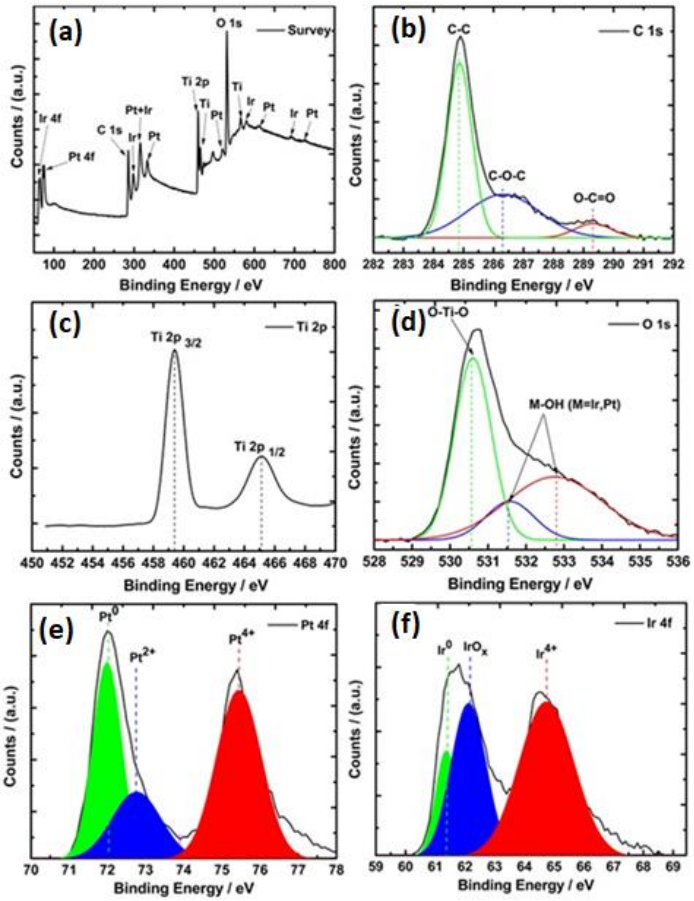

Figure 6.4. XPS data for all the catalyst compositions.

After the deconvolution, O 1s BEs were observed at 530.6, 531.5, and 532.6 eV as in figure 6.4 (d). The 530.6 eV is consistent with Huang et al. results [204] and it was shifted to a higher BE than of pure TiO_2 as reported somewhere [329]. Furthermore, the

other two peaks 531.5 and 532.6 eV are ascribed to the adventitious metal hydroxide Ir $(OH)_x$ and Pt $(OH)_x$, respectively [330],[331]. This reveals a high oxygen species on the surface which is mainly due to the $Ir(OH)_x$ [332], [333] coupled with TiO_2. Naeem et al. report that the two peaks 531.5 and 532.6 eV are developed with increasing oxygen vacancies [334]. Figure 6.4 (e) shows the oxidation state of Pt 4f. It can be seen Pt $4f_{7/2}$ and Pt $4f_{5/2}$ show BEs at 72.2 eV and 75.4 eV, respectively. Pt/C binding energy was reported elsewhere, and it was found to be 71.3 eV and 74.6 eV [335]. Thus, it is obvious Pt has a high binding energy which is attributed to the electron back donation between the Pt and the support [35]. Metallic iridium Ir^0 4f $_{7/2}$ BEs was reported elsewhere at 60.8 eV [336], and it was also reported at 60.9 eV [337]. In Pt-Ir/C-TiO_2/CNTs, Ir 4f $_{7/2}$ and Ir 4f $_{5/2}$ were recorded at 61.7 eV and 64.7 eV, respectively as in figure 6.4 (f). These values indicate the iridium has a mixed phase of metal and metal oxide. Since both precious metals are in an electronegative chemical state, it can be concluded that no alloy between Pt and Ir was formed. It could be ascribed to following reasons: (i) the low temperature of the catalysts synthesis conditions [338], (ii) Pt and Ir are face-centered cubic – fcc, and at a room temperature, they have a close lattice constant [339], (iii) the activation energy to form an alloy at a low temperature could be much higher than to share back donation between the metals and the doped-TiO_2. As a consequence, the positive shift in the BEs in Ti may indicate the TiO_2 gained electrons from Pt and Ir [204]. The areas under the curve of the XPS of the Pt and Ir 4f electrons were then used after the deconvolution to estimate the phases content of the two metals nanoparticles [340],[323] as shown in table 6.1. The high ratio of iridium oxide relatively to metallic Ir is due to the catalyst was not undergone to any calcination atmosphere [338],[332].

Table 6.1. shows the metal/metal oxide contents of Pt and Ir.

Metal	Phase	Content%
Pt	Pt^0	33.9
	Pt^{2+}	23.4
	Pt^{4+}	42.7
Ir	Ir^0	17
	IrO_x	33.2
	Ir^{4+}	49.8

6.3.2. Electrochemical Results

Figure 6.5 shows the cyclic voltammetry of Pt-Ir/C-TiO_2/CNTs and Pt/C in 0.5 H_2SO_4. It is seen that the characteristics peaks of hydrogen adsorption/desorption at range (0-0.210 V) and the metals surface oxidation peak at a potential >0.6 V are present. In Pt/C, the peak at 0.59 V is assigned to Pt-reduction; however, the Pt-Ir/C-TiO_2/CNTs peak was negatively shifted to 0.43 V which could be assigned to the change in metal-oxygen bonding in the prepared catalyst [322].

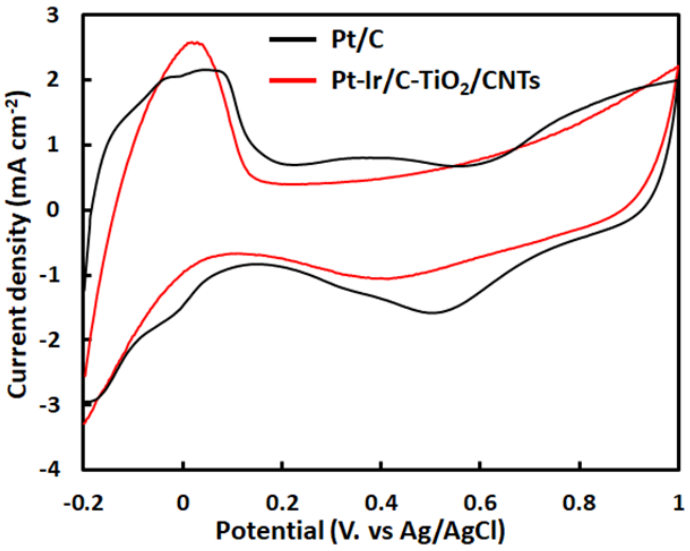

Figure 6.5. CV in 0.5MH_2SO_4 at a scan rate of 50 mV/s.

Figure 6.6 (a) presents the cyclic voltammetry of methanol oxidation on Pt/C and Pt-Ir/C-TiO_2/CNTs in 0.5M H_2SO_4+1M CH_3OH solution. The small peak at the hydrogen region in Pt-Ir/C-TiO_2/CNTs might be attributed to the dissociative adsorption of methanol on Pt (111) plane as reported elsewhere [341]. We named the three peaks in Pt-Ir/C-TiO_2/CNTs as following I_{f1} is the first anodic peak at 0.72 V, I_{f2} is the second

anodic peak at 1.0V, and I_b is a cathodic peak at 0.46 V; however, in Pt/C I_{f1} and I_b showed up at 0.73 V and 0.52 V which is in good agreement with [335]. There is a shift in the onset potential by 0.12 V in a favor of Pt-Ir/C-TiO_2/CNTs to Pt/C. The MOR mechanism starts at 0.3 V as a dehydrogenation process which involves the intermediate species and carbon monoxide formed on the catalyst active sites [342]. The reaction rate will be determined by oxidizing the CO_{ads} converting to CO_2 as illustrated in the equations below in:

$$CH_3OH_{bulk} + M \rightarrow M - CO_{ads} + 4H^+ + 4e^- \quad (6.1)$$

$$H_2O + M \rightarrow M - OH_{ads} + H^+ + e^- \quad (6.2)$$

$$M - CO_{ads} + M - OH_{ads} \rightarrow CO_2 + 2M + H^+ + e^- \quad (6.3)$$

Where: M is an active site of the catalyst.

The rate of the reaction in step (6.3) is dependent on how much generated water during step (6.2) according to Langmuir−Hinshelwood mechanism [342]. Previously, it was reported that the backward peak is not related to intermediates species.; Moreover, the same study assigned that to the degree of the oxophilicity (defined as a tendency to form water) on the catalyst surface [318]. With their interpretation, the higher I_{f1} peak, the higher number of CO_{ads} on the sites were converted to CO_2 leading to less peak current at backward I_b. The I_{f2} might be assigned to the methanol oxidation on Pt-O surface that comes from reaction (6.1) [343]. Tong's group found the I_b has no relation with the residual carbon oxidation [343]. They studied the methanol oxidation reaction (MOR) *in situ* surface enhanced IR absorption spectroscopic (SEIRAS) on two commercial electrocatalysts Pt/C and PtRu/C. In the same study, positive and negative scans were conducted while the scope online to detect the CO_{ads}. In PtRu/C, the CO_{ads} was detected in the backward scan although in the CV the I_b is unobservable. They assigned I_b to the fresh adsorbed species, not the residual carbon.

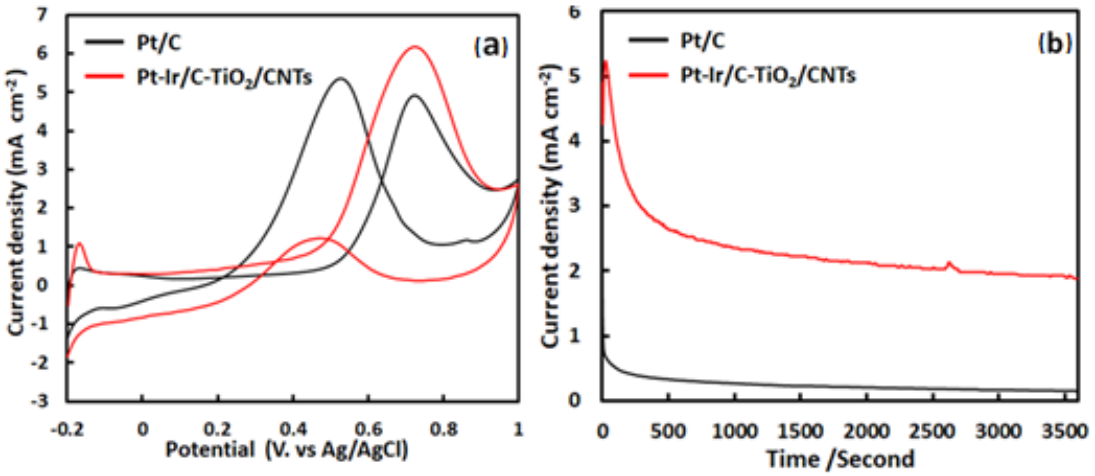

Figure 6.6. (a) Cyclic voltammetry in $0.5MH_2SO_4+1.0MCH_3OH$ at 50 mV/S, (b) *i-t* test in $0.5MH_2SO_4+1MCH_3OH$ at 0.5V.

The last study also pointed out that the negative shift in the MOR peak is to the much water dissociation generating more OH. Therefore, it can be presumed that the less current of I_{f1} leading to having a high backward peak as expressed ξ= 1-ώ, where: ώ and ξ are forward and backward available active sites that were covered by OH[344]. Pt/C shows a low forward peak due to a smaller number of methanol converted to CO_2 or even dehydrogenated in forwarding scan leading to a high backward peak which is assigned to fresh species oxidation or PtO_x-MeOH dehydrogenation. Here, the role of having Ir/IrO_x on $C\text{-}TiO_2$ is considered as an oxophilic center element that might be exposed to oxidation at a low potential assisting the redox process of Pt^0/Pt^{2+} leading to introduce more adsorb hydroxyl nearby to $Pt\text{-}CO_{ads}$ [345]. The backward peak potential position at 0.46 V is so close to Pt-O reduction as in CV in sulfuric acid; however, there is no peak observed of backward methanol oxidation at Ir and regions meaning the CH_3OH molecules have a high affinity to Pt rather than Ir/IrO_x [346]. Also, it was reported that Ir-metallic or an oxide form could destabilize OH_{ads} at the same degree of Ru but not adsorb the methanol which helps with CO oxidation [347]. These observations indicate more facile oxidation of CO on $Pt\text{-}Ir/C\text{-}TiO_2/CNTs$ than on Pt/C. Amin et al. studied methanol oxidation on platinum with metal oxide promoters (IrO_x,

RuO_x) and they suggested a high activity is related to the water displacement mechanism on the promoters [348]. Water dissociation takes place on these metal oxides at a low potential via a sequence of steps since those oxides favor water coverage on their surface followed by the dissociation step to produce hydroxyl and hydride groups [349]. Another study was conducted by using a boron-doped diamond powder (BDDP) with IrO_2 as a substrate for platinum used toward methanol oxidation in alkaline medium [350]. The latter reported 61.4 eV and 64.7 eV as a binding energy for Ir and those values were assigned to Ir $(OH)_x$ as called a hydrated-metal hydroxide. Also, they recorded an I_f/I_b=10 and this outcome was attributed to Ir $(OH)_x$ could help in CO_{ads} oxidation. To link the last study with ours, it was evidenced by XPS that Ir is in the form of Ir $(OH)_x$ according to the binding energies which are totally consistent with [350]. The Ir $(OH)_x$ is known to be hexagonal structure in which the oxygen atoms on share the edges which contains either hydroxyls or water as a bridge connection. Those bridges are more susceptible for water molecules attack from the electrolyte leading to having more water discharge on the electrode surface [351]. Also, reduced-Ti_xO_{2-x} can initiate the water due to the oxygen vacancies in the TiO_2 structure [352].

Figure 6.6 (b) exhibits the chronoamperometry test at a constant potential of 0.5 V after 3600 seconds. Pt-Ir /C-TiO_2/CNTs shows 12-fold times enhancement in the current over Pt/C. Introducing a high number of oxygen species by the support destabilize the CO_{ads} on the active sites [353] leading to holding a high current. The current gradually decreased with time in two steps. The big initial decay in the current is attributed to the double layer current. Then, it reaches to a slow steady decay. In Pt/C, the deactivation is due to active sites blockage by the adsorbed organic residues that are slowly formed from methanol oxidation., which required a high potential to be oxidized. Also, the Pt

NPs detachment from the carbon is another reason since even at that potential limit the carbon is prone to be corroded.

6.4 Conclusion

A fluffy-doped-TiO_2 layer on carbon nanotubes was made by CLD method. A reduction method was used to reduce the Pt and Ir salts on the support after adjusting the PH at 9. Such a uniform distribution of the catalyst nanoparticles was observed without forming an alloy between Ir and Pt. Also, XRD spectra revealed no sharp peak of Pt and Ir at $2\theta=39.8°$ peaks for (111) plane indicating small sizes of the metals which are assigned to the high surface area of the fluffy support. The MOR performance of the Pt-Ir /C-TiO_2/CNTs is higher than Pt by 5.6-fold times as forward to backward peak ratio. Moreover, i-t curve showed a high stability at 0.5V after 3600 seconds by 12.5 times which was assigned to the high oxyphilic surface owning to Ir $(OH)_x$ that generates enough water to oxidize the adsorbed carbon monoxide. Moreover, a high shift in the binding energy of the Pt, Ir, and Ti was observed which is confirmed the electron flowing among the catalyst elements and the support showing the mixed phase of Ir and Ir(O)x. This catalyst-composite showed a promising approach regarding the full methanol conversion to CO_2. In depth study is needed to investigate the Ir (OH)x phase contribution in MOR, though.

Chapter 7. Conformal Niobium Oxide Coating on Carbon Black as a Support to Platinum Electrocatalyst for Oxygen Reduction

- Published in Chemistry Select Journal DOI: 10.1002/slct.202003225

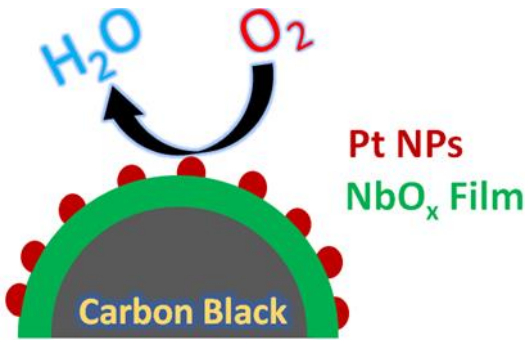

Figure 7.0. TOC

Abstract

Carbon black (CB) is commonly used to support Pt as an electrocatalyst in fuel cells. However, it is easily corroded in electrochemical reactions, such as in the oxygen reduction reaction (ORR), leading to catalyst degradation. In this work, we report results of protecting the CB using an ultrathin 5 nm film of niobium oxide conformally coated on the CB using a new coating technique. Electrochemical test in ORR shows only a 1.7% activity loss after 5000 cycles, demonstrating an excellent durability of the electrocatalyst. Compared to the electrocatalyst without niobium oxide coating, it shows a 25 mV improvement in half-wave potentials, indicative of a better kinetics. A positive shift in binding energy was found in Pt 4f, implying electron delocalization has occurred when Pt is interfaced with the niobium oxide support. The activity enhancement is attributed to the electronic structure change in the electrocatalyst as a result of metal-support interactions.

7.1 Introduction

The excessive demand for energy has become a central motivation to find energy conversion alternatives. Polymer exchange membrane fuel cells (PEMFCs) as an alternative power source are considered as a promising approach. PEMFCs require active, durable, and economically affordable catalyst to be practical. Carbon-supported electrocatalysts (e.g., Pt/C) for oxygen reduction reaction (ORR) have been under in-depth investigation for decades. Those studies have concluded that the carbon surface corrosion plays a critical role in catalyst degradation [354-356]. Therefore, metal oxides as a support for precious metal catalysts have evolved as a solution to overcome catalyst activity loss. In addition, metal oxide support can provide a strong metal-support interaction with the Pt catalyst to improve catalytic activity. These facts have been correlated to the metal oxide oxidation state (M^{n+}) and its stability in a low pH electrolyte [357]. However, metal oxide support suffers from a low-electronic conductivity and often a low specific surface area. Such issues have been tackled by making metal oxides as a thin surface coating, with improved electrical conductivity using metal [268] or carbon doping [35].

Metal oxides, such as TiO_2 [26, 33], Ta_2O_5 [358], Nb_2O_5 [359], ZrO_2 [360], and others have been studied. Huang et al. have reported carbon doped TiO_2 and Nb_2O_5 on carbon nanotubes as a support for Pt in ORR [26, 59]. They found enhancement in both the activity and the durability, attributed to the oxygen-deficient oxide support surfaces and strong metal-support interactions. ZrO_2 has also shown a promising activity for ORR due to its stability against the acidic corrosions [361]. Jia et al.[70] has reported Pt interacts with O and Nb in saturated NbO_x and only with Nb in the unsaturated NbO_x. They further confirmed electron transfer from Pt to NbO_x in both scenarios in boosting the catalyst performance. Ghoshal et al. [69] investigated metallic Nb and Nb oxide to

support Pt. They found strong ligand effect from metallic Nb to suppress the OH formation on Pt, thus enhancing the catalyst ORR activity. More recently, Ma et al.[359] has reported a selective Pt head deposition on NbO_x nails that was embedded in porous carbon. After 50,000 cycles between 0.6-1.0 V, a remarkable durability was found and ascribed to strong metal-support interactions. The idea behind employing metal oxides as a support is that electronic exchange between the metal oxide support and the Pt catalyst can enhance the catalyst activity and stability [362]. Enhancement in ORR activity is ascribed to weakening the formation of Pt-OH, which is the main impediment in ORR [363]. Another factor is that the lateral repulsion between Pt-OH and adsorbed OH on the niobium oxide allows more O molecules to be adsorbed on Pt active sites [362]. In the orthorhombic Nb_2O_5, each niobium atom is surrounded by six or seven oxygen atoms making it in polyhedral connected either by edge or the corners [364]. These oxygen sites play an important role in ORR through oxygen vacancies created in the doping process as reported before [365].

In this work, we present an electrocatalyst comprised of 20 wt.% Pt loaded on carbon-doped 5 nm Nb_2O_5 coating on carbon black (CB). The ultrathin, uniform, and conformal niobium oxide coating was made possible using a new condensed layer deposition (CLD) technique [219]. This new catalyst was compared with the benchmark catalyst of Pt supported on carbon (Pt/C, E-TEK) for control purpose. The results showed a significant enhancement in catalyst durability, as well as an improvement in the catalyst ORR activity.

7.2 Material and methods

Niobium oxide coating process was conducted by the condensed layer deposition, or CLD [219]. Briefly, carbon black (Vulcan XC-72) was surface-oxidized in 3.0 M of 3:1 vol. ratio of H_2SO_4:HNO_3, followed by washing and drying at 70 °C for 2 hours. A 100 mg of CB was dispersed in heptane for 20 minutes under a probe sonication and stirring. A 50 micro-liters of water was added in the suspension and left stirring for 10 minutes. A 8.17×10^{-4} mole of niobium ethoxide (Sigma Aldrich, 99.9%) was injected in the suspension with sonication and stirring. Coated CB was filtered and dried. They were further thermally activated with carbon in a doping process, under a gas mixture of 10% acetylene in N_2 at 700 °C for 20 minutes (sample designated as c-Nb_2O_5/CB) followed by reducing under 5% H_2. Finally, platinum salt (potassium tetra-chloroplatinate, 46% metal minimum, Sigma Aldrich) were reduced inside an aqueous solution of ethylene glycol to make a 20 wt.% Pt mass loading on the support.

7.3 Characterizations

Two types of transmission electron microscopy were used. The JEOL JEM-1400 equipped with Lanthanum-hexaboride (LaB6) filament was operated at an acceleration voltage 120 kV and data were collected on the Gatan Ultrascan 1000 CCD camera. For further investigation, we used a FEI Tecnai F30 Twin TEM equipped with analytical spectrometers (Bruker Quantax 400 Silicon Drift Detector or Quantum 963 Gatan Image filter (GIF)). Brightfield images were acquired on a Gatan Ultrascan 4000 charge coupled device at 300 Kv. XRD (Philips X-pert) equipped with Cu Kα was performed to analyze the crystalline phase of the catalysts. XPS (Kratos Axis 165) was used to analyze the binding energy of C 1s, Nb 3d, O 1s and Pt 4f. Thermal analyses were carried out by Thermogravimetric analyzer (TGA), in a Q500-TA Instruments.

The samples were analyzed using a temperature range from 20-800 ˚C at a scan rate of 10 °C/min. Air as an oxidation gas was used.

7.4 Electrochemical Tests

All electrochemical analysis tests on the Pt/c-Nb_2O_5/CB catalyst were carried out by an electrochemical workstation (BAS100). A Pt/C catalyst (E-TEK) with the same loading was used for control purpose. A Ag/AgCl (3.5M) electrode and platinum wire were used as the reference and the counter electrodes, respectively, in a three-electrode cell. The catalysts were dispersed in a solution of water and ethanol at 1:1 (v/v) to prepare catalyst inks at 1.0 mg ml^{-1}. A 20 μL of the dispersed catalyst was dripped onto a newly polished glassy carbon electrode (5 mm), and before drying, a 5 μL of Nafion solution (0.05%) (DuPont) was dropped on the electrode to cover the ink. Cyclic voltammetry (CV) was carried out at a scan rate of 50 mV s^{-1} in a N_2-purged electrolyte solution of 0.5M H_2SO_4. ORR test was carried out in the same electrolyte but saturated by O_2 for 30 min at a scan rate of 10 mV s^{-1}.

7.5 Results and Discussion

Figure 7.1 (a) shows an image of a transmission electron microscopy (TEM) of niobium oxide coating on CB, or Nb_2O_5/CB. It clearly shows the CB particles are coated with a thin metal oxide layer, with the inset revealing electron diffraction with contrast between the amorphous carbon (the core) and the metal oxide coating in a dense morphology (the shell). Energy-filtered TEM image (EF-TEM) dispays the coating with elemental mapping, indicating the existence of niobium oxide in the coating layer as in figure 7.1 (b-c). Figure 7.1 (d-f) show images of low and high magnifications of Pt nanoparticles loaded on carbon-doped-Nb_2O_5/CB, or Pt/c-Nb_2O_5/CB. The average diameter of the Pt NPs in the catalyst was calculated from the TEM image as in figure

7.1(f) and was found to be 3.8±0.2 nm, whereas that in Pt/C was 3.03±2.0 nm. The lattice interplanar distance in coating c-Nb_2O_5 was found to be 0.258 nm, implying a reduced rutile phase of niobium oxide, or NbO_2. The NbO_2 was generated due to carbon doping that leads to a reduction in the Nb_2O_5 phase [59].

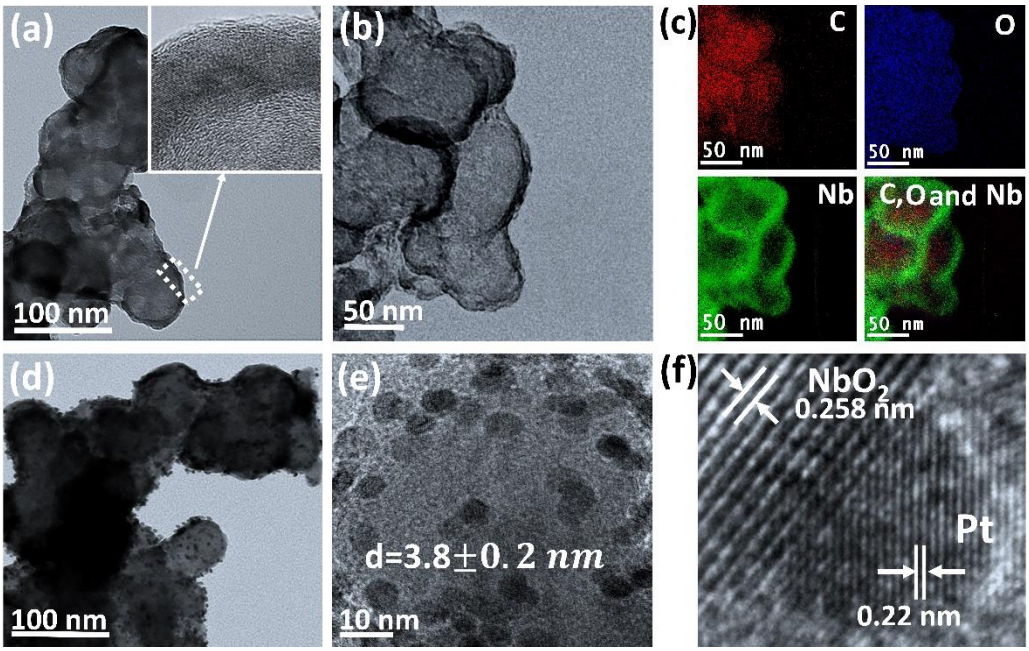

Figure 7.1. (a) A low magification TEM image for c-Nb_2O_5/C, (b) Energy-filtered EFTEM, (c) Elementals mapping for the carbon, oxygen, niobium, and aggreagted, (d) A low magification TEM image for Pt/c-Nb_2O_5/C,(e) Medium magnification TEM image for Pt/c-Nb_2O_5/CB, (f) A high resolution image showing the interplanner spacing of the Pt and NbO_x.

To know exactly how much metal oxide is loaded on the CB, thermogravimetric analysis (TGA) was conducted to combust the CB, which gives 33.7 % as shown in Figure 7.2 (a). Figure 7.2 (b) presents the X-ray diffraction (XRD) pattern for the catalyst Pt/c-Nb_2O_5/CB [366]. The four characteristics peaks for Pt appeared at 2θ = 39.8°, 46.5°, 67.8°, and 81.3°, which are indexed to fcc facets of (111), (200), (220), and (311), respectively [35]. The peak at 39.8° is not a high and sharp peak, which is an indication that the Pt nanoparticles are small in size which is consistent with what we have observed from the TEM as in figure 7.1 (e). The niobium oxide layer was further found to be mixed phases of Nb_2O_5 and NbO_2 in the XRD study [59].

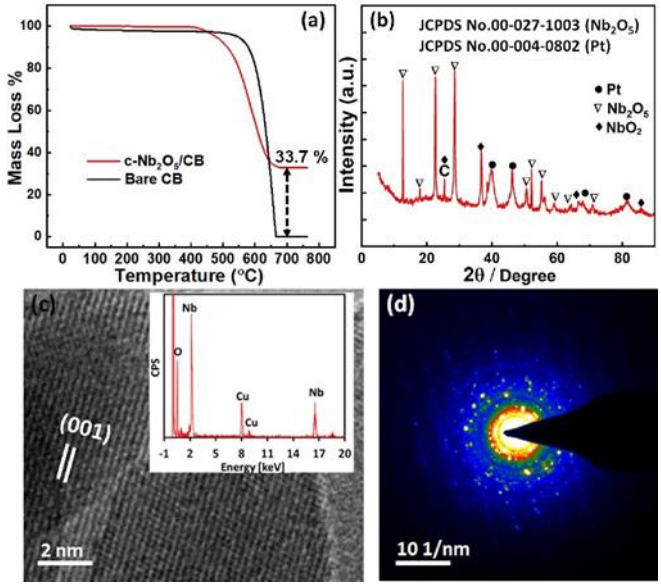

Figure 7.2. (a) TGA profile for bare CB and c-Nb_2O_5/CB showing mass losses, (b) XRD pattern for the catalyst, (c) HRTEM shows carbon doped Nb_2O_5, (d) Selected area electron diffraction with using the nanobeam.

The XRD pattern for Nb_2O_5 is in good agreement with an orthorhombic structure as it is distinguished from its characteristic peaks at 36º and 55º [367]. Figure 7.2 (c) shows the high-resolution transmission electron microscopy (HRTEM) of the carbon doped Nb_2O_5 with energy dispersive spectrum (EDS) (the inset). The selected area electron diffraction (SAED) was performed using a nanobeam to see the local crystal information and it is well-agreed with HRTEM as shown in figure 7.2 (d) [368].

To study the oxidation state for the elements in the catalyst, X-ray photoelectron spectroscopy (XPS) analysis was carried out. Figure 7.3 (a) shows the oxidation state of the core level in Pt $4f_{7/2}$ with a binding energy (BE) of 71.7 eV. The BE of Pt in Pt/C was reported at 71.3 or 71.2 eV [335, 369]. There is 0.4 eV shift to higher BE in the new Pt/c-Nb_2O_5/CB catalyst, which can be correlated to the electron flowing from Pt 4d to niobium oxide. The positive shift suggests an increase in d-vacancy at the valence band with lowering in fermi level [370]. Based on NIST database, the BEs of Nb $3d_{5/2}$ in Nb_2O_5 and NbO_2 were documented to be at 208.1 and 205.7 eV, respectively. Figure 7.3 (b) displays the binding energy of Nb 3d in Pt/c-Nb_2O_5/CB at 207.3 eV. This

indicates there was a partial phase transformation upon the carbon doping process at 700 °C producing a conductive phase [59]. The carbon doping is a reduction process, in which either some of the oxygen atoms are replaced or the carbon being incorporated inside the lattice causing a crystal expansion [369]. In Nb_2O_5, most of the electrons in the 4d orbitals of Nb are located and shared in 2p of oxygen [371, 372]; therefore, any donated or gained electrons could be in the oxygen 2p orbital. The oxidation state of the O 1s was negatively shifted to 530.1 eV as shown in figure 7.3 (c), which is further evidence of reduced oxide, see the supplementary file in the reference [59]. This reduced NbOx is required for the electronic conductivity [373, 374]. To validate the XPS analysis, the C 1s BE of C-C was collected as a reference in figure 7.3 (d) that was found at 284.8 eV [375].

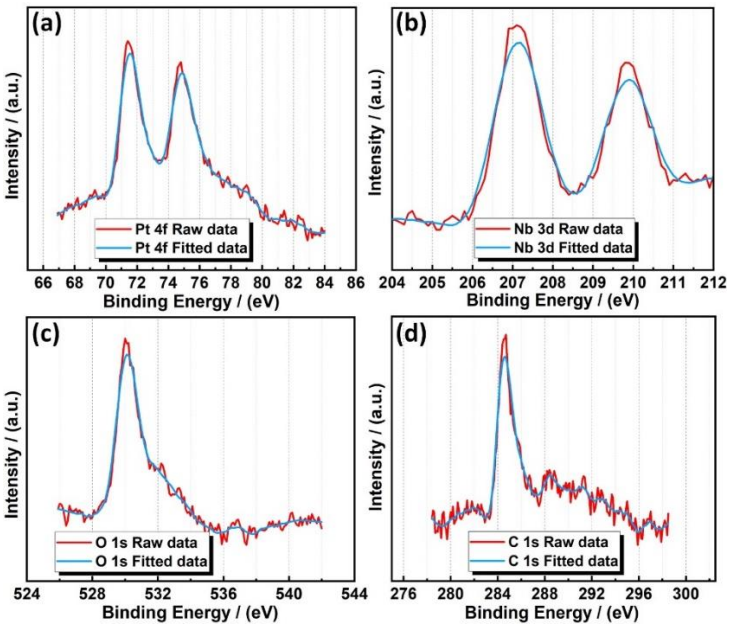

Figure 7.3. XPS analysis for the catalyst (a) Pt 4f, (b) Nb 3d, (c) O 1s, (d) C 1s.

Figure 7.4 shows electrochemical tests of the catalysts in a 3-electrode cell. The inset in figure 7.4 (a) shows the CV for both Pt/c-Nb_2O_5/CB and Pt/C in N_2-purged electrolyte solution of 0.5 M H_2SO_4. The hydrogen adsorption/desorption characteristic peaks are clearly present. The electrochemical surface area (ECSA) was obtained by integrating the hydrogen region peaks, assuming one monolayer was formed over the

Pt surface. The ECSA was 71.2 m^2/g for Pt/c-Nb_2O_5/CB, and 59.3 m^2/g for Pt/C in a good agreement with that reported previously [70].

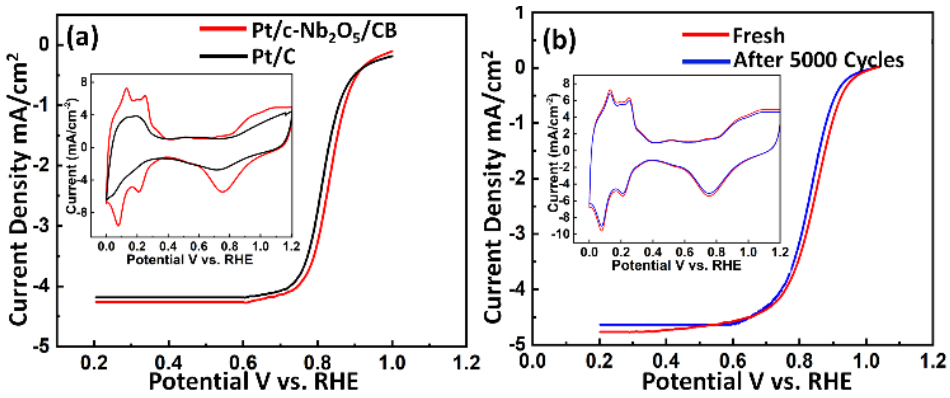

Figure 7.4. (a) ORR in O_2-saturated 0.5 M H_2SO_4 at a scan rate 10 mV/s (the inset is the CVs), (b) Durability tests before and after 5000 cycles for Pt/c-Nb_2O_5/CB.

From the inset of figure 7.4 (a), the reduction peak of Pt-O in Pt/c-Nb_2O_5/CB was 0.78 V whereas Pt-O in Pt/C at 0.73 V. Figure 7.4 (a) shows the ORR polarization curves of ORR in the same electrolytes but saturated with O_2. The onset potential was recorded for both catalysts and were found to be at 0.94 and 0.92 V for Pt/c-Nb_2O_5/CB and Pt/C, respectively. The Pt/c-Nb_2O_5/CB displays a 25 mV shift in half-wave potential when compared to Pt/C, showing a better ORR kinetic process. The metal oxide coating influences Pt electronic structure, making the Pt in a positive state in the catalyst composite as confirmed by XPS. Therefore, water binding energy with Pt-surface could be weakened. It is believed that Pt donates electrons to oxide support in both structure the oxygen-rich phase Nb_2O_5 and reduced oxygen form NbO_2 whether with Nb or O [376]. The latter study further suggests the geometry mismatch between Pt and Nb_2O_5 that implies a high distortion in Pt lattice. Consequently, a low Pt coordination number and a contraction in Pt-Pt bond (strain effect) could be expected that serve in favor to the performance enhancement. In a saturated form of niobium oxide, the 2p orbital is filled with electrons that are supplied from Nb, which causes a less charge exchange with Pt [372]. This scenario would be different if the niobium oxide is in a reduced

form where the 2p orbital of O is not fully filled. Here, we deduce that c-Nb_2O_5 has a ligand effect with Pt that may explain the activity and the durability [377]. The bonding between Pt and Nb requires a high temperature annealing up to 900 ºC [69] which is not conducted here. It is well-known Pt strongly binds with oxygen at 0.2 eV; therefore, reducing such binding energy improves the Pt performance in ORR [372, 378]. When Pt shares a strong electronic interaction (ligands effect) with the oxide support, the O=O bond requires less energy to break; in addition, Pt clustering formation arising from the Pt NPs migration could be minimized.

More recently, it was reported loading Pt on NbO/CNTs as a catalyst for ORR and compared it with Pt/CNT and Pt/C [379]. In that study, the loss after 5000 cycles was up to 12.5% in mass activity at 0.9 V and 5% in the ECSA. In our results we observed the electrocatalyst has an impressive durability as shown in Figure 7.4 (b). After 5000 cycles, the electrocatalyst has only 1.7% loss in half-wave potential, while Pt/C could lose ~50% as reported previously [26]. Having CB in a well-coated morphology with controlled thickness by Nb_2O_5 play a key role in preventing carbon corrosion, which is a major issue facing fuel cell technology.

Figure 7.5 (a) shows the mass activity comparison between Pt/C and Pt/c-Nb_2O_5/CB at various potentials of 0.75, 0.8, and 0.9 V. The mass activity illustrates the feasibility of the prepared catalyst. It is seen the big difference at 0.8 V where the ORR is controlled by diffusion and kinetic [380]. Such a difference explains the high ability of Pt/c-Nb_2O_5/CB to adsorb and to protonate the oxygen molecule. After 5000 cycles, the Pt/c-Nb_2O_5/CB shows a considerable stability as shown in Figure 7.5 (b).

It believed that the uniform coating has significantly increased utilization of the Pt due to the continuous interface. This results in a minimal access of the acidic electrolyte to the carbon surface, which remarkably reduces the risk of surface corrosion.

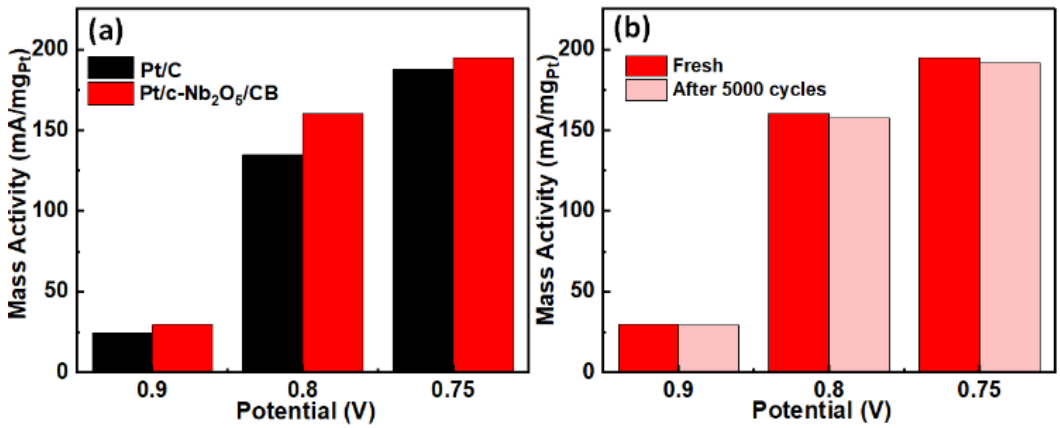

Figure 7.5. (a) Mass activity of Pt/C and Pt/c-Nb_2O_5/CB, (b) Mass activity for Pt/c-Nb_2O_5/CB before and after 5000 cycles.

To further study the kinetics of the ORR in Pt/c-Nb_2O_5/CB, rotating disk electrode was used. Figure 7.6 (a) shows the rotation-rate-dependent current-potential curves of the Pt/c-Nb_2O_5/CB at different potentials 0.70, 0.75, 0.80, and 0.85 V. The number of electrons transferred (n) were calculated to be 3.97 from the slopes of the Koutecky-Levich plots (I_d^{-1} vs. $\omega^{-0.5}$ at a potential of 0.5 V), indicating the nearly complete 4e reduction of O_2 to H_2O on the surface of the Pt/c-Nb_2O_5/CB. The B value was found to be 0.07668 mA/$s^{0.5}$, in good agreement with the theoretical value 0.0771 mA/$s^{0.5}$ and those from experimental findings of Pt supported on the niobium oxides [362, 376, 381]. The linearity of the Koutecky-Levich plot, see figure 7.6 (b) indicates first-order kinetics with respect to molecular oxygen. The kinetic current (I_k) can be determined by using the below formula [382, 383]:

$$1/I=1/I_K+1/I_d \qquad (7.1)$$

where I is the measured current and I_d the diffusion limited current.

The I_d term can be obtained from the Levich's equation:

$$B=0.62nFACD^{2/3}\nu^{-1/6} \quad (7.2)$$

$$I_d=B\omega^{1/2} \quad (7.3)$$

where n is the number of electrons transferred; F is Faraday's constant (96,485 C mol^{-1}); A is the area of the electrode (0.196 cm^2); D is the diffusion coefficient of O_2 in 0.5M H_2SO_4 solution (1.7×10^{-5} m^2/s); ν is the kinematic viscosity of the electrolyte (9.87×10^{-3} cm^2/s); ω is the angular speed of rotation, $\omega= 2\pi f/60$, with f being the RDE rotation rate in (rpm) and C being the concentration of molecular oxygen in 0.5 M H_2SO_4 solution (1.13 mM) [382].

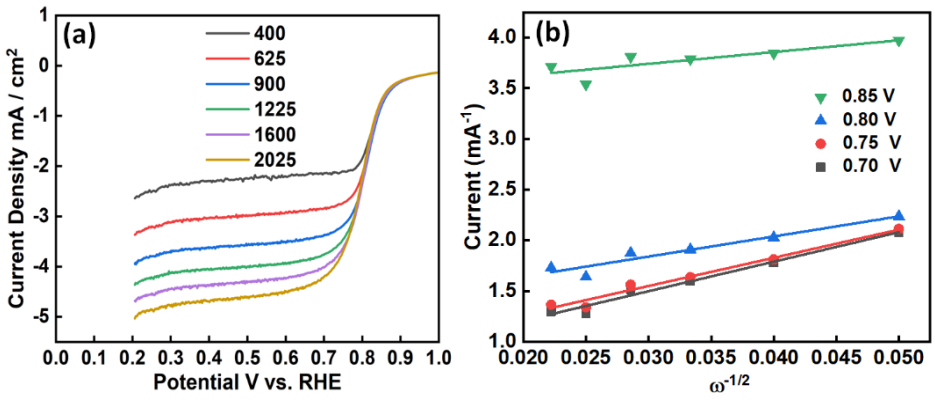

Figure 7.6. (a) ORR versus rotation speed, (b) Current at kinetics region.

7.6 Conclusion

This work reported a thin layer of C-doped niobium oxide on carbon black via CLD coating process as a support for Pt NPs for ORR. Such a conformable coating was achieved, which is thermally activated by carbon to increase the conductivity. The doping process was associated with a partial phase transformation from Nb_2O_5 to NbO_2. The coating layer remained as a layer even after the pyrolysis at 700 °C process, which help prevent any acid from reaching to the CB surface providing full protection. This protection layer enhances the durability and improves the activity both. The activity is related to the electronic interaction between Pt NPs and the oxide layer due to the electron's delocalization leading to weakening the bond between Pt NPs and OH.

Chapter 8. Durable Catalyst Comprised of Platinum and Tin Oxide Supported on Niobium Oxide Nanocoating on Carbon Black Toward Methanol Oxidation

- This chapter is written in a manuscript under preparation

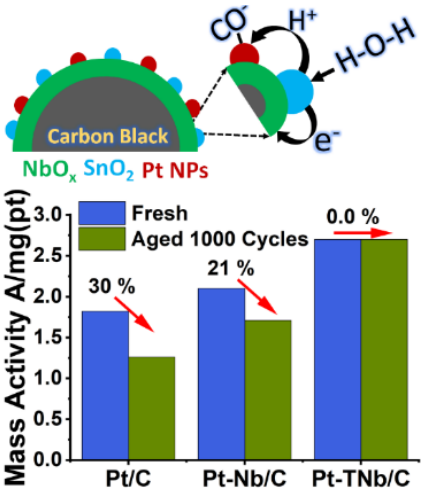

Figure 8.0. TOC

Abstract

In methanol electrooxidation, the deactivation of the catalyst's active sites is undeniable fact which is considered as a major obstacle impeding the direct methanol fuel cells technology. Coupling platinum with metals oxides have shown a substantial enhancement. Here, combining different valences metal oxides, we used niobium pentoxide (Z^{+5}) as a coating agent on carbon black and tin oxide (Z^{+2}) as a promoter with platinum nanoparticles (Pt NPs) in methanol oxidation (MOR), the catalysts are denoted Pt-TNb/C (with tin oxide) and Pt-Nb/C (no tin oxide). XRD revealed a change in NbO_x phase from a partial orthorhombic phase to fully orthorhombic upon tin oxide loading after which a pyrolysis process was taken place at 600 ºC under the nitrogen gas. XPS analysis displays and further confirms there is a synergistic effect between carbon doped-NbO_x and SnO_2. After the carbon doping, oxygen defects are created leading to have sub-stoichiometric of niobium oxide. This has produced a stable SnO_2 and has reversed c-NbO_x to highly oxidized form which both are required in MOR

anode reaction as oxygen surface sources. After 1000 cycles in 1.0 M CH_3OH, Pt-TNb/C has shown (0%) loss in the mass activity compared to (20%) and (31%) in Pt-Nb/C and Pt/C, respectively. Moreover, the Pt-TNb/C shows a remarkable mass activity of 2.7 A/mg(pt) which is a superior compared with a list of papers. We highlight that tin oxide with niobium oxide have the key role on the catalyst activity and stability; however, niobium oxide solely failed.

8.1 Introduction

Direct methanol fuel cells (DMFCs) have gained a substantial attention due to their potential applications in renewable energy conversion, power generation, and automobile sector in addition to their zero greenhouse gases emission. Researchers have sought to find a catalyst that is active with practical durability to put the DMFCs in a practical level [384-392]. Out of the catalyst's materials, platinum is considered as one of the top performer metals. Despite the serious attempts in replacing the platinum by other metals, the durability is still the main impendence. Logistically, platinum scarcity represents a threat on its prospective use which undermines the entire approach. Therefore, design a durable Pt-based catalyst becomes essential to prolong the catalyst life. In DMFCs reaction mechanisms, platinum suffers from the poisoning species produced from the methanol molecules that block the Pt active sites [393]; in addition, the carbon support corrosion in the long-term testing if carbon materials used in the catalyst's composite [394, 395].

These issues have been addressed by either smart designs of the catalyst's support [390] or alloying platinum with other less expensive elements [396]. Pt alloys with first row of transition elements such as (Co, Ni) are unstable in the acidic medium as they selectively leach out from the catalyst's structure [397, 398]. Metal oxides supports

have been extensively considered in MOR approach such as TiO_2 [399], SnO_2 [400], MnO_2 [401], and ZrO_2 [402], CeO_2 [403], WO_3 [404], and Nb_2O_5 [369]. These oxides work well in MOR performance as they are believed to satisfy *Langmuir-Hinshelwood* mechanism [405]. Our group has previously reported an enhancement in the kinetics and the stability by using a bi-metal oxides support consists of TiO_2 and SnO_2 supporting Pt NPs [392]. A study has reported an enhancement in MOR using titanium mesh as a substrate supporting tin oxide that was doped by two elements Sb and Nb [386]. Another study reported using pseudohexagonal TT-Nb_2O_5 supported Pt that showed an enhancement in the activity and the durability [406]. Theessence is anchoring Pt NPs on metal oxides improve the CO tolerance which prolongs the catalyst's life. This improvement is correlated to the following reasons (1) bifunctional effect [407-409], (2) change the electronic structure of the catalyst [410, 411].

In this study, Pt NPs were deposited on a bi-metal oxide support loaded on carbon black. The niobium oxide was used as a protection layer to avoid the carbon corrosion effect and tin oxide as an oxyphilic element that promotes water mobility to oxidize the carbon monoxide adsorbed on Pt active sites. Tin dioxide, SnO_2, as an n-type semiconductor is stable in the acidic solutions and it works well for the anode side. Interestingly, after loading the SnO_2 which is followed by annealing step at 600 °C under N_2 gas, a change in NbO_x phase from a partial orthorhombic phase to fully orthorhombic was observed by both XRD characterization and the electron diffraction. The change in the atomic structure of NbO_x was further confirmed by the pair distribution function under transmission electron microscopy. In line with that, an obvious shift in the binding energy of NbO_x of Nb 3d from 207.3 eV to 207.8 eV was observed. In addition, the binding energy of Sn 3d suffers a positive shift relative to previous studies [412]. Pt-TNb/C showed 2.7 $A/mg_{(Pt)}$ a mass activity at 0.8 V vs. Ag/AgCl which is higher than

a descent number of relevant publications reported in the literature that we reviewed them in this work. Moreover, the Pt-TNb/C shows 0.0% loss after 1000 cycles at 1.0 M CH_3OH, whereas, Pt-Nb/C and Pt/C suffer 21%, 30% loss, respectively. The chronoamperometry (CA) results show also a high CO_{ads} tolerance after 7200 seconds and a remarkable stability.

8.2 Material and Methods

8.2.1 Niobium Oxide Nanocoating, Tin oxide, and Platinum Loading

Niobium oxide coating process was performed by using condensed layer deposition CLD [219]. Briefly, carbon black (Vulcan XC-72) was surface-oxidized by 3 M of 3:1 Vol. ratio of H_2SO_4:HNO_3 followed by washing and drying at 70 °C for 2 hours. 100 mg of CB was dispersed in heptane for 20 minutes under a probe sonication and stirring. A 50 micro-liters of water was added onto the slurry and left stirring for 10 min. A (0.000817mole) of niobium ethoxide (sigma Aldrich, 99.9%) was added as a metal oxide precursor. The Nb_2O_5/CB thermally activated with carbon under a gas mixture of 10% acetylene in N_2 at 700 °C for 20 min (sample after the doping designated as C-NbO_x) followed by reducing under 5% H_2 at 600 °C for 1 hour. Tin dioxide was deposited on c-NbO_x by hydrolysis of $SnCl_2 \cdot 2H_2O$ in hot water and it was annealed at 600 ºC under N_2 gas for 2 hours. Finally, platinum salt (potassium tetra-chloroplatinate 46% minimum, Sigma Aldrich) were reduced inside an aqueous solution of ethylene glycol and water to make a 20 wt.% mass loading.

8.2.2 Characterization and Electrochemical Testing

X-ray diffraction (XRD, Philips X-pert) equipped with Cu Kα was performed to analyze the crystalline phase of the catalysts. The data was collected over an angle range of 2θ= 5º – 90˚ at a scan rate of 0.026˚ s^{-1}. X-ray photoelectron spectroscopy (XPS, Kratos Axis 165) was conducted to analyze the C 1s, Nb 3d , Sn 3d, O 1s and Pt 4f.

Two types of transmission electron microscopy were used. The JEOL JEM-1400 equipped with Lanthanum-hexaboride (LaB6) filament was operated at an acceleration voltage of 120 kV and data were collected on the Gatan Ultrascan 1000 CCD camera. For further investigation, we used a FEI Tecnai F30 Twin TEM equipped with analytical spectrometers (Bruker Quantax 400 Silicon Drift Detector or Quantum 963 Gatan Image filter (GIF)). Brightfield images were acquired on a Gatan Ultrascan 4000 charge coupled device at 300 Kv. The F30 is also equipped Bruker energy dispersive X- ray spectrometer (EDS) QUANTAX 400-STEM. PDF analysis was performed using GSAS II [413]. Firstly, we recorded the electron diffraction using acceleration voltage of 200 kV using the nanobeam. Secondly, silicon wafer was used to calibrate camera length and to get more confidence in the data processing. The electrochemical tests were carried out by an electrochemical workstation (BAS100) to study catalytic performances. Ag/AgCl (3.5M) electrode and platinum wire were used as the reference and the counter electrodes, respectively, in a three-electrode cell by an electrochemical workstation (BAS100). The catalysts were dispersed in a solution of water and ethanol at 1:1 (v/v) to prepare catalyst inks at a density of 1.0 mg ml^{-1}. A 20 μL of the dispersed catalyst was dripped onto a newly polished glassy carbon electrode (5 mm), and before drying a 5 μL of Nafion solution (0.05%) (DuPont) was dropped on the electrode to cover the ink.

8.3 Results and Discussion

8.3.1 Characterizations

Figure 8.1 shows transmission electron microscopy (TEM) images for the catalyst elements. Figure 8.1 (a) depicts a TEM image for the niobium oxide dense coating on carbon black with a conformal morphology. The inset in figure 8.1 (a) shows clearly the core-shell structure of Nb_2O_5/C even after the film is doped by carbon at 700 °C.

Having a dense coating assures us that there is a minimal possibility for the acid to reach the carbon substrate where the carbon corrosion event occurs [394, 395]. To further confirm the coating uniformity, Nb_2O_5/C was burned under oxygen at 600 °C to see the left-over Nb_2O_5 nanoshells. As expected the nanoshells were obtained in a core-shell structure as shown in the figure 2.22 (d-e).

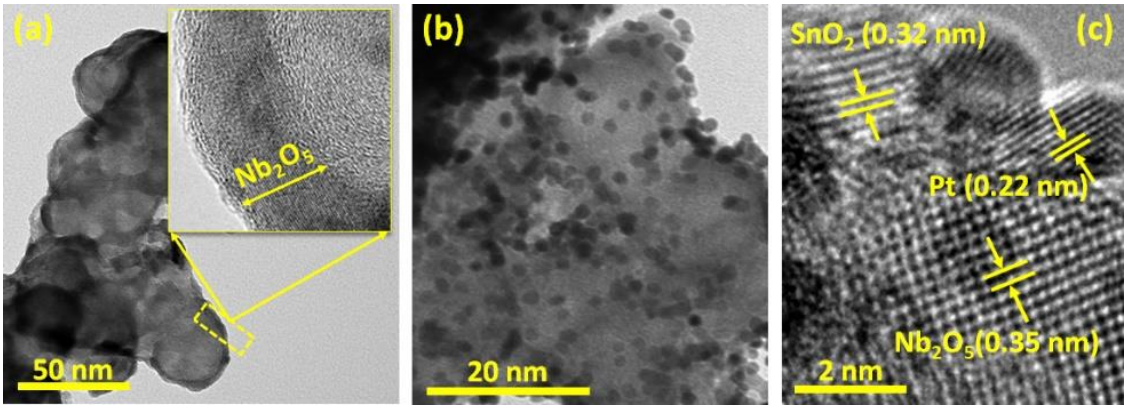

Figure 8.1. (a) A low magnification TEM image for Nb_2O_5/C (the inset shows core-shell structure where the Nb_2O_5 film is the shell and the carbon black is the core), (b) Pt NPs loaded on bimetal oxides support, (c) A high resolution TEM shows the catalyst's elements as they are designated by the interplanar spacing.

Figure 8.1 (b) shows the Pt NPs deposited on the support and it is seen that there is a minimal aggregation. They are amostly in an identical size of 3.4 nm. Figure 8.1 (c) displays the high-resolution transmission electron microscopy (HR-TEM) images showing the three different crystals interplanar for Nb_2O_5, SnO_2, and Pt NPs. Based on Langmuir-Hinshelwood mechanism [405], a bifunctional agent has to be located adjacent to Pt NPs to secure the supplying the protons [414].

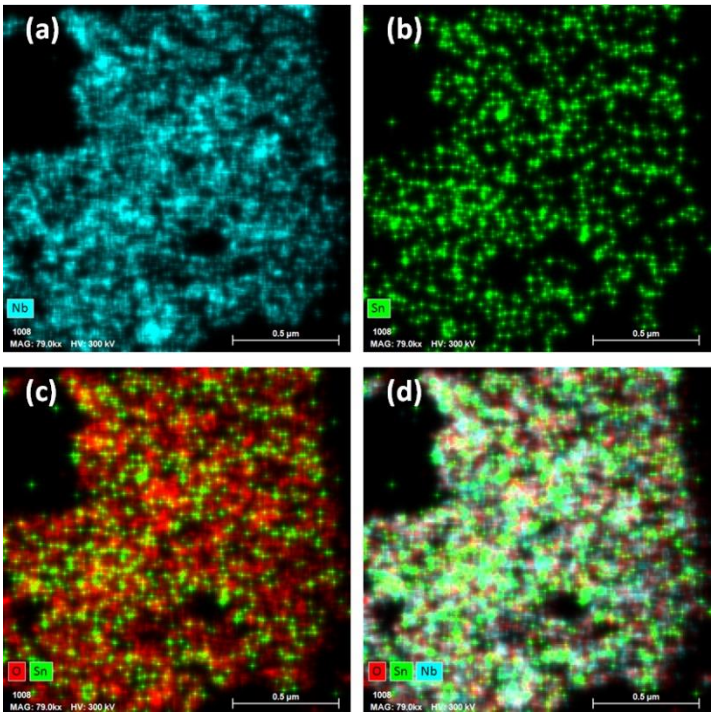

Figure 8.2. Energy dispersive spectrum -transmission electron microscopy (EDS-TEM) for the support after removal the carbon black, (a) Niobium, (b) Tin, (c) Oxygen and Tin, (d) Aggregated oxygen, tin, and niobium.

The HR-TEM exhibits a detailed-image on how the Pt NPs are oriented and surrounded by SnO_2 and NbOx. To check the SnO_2 uniformity, TEM-EDS elementals mapping showed a uniform distribution on niobium oxide as in figure 8.2 . Figure 8.3 shows the XRD patterns for the Pt-TNb/C and Pt-Nb/C. It is seen that all the catalyst's elements are detectable, Nb_2O_5, NbO_2, SnO_2, and Pt. Upon the SnO_2 incorporation, the XRD patterns shows an obvious change in the NbO_x from a partial orthorhombic phase to fully orthorhombic as the peaks at $2\theta°$=16.2 and 18.7 disappeared [415]. This change confirms a modification in the average atomic structure of Nb_2O_5.

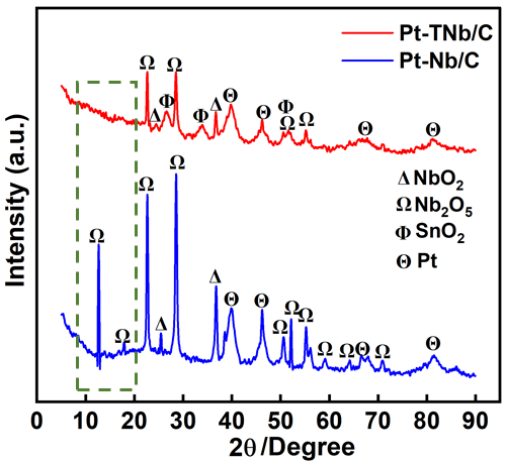

Figure 8.3. XRD pattern for the both catalysts, Pt-Nb/C and Pt-TNb/C.

The peaks for NbO_2 are still available at 2θ°=24.6 and 36.7; however, they appear with less intensity after adding SnO_2 which indicates a change in the structure occurred, indeed. The characteristic peaks for SnO_2 appear at 2θ°=26.6, 33.8 and 52.5 which are attributed to (110), (101), and (211) planes, respectively [264, 416].

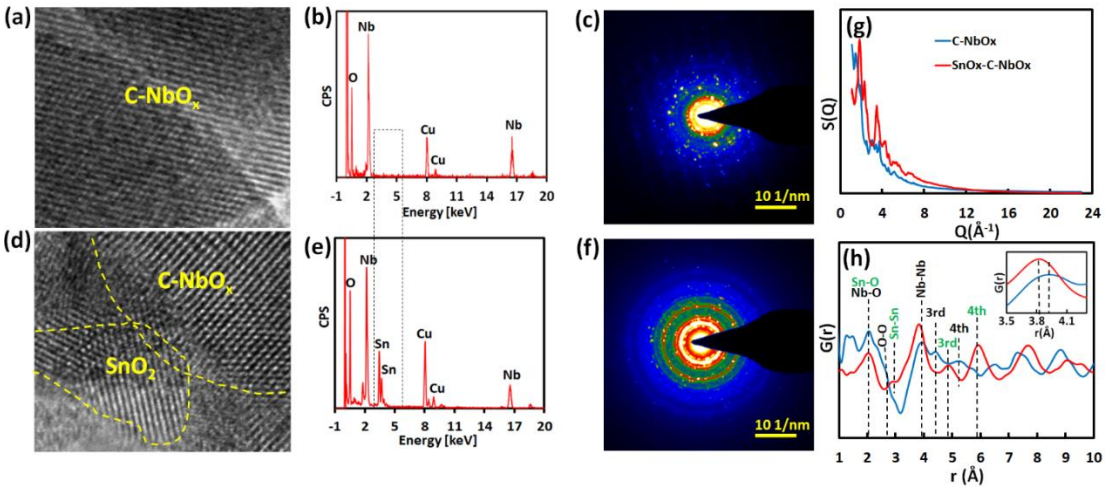

Figure 8.4. Local structure information (a) HR-TEM image for C-NbOx, (b) EDS-TEM shows only Nb and O signal, (c) Electron diffraction (ED) on C-NbOx, (d) HR-TEM image for SnO_2-C-NbOx, (e) EDS-TEM shows Nb, O, and Sn signals, (f) Electron diffraction (ED) on SnOx-C-NbOx, (g) Structure factor for both materials after integrating the EDs, (h) PDF analysis by taking the fourier transform for both materials.

The characteristics peaks for Pt NPs are shown as well and it is seen after adding SnO_2 the peak at 2θ°=39.9 (Pt 111) seems to be less sharper than in Pt-Nb/C, indicating a low aggregation of Pt NPs and small sizes which are in line with the TEM results. We further analyzed the supports under the electron diffraction for the carbon-doped NbO_x and SnO_2 on carbon-doped NbO_x before loading the Pt NPs as shown in figure 8.4.

Figure 8.4 (a) shows the HR-TEM images for carbon doped NbO_x which is confirmed by the EDS analysis as in figure 8.4 (b). By using the nanobeam, we obtained the electron diffraction locally on C-NbOx with well-calibrated camera length of 460 mm. The same protocol was conducted after loading the SnO_2 and it is clearly seen the Sn signal in figure 8.4 (e). We have integrated the 2-D ED for both samples C-NbO_x and SnO_2-C-NbO_x using GSASII [413] to convert the data to 1-D plot of diffraction intensity S(Q) vs momentum transfer (Q) of Q=23 $Å^{-1}$. Figure 8.4 (g) shows the structure factor for both samples with their distinct peaks [417]. After taking Fourier transform for figure 8.4 (g), the pair distribution function data was obtained. A clear peak at ~ 2 Å is attributed to Nb-O, and Sn-O pairs and at ~ 4 Å for Nb-Nb pairs [417, 418]. In SnO_2-C-NbOx, a peak at ~ 3 Å is assigned for Sn-Sn pairs [418]. The peak of 4 Å assigned to Nb-Nb corner sharing in NbO_6 polyhedra [419, 420]. It is seen in both samples that there is no peak at ~ 3.4 Å indicating the niobium oxide here structure does not share bonding at their edges; however, they do at the corners only [421]. On the other hand, the exact location of the peak at ~4 Å is negatively shifted from 3.96 Å to 3.87 Å after loading the SnO_2 (see the inset at figure 8.4 (h)). This shift indicates that SnO_2 incorporation could disturb the Nb-Nb pairs at the corner [421]. Such change in the 2r-pairs indeed confirms there is a change in the NbO_x structure upon SnO_2 loading at the atomic level.

The electronic states (XPS) reveal more useful information to know the binding energy and to predict the phases based on carbon C-C binding energy as a calibrator as in figure 7.3 (d) (*chapter 7*). In figure 8.5 (a), the oxidation state of Sn 3d shows at 487.3 eV and 495.7 eV. This is positively shifted compared with reduced-SnO_2 [412]. Relatively to Pt-Nb/C, the binding energy of Pt 4f has slightly shifted to be positive by 0.1 eV and this is related to possibility of sharing with SnO_2 as in figure 8.5 (b). This shift is

attributed to the electron delocalization between the d orbitals of Pt and the adjacent Sn_{pz} orbitals [267, 422]. On the other hand, in figure 8.5 (c) the binding energy for Nb 3d has shown a significant-positive shift in Pt-TNb/C relatively to Pt-Nb/C. The shift after loading SnO_2 was from 207.3 to 207.8 eV in Nb $3d_{5/2}$ shell and 209.9 to 210.5 eV in Nb $3d_{3/2}$ shell.

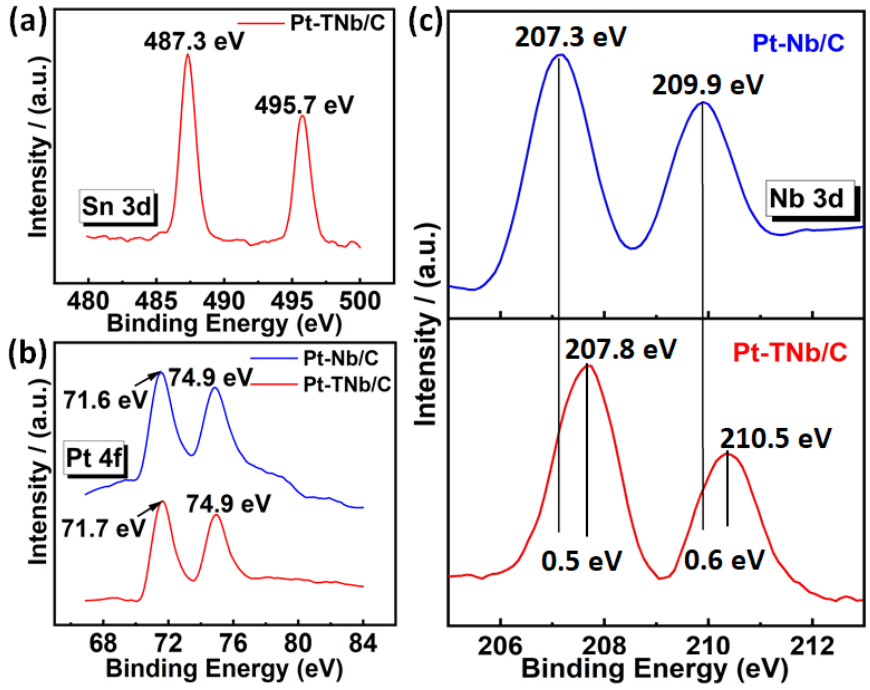

Figure 8.5. XPS analysis (a) Sn 3d, (b) Pt 4f, (c) top- carbon doped Nb 3d for Pt-Nb/C, bottom- tin oxide incorporated Nb 3d for Pt-TNb/C.

Huang et al. [59] reported the binding energy for undoped-Nb_2O_5 to be 208.1 eV and 210.9 eV, whereas, they reported the carbon-doped NbO_x to be 207.3 eV and 210.1 eV. Their results for the carbon-doped sample are in a good agreement with ours in Pt-Nb/C catalyst. However, the positive shift in Pt-TNb/C tells us that the oxidation state of NbO_x has reversed back to the oxidized form. The carbon doping mechanism is defined as the carbon either reacts with oxygen (substitution) or interstitially incorporates inside the crystal lattice causing some lattice distortion [26, 59]. In both cases, the oxygen vacancies are formed producing weak or dangling bonds between the oxygen and Nb. The carbon doped NbO_x could behave as a metastate phase for phase transformation. In

Nb_2O_5, most of the electrons in 4d of Nb are located and shared in 2p band of oxygen therefore any donated or gained electrons are expected to be at the oxygen 2p [371]. We believe that Sn 3d donated electrons to doped Nb 4d in the oxygen subshells 2p. It is reasonable since the Sn 3d is more energetic than 2p. In additions, the stoichiometry of carbon doped-NbOx is not in an equilibrium state between the oxygen and the niobium therefore there is less activation energy for a charge flow. This process is a hybridization process since it takes place between two non-identical metal oxides with an electron transfer from different energetics orbitals [423]. A previous study has reported a potential doping of SnO_2 by Nb element [412]. The latter study showed a close XPS data for Nb 3d to ours; however, they have annealed the sample at 900 °C, whereas in our case the annealing was conducted at 600 °C.

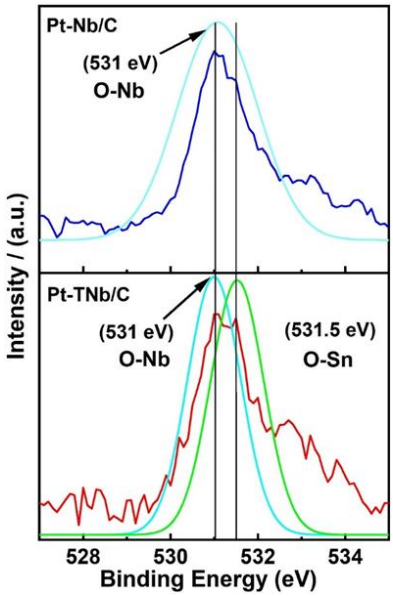

Figure 8.6. XPS analysis for O1s (top) only niobium oxide support, (bottom) after tin oxide incorporated.

In a word, the SnO_2 has synergistic effect with the carbon doped NbOx film by filling some of the oxygen vacancies that had been created due to the carbon doping process. This process makes the SnO_2 highly oxidized with electron-poor valence; in addition, NbO_x has a high oxide degree. Both states are essential for enhancing Pt activity as an

anodic electrode [69]. The oxygen binding energy is shown in figure 8.6 and it shows two distinct peaks at 531 eV (O-Nb) and at 531.5 eV(O-Sn).

8.3.2 Electrochemical Performance

The electrochemical performance for Pt-TNb/C was compared with Pt-Nb/C and both were benched marked with the E-TEK (Pt/C) for a control purpose. Figure 8.7 shows the cyclic voltammetry (CV) for the three catalysts in 0.5 M H_2SO_4 . It is seen that the catalyst Pt-TNb/C showed a well-defined hydrogen adsorption/desorption behavior in comparison with the other catalysts. From the hydrogen adsorption, assuming a mono layer of hydrogen is formed, the electrochemical surface area (ECSA) was calculated, and it was found in the order of 83.5, 68.6, and 59 m^2/g for Pt-TNb/C, Pt-Nb/C, and Pt/C, respectively.

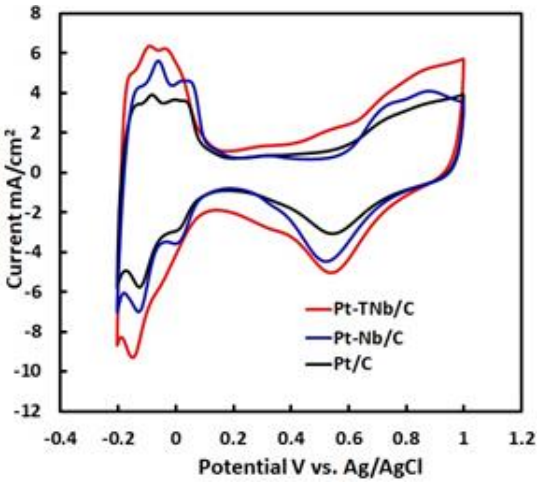

Figure 8.7. CV at 0.5M H_2SO_4 at a scan rate of 0.05 V/s.

The platinum surface at a high potential is not a pure metal but it is a mix of Pt-OH and Pt-O [424]. It is reported in many papers that those attached oxygen groups have a forbidden influence on the MOR [318, 425, 426]. Methanol oxidation at a high potential lowers the commercial side for the DMFCs; therefore, lowering the potentials limit becomes practically essential. Thus, we thought that testing the electrocatalysts at different potentials give us a sense on how promising and active they could be. After

the catalysts stabilized in 0.5 M H_2SO_4 for 20 cycles, they were tested up to different potentials (0.4, 0.6, 0.8, 1.0 V all vs. 3.5 Ag/AgCl). Figure 8.8 (a-d) show the activities in MOR at 0.4 V to 1.0 V are enhanced in order of Pt-TNb/C, Pt-Nb/C, and Pt/C.

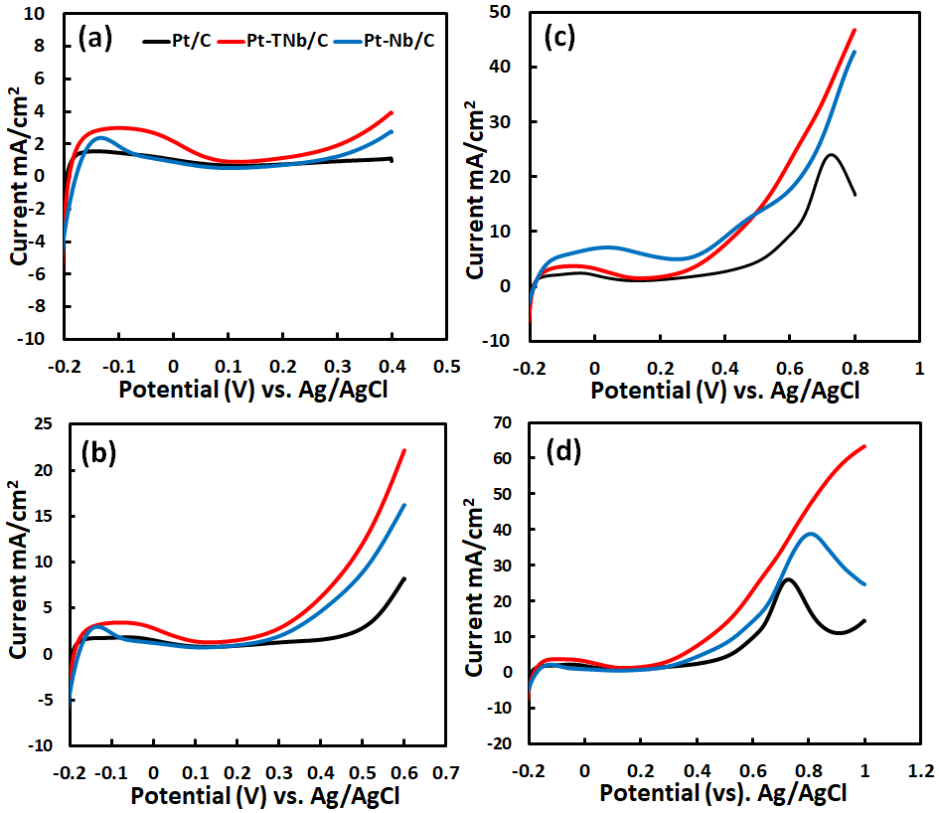

Figure 8.8. CV (only forward scan) for the three catalysts at various potential windows (a-d) from 0.4 V to 1.0 V at a scan rate of 0.05 V/s in 1.0M CH_3OH+0.5MH_2SO_4.

It is seen that the Pt-TNb/C catalyst displays the best activity comparing with others even at a low potential. This performance is attributed to the presence of SnO_2 in the support matrix which significantly enhances the methanol oxidation. SnO_2 is well-known oxide for water dissociation and its performance depends on where the oxidation state stands [35, 427]. It is expected that the role of NbO_x in Pt-TNb/C is different from Pt-Nb/C due to the significant change in the phase and the oxidation state. Based on NbO_x oxidation state in Pt-TNb/C, it exhibits an oxidized form which is required for water initiation at the anode side [428, 429]. When methanol is adsorbed on the Pt active sites, they are blocked by CO_{-ads} diminishing the catalyst's performance after a certain time. One way to activate them is to reduce the CO_{-ads} to CO_2 [430, 431]. On Pt-Nb/C

surface, NbO_x is in reduced form due to the carbon doping which it could be not favorable for water initiation in the anode side since it lacks the ability to surface oxygen source unlike Nb_2O_5 [429, 432]. The Pt-TNb/C exhibits a remarkable mass activity up to 2.7 A/mg(pt) relative to the most recent relevant studies in the literature as seen in Table 8.1.

Table 8.1 shows catalysts mass activities from studies reported in literature.

Samples	Scan Rate mV/s	Mass activity $A\ mg^{-1}_{Pt}$	Reference
Pt-CeO_2/TiN NTs	50	0.67	[390]
Pt/Nb_2O_5/C	50	0.605	[369]
PtNPs/SnOx/TiO_2/mC	50	2.2	[388]
Pt/nano-TT-Nb_2O_5/C	50	0.67	[406]
Pt/TiO_2/graphene	50	0.226	[433]
Pt/MoO_3/graphene	50	0.61	[434]
Pt/SnO_2/graphene	100	0.67	[435]
Pt/V_2O_5/C	50	0.043	[436]
Commercial (E-TEK)	25	0.41	[437]
Pt-TNb/C	50	2.7	This study

Figure 8.8 (a) displays the CV test at a maximum potential of 0.4 V Ag/AgCl for the three catalysts. It is expected to see minimum activity since at such a low potential methanol undergoes only for the dehydrogenation step. Relatively to Pt-Nb/C and Pt/C, it can be seen that the Pt-TNb/C shows a high activity associated with an early onset at 0.1-0.18 V which indicates that the incorporation of SnO_2 with NbOx promotes the MOR at a lower potential than on the other catalysts. The CV test at 0.6 V which is lower than the platinum oxidation (0.68 vs Ag/AgCl) tells us the MOR activity related to the protons supply from the support since there is no protons coverage on the Pt active sites within such a range; therefore, the proton generation kinetic is mainly driven

by the support help. In figure 8.8 (b), Pt-TNb/C shows a remarkable activity at 0.6 V. Pt-TNb/C shows a current density of 23.4 mA/cm^2 which is higher than the Pt/C of 7.6 mA/cm^2 and Pt-Nb/C of 15.6 mA/cm^2 by 3 time and 1.5 times, respectively. In figures 8.8 (c-d), the catalyst activities follow the same pattern but in narrow enhancement ratio. This might be attributed to the different kinetic as in those potentials the Pt surface will be either Pt-OH or Pt-O [438]. Therefore, the MOR mechanism depends on protons supply from the Pt surface and the supports as well.

As it was confirmed by XRD that the diffraction peaks of NbO_x in Pt-TNb/C are assigned to orthorhombic phase [366]. This phase offers multi interfaces that able to provide a high amount of hydroxide helping in oxidizing the adsorbed species on the Pt active sites [406]. The orthorhombic phase of Nb_2O_5 is constructed in a unit cell where each Nb atom is surrounded by six or seven oxygen atoms, creating distorted octahedra [364]. Alongside with Nb_2O_5, SnO_2 has a decisive role in water initiation at low potentials as reported by many studies [392, 435]. Figure 8.9 (a-c) show the stability test under 1.0 M of methanol for 1000 cycles. Again, the Pt-TNb/C shows a superior stability by showing 0% loss after 1000 cycles at the presence of methanol. However, Pt-Nb/C and Pt/C showed 20%, 31% loss, respectively, under the same conditions. This remarkable stability is due to the well-designed support. Chronoamperometry (CA) is used to examine the catalyst tolerance towards the CO_{ads} poisoning in an alcoholic medium at a constant potential. Figure 8.9 (d) shows the CA test at 0.6 V for 7200 seconds. It is clearly seen that the Pt-TNb/C retains a high current for all the period showing a superior performance and stability. The other two catalysts Pt-Nb/C and Pt/C suffer a sharp current decrement at a time less than 1000 seconds. The loss in Pt-Nb/C indicates the reason of demolishing the active sites is not the corrosion, it is the poisoning species, instead. As discussed in XPS results, NbO_x

binding energy was positively shifted with SnO_2. This results in a highly stable SnO_2 in the support matrix and subsequently sustains the protons flowing to Pt-CO_{ads} nest. In addition, at the interface of SnO_2 and NbO_x the PDF analysis shows a negative shift in Nb-Nb pairs. This could result in creating Nb-O-Sn moiety where the water could be easily initiated forming OH_{ads}.

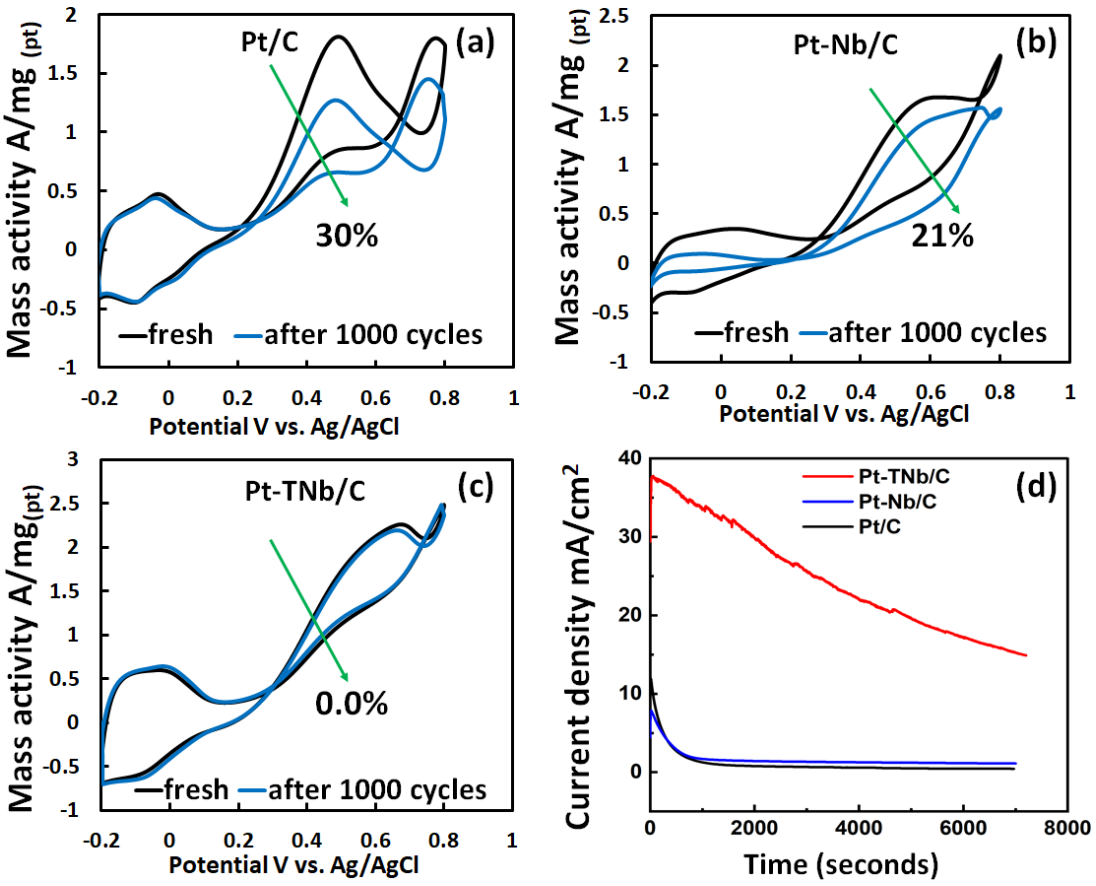

Figure 8.9. (a-c) Stability test before and after 1000 cycles at 0.1 V/s at 1.0M CH_3OH+0.5M H_2SO_4, (d) CA test at 0.6 V for 7200 seconds.

8.4 Conclusion

In this study, we have synthesized a Pt-based catalyst supported on 5-nm dense film of niobium oxide on carbon black as a protection layer and tin oxide as a promotor for water activation. Upon loading SnO_2 on carbon doped NbO_x, a phase change in NbO_x has occurred from a partial orthorhombic phase to fully orthorhombic. The atomic structure for NbO_x was further investigated by PDF analysis locally under the nanobeam of electron diffraction. It was found there is a negative shift in Nb-Nb corners pairs from 3.94 Å to 3.84 Å due to SnO_2 incorporation. Moreover, a substantial positive shift in Nb 3d binding energy was observed from a reduced form to an oxidized state. In line with that, Sn 3d suffers a positive shift and Pt 4f showed a minimal positive shift by 0.1 eV. We deduce that the doped-NbO_x has accepted electrons from the outer orbitals of Sn 3d to 2p of oxygen in niobium oxide after annealing at 600 °C under nitrogen gas. This modification in support has shown remarkable activities at even low potentials. A promising durability was observed as well after 7200 seconds relatively to the only carbon-doped niobium oxide supported on carbon black and E-TEK. We think this catalyst design is promising approach however more in-depth investigation is needed especially the oxides interface to check water adsorption sites and the water adsorption energies.

Chapter 9. Dissertation Conclusions and Future Work

9.1 Conclusions

In this dissertation, a new, novel, and feasible coating technique has been presented. The process is based on the physics principles of the water saturation limit in heptane solvent in which nanosubstrates are dispersed. Upon saturation, any extra water content would condense on the nanosubstrates surfaces due to the presence of the functional groups on the nanosubstrates surfaces that offer a high surface area to adsorb water. Once the nanosubstrate's surface is covered by a water film, the film is believed to be stable against any distortions due to the severe surface tension between the water film and heptane. Such surface energy would be extremely high, and it relatively depends on the nanosubstartes diameter based on the Young-Laplace equation.

Due to their wide range of applications, carbon nanotubes, iron oxide nanoparticles, and carbon black as nanosubstrates have been used in this work. The critical point in this new developed technique is how to form a water film on those nanosubstartes. Indeed, we were able to visualize the water film by performing a Cryo-EM under cryogenic conditions. Subsequently, various metal organic precursors such as titanium ethoxide/isopropoxide, niobium ethoxide, and trimethylaluminum have been used. Conformal coating has been achieved by using the ethoxide groups and trimethylaluminum; however, a fluffy morphology was observed when large precursor molecules such as isopropoxide and butoxide groups are used. A crucial point to be mentioned is all the coating experiments were done at a room temperature.

Further aspect for this method is controlling the metal oxide thickness. As more water condenses on the surfaces, the thickness grows by applying a correspondent precursor mole ratio to the substrate, taking into account the substrate surface area. Such coating

thicknesses can be obtained from 5 nm up to 80 nm by one pass process. A deviation from the predicted coating thickness and the actual thickness is due to left-over organic ligands that are retained in the layer of the coating. These ligands retard reaction completion in which a crystalline phase is not achievable as confirmed by the XRD characterizations.

The flexibility of coating different nanosubstrates provides another practical aspect which is to make metal oxide nanostructures such as metal oxide nanotubes or metal oxide nanoshells. We were able to make TiO_2 nanotubes, Al_2O_3 nanotubes and Nb_2O_5 nanoshells. Dense and conformal of TiO_2 and Nb_2O_5 nanotubes and nanoshells were made and confirmed by high magnification electron micrographs. However, porous-Al_2O_3 nanotubes were made with a high surface area up to 300 m^2/g. The high porosity belongs to the TMA reaction conditions where the ligands are released in a gas phase (mainly methane). That gas is trapped inside the layer and when it is annealed under oxygen or air the trapped gas will be released producing the high porous Al_2O_3 morphology.

Working at room temperature conditions leads to forming hydroxides as an initial materials phase due to an incomplete reaction. The incomplete reaction effect becomes severe when titanium isopropoxide is used. Fluffy and porous TiO_2 layer was obtained. The reason for having such morphology was attributed to the presence of i-CH_x ligands preventing forming metal-metal interaction during the hydrolysis and condensation reactions. Three characterization tools have been utilized, TGA-DTA, GC-MS, FT-IR, to study the layer properties. By increasing the water ratio relative to TTIP, a less organic content was detected by FT-IR and TGA; however, GC-MS showed an increase of the reduced ligands desorbed in the heptane. TTiP has large ligands around the Ti-atom, which causes titanium dioxide to retain some of the ligands. Consequently, a

cross-linkage structure of metal hydroxides ($Ti(OH)_x(OR)_{4-x}$) is formed and defined as an incomplete hydrolysis. On the other hand, when titanium ethoxides (small ligands precursor) were used, the results showed a super uniform and conformal layer of TiO_2. This may be because of a greater number of Ti-atoms relatively to the ligands size inside the titanium ethoxide structure, which induces more metal cations (Ti^{+4}) to interact. It is believed each metal atom behaves as a condensation center.

The fluffy coating offers a high surface area (*ca.* 300 m^2/g) which is a good candidate to be a catalyst support. Owing to this fact, a catalyst comprised of platinum nanoparticles coupled with tin oxide loaded on CNTs has been used for ethanol electrooxidation reaction (EOR) and oxygen reduction reaction (ORR). Due to the high surface area, Pt NPs have been uniformly dispersed on the support. The catalyst showed a high stability after 1000-cycles in 0.5 M H_2SO_4 leading to a decrease in the ECSA to 74.4 m^2/g. In term of ethanol electro-oxidation, the prepared catalyst exhibited a high current density with an increase by ~2 times relative to Pt/C; in addition, the onset potential shift difference was 350 mV. Time-base test for 1800 seconds showed a difference in the current density by 2.2 times. We assigned the high activity and durability to the two oxide coatings, which results in eliminating the support corrosion toward Pt NPs and protects SnO_2 from dissolution in acid.

The ORR onset potential was positively shifted by 40 mV on the catalyst and a half-wave potential improved by 38 mV. The mass activity that represents the actual activity of Pt NPs revealed a 2.66-fold increase over that of Pt/C at 900 mV. The high surface area offered by the fluffy TiO_2 layer enabled the Pt NPs and SnO_2 to be uniformly dispersed and stabilized. The electronic structure change in SnO_2 supported on the rutile phase fluffy TiO_2, as evidenced by a shift in BE of 0.9 eV, was attributed as the main reason to having the early onset potential and significant improvement of the Pt activity

in ORR. In methanol electrooxidation (MOR) using the same support, platinum and iridium nanoparticles were decorated onto a fluffy 10-nm doped -titanium dioxide layer on carbon nanotubes with a uniform and small sizes as it was confirmed by TEM. Also, XRD spectra revealed no sharp peak of Pt and Ir at 2θ=39.8° peaks for (111) plane, indicating small sizes of the metal NPs, which are ascribed to the high surface area of the fluffy support. The MOR performance of the Pt-Ir /C-TiO_2/CNTs is higher than Pt by 5.6-fold times in the forward to the backward peak ratio. Moreover, *i-t* curve showed a high stability at 0.5 V after 3600 seconds by 12.5 times which was attributed to the high oxyphilic surface owning to Ir $(OH)_x$ that generates enough water to oxidize adsorbed carbon monoxide.

In using niobium oxide, a thin layer of carbon-doped niobium oxide on carbon black via CLD coating process as a support for Pt NPs for ORR was made. The metal oxide layer is conformal and uniform on the carbon black, protecting it from corrosion in sulfuric acid electrolytes. The conformal coating was thermally doped by carbon to increase its conductivity. The doping process partially transforms Nb_2O_5 to NbO_2, a rutile phase with increased electrical conductivity. The niobium coating as support to Pt was found to have significantly enhanced durability and catalytic activity. The improved electrochemical performances were attributed to metal-support interactions, leading to electronic structure change in the metal and metal oxide support.

We have further investigated electrocatalysts using Nb_2O_5 based support. We have synthesized a Pt-based catalyst supported on 5-nm dense film of niobium oxide on carbon black as a protection layer and tin oxide as a promotor for water activation. Upon loading SnO_2 on carbon doped NbO_x, a phase change in NbO_x has occurred from a partial orthorhombic phase to fully orthorhombic. The atomic structure for NbO_x was further investigated by pair distribution function analysis locally under the nanobeam

of electron diffraction. It was found there is a negative shift in Nb-Nb corner pairs from 3.94 Å to 3.84 Å due to SnO_2 incorporation. Moreover, a substantial positive shift in Nb 3d binding energy was observed from a reduced form to an oxidized state. In line with that, Sn 3d suffered a positive shift and Pt 4f showed a minimal positive shift by 0.1 eV. We concluded that there is a charge transfer between the doped-NbO_x and the outer orbitals of Sn 3d to 2p of oxygen in niobium oxide after annealing at 600 °C under nitrogen gas. This modification in support has shown remarkable activities at even low potentials. A promising durability was observed as well after 7200 seconds in durability tests as compared relatively to the carbon-doped niobium oxide only supported on carbon black, and the E-TEK catalyst. We believe this catalyst design is a promising approach. However, more in-depth investigation is needed, especially on the metal oxide interface to check water adsorption sites and the water adsorption energies.

In summary, in this dissertation, a new method was developed to make metal oxide nanocoatings on various substrates with a few feasible applications, especially in electrocatalysis. It is hoped that this work could inspire many of the researchers in the material science and electrocatalysis community.

9.2 Potential Future Work

We have confirmed fabricating various metal oxide (TiO_2, Nb_2O_5, Al_2O_3) forming one layer on different substrates. We think to extend the chemistry window in this technology for more interesting materials such as hafnium oxide (HfO_2) [439], gallium oxide (Ga_2O_3) [440], cerium oxide (CeO_2) [441], ruthenium oxide (RuO_2) [442], and beyond. We may start building multi-layers of different coating materials on nano/micro substrates. This work may also be extended to include inorganic precursors

such as some salts to derive as known metal-organic-frame (MOF). Moreover, this technique may be tested in a new way for making polymer nanocoatings.

Bibliography

[1] G. Pfaff, P. Reynders, Angle-dependent optical effects deriving from submicron structures of films and pigments, Chemical reviews, 99 (1999) 1963-1982.
[2] A. Salvador, PASCUAL-MARTÍ, m. C., ADELL, JR, REGUENI, A., MARCH, JG: Analytical methodologies for atomic spectrometric determination of metallic oxides in UV sunscreen creams, Journal of Pharmaceutical and Biomedical Analysis, 22 (2000) 301-306.
[3] J.H. Braun, A. Baidins, R.E. Marganski, TiO2 pigment technology: a review, Progress in organic coatings, 20 (1992) 105-138.
[4] S. Yuan, W. Chen, S. Hu, Fabrication of TiO2 nanoparticles/surfactant polymer complex film on glassy carbon electrode and its application to sensing trace dopamine, Materials Science and Engineering: C, 25 (2005) 479-485.
[5] A. Fujishima, K. Honda, Photolysis-decomposition of water at the surface of an irradiated semiconductor, Nature, 238 (1972) 37-38.
[6] A.P. Alivisatos, Semiconductor clusters, nanocrystals, and quantum dots, science, 271 (1996) 933-937.
[7] C.B. Murray, a.C. Kagan, M. Bawendi, Synthesis and characterization of monodisperse nanocrystals and close-packed nanocrystal assemblies, Annual review of materials science, 30 (2000) 545-610.
[8] M. Wei, Y. Konishi, H. Zhou, M. Yanagida, H. Sugihara, H. Arakawa, Highly efficient dye-sensitized solar cells composed of mesoporous titanium dioxide, Journal of Materials Chemistry, 16 (2006) 1287-1293.
[9] M. Pelaez, N.T. Nolan, S.C. Pillai, M.K. Seery, P. Falaras, A.G. Kontos, P.S.M. Dunlop, J.W.J. Hamilton, J.A. Byrne, K. O'Shea, M.H. Entezari, D.D. Dionysiou, A review on the visible light active titanium dioxide photocatalysts for environmental applications, Applied Catalysis B: Environmental, 125 (2012) 331-349.
[10] M. Koelsch, S. Cassaignon, C. Ta Thanh Minh, J.F. Guillemoles, J.P. Jolivet, Electrochemical comparative study of titania (anatase, brookite and rutile) nanoparticles synthesized in aqueous medium, Thin Solid Films, 451-452 (2004) 86-92.
[11] S.N. Frank, A.J. Bard, Heterogeneous photocatalytic oxidation of cyanide ion in aqueous solutions at titanium dioxide powder, Journal of the American Chemical Society, 99 (1977) 303-304.
[12] A.J. Hoffman, E.R. Carraway, M.R. Hoffmann, Photocatalytic Production of H2O2 and Organic Peroxides on Quantum-Sized Semiconductor Colloids, Environmental Science & Technology, 28 (1994) 776-785.
[13] R. Asahi, T. Morikawa, T. Ohwaki, K. Aoki, Y. Taga, Visible-light photocatalysis in nitrogen-doped titanium oxides, science, 293 (2001) 269-271.
[14] V. Pore, M. Heikkilä, M. Ritala, M. Leskelä, S. Areva, Atomic layer deposition of TiO2−xNx thin films for photocatalytic applications, Journal of Photochemistry and Photobiology A: Chemistry, 177 (2006) 68-75.
[15] T. Umebayashi, T. Yamaki, H. Itoh, K. Asai, Band gap narrowing of titanium dioxide by sulfur doping, Applied Physics Letters, 81 (2002) 454-456.
[16] H. Irie, Y. Watanabe, K. Hashimoto, Carbon-doped anatase TiO2 powders as a visible-light sensitive photocatalyst, Chemistry Letters, 32 (2003) 772-773.
[17] A.M. Czoska, S. Livraghi, M. Chiesa, E. Giamello, S. Agnoli, G. Granozzi, E. Finazzi, C.D. Valentin, G. Pacchioni, The Nature of Defects in Fluorine-Doped TiO2, The Journal of Physical Chemistry C, 112 (2008) 8951-8956.

[18] J. Senthilnathan, L. Philip, Photocatalytic degradation of lindane under UV and visible light using N-doped TiO2, Chemical engineering journal, 161 (2010) 83-92.
[19] X. Wang, T.-T. Lim, Solvothermal synthesis of C–N codoped TiO2 and photocatalytic evaluation for bisphenol A degradation using a visible-light irradiated LED photoreactor, Applied Catalysis B: Environmental, 100 (2010) 355-364.
[20] D. Li, Z. Chen, Y. Chen, W. Li, H. Huang, Y. He, X. Fu, A New Route for Degradation of Volatile Organic Compounds under Visible Light: Using the Bifunctional Photocatalyst Pt/TiO2−xNx in H2−O2 Atmosphere, Environmental Science & Technology, 42 (2008) 2130-2135.
[21] Z. Wei, J. Sun, Z. Xie, M. Liang, S. Chen, Removal of gaseous toluene by the combination of photocatalytic oxidation under complex light irradiation of UV and visible light and biological process, Journal of Hazardous Materials, 177 (2010) 814-821.
[22] T. Matsunaga, R. Tomoda, T. Nakajima, H. Wake, Photoelectrochemical sterilization of microbial cells by semiconductor powders, FEMS Microbiology letters, 29 (1985) 211-214.
[23] J.C. Yu, W. Ho, J. Yu, H. Yip, P.K. Wong, J. Zhao, Efficient Visible-Light-Induced Photocatalytic Disinfection on Sulfur-Doped Nanocrystalline Titania, Environmental Science & Technology, 39 (2005) 1175-1179.
[24] D. Mitoraj, A. Jan czyk, M. Strus, H. Kirsch, G. Stochel, PB Heczko, W. Macyk, Photochem. Photobiol. Sci, 6 (2007) 642-648.
[25] Q. Li, M.A. Page, B.J. Mariñas, J.K. Shang, Treatment of Coliphage MS2 with Palladium-Modified Nitrogen-Doped Titanium Oxide Photocatalyst Illuminated by Visible Light, Environmental Science & Technology, 42 (2008) 6148-6153.
[26] K. Huang, K. Sasaki, R.R. Adzic, Y. Xing, Increasing Pt oxygen reduction reaction activity and durability with a carbon-doped TiO_2 nanocoating catalyst support, Journal of Materials Chemistry, 22 (2012) 16824-16832.
[27] G.R. Mirshekari, A.P. Shirvanian, Electrochemical behavior of titanium oxide nanoparticles for oxygen reduction reaction environment in PEM fuel cells, Materials Today Energy, 9 (2018) 235-239.
[28] X. Li, C. Liu, W. Xing, T. Lu, Development of durable carbon black/titanium dioxide supported macrocycle catalysts for oxygen reduction reaction, Journal of Power Sources, 193 (2009) 470-476.
[29] G. Wu, M.A. Nelson, N.H. Mack, S. Ma, P. Sekhar, F.H. Garzon, P. Zelenay, Titanium dioxide-supported non-precious metal oxygen reduction electrocatalyst, Chemical Communications, 46 (2010) 7489-7491.
[30] E.C. Barbosa, L.S. Parreira, I.C. de Freitas, L.R. Aveiro, D.C. de Oliveira, M.C. dos Santos, P.H. Camargo, Pt-Decorated TiO2 Materials Supported on Carbon: Increasing Activities and Stabilities toward the ORR by Tuning the Pt Loading, ACS Applied Energy Materials, 2 (2019) 5759-5768.
[31] L. He, J. Liu, Y. Liu, B. Cui, B. Hu, M. Wang, K. Tian, Y. Song, S. Wu, Z. Zhang, Titanium dioxide encapsulated carbon-nitride nanosheets derived from MXene and melamine-cyanuric acid composite as a multifunctional electrocatalyst for hydrogen and oxygen evolution reaction and oxygen reduction reaction, Applied Catalysis B: Environmental, 248 (2019) 366-379.
[32] K. Huang, K. Sasaki, R.R. Adzic, Y.J.J.o.M.C. Xing, Increasing Pt oxygen reduction reaction activity and durability with a carbon-doped TiO 2 nanocoating catalyst support, 22 (2012) 16824-16832.

[33] A.M. Jasim, S. Al-Salihi, Y. Xing, Communication—Platinum and Tin Oxide Dispersed in a Fluffy TiO_2 Nanolayer for Electrocatalytic Reduction of Oxygen, Journal of The Electrochemical Society, 167 (2020) 116526.
[34] B. Abida, L. Chirchi, S. Baranton, T.W. Napporn, H. Kochkar, J.-M. Léger, A.J.A.C.B.E. Ghorbel, Preparation and characterization of Pt/TiO2 nanotubes catalyst for methanol electro-oxidation, 106 (2011) 609-615.
[35] A.M. Jasim, S.E. Hoff, Y. Xing, Enhancing methanol electrooxidation activity using double oxide catalyst support of tin oxide clusters on doped titanium dioxides, Electrochimica Acta, 261 (2018) 221-226.
[36] D. Zheng, W. Zhu, S. Xun, M. Zhou, M. Zhang, W. Jiang, Y. Qin, H.J.F. Li, Deep oxidative desulfurization of dibenzothiophene using low-temperature-mediated titanium dioxide catalyst in ionic liquids, 159 (2015) 446-453.
[37] C. Carlucci, L. Degennaro, R.J.C. Luisi, Titanium Dioxide as a Catalyst in Biodiesel Production, 9 (2019) 75.
[38] S. Yu, Y. Ma, Y. Zhi, H. Jing, H.-Q. Su, Synthesis of Cobalt–Based Catalyst Supported on TiO2 Nanotubes and its Fischer–Tropsch Reaction, Integrated Ferroelectrics, 147 (2013) 59-66.
[39] V.M. Shinde, G. Madras, CO methanation toward the production of synthetic natural gas over highly active Ni/TiO2 catalyst, AIChE Journal, 60 (2014) 1027-1035.
[40] O.K. Varghese, D. Gong, M. Paulose, K.G. Ong, C.A. Grimes, Hydrogen sensing using titania nanotubes, Sensors and Actuators B: Chemical, 93 (2003) 338-344.
[41] J. Gong, Y. Li, Z. Hu, Z. Zhou, Y. Deng, Ultrasensitive NH3 gas sensor from polyaniline nanograin enchased TiO2 fibers, The Journal of Physical Chemistry C, 114 (2010) 9970-9974.
[42] Z. Zhang, Y. Yuan, Y. Fang, L. Liang, H. Ding, L. Jin, Preparation of photocatalytic nano-ZnO/TiO2 film and application for determination of chemical oxygen demand, Talanta, 73 (2007) 523-528.
[43] J.-C. Chou, H.-Y. Yang, C.-W. Chen, Glucose biosensor of ruthenium-doped TiO2 sensing electrode by co-sputtering system, Microelectronics Reliability, 50 (2010) 753-756.
[44] Y.-K. Jun, H.-S. Kim, J.-H. Lee, S.-H. Hong, High H2 sensing behavior of TiO2 films formed by thermal oxidation, Sensors and Actuators B: Chemical, 107 (2005) 264-270.
[45] G.K. Mor, O.K. Varghese, M. Paulose, K. Shankar, C.A. Grimes, A review on highly ordered, vertically oriented TiO2 nanotube arrays: Fabrication, material properties, and solar energy applications, Solar Energy Materials and Solar Cells, 90 (2006) 2011-2075.
[46] S. Khameneh Asl, B. Alavi, S. Ahmadi, The effect of highly ordered titania nanotube structures on hydrogen gas detection, Surface and Interface Analysis, 44 (2012) 1051-1053.
[47] A. Kolmakov, Y. Zhang, G. Cheng, M. Moskovits, Detection of CO and O2 using tin oxide nanowire sensors, Advanced materials, 15 (2003) 997-1000.
[48] A. Zuruzi, A. Kolmakov, N. MacDonald, M. Moskovits, Highly sensitive gas sensor based on integrated titania nanosponge arrays, Applied physics letters, 88 (2006) 102904.
[49] T. Tien, T. TY, S. HL, G. EF, Z. PJ, TIO2 AS AN AIR-TO-FUEL RADIO SENSOR FOR AUTOMOBILE EXHAUSTS, (1975).
[50] C.-C. Lu, Y.-S. Huang, J.-W. Huang, C.-K. Chang, S.-P. Wu, A macroporous TiO2 oxygen sensor fabricated using anodic aluminium oxide as an etching mask, Sensors, 10 (2010) 670-683.

[51] H.G. Moon, Y.-S. Shim, H.W. Jang, J.-S. Kim, K.J. Choi, C.-Y. Kang, J.-W. Choi, H.-H. Park, S.-J. Yoon, Highly sensitive CO sensors based on cross-linked TiO2 hollow hemispheres, Sensors and Actuators B: Chemical, 149 (2010) 116-121.
[52] J.-A. Park, J. Moon, S.-J. Lee, S.H. Kim, T. Zyung, H.Y. Chu, Structure and CO gas sensing properties of electrospun TiO2 nanofibers, Materials Letters, 64 (2010) 255-257.
[53] J.-S. Lee, T.-J. Ha, M.-H. Hong, H.-H. Park, The effect of porosity on the CO sensing properties of TiO2 xerogel thin films, Thin Solid Films, 529 (2013) 98-102.
[54] Z.M. Seeley, A. Bandyopadhyay, S. Bose, Influence of crystallinity on CO gas sensing for TiO2 films, Materials Science and Engineering: B, 164 (2009) 38-43.
[55] G. Chaudhari, D. Bambole, A. Bodade, P. Padole, Characterization of nanosized TiO 2 based H 2 S gas sensor, Journal of materials science, 41 (2006) 4860-4864.
[56] J. Moon, J.-A. Park, S.-J. Lee, T. Zyung, I.-D. Kim, Pd-doped TiO2 nanofiber networks for gas sensor applications, Sensors and Actuators B: Chemical, 149 (2010) 301-305.
[57] M.A. Aegerter, Sol–gel niobium pentoxide: a promising material for electrochromic coatings, batteries, nanocrystalline solar cells and catalysis, Solar energy materials and solar cells, 68 (2001) 401-422.
[58] A. Le Viet, R. Jose, M. Reddy, B. Chowdari, S. Ramakrishna, Nb2O5 photoelectrodes for dye-sensitized solar cells: choice of the polymorph, The Journal of Physical Chemistry C, 114 (2010) 21795-21800.
[59] K. Huang, Y. Li, L. Yan, Y. Xing, Nanoscale conductive niobium oxides made through low temperature phase transformation for electrocatalyst support, RSC Advances, 4 (2014) 9701-9708.
[60] M. Duffy, C. Wang, A. Waxman, K. Zaininger, Preparation, Optical and Dielectric Properties of Vapor-Deposited Niobium Oxide Thin Films, Journal of The Electrochemical Society, 116 (1969) 234-239.
[61] A. Pignolet, G.M. Rao, S. Krupanidhi, Rapid thermal processed thin films of niobium pentoxide (Nb2 O5) deposited by reactive magnetron sputtering, Thin solid films, 261 (1995) 18-24.
[62] D. Rosenfeld, R. Sanjines, F. Levy, P. Buffat, V. Demarne, A. Grisel, Structural and morphological characterization of Nb2O5 thin films deposited by reactive sputtering, Journal of Vacuum Science & Technology A: Vacuum, Surfaces, and Films, 12 (1994) 135-139.
[63] N. Hara, E. Takahashi, J.H. Yoon, K. Sugimoto, Ellipsometric Analysis of Growth Process and Corrosion Resistance of Nb2 O 5 Films Formed by MOCVD, Journal of The Electrochemical Society, 141 (1994) 1669-1674.
[64] J.Z. Ou, R.A. Rani, M.-H. Ham, M.R. Field, Y. Zhang, H. Zheng, P. Reece, S. Zhuiykov, S. Sriram, M. Bhaskaran, Elevated temperature anodized Nb2O5: a photoanode material with exceptionally large photoconversion efficiencies, ACS nano, 6 (2012) 4045-4053.
[65] S. Ghoshal, Q. Jia, M.K. Bates, J. Li, C. Xu, K. Gath, J. Yang, J. Waldecker, H. Che, W.J.A.C. Liang, Tuning nb–pt interactions to facilitate fuel cell electrocatalysis, 7 (2017) 4936-4946.
[66] B. Li, M. Gu, Z. Nie, X. Wei, C. Wang, V. Sprenkle, W. Wang, Nanorod niobium oxide as powerful catalysts for an all vanadium redox flow battery, Nano letters, 14 (2014) 158-165.
[67] H.-J. Chun, D.B. Kim, D.-H. Lim, W.-D. Lee, H.-I. Lee, A synthesis of CO-tolerant Nb2O5-promoted Pt/C catalyst for direct methanol fuel cell; its physical and

electrochemical characterization, International Journal of Hydrogen Energy, 35 (2010) 6399-6408.
[68] D. Papageorgopoulos, M. Keijzer, F. De Bruijn, The inclusion of Mo, Nb and Ta in Pt and PtRu carbon supported electrocatalysts in the quest for improved CO tolerant PEMFC anodes, Electrochimica Acta, 48 (2002) 197-204.
[69] S. Ghoshal, Q. Jia, M.K. Bates, J. Li, C. Xu, K. Gath, J. Yang, J. Waldecker, H. Che, W. Liang, Tuning nb–pt interactions to facilitate fuel cell electrocatalysis, ACS Catalysis, 7 (2017) 4936-4946.
[70] Q. Jia, S. Ghoshal, J. Li, W. Liang, G. Meng, H. Che, S. Zhang, Z.-F. Ma, S. Mukerjee, Metal and metal oxide interactions and their catalytic consequences for oxygen reduction reaction, Journal of the American Chemical Society, 139 (2017) 7893-7903.
[71] K. Tanabe, Catalytic application of niobium compounds, Catalysis Today, 78 (2003) 65-77.
[72] R.D. Perlack, Biomass as feedstock for a bioenergy and bioproducts industry: the technical feasibility of a billion-ton annual supply, Oak Ridge National Laboratory2005.
[73] J.M. Thornton, D. Raftery, Chapter 8 - Photocatalysts for Solar Hydrogen Conversion, in: S.L. Suib (Ed.) New and Future Developments in Catalysis, Elsevier, Amsterdam, 2013, pp. 191-217.
[74] T. Iizuka, Y. Tanaka, K. Tanabe, Hydrogenation of carbon monoxide and carbon dioxide over supported rhodium catalysts, Journal of Molecular Catalysis, 17 (1982) 381-389.
[75] G. Ramírez, S.E. Rodil, H. Arzate, S. Muhl, J.J. Olaya, Niobium based coatings for dental implants, Applied Surface Science, 257 (2011) 2555-2559.
[76] W.N. Dos Santos, P.I. Paulin Filho, R. Taylor, Effect of addition of niobium oxide on the thermal conductivity of alumina, Journal of the European Ceramic Society, 18 (1998) 807-811.
[77] A. Shirani, J. Gu, B. Wei, J. Lee, S.M. Aouadi, D. Berman, Tribologically enhanced self-healing of niobium oxide surfaces, Surface and Coatings Technology, 364 (2019) 273-278.
[78] L.M. Marcondes, S. Maestri, B. Sousa, R.R. Gonçalves, F.C. Cassanjes, G.Y. Poirier, High niobium oxide content in germanate glasses: Thermal, structural, and optical properties, Journal of the American Ceramic Society, 101 (2018) 220-230.
[79] H. Kondo, H. Takahashi, T. Takeuchi, I. Igarashi, Nb2O5 thin-film oxygen sensor, Proc. 3rd Sensor Symp., Japan, 1983, pp. 185-190.
[80] A. Kohli, C.C. Wang, S.A. Akbar, Niobium pentoxide as a lean-range oxygen sensor, Sensors and Actuators B: Chemical, 56 (1999) 121-128.
[81] R.A. Rani, A.S. Zoolfakar, J.Z. Ou, M.R. Field, M. Austin, K. Kalantar-zadeh, Nanoporous Nb2O5 hydrogen gas sensor, Sensors and Actuators B: Chemical, 176 (2013) 149-156.
[82] N. Kurioka, D. Watanabe, M. Haneda, T. Shimanouchi, T. Mizushima, N. Kakuta, A. Ueno, T. Hanaoka, Y. Sugi, Preparation of niobium oxide films as a humidity sensor, Catalysis Today, 16 (1993) 495-501.
[83] E. Kurmaev, A. Moewes, O. Bureev, I. Nekrasov, V. Cherkashenko, M. Korotin, D. Ederer, Electronic structure of niobium oxides, Journal of alloys and compounds, 347 (2002) 213-218.
[84] T. Isoda, S. Nagao, X. Ma, Y. Korai, I. Mochida, Hydrodesulfurization Pathway of 4,6-Dimethyldibenzothiophene through Isomerization over Y-Zeolite Containing CoMo/Al2O3 Catalyst, Energy & Fuels, 10 (1996) 1078-1082.

[85] N. Bayat, M. Rezaei, F.J.I.J.o.H.E. Meshkani, Hydrogen and carbon nanofibers synthesis by methane decomposition over Ni–Pd/Al2O3 catalyst, 41 (2016) 5494-5503.
[86] A. Karelovic, P. Ruiz, CO2 hydrogenation at low temperature over Rh/γ-Al2O3 catalysts: Effect of the metal particle size on catalytic performances and reaction mechanism, Applied Catalysis B: Environmental, 113-114 (2012) 237-249.
[87] J. Benick, A. Richter, M. Hermle, S.W.J.p.s.s.R.R.L. Glunz, Thermal stability of the Al2O3 passivation on p-type silicon surfaces for solar cell applications, 3 (2009) 233-235.
[88] L.J. Antila, M.J. Heikkilä, V. Mäkinen, N. Humalamäki, M. Laitinen, V. Linko, P. Jalkanen, J. Toppari, V. Aumanen, M. Kemell, P. Myllyperkiö, K. Honkala, H. Häkkinen, M. Leskelä, J.E.I. Korppi-Tommola, ALD Grown Aluminum Oxide Submonolayers in Dye-Sensitized Solar Cells: The Effect on Interfacial Electron Transfer and Performance, The Journal of Physical Chemistry C, 115 (2011) 16720-16729.
[89] M. Breida, S.A. Younssi, A. Bouazizi, B. Achiou, M. Ouammou, M.J.H. El Rhazi, Nitrate removal from aqueous solutions by γ-Al2O3 ultrafiltration membranes, 4 (2018) e00498.
[90] W. Fu, X. Zhang, Y. Mao, T. Pei, B. Sun, S. Mei, L.J.C.I. Chen, A novel γ-Al2O3 nanofiltration membrane via introducing hollow microspheres into interlayers for improving water permeability, 44 (2018) 15824-15832.
[91] M. Rezakazemi, S. Mirzaei, M. Asghari, J. Ivakpour, Aluminum oxide nanoparticles for highly efficient asphaltene separation from crude oil using ceramic membrane technology, Oil & Gas Sciences and Technology–Revue d'IFP Energies nouvelles, 72 (2017) 34.
[92] M.J. Nalbandian, M. Zhang, J. Sanchez, J. Nam, D.M. Cwiertny, N.V.J.S.o.A.M. Myung, Mesoporous ・-Alumina/Hematite (・-Al2O3/Fe2O3) Composite Nanofibers for Heavy Metal Removal, 9 (2017) 22-29.
[93] W. Cai, Y. Hu, J. Chen, G. Zhang, T.J.C. Xia, Synthesis of nanorod-like mesoporous γ-Al2O3 with enhanced affinity towards Congo red removal: effects of anions and structure-directing agents, 14 (2012) 972-977.
[94] X. Zhang, I. Belharouak, L. Li, Y. Lei, J.W. Elam, A. Nie, X. Chen, R.S. Yassar, R.L. Axelbaum, Structural and electrochemical study of Al2O3 and TiO2 coated Li1. 2Ni0. 13Mn0. 54Co0. 13O2 cathode material using ALD, Advanced Energy Materials, 3 (2013) 1299-1307.
[95] P. Yan, J. Zheng, X. Zhang, R. Xu, K. Amine, J. Xiao, J.-G. Zhang, C.-M. Wang, Atomic to Nanoscale Investigation of Functionalities of an Al2O3 Coating Layer on a Cathode for Enhanced Battery Performance, Chemistry of Materials, 28 (2016) 857-863.
[96] A.L. Hoskins, W.W. McNeary, S.L. Millican, T.A. Gossett, A. Lai, Y. Gao, X. Liang, C.B. Musgrave, A.W. Weimer, Nonuniform Growth of Sub-2 Nanometer Atomic Layer Deposited Alumina Films on Lithium Nickel Manganese Cobalt Oxide Cathode Battery Materials, ACS Applied Nano Materials, 2 (2019) 6989-6997.
[97] M.R. Laskar, D.H. Jackson, Y. Guan, S. Xu, S. Fang, M. Dreibelbis, M.K. Mahanthappa, D. Morgan, R.J. Hamers, T.F. Kuech, Atomic layer deposition of Al2O3–Ga2O3 alloy coatings for Li [Ni0. 5Mn0. 3Co0. 2] O2 cathode to improve rate performance in Li-Ion battery, ACS applied materials & interfaces, 8 (2016) 10572-10580.
[98] L. Niinistö, M. Ritala, M. Leskelä, Synthesis of oxide thin films and overlayers by atomic layer epitaxy for advanced applications, Materials Science and Engineering: B, 41 (1996) 23-29.

[99] M. Ritala, Advanced ALE processes of amorphous and polycrystalline films, Applied Surface Science, 112 (1997) 223-230.
[100] V. Miikkulainen, M. Leskelä, M. Ritala, R.L. Puurunen, Crystallinity of inorganic films grown by atomic layer deposition: Overview and general trends, Journal of Applied Physics, 113 (2013) 2.
[101] M. Leskelä, M. Ritala, Atomic layer deposition (ALD): from precursors to thin film structures, Thin solid films, 409 (2002) 138-146.
[102] A. Rahtu, Atomic Layer Deposition of High Permittivity Oxides: Film Growth and, University of Helsinki, Helsinki, Citeseer.
[103] P.M. Martin, Handbook of deposition technologies for films and coatings: science, applications and technology, William Andrew2009.
[104] J. Creighton, P.J.C.v.d. Ho, Introduction to chemical vapor deposition (CVD), 2 (2001) 1-22.
[105] H. Lee, M.Y. Song, J. Jurng, Y.-K. Park, The synthesis and coating process of TiO2 nanoparticles using CVD process, Powder technology, 214 (2011) 64-68.
[106] L.L. Hench, J.K.J.C.r. West, The sol-gel process, 90 (1990) 33-72.
[107] M.J.C.r.d.l.a.d.S. Ebelmen, Sur l'hyalite artificielle et l'hydrophane, 25 (1847) 854-856.
[108] T.J.J.o.t.C.S. Graham, XXXV.—On the properties of silicic acid and other analogous colloidal substances, 17 (1864) 318-327.
[109] W. Stöber, A. Fink, E.J.J.o.c. Bohn, i. science, Controlled growth of monodisperse silica spheres in the micron size range, 26 (1968) 62-69.
[110] J.T.G.J.A.i.C. Overbeek, I. Science, Monodisperse colloidal systems, fascinating and useful, 15 (1982) 251-277.
[111] R.K.J.J.o.C.A. Iler, Silanol groups on silica gel, 209 (1981) 341-342.
[112] J.D.J.J.o.N.-C.S. Mackenzie, Applications of the sol-gel process, 100 (1988) 162-168.
[113] Sols, Gels, and Organic Chemistry, Ceramic Materials: Science and Engineering, Springer New York, New York, NY, 2007, pp. 400-411.
[114] N. Agoudjil, S. Kermadi, A. Larbot, Synthesis of inorganic membrane by sol–gel process, Desalination, 223 (2008) 417-424.
[115] A. Singh, S. Mittal, D. Mudgal, P. Gupta, Design, Development and Application of Nanocoatings, Nanomaterials and Their Applications, Springer2018, pp. 191-207.
[116] C.J. Brinker, A.J. Hurd, P.R. Schunk, G.C. Frye, C.S. Ashley, Review of sol-gel thin film formation, Journal of Non-Crystalline Solids, 147-148 (1992) 424-436.
[117] B. Ben-Nissan, A. Choi, I. Macha, S. Cazalbou, Sol-gel Nanocoatings of Bioceramics, in: I.V. Antoniac (Ed.) Handbook of Bioceramics and Biocomposites, Springer2016, pp. 735-756.
[118] R.A. Caruso, M. Antonietti, Sol− gel nanocoating: an approach to the preparation of structured materials, Chemistry of materials, 13 (2001) 3272-3282.
[119] S. Sakka, Preparation and properties of sol-gel coating films, Journal of Sol-Gel Science and Technology, 2 (1994) 451-455.
[120] C.J. Brinker, G.W. Scherer, Sol-gel science: the physics and chemistry of sol-gel processing, Academic press2013.
[121] J.-H. Park, T. Sudarshan, Chemical vapor deposition, ASM international2001.
[122] H.O. Pierson, Handbook of chemical vapor deposition: principles, technology and applications, William Andrew1999.
[123] S.M. George, Atomic Layer Deposition: An Overview, Chemical Reviews, 110 (2010) 111-131.

[124] A.W. Weimer, Particle atomic layer deposition, Journal of Nanoparticle Research, 21 (2019) 9.
[125] H. Van Bui, F. Grillo, J.R. van Ommen, Atomic and molecular layer deposition: off the beaten track, Chemical Communications, 53 (2017) 45-71.
[126] R.L. Puurunen, Surface chemistry of atomic layer deposition: A case study for the trimethylaluminum/water process, Journal of applied physics, 97 (2005) 9.
[127] Y. Wu, D. Döhler, M. Barr, E. Oks, M. Wolf, L. Santinacci, J. Bachmann, Atomic layer deposition from dissolved precursors, Nano letters, 15 (2015) 6379-6385.
[128] S.-M. Lee, E. Pippel, U. Gösele, C. Dresbach, Y. Qin, C.V. Chandran, T. Bräuniger, G. Hause, M. Knez, Greatly increased toughness of infiltrated spider silk, Science, 324 (2009) 488-492.
[129] I. Azpitarte, M. Knez, Vapor phase infiltration: from a bioinspired process to technologic application, a prospective review, MRS Communications, 8 (2018) 727-741.
[130] C. Bae, H. Kim, Y. Yang, H. Yoo, J.M.M. Moreno, J. Bachmann, K. Nielsch, H. Shin, Rapid, conformal gas-phase formation of silica (SiO 2) nanotubes from water condensates, Nanoscale, 5 (2013) 5825-5832.
[131] M. Fanun, Microemulsions: properties and applications, CRC press2008.
[132] L.M. Prince, The Mixed Film Theory, in: L.M. Prince (Ed.) Microemulsions Theory and Practice, Academic Press1977, pp. 91-131.
[133] J. Ricka, M. Borkovec, U. Hofmeier, Coated droplet model of microemulsions: Optical matching and polydispersity, The Journal of chemical physics, 94 (1991) 8503-8509.
[134] X. Fu, S. Qutubuddin, Synthesis of titania-coated silica nanoparticles using a nonionic water-in-oil microemulsion, Colloids and Surfaces A: Physicochemical and Engineering Aspects, 179 (2001) 65-70.
[135] T. Tago, T. Hatsuta, K. Miyajima, M. Kishida, S. Tashiro, K. Wakabayashi, Novel synthesis of silica-coated ferrite nanoparticles prepared using water-in-oil microemulsion, Journal of the American Ceramic Society, 85 (2002) 2188-2194.
[136] J. Blanchard, M. In, B. Schaudel, C. Sanchez, Hydrolysis and condensation reactions of transition metal alkoxides: calorimetric study and evaluation of the extent of reaction, European journal of inorganic chemistry, 1998 (1998) 1115-1127.
[137] Y. Xing, L. Li, C.C. Chusuei, R.V. Hull, Sonochemical oxidation of multiwalled carbon nanotubes, Langmuir, 21 (2005) 4185-4190.
[138] C. Tsonopoulos, Thermodynamic analysis of the mutual solubilities of normal alkanes and water, Fluid Phase Equilibria, 156 (1999) 21-33.
[139] M.K. Johnson, R.B. King, D.M. Kurtz Jr, C. Kutal, M.L. Norton, R.A. Scott, Electron transfer in biology and the solid state: inorganic compounds with unusual properties, ACS Publications1989.
[140] C. Sanchez, J. Livage, M. Henry, F. Babonneau, Chemical modification of alkoxide precursors, Journal of Non-Crystalline Solids, 100 (1988) 65-76.
[141] D.J. Eichorst, K.E. Howard, D.A. Payne, S.R. Wilson, Crystal structure of lithium niobium ethoxide (LiNb(OCH2CH3)6: a precursor for lithium niobate ceramics, Inorganic Chemistry, 29 (1990) 1458-1459.
[142] S. Mahshid, M. Askari, M.S. Ghamsari, Synthesis of TiO2 nanoparticles by hydrolysis and peptization of titanium isopropoxide solution, Journal of Materials Processing Technology, 189 (2007) 296-300.
[143] U. Schubert, N. Huesing, A. Lorenz, Hybrid inorganic-organic materials by sol-gel processing of organofunctional metal alkoxides, Chemistry of materials, 7 (1995) 2010-2027.

[144] J. Mark, S. Wang, Z. Ahmad, Inorganic-organic composites, including some examples involving polyamides and polyimides, Macromolecular Symposia, Wiley Online Library, 1995, pp. 731-751.
[145] P. Judeinstein, C. Sanchez, Hybrid organic–inorganic materials: a land of multidisciplinarity, Journal of Materials Chemistry, 6 (1996) 511-525.
[146] F. Ribot, P. Toledano, C. Sanchez, Hydrolysis-condensation process of. beta.-diketonates-modified cerium (IV) isopropoxide, Chemistry of materials, 3 (1991) 759-764.
[147] J. Wen, G.L. Wilkes, Organic/inorganic hybrid network materials by the sol− gel approach, Chemistry of materials, 8 (1996) 1667-1681.
[148] K. Li, D. Xue, Estimation of electronegativity values of elements in different valence states, The Journal of Physical Chemistry A, 110 (2006) 11332-11337.
[149] D. Wright, D. Williams, The crystal and molecular structure of titanium tetramethoxide, Acta Crystallographica Section B: Structural Crystallography and Crystal Chemistry, 24 (1968) 1107-1114.
[150] C. Guerra-Nuñez, M. Döbeli, J. Michler, I. Utke, Reaction and growth mechanisms in Al_2O_3 deposited via atomic layer deposition: elucidating the hydrogen source, Chemistry of Materials, 29 (2017) 8690-8703.
[151] M.D. Groner, F.H. Fabreguette, J.W. Elam, S.M. George, Low-Temperature Al2O3 Atomic Layer Deposition, Chemistry of Materials, 16 (2004) 639-645.
[152] S.M. George, A.W. Ott, J.W. Klaus, Surface Chemistry for Atomic Layer Growth, The Journal of Physical Chemistry, 100 (1996) 13121-13131.
[153] E. Ahvenniemi, A.R. Akbashev, S. Ali, M. Bechelany, M. Berdova, S. Boyadjiev, D.C. Cameron, R. Chen, M. Chubarov, V.J.J.o.V.S. Cremers, S. Technology A: Vacuum, Films, Recommended reading list of early publications on atomic layer deposition—Outcome of the "Virtual Project on the History of ALD", 35 (2017) 010801.
[154] B.L. García, R. Fuentes, J.W.J.E. Weidner, S.-S. Letters, Low-Temperature Synthesis of a PtRu⁄Nb0. 1Ti0. 9O2 Electrocatalyst for Methanol Oxidation, 10 (2007) B108-B110.
[155] S. Venkataraj, R. Drese, C. Liesch, O. Kappertz, R. Jayavel, M.J.J.o.A.P. Wuttig, Temperature stability of sputtered niobium–oxide films, 91 (2002) 4863-4871.
[156] M.J. Young, N. Bedford, J.W. Elam, A. Yanguas-Gil, S. Letourneau, M. Coile, D. Mandia, S.M. George, A.S. Cavanagh, X. He, Probing the Atomic-Scale Structure of Thin Films Grown By Atomic Layer Deposition, 236th ECS Meeting (October 13-17, 2019), ECS, 2019.
[157] J. Aarik, A. Aidla, T. Uustare, V.J.J.o.c.g. Sammelselg, Morphology and structure of TiO2 thin films grown by atomic layer deposition, 148 (1995) 268-275.
[158] D. Mitchell, G. Triani, D. Attard, K. Finnie, P. Evans, C. Barbé, J.J.S.m. Bartlett, structures, Atomic layer deposition of TiO2 and Al2O3 thin films and nanolaminates, 15 (2005) S57.
[159] Y.-F. Chen, C.-Y. Lee, M.-Y. Yeng, H.-T.J.J.o.c.g. Chiu, The effect of calcination temperature on the crystallinity of TiO2 nanopowders, 247 (2003) 363-370.
[160] S. Jakschik, U. Schroeder, T. Hecht, M. Gutsche, H. Seidl, J.W. Bartha, Crystallization behavior of thin ALD-Al_2O_3 films, Thin Solid Films 425 (2003) 216-220.
[161] K. Kukli, M. Ritala, J. Aarik, T. Uustare, M.J.J.o.a.p. Leskelä, Influence of growth temperature on properties of zirconium dioxide films grown by atomic layer deposition, 92 (2002) 1833-1840.

[162] J. Hu, G. Chen, I.M.J.W.r. Lo, Removal and recovery of Cr (VI) from wastewater by maghemite nanoparticles, 39 (2005) 4528-4536.
[163] T. Phuengprasop, J. Sittiwong, F. Unob, Removal of heavy metal ions by iron oxide coated sewage sludge, Journal of Hazardous Materials, 186 (2011) 502-507.
[164] C. Chen, J. Hu, D. Shao, J. Li, X. Wang, Adsorption behavior of multiwall carbon nanotube/iron oxide magnetic composites for Ni(II) and Sr(II), Journal of Hazardous Materials, 164 (2009) 923-928.
[165] R.J.-M. Pellenq, H.J.M.B. Van Damme, Why does concrete set?: The nature of cohesion forces in hardened cement-based materials, 29 (2004) 319-323.
[166] H. Liu, G. Cao, Effectiveness of the Young-Laplace equation at nanoscale, Scientific Reports, 6 (2016) 23936.
[167] S.M.A. Malek, F. Sciortino, P.H. Poole, I. Saika-Voivod, Evaluating the Laplace pressure of water nanodroplets from simulations, Journal of Physics: Condensed Matter, 30 (2018) 144005.
[168] J. Dubochet, A.W. McDowall, Vitrification of Pure Water for Electron Microscopy, Journal of Microscopy, 124 (1981) 3-4.
[169] K. Kobayashi, M. Koshino, K. Suenaga, Atomically resolved images of I h ice single crystals in the solid phase, Physical review letters, 106 (2011) 206101.
[170] G. Algara-Siller, O. Lehtinen, F. Wang, R. Nair, U. Kaiser, H. Wu, A. Geim, I. Grigorieva, Square ice in graphene nanocapillaries, Nature, 519 (2015) 443.
[171] J. Polak, B.C.-Y.J.C.J.o.C. Lu, Mutual solubilities of hydrocarbons and water at 0 and 25 C, 51 (1973) 4018-4023.
[172] D. Chouikhi, I. Kulai, D. Bergbreiter, M. Al-Hashimi, H.J.A.S. Bazzi, Functionalized Polyisobutylene and Liquid/Liquid Separations as a Method for Scavenging Transition Metals from Homogeneously Catalyzed Reactions, 9 (2019) 120.
[173] A.V. Shevade, S. Jiang, K.E.J.T.J.o.C.P. Gubbins, Molecular simulation study of water–methanol mixtures in activated carbon pores, 113 (2000) 6933-6942.
[174] S. Hamad, J.A. Mejias, S. Lago, S. Picaud, P.N.J.T.J.o.P.C.B. Hoang, Theoretical study of the adsorption of water on a model soot surface: I. Quantum chemical calculations, 108 (2004) 5405-5409.
[175] P. Cabrera-Sanfelix, G.R. Darling, Dissociative adsorption of water at vacancy defects in graphite, The Journal of Physical Chemistry C, 111 (2007) 18258-18263.
[176] W. Thomson, 4. On the equilibrium of vapour at a curved surface of liquid, Proceedings of the Royal Society of Edinburgh, 7 (1872) 63-68.
[177] P. Calderbank, M.J.c.E.s. Moo-Young, The continuous phase heat and mass-transfer properties of dispersions, 16 (1961) 39-54.
[178] A. Nienow, D.J.T.C.E.J. Miles, The effect of impeller/tank, configurations on fluid-particle mass transfer, 15 (1978) 13-24.
[179] T.F. Whale, M. Rosillo-Lopez, B.J. Murray, C.G. Salzmann, Ice nucleation properties of oxidized carbon nanomaterials, The journal of physical chemistry letters, 6 (2015) 3012-3016.
[180] M. Kumai, Hexagonal and cubic ice at low temperatures, Journal of Glaciology, 7 (1968) 95-108.
[181] A. Narten, C.-G. Venkatesh, S. Rice, Diffraction pattern and structure of amorphous solid water at 10 and 77 K, The Journal of Chemical Physics, 64 (1976) 1106-1121.
[182] P.G.J.J.o.P.C.M. Debenedetti, Supercooled and glassy water, 15 (2003) R1669.
[183] O.J.N. Mishima, MISHIMA O, 314 (1985) 76.

[184] O. Mishima, L. Calvert, E.J.N. Whalley, 'Melting ice'I at 77 K and 10 kbar: A new method of making amorphous solids, 310 (1984) 393.
[185] K. Amann-Winkel, C. Gainaru, P.H. Handle, M. Seidl, H. Nelson, R. Böhmer, T. Loerting, Water's second glass transition, Proceedings of the National Academy of Sciences, 110 (2013) 17720-17725.
[186] T. Loerting, C. Salzmann, I. Kohl, E. Mayer, A.J.P.C.C.P. Hallbrucker, A second distinct structural "state" of high-density amorphous ice at 77 K and 1 bar, 3 (2001) 5355-5357.
[187] J. Finney, D. Bowron, A. Soper, T. Loerting, E. Mayer, A.J.P.r.l. Hallbrucker, Structure of a new dense amorphous ice, 89 (2002) 205503.
[188] H. Song, M. Dai, H. Song, X. Wan, X. Xu, C. Zhang, H.J.C.C. Wang, Synthesis of a Ni2P catalyst supported on anatase–TiO2 whiskers with high hydrodesulfurization activity, based on triphenylphosphine, 43 (2014) 151-154.
[189] E. Storti, S. Dudczig, G. Schmidt, P. Colombo, C.G.J.J.o.t.E.C.S. Aneziris, Short-time performance of MWCNTs-coated Al2O3-C filters in a steel melt, 36 (2016) 857-866.
[190] C. Jing, X. Meng, E. Calvache, G.J.E.p. Jiang, Remediation of organic and inorganic arsenic contaminated groundwater using a nanocrystalline TiO2-based adsorbent, 157 (2009) 2514-2519.
[191] S. Bagheri, N. Muhd Julkapli, S.J.T.S.W.J. Bee Abd Hamid, Titanium dioxide as a catalyst support in heterogeneous catalysis, 2014 (2014).
[192] V.M. Shinde, G.J.A.J. Madras, CO methanation toward the production of synthetic natural gas over highly active Ni/TiO2 catalyst, 60 (2014) 1027-1035.
[193] E.A. Sánchez, M.A. D'Angelo, R.A. Comelli, Hydrogen production from glycerol on Ni/Al2O3 catalyst, International Journal of Hydrogen Energy, 35 (2010) 5902-5907.
[194] A. Afkhami, M. Saber-Tehrani, H.J.J.o.H.M. Bagheri, Simultaneous removal of heavy-metal ions in wastewater samples using nano-alumina modified with 2, 4-dinitrophenylhydrazine, 181 (2010) 836-844.
[195] S. Eri, J.G. Goodwin Jr, G. Marcelin, T. Riis, Process using a supported catalyst for hydrocarbon synthesis, Google Patents, 1992.
[196] B.E. Solsona, J.K. Edwards, P. Landon, A.F. Carley, A. Herzing, C.J. Kiely, G.J.J.C.o.m. Hutchings, Direct synthesis of hydrogen peroxide from H2 and O2 using Al2O3 supported Au− Pd catalysts, 18 (2006) 2689-2695.
[197] K. Sing, D. Everett, R. Haul, L. Moscou, R. Pierotti, J. Rouquerol, T.J.P.A.C. Siemieniewska, International union of pure and applied chemistry, IUPAC, 57 (1985) 603.
[198] A.M. Jasim, G. Xu, S. Al-Salihi, Y. Xing, Dense Niobium Oxide Coating on Carbon Black as a Support to Platinum Electrocatalyst for Oxygen Reduction, ChemistrySelect, 5 (2020) 11431-11437.
[199] D.B. Farmer, R.G. Gordon, Atomic layer deposition on suspended single-walled carbon nanotubes via gas-phase noncovalent functionalization, Nano letters, 6 (2006) 699-703.
[200] M. Ritala, M. Leskelä, E. Nykänen, P. Soininen, L. Niinistö, Growth of titanium dioxide thin films by atomic layer epitaxy, Thin solid films, 225 (1993) 288-295.
[201] D.M. Hausmann, E. Kim, J. Becker, R.G. Gordon, Atomic layer deposition of hafnium and zirconium oxides using metal amide precursors, Chemistry of materials, 14 (2002) 4350-4358.
[202] J. Ferguson, E. Smith, A. Weimer, S. George, ALD of SiO2 at Room Temperature Using TEOS and H 2 O with NH 3 as the Catalyst, Journal of The Electrochemical Society, 151 (2004) G528-G535.

[203] A. Yamada, B. Sang, M. Konagai, Atomic layer deposition of ZnO transparent conducting oxides, Applied Surface Science, 112 (1997) 216-222.
[204] K. Huang, K. Sasaki, R.R. Adzic, Y. Xing, Increasing Pt oxygen reduction reaction activity and durability with a carbon-doped TiO 2 nanocoating catalyst support, Journal of Materials Chemistry, 22 (2012) 16824-16832.
[205] O. Carp, C.L. Huisman, A. Reller, Photoinduced reactivity of titanium dioxide, Progress in solid state chemistry, 32 (2004) 33-177.
[206] P. Poizot, S. Laruelle, S. Grugeon, L. Dupont, J. Tarascon, Nano-sized transition-metal oxides as negative-electrode materials for lithium-ion batteries, Nature, 407 (2000) 496.
[207] C. Wang, L. Yin, L. Zhang, D. Xiang, R. Gao, Metal oxide gas sensors: sensitivity and influencing factors, Sensors, 10 (2010) 2088-2106.
[208] H. Zhang, Z. Ji, T. Xia, H. Meng, C. Low-Kam, R. Liu, S. Pokhrel, S. Lin, X. Wang, Y.-P. Liao, Use of metal oxide nanoparticle band gap to develop a predictive paradigm for oxidative stress and acute pulmonary inflammation, ACS nano, 6 (2012) 4349-4368.
[209] A.N. Subba Rao, V.T. Venkatarangaiah, Metal oxide-coated anodes in wastewater treatment, Environmental Science and Pollution Research, 21 (2014) 3197-3217.
[210] V. Zharvan, R. Daniyati, G. Yudoyono, Darminto, Study on fabrication of TiO2 thin films by spin–coating and their optical properties, AIP Conference Proceedings, AIP Publishing, 2016, pp. 030018.
[211] A.T. Iancu, M. Logar, J. Park, F.B. Prinz, Atomic layer deposition of undoped TiO2 exhibiting p-type conductivity, ACS applied materials & interfaces, 7 (2015) 5134-5140.
[212] M. May-Lozano, G. Ramos-Reyes, R. López-Medina, S. Martínez-Delgadillo, J. Flores-Moreno, I. Hernández-Pérez, Effect of the Amount of Water in the Synthesis of B-TiO2: Orange II Photodegradation, International Journal of Photochemistry, 2014 (2014).
[213] C.-C. Wang, J.Y. Ying, Sol−Gel Synthesis and Hydrothermal Processing of Anatase and Rutile Titania Nanocrystals, Chemistry of Materials, 11 (1999) 3113-3120.
[214] R.A. Caruso, J.H. Schattka, A. Greiner, Titanium Dioxide Tubes from Sol–Gel Coating of Electrospun Polymer Fibers, Advanced Materials, 13 (2001) 1577-1579.
[215] Y.V. Kolen'ko, A.V. Garshev, B.R. Churagulov, S. Boujday, P. Portes, C. Colbeau-Justin, Photocatalytic activity of sol–gel derived titania converted into nanocrystalline powders by supercritical drying, Journal of Photochemistry and Photobiology A: Chemistry, 172 (2005) 19-26.
[216] M. Ivanda, S. Musić, S. Popović, M. Gotić, XRD, Raman and FT-IR spectroscopic observations of nanosized TiO2 synthesized by the sol–gel method based on an esterification reaction, Journal of Molecular Structure, 480-481 (1999) 645-649.
[217] D. Bradley, D. Carter, Metal oxide alkoxide polymers: part I. the hydrolysis of some primary alkoxides of zirconium, Canadian Journal of Chemistry, 39 (1961) 1434-1443.
[218] D. Bradley, D. Carter, Metal oxide alkoxide polymers: Part III. The hydrolysis of secondary and tertiary alkoxides of zirconium, Canadian Journal of Chemistry, 40 (1962) 15-21.
[219] A.M. Jasim, X. He, T.A. White, Y. Xing, Nano-layer deposition of metal oxides via a condensed water film, Communications Materials, 1 (2020) 9.
[220] S. Picaud, B. Collignon, P.N. Hoang, J.-C. Rayez, Adsorption of water molecules on partially oxidized graphite surfaces: a molecular dynamics study of the competition

between OH and COOH sites, Physical Chemistry Chemical Physics, 10 (2008) 6998-7009.
[221] D.A. Hanaor, I. Chironi, I. Karatchevtseva, G. Triani, C.C. Sorrell, Single and mixed phase TiO2 powders prepared by excess hydrolysis of titanium alkoxide, Advances in Applied Ceramics, 111 (2012) 149-158.
[222] C. Black, G.G. Joris, H.S. Taylor, The solubility of water in hydrocarbons, The Journal of Chemical Physics, 16 (1948) 537-543.
[223] T. Nishide, F. Mizukami, Effect of ligands on crystal structures and optical properties of TiO2 prepared by sol–gel processes, Thin Solid Films, 353 (1999) 67-71.
[224] J.Y. Cho, W.H. Nam, Y.S. Lim, W.-S. Seo, H.-H. Park, J.Y. Lee, Bulky mesoporous TiO 2 structure, RSC Advances, 2 (2012) 2449-2453.
[225] P. Buerger, D. Nurkowski, J. Akroyd, M. Kraft, A kinetic mechanism for the thermal decomposition of titanium tetraisopropoxide, Proceedings of the Combustion Institute, 36 (2017) 1019-1027.
[226] M.V. Johnson, S.S. Goldsborough, Z. Serinyel, P. O'Toole, E. Larkin, G. O'Malley, H.J. Curran, A Shock Tube Study of n- and iso-Propanol Ignition, Energy & Fuels, 23 (2009) 5886-5898.
[227] G. Socrates, Infrared and Raman characteristic group frequencies: tables and charts, John Wiley & Sons2001.
[228] G.D. Venkatasubbu, S. Ramasamy, V. Ramakrishnan, J. Kumar, Folate targeted PEGylated titanium dioxide nanoparticles as a nanocarrier for targeted paclitaxel drug delivery, Advanced Powder Technology, 24 (2013) 947-954.
[229] A. Parada-Bustamante, C. Valencia, P. Reuquén, P. Díaz, R. Rincion-Rodriguez, P. A Orihuela, Role of 2-methoxyestradiol, an endogenous estrogen metabolite, in health and disease, Mini reviews in medicinal chemistry, 15 (2015) 427-438.
[230] A. León, P. Reuquen, C. Garín, R. Segura, P. Vargas, P. Zapata, P.A. Orihuela, FTIR and Raman characterization of TiO2 nanoparticles coated with polyethylene glycol as carrier for 2-methoxyestradiol, Applied Sciences, 7 (2017) 49.
[231] R. Campostrini, M. Ischia, L. Palmisano, Pyrolysis study of Sol-gel derived TiO2powders: Part I. TiO2-anatase prepared by reacting titanium (IV) isopropoxide with formic acid, Journal of thermal analysis and calorimetry, 71 (2003) 997-1010.
[232] R. Robinson Jr, W. Edmister, F. Dullien, Diffusion coefficients for four homomorphic binary liquid systems, Industrial & Engineering Chemistry Fundamentals, 5 (1966) 74-79.
[233] C. Ramakanth, A.K. Mukherjee, T.R. Das, Diffusion coefficients for selected binary liquid systems: cyclohexanes and n-alkyl alcohols, Journal of Chemical & Engineering Data, 36 (1991) 384-387.
[234] J.-K. Park, J.-J. Myoung, J.-B. Kyong, H.-K. Kim, Reaction mechanism for the hydrolysis of titanium alkoxides, Bulletin of the Korean Chemical Society, 24 (2003) 671-673.
[235] B.E. Yoldas, Modification of polymer-gel structures, Journal of Non-Crystalline Solids, 63 (1984) 145-154.
[236] C. Sanchez, J. Livage, M. Henry, F. Babonneau, Chemical modification of alkoxide precursors, Journal of Non-Crystalline Solids, 100 (1988) 65-76.
[237] B.E. Yoldas, Introduction and effect of structural variations in inorganic polymers and glass networks, Journal of Non-Crystalline Solids, 51 (1982) 105-121.
[238] B.E. Yoldas, Hydrolysis of titanium alkoxide and effects of hydrolytic polycondensation parameters, Journal of Materials Science, 21 (1986) 1087-1092.

[239] Y.-F. Chen, C.-Y. Lee, M.-Y. Yeng, H.-T. Chiu, The effect of calcination temperature on the crystallinity of TiO2 nanopowders, Journal of crystal growth, 247 (2003) 363-370.
[240] R. Ghosh, M. Nethaji, A.G. Samuelson, Reversible double insertion of aryl isocyanates into the Ti–O bond of titanium (IV) isopropoxide, Journal of organometallic chemistry, 690 (2005) 1282-1293.
[241] J.A. Ibers, Crystal and molecular structure of titanium (IV) ethoxide, Nature, 197 (1963) 686.
[242] A.F. Cotton, G. Wilkinson, M. Bochmann, C.A. Murillo, Advanced inorganic chemistry, Wiley1999.
[243] M. Gopal, W.M. Chan, L. De Jonghe, Room temperature synthesis of crystalline metal oxides, Journal of Materials Science, 32 (1997) 6001-6008.
[244] S. Sivakumar, P. Krishna Pillai, P. Mukundan, K.G.K. Warrier, Sol–gel synthesis of nanosized anatase from titanyl sulfate, Materials Letters, 57 (2002) 330-335.
[245] X. Han, D. Wang, D. Liu, J. Huang, T. You, Synthesis and electrocatalytic activity of Au/Pt bimetallic nanodendrites for ethanol oxidation in alkaline medium, Journal of colloid and interface science, 367 (2012) 342-347.
[246] C. Lamy, E. Belgsir, J. Leger, Electrocatalytic oxidation of aliphatic alcohols: application to the direct alcohol fuel cell (DAFC), Journal of Applied Electrochemistry, 31 (2001) 799-809.
[247] B. Liu, J. Chen, X. Zhong, K. Cui, H. Zhou, Y. Kuang, Preparation and electrocatalytic properties of Pt–SiO2 nanocatalysts for ethanol electrooxidation, Journal of colloid and interface science, 307 (2007) 139-144.
[248] W. Zhou, Z. Zhou, S. Song, W. Li, G. Sun, P. Tsiakaras, Q. Xin, Pt based anode catalysts for direct ethanol fuel cells, Applied Catalysis B: Environmental, 46 (2003) 273-285.
[249] W. Tsang, Thermal stability of alcohols, International Journal of Chemical Kinetics, 8 (1976) 173-192.
[250] G.A. Camara, T. Iwasita, Parallel pathways of ethanol oxidation: The effect of ethanol concentration, Journal of Electroanalytical Chemistry, 578 (2005) 315-321.
[251] S. Rousseau, C. Coutanceau, C. Lamy, J.M. Léger, Direct ethanol fuel cell (DEFC): Electrical performances and reaction products distribution under operating conditions with different platinum-based anodes, Journal of Power Sources, 158 (2006) 18-24.
[252] F. Saleem, Z. Zhang, B. Xu, X. Xu, P. He, X. Wang, Ultrathin Pt–Cu Nanosheets and Nanocones, Journal of the American Chemical Society, 135 (2013) 18304-18307.
[253] J.W. Magee, W.-P. Zhou, M.G. White, Promotion of Pt surfaces for ethanol electro-oxidation by the addition of small SnO2 nanoparticles: Activity and mechanism, Applied Catalysis B: Environmental, 152 (2014) 397-402.
[254] E. Kuyuldar, H. Burhan, A. Şavk, B. Güven, C. Özdemir, S. Şahin, A. Khan, F. Şen, Enhanced Electrocatalytic Activity and Durability of PtRu Nanoparticles Decorated on rGO Material for Ethanol Oxidation Reaction, Graphene Functionalization Strategies, Springer2019, pp. 389-398.
[255] E. Antolini, E.R. Gonzalez, Alkaline direct alcohol fuel cells, Journal of Power Sources, 195 (2010) 3431-3450.
[256] J. Corchado-García, C. Morais, N. Alonso-Vante, C.R. Cabrera, Probing ethanol oxidation mechanism with in-situ FTIR spectroscopy via photodeposited Pt nanoparticles onto titania, Journal of Electroanalytical Chemistry, 799 (2017) 228-234.
[257] I.A. Rutkowska, P.J. Kulesza, Electrocatalytic oxidation of ethanol in acid medium: Enhancement of activity of vulcan-supported Platinum-based nanoparticles

upon immobilization within nanostructured zirconia matrices, Functional Materials Letters, 7 (2014) 1440005.
[258] Y. Qu, Y. Gao, L. Wang, J. Rao, G. Yin, Mild Synthesis of Pt/SnO2 /Graphene Nanocomposites with Remarkably Enhanced Ethanol Electro-oxidation Activity and Durability, Chemistry, 22 (2016) 193-198.
[259] H. Zhang, C. Hu, X. He, L. Hong, G. Du, Y. Zhang, Pt support of multidimensional active sites and radial channels formed by SnO2 flower-like crystals for methanol and ethanol oxidation, Journal of Power Sources, 196 (2011) 4499-4505.
[260] X. Zhang, H. Zhu, Z. Guo, Y. Wei, F. Wang, Sulfated SnO2 modified multi-walled carbon nanotubes–A mixed proton–electron conducting support for Pt catalysts in direct ethanol fuel cells, Journal of Power Sources, 196 (2011) 3048-3053.
[261] N. Kamyar, S. Rezaee, S. Shahrokhian, M.M. Amini, Direct conversion of inorganic complexes to platinum/thin oxide nanoparticles decorated on MOF-derived chromium oxide/nanoporous carbon composite as an efficient electrocatalyst for ethanol oxidation reaction, Journal of colloid and interface science, 555 (2019) 655-666.
[262] K. Huang, K. Sasaki, R.R. Adzic, Y. Xing, Increasing Pt oxygen reduction reaction activity and durability with a carbon-doped TiO2 nanocoating catalyst support, Journal of Materials Chemistry, 22 (2012) 16824.
[263] A.K. Srivastava, M. Deepa, S. Bhandari, H. Fuess, Tunable Nanostructures and Crystal Structures in Titanium Oxide Films, Nanoscale Res Lett, 4 (2009) 54-62.
[264] X. Li, J. Wei, Y. Chai, S. Zhang, Carbon nanotubes/tin oxide nanocomposite-supported Pt catalysts for methanol electro-oxidation, Journal of Colloid and Interface Science, 450 (2015) 74-81.
[265] A. Khataee, M. Sheydaei, A. Hassani, M. Taseidifar, S. Karaca, Sonocatalytic removal of an organic dye using TiO2/Montmorillonite nanocomposite, Ultrasonics Sonochemistry, 22 (2015) 404-411.
[266] Y. Xin, J.-g. Liu, Y. Zhou, W. Liu, J. Gao, Y. Xie, Y. Yin, Z. Zou, Preparation and characterization of Pt supported on graphene with enhanced electrocatalytic activity in fuel cell, Journal of Power Sources, 196 (2011) 1012-1018.
[267] Y. Liu, W.E. Mustain, High stability, high activity Pt/ITO oxygen reduction electrocatalysts, Journal of the American Chemical Society, 135 (2013) 530-533.
[268] L. Yan, K. Huang, Y. Chen, Y. Xing, High Content Niobium in Rutile Titania as Catalyst Support to Promote Methanol Electro-Oxidation, ECS Electrochemistry Letters, 3 (2014) F27-F29.
[269] H.-J. Ahn, H.-C. Choi, K.-W. Park, S.-B. Kim, Y.-E. Sung, Investigation of the structural and electrochemical properties of size-controlled SnO2 nanoparticles, The Journal of Physical Chemistry B, 108 (2004) 9815-9820.
[270] X. Li, A.L. Zhu, W. Qu, H. Wang, R. Hui, L. Zhang, J. Zhang, Magneli phase Ti4O7 electrode for oxygen reduction reaction and its implication for zinc-air rechargeable batteries, Electrochimica Acta, 55 (2010) 5891-5898.
[271] Y. Xing, Synthesis and Electrochemical Characterization of Uniformly-Dispersed High Loading Pt Nanoparticles on Sonochemically-Treated Carbon Nanotubes, The Journal of Physical Chemistry B, 108 (2004) 19255-19259.
[272] B.L. García, R. Fuentes, J.W. Weidner, Low-Temperature Synthesis of a PtRu⁄Nb[sub 0.1]Ti[sub 0.9]O[sub 2] Electrocatalyst for Methanol Oxidation, Electrochemical and Solid-State Letters, 10 (2007) B108.
[273] S. Yu, Q. Liu, W. Yang, K. Han, Z. Wang, H. Zhu, Graphene–CeO2 hybrid support for Pt nanoparticles as potential electrocatalyst for direct methanol fuel cells, Electrochimica Acta, 94 (2013) 245-251.

[274] S.G. Bratsch, Standard Electrode Potentials and Temperature Coefficients in Water at 298.15 K, Journal of Physical and Chemical Reference Data, 18 (1989) 1-21.
[275] J.B. Goodenough, R. Manoharan, A.K. Shukla, K.V. Ramesh, Intraalloy electron transfer and catalyst performance: a spectroscopic and electrochemical study, Chemistry of Materials, 1 (1989) 391-398.
[276] F. Vigier, C. Coutanceau, F. Hahn, E.M. Belgsir, C. Lamy, On the mechanism of ethanol electro-oxidation on Pt and PtSn catalysts: electrochemical and in situ IR reflectance spectroscopy studies, Journal of Electroanalytical Chemistry, 563 (2004) 81-89.
[277] J. Willsau, J. Heitbaum, Elementary steps of ethanol oxidation on Pt in sulfuric acid as evidenced by isotope labelling, Journal of Electroanalytical Chemistry and Interfacial Electrochemistry, 194 (1985) 27-35.
[278] W. Du, G. Yang, E. Wong, N.A. Deskins, A.I. Frenkel, D. Su, X. Teng, Platinum-tin oxide core-shell catalysts for efficient electro-oxidation of ethanol, J Am Chem Soc, 136 (2014) 10862-10865.
[279] L. Jiang, G. Sun, S. Sun, J. Liu, S. Tang, H. Li, B. Zhou, Q. Xin, Structure and chemical composition of supported Pt–Sn electrocatalysts for ethanol oxidation, Electrochimica Acta, 50 (2005) 5384-5389.
[280] Q. Wang, G.Q. Sun, L.H. Jiang, Q. Xin, S.G. Sun, Y.X. Jiang, S.P. Chen, Z. Jusys, R.J. Behm, Adsorption and oxidation of ethanol on colloid-based Pt/C, PtRu/C and Pt3Sn/C catalysts: In situ FTIR spectroscopy and on-line DEMS studies, Physical Chemistry Chemical Physics, 9 (2007) 2686-2696.
[281] W. Du, G. Yang, E. Wong, N.A. Deskins, A.I. Frenkel, D. Su, X. Teng, Platinum-Tin Oxide Core–Shell Catalysts for Efficient Electro-Oxidation of Ethanol, Journal of the American Chemical Society, 136 (2014) 10862-10865.
[282] G.-Y. Zhao, H.-L. Li, Electrochemical oxidation of methanol on Pt nanoparticles composited MnO2 nanowire arrayed electrode, Applied Surface Science, 254 (2008) 3232-3235.
[283] C. Lamy, A. Lima, V. LeRhun, F. Delime, C. Coutanceau, J.-M. Léger, Recent advances in the development of direct alcohol fuel cells (DAFC), Journal of Power Sources, 105 (2002) 283-296.
[284] Y.-H. Qin, Y. Li, T. Lam, Y. Xing, Nitrogen-doped carbon-TiO2 composite as support of Pd electrocatalyst for formic acid oxidation, Journal of Power Sources, 284 (2015) 186-193.
[285] B. Fang, N.K. Chaudhari, M.-S. Kim, J.H. Kim, J.-S. Yu, Homogeneous deposition of platinum nanoparticles on carbon black for proton exchange membrane fuel cell, Journal of the American chemical society, 131 (2009) 15330-15338.
[286] L.M. Ombaka, P. Ndungu, V.O. Nyamori, Usage of carbon nanotubes as platinum and nickel catalyst support in dehydrogenation reactions, Catalysis Today, 217 (2013) 65-75.
[287] C.V. Subban, Q. Zhou, A. Hu, T.E. Moylan, F.T. Wagner, F.J. DiSalvo, Sol−Gel Synthesis, Electrochemical Characterization, and Stability Testing of Ti0.7W0.3O2 Nanoparticles for Catalyst Support Applications in Proton-Exchange Membrane Fuel Cells, Journal of the American Chemical Society, 132 (2010) 17531-17536.
[288] Y.-H. Lin, Y.-C. Hsueh, P.-S. Lee, C.-C. Wang, J.M. Wu, T.-P. Perng, H.C. Shih, Fabrication of tin dioxide nanowires with ultrahigh gas sensitivity by atomic layer deposition of platinum, Journal of Materials Chemistry, 21 (2011) 10552-10558.
[289] R.I. Jafri, N. Sujatha, N. Rajalakshmi, S. Ramaprabhu, Au–MnO2/MWNT and Au–ZnO/MWNT as oxygen reduction reaction electrocatalyst for polymer electrolyte membrane fuel cell, international journal of hydrogen energy, 34 (2009) 6371-6376.

[290] Y. Chen, J. Wang, X. Meng, Y. Zhong, R. Li, X. Sun, S. Ye, S. Knights, Atomic layer deposition assisted Pt-SnO2 hybrid catalysts on nitrogen-doped CNTs with enhanced electrocatalytic activities for low temperature fuel cells, international journal of hydrogen energy, 36 (2011) 11085-11092.
[291] A.A. Gribb, J.F. Banfield, Particle size effects on transformation kinetics and phase stability in nanocrystalline TiO2, American Mineralogist, 82 (1997) 717-728.
[292] F. Luo, S. Liao, D. Dang, Y. Zheng, D. Xu, H. Nan, T. Shu, Z. Fu, Tin and silicon binary oxide on the carbon support of a Pt electrocatalyst with enhanced activity and durability, ACS Catalysis, 5 (2015) 2242-2249.
[293] A. Kowal, M. Li, M. Shao, K. Sasaki, M. Vukmirovic, J.h. Zhang, N. Marinkovic, P. Liu, A. Frenkel, R. Adzic, Ternary Pt/Rh/SnO 2 electrocatalysts for oxidizing ethanol to CO 2, Nature materials, 8 (2009) 325.
[294] N. Zhang, S. Zhang, C. Du, Z. Wang, Y. Shao, F. Kong, Y. Lin, G. Yin, Pt/Tin oxide/carbon nanocomposites as promising oxygen reduction electrocatalyst with improved stability and activity, Electrochimica Acta, 117 (2014) 413-419.
[295] A. Ishihara, T. Nagai, N. Murase, M. Arao, Y. Kuroda, K. Matsuzawa, S. Mitsushima, K. Furukawa, H. Imai, K. Lee, Effect of Nitrogen Doping on Oxygen Reduction Activity of TiO2 in Acidic Media, ECS Transactions, 92 (2019) 613-620.
[296] A. Stassi, C. D'urso, V. Baglio, A. Di Blasi, V. Antonucci, A. Arico, A.C. Luna, A. Bonesi, W. Triaca, Electrocatalytic behaviour for oxygen reduction reaction of small nanostructured crystalline bimetallic Pt–M supported catalysts, Journal of applied electrochemistry, 36 (2006) 1143-1149.
[297] J.R. Kitchin, J.K. Nørskov, M.A. Barteau, J.G. Chen, Role of Strain and Ligand Effects in the Modification of the Electronic and Chemical Properties of Bimetallic Surfaces, Physical Review Letters, 93 (2004) 156801.
[298] J.-H. Kim, G. Kwon, H. Lim, C. Zhu, H. You, Y.-T. Kim, Effects of transition metal doping in Pt/M-TiO2 (M= V, Cr, and Nb) on oxygen reduction reaction activity, Journal of Power Sources, 320 (2016) 188-195.
[299] M.M. Islam, T. Bredow, A. Gerson, Electronic properties of vanadium-doped TiO2, Chemphyschem, 12 (2011) 3467-3473.
[300] M. Mavrikakis, B. Hammer, J.K. Nørskov, Effect of Strain on the Reactivity of Metal Surfaces, Physical Review Letters, 81 (1998) 2819-2822.
[301] P. Liu, J.K. Norskov, Ligand and ensemble effects in adsorption on alloy surfaces, Physical Chemistry Chemical Physics, 3 (2001) 3814-3818.
[302] K. Sasaki, L. Zhang, R.R. Adzic, Niobium oxide-supported platinum ultra-low amount electrocatalysts for oxygen reduction, Physical Chemistry Chemical Physics, 10 (2008) 159-167.
[303] J.K. Nørskov, T. Bligaard, A. Logadottir, S. Bahn, L.B. Hansen, M. Bollinger, H. Bengaard, B. Hammer, Z. Sljivancanin, M. Mavrikakis, Y. Xu, S. Dahl, C.J.H. Jacobsen, Universality in Heterogeneous Catalysis, Journal of Catalysis, 209 (2002) 275-278.
[304] J. Nowotny, T. Bak, M.K. Nowotny, L.R. Sheppard, TiO2 Surface Active Sites for Water Splitting, The Journal of Physical Chemistry B, 110 (2006) 18492-18495.
[305] R. Schaub, P. Thostrup, N. Lopez, E. Lægsgaard, I. Stensgaard, J.K. Nørskov, F. Besenbacher, Oxygen Vacancies as Active Sites for Water Dissociation on Rutile ${\mathrm{TiO}}_{2}(110)$, Physical Review Letters, 87 (2001) 266104.
[306] J.-H. Kim, G. Kwon, H. Lim, C. Zhu, H. You, Y.-T. Kim, Effects of transition metal doping in Pt/M-TiO2 (M = V, Cr, and Nb) on oxygen reduction reaction activity, Journal of Power Sources, 320 (2016) 188-195.

[307] E. Antolini, Catalysts for direct ethanol fuel cells, Journal of Power Sources, 170 (2007) 1-12.
[308] D.A. Cantane, F.E.R. Oliveira, S.F. Santos, F.H.B. Lima, Synthesis of Pt-based hollow nanoparticles using carbon-supported Co@Pt and Ni@Pt core–shell structures as templates: Electrocatalytic activity for the oxygen reduction reaction, Applied Catalysis B: Environmental, 136 (2013) 351-360.
[309] X. Peng, S. Zhao, T.J. Omasta, J.M. Roller, W.E. Mustain, Activity and durability of Pt-Ni nanocage electocatalysts in proton exchange membrane fuel cells, Applied Catalysis B: Environmental, 203 (2017) 927-935.
[310] L. Xiong, A. Manthiram, Effect of Atomic Ordering on the Catalytic Activity of Carbon Supported PtM (M=Fe, Co, Ni, and Cu) Alloys for Oxygen Reduction in PEMFCs, Journal of The Electrochemical Society, 152 (2005) A697.
[311] V. Baglio, D. Sebastián, C. D'Urso, A. Stassi, R.S. Amin, K.M. El-Khatib, A.S. Aricò, Composite anode electrode based on iridium oxide promoter for direct methanol fuel cells, Electrochimica Acta, 128 (2014) 304-310.
[312] P. Yu, M. Pemberton, P. Plasse, PtCo/C cathode catalyst for improved durability in PEMFCs, Journal of Power Sources, 144 (2005) 11-20.
[313] V. Bagotzky, Y.B. Vassiliev, O. Khazova, Generalized scheme of chemisorption, electrooxidation and electroreduction of simple organic compounds on platinum group metals, Journal of Electroanalytical Chemistry and Interfacial Electrochemistry, 81 (1977) 229-238.
[314] C. Hu, Y. Cao, L. Yang, Z. Bai, Y. Guo, K. Wang, P. Xu, Preparation of highly dispersed Pt-SnOx nanoparticles supported on multi-walled carbon nanotubes for methanol oxidation, Applied Surface Science, 257 (2011) 7968-7974.
[315] C.-T. Hsieh, D.-Y. Tzou, M.-T. Jiang, Methanol electro-oxidation on Pt nanocatalysts prepared by atomic layer deposition, Journal of Electroanalytical Chemistry, 794 (2017) 139-147.
[316] S. Siracusano, V. Baglio, A. Stassi, R. Ornelas, V. Antonucci, A.S. Aric, Investigation of IrO2 electrocatalysts prepared by a sulfite-couplex route for the O2 evolution reaction in solid polymer electrolyte water electrolyzers, International Journal of Hydrogen Energy, 36 (2011) 7822-7831.
[317] T. Iwasita, H. Hoster, A. John-Anacker, W.F. Lin, W. Vielstich, Methanol Oxidation on PtRu Electrodes. Influence of Surface Structure and Pt−Ru Atom Distribution, Langmuir, 16 (2000) 522-529.
[318] D.Y. Chung, K.-J. Lee, Y.-E. Sung, Methanol electro-oxidation on the Pt surface: revisiting the cyclic voltammetry interpretation, The Journal of Physical Chemistry C, 120 (2016) 9028-9035.
[319] C.-T. Hsieh, D.-Y. Tzou, M.-T. Jiang, Methanol electro-oxidation on Pt nanocatalysts prepared by atomic layer deposition, Journal of Electroanalytical Chemistry, 794 (2017) 139-147.
[320] A. Jasim, X. He, T. White, Y. Xing, Nano-Layer Deposition in Liquid Hydrocarbons with Condensed Water Film, Nature Communication Under review (2019).
[321] M.C. Morris, H.F. McMurdie, E.H. Evans, B. Paretzkin, C. Hubbard, S. Carmel, Standards X-ray diffraction powder patterns. Section 17: Data for 54 substances, Final Report National Bureau of Standards, Washington, DC. National Measurement Lab., (1980).
[322] W. Du, Q. Wang, D. Saxner, N.A. Deskins, D. Su, J.E. Krzanowski, A.I. Frenkel, X. Teng, Highly Active Iridium/Iridium–Tin/Tin Oxide Heterogeneous Nanoparticles

as Alternative Electrocatalysts for the Ethanol Oxidation Reaction, Journal of the American Chemical Society, 133 (2011) 15172-15183.
[323] V. Pfeifer, T. Jones, J.V. Vélez, C. Massué, M. Greiner, R. Arrigo, D. Teschner, F. Girgsdies, M. Scherzer, J. Allan, The electronic structure of iridium oxide electrodes active in water splitting, Physical Chemistry Chemical Physics, 18 (2016) 2292-2296.
[324] H. Ohno, S. Nohara, K. Kakinuma, M. Uchida, A. Miyake, S. Deki, H. Uchida, Remarkable Mass Activities for the Oxygen Evolution Reaction at Iridium Oxide Nanocatalysts Dispersed on Tin Oxides for Polymer Electrolyte Membrane Water Electrolysis, Journal of The Electrochemical Society, 164 (2017) F944-F947.
[325] R. Hahn, A. Ghicov, J. Salonen, V.-P. Lehto, P. Schmuki, Carbon doping of self-organized TiO2 nanotube layers by thermal acetylene treatment, Nanotechnology, 18 (2007) 105604.
[326] M.W. Lee, D.L. Lee, W.N. Yen, C.Y. Yeh, Synthesis, Optical and Photovoltaic Properties of Porphyrin Dyes, Journal of Macromolecular Science, Part A, 46 (2009) 730-737.
[327] C. Di Valentin, G. Pacchioni, A. Selloni, Theory of carbon doping of titanium dioxide, Chemistry of materials, 17 (2005) 6656-6665.
[328] C. Yu, X. Dong, L. Guo, J. Li, F. Qin, L. Zhang, J. Shi, D.J.T.J.o.P.C.C. Yan, Template-free preparation of mesoporous Fe2O3 and its application as absorbents, 112 (2008) 13378-13382.
[329] R. Hahn, F. Schmidt-Stein, J. Salonen, S. Thiemann, Y. Song, J. Kunze, V.P. Lehto, P. Schmuki, Semimetallic TiO2 Nanotubes, Angewandte Chemie, 121 (2009) 7372-7375.
[330] G. Beamson, D. Briggs, High Resolution XPS of Organic Polymers. The Scienta ESCA300 Database. Chichester, New York, (1992).
[331] G.B. Fisher, J.L. Gland, The interaction of water with the Pt (111) surface, Surface Science, 94 (1980) 446-455.
[332] C.-C. Shan, D.-S. Tsai, Y.-S. Huang, S.-H. Jian, C.-L. Cheng, Pt− Ir− IrO2NT Thin-Wall Electrocatalysts derived from IrO2 nanotubes and their catalytic activities in methanol oxidation, Chemistry of materials, 19 (2007) 424-431.
[333] R.-S. Chen, Y.-S. Huang, Y.-M. Liang, D.-S. Tsai, Y. Chi, J.-J. Kai, Growth control and characterization of vertically aligned IrO 2 nanorods, Journal of Materials Chemistry, 13 (2003) 2525-2529.
[334] M. Naeem, S. Hasanain, M. Kobayashi, Y. Ishida, A. Fujimori, S. Buzby, S.I. Shah, Effect of reducing atmosphere on the magnetism of Zn1− xCoxO ($0 \leq x \leq 0.10$) nanoparticles, Nanotechnology, 17 (2006) 2675.
[335] D. Santiago, G.G. Rodríguez-Calero, H. Rivera, D.A. Tryk, M.A. Scibioh, C.R. Cabrera, Platinum electrodeposition at high surface area carbon vulcan-XC-72R material using a rotating disk-slurry electrode technique, Journal of The Electrochemical Society, 157 (2010) F189-F195.
[336] V. Pfeifer, T.E. Jones, J.J.V. Vélez, R. Arrigo, S. Piccinin, M. Hävecker, A. Knop-Gericke, R. Schlögl, In situ observation of reactive oxygen species forming on oxygen-evolving iridium surfaces, Chemical science, 8 (2017) 2143-2149.
[337] R. Kötz, H. Neff, S. Stucki, Anodic Iridium Oxide Films XPS-Studies of Oxidation State Changes and, Journal of The Electrochemical Society, 131 (1984) 72-77.
[338] D. Liu, X. Chen, G. Xu, J. Guan, Q. Cao, B. Dong, Y. Qi, C. Li, X. Mu, Iridium nanoparticles supported on hierarchical porous N-doped carbon: an efficient water-tolerant catalyst for bio-alcohol condensation in water, Scientific reports, 6 (2016) 21365.

[339] R. Bedford, G. Bonnier, H. Maas, F. Pavese, Recommended values of temperature on the International Temperature Scale of 1990 for a selected set of secondary reference points, Metrologia, 33 (1996) 133.
[340] W. Chen, S. Chen, Iridium-platinum alloy nanoparticles: Composition-dependent electrocatalytic activity for formic acid oxidation, Journal of Materials Chemistry, 21 (2011) 9169-9178.
[341] T. Iwasita, Methanol and CO electrooxidation, Handbook of fuel cells, 047-097-4001 (2003) 604-622.
[342] N.P. Lebedeva, M.T.M. Koper, J.M. Feliu, R.A. van Santen, Role of Crystalline Defects in Electrocatalysis: Mechanism and Kinetics of CO Adlayer Oxidation on Stepped Platinum Electrodes, The Journal of Physical Chemistry B, 106 (2002) 12938-12947.
[343] A.M. Hofstead-Duffy, D.-J. Chen, S.-G. Sun, Y.J. Tong, Origin of the current peak of negative scan in the cyclic voltammetry of methanol electro-oxidation on Pt-based electrocatalysts: a revisit to the current ratio criterion, Journal of Materials Chemistry, 22 (2012) 5205-5208.
[344] N.M. Marković, H.A. Gasteiger, B.N. Grgur, P.N. Ross, Oxygen reduction reaction on Pt(111): effects of bromide, Journal of Electroanalytical Chemistry, 467 (1999) 157-163.
[345] S. Harish, S. Baranton, C. Coutanceau, J. Joseph, Microwave assisted polyol method for the preparation of Pt/C, Ru/C and PtRu/C nanoparticles and its application in electrooxidation of methanol, Journal of Power Sources, 214 (2012) 33-39.
[346] T.H.M. Housmans, A.H. Wonders, M.T.M. Koper, Structure Sensitivity of Methanol Electrooxidation Pathways on Platinum: An On-Line Electrochemical Mass Spectrometry Study, The Journal of Physical Chemistry B, 110 (2006) 10021-10031.
[347] S. Liao, K.-A. Holmes, H. Tsaprailis, V.I. Birss, High Performance PtRuIr Catalysts Supported on Carbon Nanotubes for the Anodic Oxidation of Methanol, Journal of the American Chemical Society, 128 (2006) 3504-3505.
[348] R. Amin, K. El-Khatib, S. Siracusano, V. Baglio, A. Stassi, A. Arico, Metal oxide promoters for methanol electro-oxidation, international journal of hydrogen energy, 39 (2014) 9782-9790.
[349] J. Cruz, V. Baglio, S. Siracusano, V. Antonucci, A. Aricò, R. Ornelas, L. Ortiz-Frade, G. Osorio-Monreal, S. Durón-Torres, L. Arriaga, Preparation and characterization of RuO2 catalysts for oxygen evolution in a solid polymer electrolyte, Int J Electrochem Sci, 6 (2011) 660.
[350] L. Preda, T. Kondo, T. Spataru, M. Marin, M. Radu, P. Osiceanu, A. Fujishima, N. Spataru, Enhanced Activity for Methanol Oxidation of Platinum Particles Supported on Iridium Oxide Modified Boron-Doped Diamond Powder, ChemElectroChem, 4 (2017) 1908-1915.
[351] E. Willinger, C. Massué, R. Schlögl, M.G. Willinger, Identifying key structural features of IrOx water splitting catalysts, Journal of the American Chemical Society, 139 (2017) 12093-12101.
[352] J.M. Jaksic, C.M. Lacnjevac, M.M. Jaksic, Poetics of Interplay and Interferences of Potentiodynamic Sweeps and Peaks in Electrocatalysis for Oxygen Electrode Reactions, Croatica Chemica Acta, 90 (2017) 1-17.
[353] Q. Wang, G. Wang, H. Tao, Z. Li, L. Han, Highly CO tolerant PtRu/PtNi/C catalyst for polymer electrolyte membrane fuel cell, RSC Adv., 7 (2017) 8453-8459.
[354] X. Yu, S. Ye, Recent advances in activity and durability enhancement of Pt/C catalytic cathode in PEMFC: Part I. Physico-chemical and electronic interaction

between Pt and carbon support, and activity enhancement of Pt/C catalyst, Journal of power sources, 172 (2007) 133-144.
[355] X. Yu, S. Ye, Recent advances in activity and durability enhancement of Pt/C catalytic cathode in PEMFC: Part II: Degradation mechanism and durability enhancement of carbon supported platinum catalyst, Journal of power sources, 172 (2007) 145-154.
[356] S. Maass, F. Finsterwalder, G. Frank, R. Hartmann, C. Merten, Carbon support oxidation in PEM fuel cell cathodes, Journal of Power Sources, 176 (2008) 444-451.
[357] A. Lewera, L. Timperman, A. Roguska, N. Alonso-Vante, Metal–Support Interactions between Nanosized Pt and Metal Oxides (WO3 and TiO2) Studied Using X-ray Photoelectron Spectroscopy, The Journal of Physical Chemistry C, 115 (2011) 20153-20159.
[358] O.A. Baturina, Y. Garsany, T.J. Zega, R.M. Stroud, T. Schull, K.E. Swider-Lyons, Oxygen reduction reaction on platinum/tantalum oxide electrocatalysts for PEM fuel cells, Journal of the Electrochemical Society, 155 (2008) B1314-B1321.
[359] Z. Ma, S. Li, L. Wu, L. Song, G. Jiang, Z. Liang, D. Su, Y. Zhu, R.R. Adzic, J.X. Wang, Z. Chen, NbOx nano-nail with a Pt head embedded in carbon as a highly active and durable oxygen reduction catalyst, Nano Energy, 69 (2020) 104455.
[360] Y. Maekawa, A. Ishihara, J.-H. Kim, S. Mitsushima, K.-i. Ota, Catalytic activity of zirconium oxynitride prepared by reactive sputtering for ORR in sulfuric acid, J Electrochemical Solid-State Letters, 11 (2008) B109-B112.
[361] Y. Liu, A. Ishihara, S. Mitsushima, N. Kamiya, K.-i. Ota, Zirconium oxide for PEFC cathodes, J Electrochemical Solid-State Letters, 8 (2005) A400-A402.
[362] K. Sasaki, L. Zhang, R. Adzic, Niobium oxide-supported platinum ultra-low amount electrocatalysts for oxygen reduction, J Physical Chemistry Chemical Physics, 10 (2008) 159-167.
[363] M. Teliska, V.S. Murthi, S. Mukerjee, D.E. Ramaker, Correlation of water activation, surface properties, and oxygen reduction reactivity of supported Pt–M/C bimetallic electrocatalysts using XAS, Journal of the Electrochemical Society, 152 (2005) A2159-A2169.
[364] Y. Zhao, X. Zhou, L. Ye, S. Chi Edman Tsang, Nanostructured Nb_2O_5 catalysts, Nano Reviews, 3 (2012) 17631.
[365] M. Matsumoto, T. Miyazaki, S. Fujieda, Y. Ohgi, A. Ishihara, K.-i. Ota, H. Imai, Structural Characterization of ORR Active Surface Niobium Oxides on Partially Oxidized Nb Carbonitrides, ECS Transactions, 35 (2019) 77-83.
[366] J. Waring, R. Roth, H. Parker, Temperature-Pressure Phase Relationships in Niobium Pentoxide, Journal of Research of the National Bureau of Standards. Section A, Physics and Chemistry, 77 (1973) 705-711.
[367] A.K. Kulkarni, C.S. Praveen, Y.A. Sethi, R.P. Panmand, S.S. Arbuj, S.D. Naik, A.V. Ghule, B.B. Kale, Nanostructured N-doped orthorhombic Nb_2O_5 as an efficient stable photocatalyst for hydrogen generation under visible light, Dalton Transactions, 46 (2017) 14859-14868.
[368] Z. Liu, W. Dong, J. Wang, C. Dong, Y. Lin, I.W. Chen, F. Huang, Orthorhombic Nb_2O_5-x for Durable High-Rate Anode of Li-Ion Batteries, iScience, 23 (2020) 100767.
[369] B. Liu, H. Wang, Y. Chen, J. Wang, L. Peng, L. Li, Pt nanoparticles anchored on Nb_2O_5 and carbon fibers as an enhanced performance catalyst for methanol oxidation, Journal of Alloys and Compounds, 682 (2016) 584-589.
[370] Y. Zeng, X. Guo, Z. Wang, J. Geng, H. Zhang, W. Song, H. Yu, Z. Shao, B. Yi, Highly stable nanostructured membrane electrode assembly based on Pt/Nb2O5

nanobelts with reduced platinum loading for proton exchange membrane fuel cells, Nanoscale, 9 (2017) 6910-6919.
[371] H.T. Kreissl, M.M. Li, Y.-K. Peng, K. Nakagawa, T.J. Hooper, J.V. Hanna, A. Shepherd, T.-S. Wu, Y.-L. Soo, S.E. Tsang, Structural studies of bulk to nanosize niobium oxides with correlation to their acidity, Journal of the American Chemical Society, 139 (2017) 12670-12680.
[372] C. Xu, J. Yang, E. Liu, Q. Jia, G.M. Veith, G. Nair, S. DiPietro, K. Sun, J. Chen, P. Pietrasz, Z. Lu, M. Jagner, K.K. Gath, S. Mukerjee, J.R. Waldecker, Physical vapor deposition process for engineering Pt based oxygen reduction reaction catalysts on NbOx templated carbon support, Journal of Power Sources, 451 (2020) 227709.
[373] C. Xu, J. Yang, B. Pence, K. Gath, P. Pietrasz, M. Sulek, K. Sun, E. Sohm, G. Meng, 2D Platinum Network ORR Catalyst on Carbon and Niobium Oxide Hybrid Support, ECS Transactions, 64 (2014) 181.
[374] R. Janninck, D. Whitmore, Electrical Conduction in Nonstoichiometric α-Nb2O5, The Journal of Chemical Physics, 37 (1962) 2750-2754.
[375] D.N. Hendrickson, J.M. Hollander, W.L. Jolly, Core-electron binding energies for compounds of boron, carbon, and chromium, Inorganic Chemistry, 9 (1970) 612-615.
[376] L. Zhang, L. Wang, C.M. Holt, T. Navessin, K. Malek, M.H. Eikerling, D. Mitlin, Oxygen reduction reaction activity and electrochemical stability of thin-film bilayer systems of platinum on niobium oxide, The Journal of Physical Chemistry C, 114 (2010) 16463-16474.
[377] I.E. Stephens, A.S. Bondarenko, U. Grønbjerg, J. Rossmeisl, I. Chorkendorff, Understanding the electrocatalysis of oxygen reduction on platinum and its alloys, Energy & Environmental Science, 5 (2012) 6744-6762.
[378] S. Shrestha, Y. Liu, W.E. Mustain, Electrocatalytic activity and stability of Pt clusters on state-of-the-art supports: a review, Catalysis Reviews, 53 (2011) 256-336.
[379] R. Alipour MoghadamEsfahani, S.K. Vankova, E.B. Easton, I.I. Ebralidze, S. Specchia, A hybrid Pt/NbO/CNTs catalyst with high activity and durability for oxygen reduction reaction in PEMFC, Renewable Energy, 154 (2020) 913-924.
[380] J. Rossmeisl, G.S. Karlberg, T. Jaramillo, J.K. Nørskov, Steady state oxygen reduction and cyclic voltammetry, Faraday discussions, 140 (2009) 337-346.
[381] L. Zhang, L. Wang, C.M. Holt, B. Zahiri, Z. Li, K. Malek, T. Navessin, M.H. Eikerling, D.J.E. Mitlin, E. Science, Highly corrosion resistant platinum–niobium oxide–carbon nanotube electrodes for the oxygen reduction in PEM fuel cells, 5 (2012) 6156-6172.
[382] L.J.X.X.W.F.L.J.L.Z.J. Liu H, J., Highly graphitic carbon black-supported platinum nanoparticle catalyst and its enhanced electrocatalytic activity for the oxygen reduction reaction in acidic medium, Electrochimica Acta, 93 (2013) 25.
[383] J. Floriano, E. Ticianelli, E. Gonzalez, Influence of the supporting electrolyte on the oxygen reduction reaction at the platinum/proton exchange membrane interface, Journal of Electroanalytical Chemistry, 367 (1994) 157-164.
[384] H. Liu, K. Liu, P. Zhong, J. Qi, J. Bian, Q. Fan, K. Ren, H. Zheng, L. Han, Y. Yin, Ultrathin Pt–Ag Alloy Nanotubes with Regular Nanopores for Enhanced Electrocatalytic Activity, Chemistry of Materials, 30 (2018) 7744-7751.
[385] Q. Lu, L. Sun, X. Zhao, J. Huang, C. Han, X. Yang, One-pot synthesis of interconnected Pt 95 Co 5 nanowires with enhanced electrocatalytic performance for methanol oxidation reaction, Nano Research, 11 (2018) 2562-2572.

[386] Z. Merati, J. Basiri Parsa, Enhancement of the catalytic activity of Pt nanoparticles toward methanol electro-oxidation using doped-SnO2 supporting materials, Applied Surface Science, 435 (2018) 535-542.
[387] Y.-Y. Feng, G.-H. Song, Q. Zhang, J.-N. Lv, X.-Y. Hu, Y.-L. He, X. Shen, Morphology effect of MnO2 promoter to the catalytic performance of Pt toward methanol electrooxidation reaction, International Journal of Hydrogen Energy, 44 (2019) 3744-3750.
[388] Y. Ma, B. Cui, L. He, K. Tian, Z. Zhang, M. Wang, A novel support for platinum electrocatalyst based on mesoporous carbon embedded with bimetallic SnTi oxide as a bifunctional electrocatalyst, Journal of Electroanalytical Chemistry, 850 (2019) 113435.
[389] Y. Zheng, J. Qiao, J. Hu, F. Song, D. Huo, J. Yuan, J. Shen, L. Niu, A.-j. Wang, PtIr alloy nanowire assembly on carbon cloth as advanced anode catalysts for methanol oxidation, International Journal of Hydrogen Energy, (2019).
[390] Q. Zhou, Z. Pan, D. Wu, G. Hu, S. Wu, C. Chen, L. Lin, Y. Lin, Pt-CeO2/TiN NTs derived from metal organic frameworks as high-performance electrocatalyst for methanol electrooxidation, International Journal of Hydrogen Energy, 44 (2019) 10646-10652.
[391] X. Long, P. Yin, T. Lei, K. Wang, Z. Zhan, Methanol electro-oxidation on Cu@Pt/C core-shell catalyst derived from Cu-MOF, Applied Catalysis B: Environmental, 260 (2020) 118187.
[392] A.M. Jasim, S.E. Hoff, Y. Xing, Enhancing methanol electrooxidation activity using double oxide catalyst support of tin oxide clusters on doped titanium dioxides, J Electrochimica Acta, 261 (2018) 221-226.
[393] A. Papaderakis, O. Spyridou, N. Karanasios, A. Touni, A. Banti, N. Dimitrova, S. Armyanov, E. Valova, J. Georgieva, S. Sotiropoulos, The Effect of Carbon Content on Methanol Oxidation and Photo-Oxidation at Pt-TiO2-C Electrodes, Catalysts, 10 (2020) 248.
[394] C. Wang, D. Van Der Vliet, K.L. More, N.J. Zaluzec, S. Peng, S. Sun, H. Daimon, G. Wang, J. Greeley, J. Pearson, Multimetallic Au/FePt3 nanoparticles as highly durable electrocatalyst, Nano letters, 11 (2011) 919-926.
[395] R. Kou, Y. Shao, D. Mei, Z. Nie, D. Wang, C. Wang, V.V. Viswanathan, S. Park, I.A. Aksay, Y. Lin, Stabilization of electrocatalytic metal nanoparticles at metal− metal oxide− graphene triple junction points, Journal of the American Chemical Society, 133 (2011) 2541-2547.
[396] J. Li, L. Zhao, X. Li, S. Hao, Z. Wang, Fabrication of C@ MoxTi1− xO2− δ nanocrystalline with functionalized interface as efficient and robust PtRu catalyst support for methanol electrooxidation, Journal of Energy Chemistry, 40 (2020) 7-14.
[397] Y. Bing, H. Liu, L. Zhang, D. Ghosh, J. Zhang, Nanostructured Pt-alloy electrocatalysts for PEM fuel cell oxygen reduction reaction, Chemical Society Reviews, 39 (2010) 2184-2202.
[398] Q. Jia, K. Caldwell, K. Strickland, J.M. Ziegelbauer, Z. Liu, Z. Yu, D.E. Ramaker, S. Mukerjee, Improved oxygen reduction activity and durability of dealloyed PtCo x catalysts for proton exchange membrane fuel cells: strain, ligand, and particle size effects, ACS catalysis, 5 (2015) 176-186.
[399] K. Rasmi, S. Vanithakumari, R. George, C. Mallika, U.K. Mudali, Nanoparticles of Pt loaded on a vertically aligned TiO 2 nanotube bed: synthesis and evaluation of electrocatalytic activity, RSC Advances, 5 (2015) 108050-108057.
[400] A.S. Pushkarev, I.V. Pushkareva, N.A. Ivanova, S.P. du Preez, D. Bessarabov, R.G. Chumakov, V.G. Stankevich, V.N. Fateev, A.A. Evdokimov, S.A. Grigoriev, Pt/C

and Pt/SnOx/C catalysts for ethanol electrooxidation: rotating disk electrode study, Catalysts, 9 (2019) 271.
[401] A. Nouralishahi, A.A. Khodadadi, Y. Mortazavi, A. Rashidi, M. Choolaei, Enhanced methanol electro-oxidation activity of Pt/MWCNTs electro-catalyst using manganese oxide deposited on MWCNTs, Electrochimica Acta, 147 (2014) 192-200.
[402] A. Aguilar-Vallejo, L. Álvarez-Contreras, M. Guerra-Balcázar, J. Ledesma-García, L. Gerardo Arriaga, N. Arjona, S. Rivas, Electrocatalytic Evaluation of Highly Stable Pt/ZrO2 Electrocatalysts for the Methanol Oxidation Reaction Synthesized Without the Assistance of Any Carbon Support, ChemElectroChem, 6 (2019) 2107-2118.
[403] M.A. Scibioh, S.-K. Kim, E.A. Cho, T.-H. Lim, S.-A. Hong, H.Y. Ha, Pt-CeO2/C anode catalyst for direct methanol fuel cells, Applied Catalysis B: Environmental, 84 (2008) 773-782.
[404] B. Rajesh, K. Ravindranathan Thampi, J.-M. Bonard, N. Xanthopoulos, H. Mathieu, B. Viswanathan, Carbon nanotubes generated from template carbonization of polyphenyl acetylene as the support for electrooxidation of methanol, The Journal of Physical Chemistry B, 107 (2003) 2701-2708.
[405] T. Iwasita, Electrochim Acta 47: 3663. doi: 10.1016, S0013-4686 (02), (2002) 00336-00335.
[406] E. Umeshbabu, G. Ranga Rao, High Electrocatalytic Activity of Pt/C Catalyst Promoted by TT-Nb2O5 Nanoparticles under Acidic Conditions, ChemistrySelect, 2 (2017) 4204-4212.
[407] S.J. Hwang, S.J. Yoo, T.-Y. Jeon, K.-S. Lee, T.-H. Lim, Y.-E. Sung, S.-K. Kim, Facile synthesis of highly active and stable Pt–Ir/C electrocatalysts for oxygen reduction and liquid fuel oxidation reaction, Chemical Communications, 46 (2010) 8401-8403.
[408] L.A. Frolova, Y.A. Dobrovolsky, Platinum electrocatalysts based on oxide supports for hydrogen and methanol fuel cells, Russian Chemical Bulletin, 60 (2011) 1101-1111.
[409] Q. Chang, S. Kattel, X. Li, Z. Liang, B.M. Tackett, S.R. Denny, P. Zhang, D. Su, J.G. Chen, Z. Chen, Enhancing C–C Bond Scission for Efficient Ethanol Oxidation using PtIr Nanocube Electrocatalysts, ACS Catalysis, 9 (2019) 7618-7625.
[410] V.T.T. Phan, T.T. Huynh, H.Q. Pham, A.T.N. Mai, T.H.T. Anh, T.H.T. Nguyen, T.M. Ngo, V.T.T. Ho, Investigation of iridium composition in Ti1–xIrxO2 (x = 0.1, 0.2, 0.3) nanostructures as potential supports for platinum in methanol electro-oxidation, Comptes Rendus Chimie, 22 (2019) 844-854.
[411] N. Shakibi Nia, O. Guillén-Villafuerte, C. Griesser, G. Manning, J. Kunze-Liebhäuser, C. Arévalo, E. Pastor, G. García, W2C-Supported PtAuSn—A Catalyst with the Earliest Ethanol Oxidation Onset Potential and the Highest Ethanol Conversion Efficiency to CO2 Known till Date, ACS Catalysis, 10 (2020) 1113-1122.
[412] K. Kakinuma, K. Suda, R. Kobayashi, T. Tano, C. Arata, I. Amemiya, S. Watanabe, M. Matsumoto, H. Imai, A. Iiyama, Electronic states and transport phenomena of Pt nanoparticle catalysts supported on Nb-doped SnO2 for polymer electrolyte fuel cells, ACS applied materials & interfaces, 11 (2019) 34957-34963.
[413] B.H. Toby, R.B. Von Dreele, GSAS-II: the genesis of a modern open-source all purpose crystallography software package, Journal of Applied Crystallography, 46 (2013) 544-549.
[414] B. Ren, J. Lu, Y. Wang, X. Gu, B.B. Xu, Y. Fu, K. Luo, M. Bayati, T.X. Liu, Half-Sphere Shell Supported Pt Catalyst for Electrochemical Methanol Oxidation, Journal of The Electrochemical Society, 167 (2020) 084510.

[415] L. Pan, Y. Wang, X. Wang, H. Qu, J. Zhao, Y. Li, A. Gavrilyuk, Hydrogen photochromism in Nb2O5 powders, Physical Chemistry Chemical Physics, 16 (2014) 20828-20833.
[416] G.J. McCarthy, J.M. Welton, X-ray diffraction data for SnO 2. An illustration of the new powder data evaluation methods, Powder Diffraction, 4 (1989) 156-159.
[417] G. Sajiki, Y. Benino, C. Oki, K. Ohara, H. Okano, T. Nanba, Structural analyses and reverse Monte Carlo modeling of niobium oxide amorphous film prepared by sputtering method, Journal of the Ceramic Society of Japan, 125 (2017) 760-765.
[418] H.-W. Wang, D.J. Wesolowski, T.E. Proffen, L. Vlcek, W. Wang, L.F. Allard, A.I. Kolesnikov, M. Feygenson, L.M. Anovitz, R.L. Paul, Structure and Stability of SnO2 Nanocrystals and Surface-Bound Water Species, Journal of the American Chemical Society, 135 (2013) 6885-6895.
[419] F. Laves, W. Petter, H. Wulf, Die Kristallstruktur von ζ-Nb 2 O 5, NW, 51 (1964) 633-634.
[420] J.L. FOURQUET, M.F. RENOU, R. De Pape, TOPOTACTIC EXCHANGE REACTION LITHIUM NIOBATE (LINBO3)→ HYDROGEN NIOBATE (HNBO3) IN AN ACIDIC MEDIUM, Chemischer Informationsdienst, 16 (1985) no-no.
[421] A. Llordés, Y. Wang, A. Fernandez-Martinez, P. Xiao, T. Lee, A. Poulain, O. Zandi, C.A. Saez Cabezas, G. Henkelman, D.J. Milliron, Linear topology in amorphous metal oxide electrochromic networks obtained via low-temperature solution processing, Nature Materials, 15 (2016) 1267-1273.
[422] H.-Y. Park, T.-Y. Jeon, J.H. Jang, S.J. Yoo, K.-H. Choi, N. Jung, Y.-H. Chung, M. Ahn, Y.-H. Cho, K.-S. Lee, Enhancement of oxygen reduction reaction on PtAu nanoparticles via CO induced surface Pt enrichment, Applied Catalysis B: Environmental, 129 (2013) 375-381.
[423] F. De Groot, M. Grioni, J.C. Fuggle, J. Ghijsen, G.A. Sawatzky, H. Petersen, Oxygen 1s x-ray-absorption edges of transition-metal oxides, Physical Review B, 40 (1989) 5715.
[424] E.L. Redmond, B.P. Setzler, F.M. Alamgir, T.F. Fuller, Elucidating the oxide growth mechanism on platinum at the cathode in PEM fuel cells, Physical Chemistry Chemical Physics, 16 (2014) 5301-5311.
[425] C. Eickes, P. Piela, J. Davey, P. Zelenay, Recoverable cathode performance loss in direct methanol fuel cells, Journal of The Electrochemical Society, 153 (2006) A171-A178.
[426] Y. Zhao, X. Li, J.M. Schechter, Y. Yang, Revisiting the oxidation peak in the cathodic scan of the cyclic voltammogram of alcohol oxidation on noble metal electrodes, RSC advances, 6 (2016) 5384-5390.
[427] C. Du, M. Chen, X. Cao, G. Yin, P. Shi, A novel CNT@ SnO2 core–sheath nanocomposite as a stabilizing support for catalysts of proton exchange membrane fuel cells, Electrochemistry Communications, 11 (2009) 496-498.
[428] X. Liu, X. Wu, K. Scott, Study of niobium and tantalum doped titania-supported Pt electrocatalysts for methanol oxidation and oxygen reduction reactions, Catalysis Science & Technology, 4 (2014) 3891-3898.
[429] P. Justin, P. Hari Krishna Charan, G. Ranga Rao, High performance Pt–Nb2O5/C electrocatalysts for methanol electrooxidation in acidic media, Applied Catalysis B: Environmental, 100 (2010) 510-515.
[430] T. Frelink, W. Visscher, J. Van Veen, On the role of Ru and Sn as promotors of methanol electro-oxidation over Pt, Surface Science, 335 (1995) 353-360.

[431] M. Watanabe, S. Motoo, Electrocatalysis by ad-atoms: Part II. Enhancement of the oxidation of methanol on platinum by ruthenium ad-atoms, Journal of Electroanalytical Chemistry and Interfacial Electrochemistry, 60 (1975) 267-273.
[432] E. Antolini, J.R. Salgado, E.R. Gonzalez, The methanol oxidation reaction on platinum alloys with the first row transition metals: the case of Pt–Co and–Ni alloy electrocatalysts for DMFCs: a short review, Applied Catalysis B: Environmental, 63 (2006) 137-149.
[433] B.Y. Xia, B. Wang, H.B. Wu, Z. Liu, X. Wang, X.W.D. Lou, Sandwich-structured TiO 2–Pt–graphene ternary hybrid electrocatalysts with high efficiency and stability, Journal of Materials Chemistry, 22 (2012) 16499-16505.
[434] X. Wang, Y. Zheng, J. Yuan, J. Shen, A.-j. Wang, L. Niu, S. Huang, Uniform deposition of Co3O4 nanosheets on exfoliated MoS2 nanosheets as advanced catalysts for water splitting, Electrochimica Acta, 212 (2016) 890-897.
[435] F. Lei, Z. Li, L. Ye, Y. Wang, S. Lin, One-pot synthesis of Pt/SnO2/GNs and its electro-photo-synergistic catalysis for methanol oxidation, International Journal of Hydrogen Energy, 41 (2016) 255-264.
[436] T. Maiyalagan, F.N. Khan, Electrochemical oxidation of methanol on Pt/V2O5–C composite catalysts, Catalysis Communications, 10 (2009) 433-436.
[437] J. Zeng, C. Francia, C. Gerbaldi, V. Baglio, S. Specchia, A. Aricò, P. Spinelli, Hybrid ordered mesoporous carbons doped with tungsten trioxide as supports for Pt electrocatalysts for methanol oxidation reaction, Electrochimica Acta, 94 (2013) 80-91.
[438] S. Cherevko, G.P. Keeley, S. Geiger, A.R. Zeradjanin, N. Hodnik, N. Kulyk, K.J. Mayrhofer, Dissolution of platinum in the operational range of fuel cells, ChemElectroChem, 2 (2015) 1471.
[439] M. Li, Z.-X. Jin, W. Zhang, Y.-H. Bai, Y.-Q. Cao, W.-M. Li, D. Wu, A.-D. Li, Comparison of chemical stability and corrosion resistance of group IV metal oxide films formed by thermal and plasma-enhanced atomic layer deposition, Scientific reports, 9 (2019) 1-12.
[440] H. Deng, K.J. Leedle, Y. Miao, D.S. Black, K.E. Urbanek, J. McNeur, M. Kozák, A. Ceballos, P. Hommelhoff, O. Solgaard, Gallium Oxide for High-Power Optical Applications, Advanced Optical Materials, 8 (2020) 1901522.
[441] C. Walkey, Das S Seal S Erlichman J Heckman VKK Ghibelli L Traversa E McGinnis JF and Self WT 2015, Environ. Sci. Nano, 2 33-53.
[442] D. Majumdar, T. Maiyalagan, Z. Jiang, Recent progress in ruthenium oxide-based composites for supercapacitor applications, ChemElectroChem, 6 (2019) 4343-4372.

VITA

Ahmed Mohammed Jasim was born in the city of Balad, January 1, 1987, Iraq. He received his B.Sc. from the University of Tikrit on 2008, Iraq. He was hired as a process chemical engineer at the North Refineries Company (NRC). On 2013, he was selected for a scholarship from the office of the prime minister to be sent to the University of Missouri for the Master degree.

After he finished his Master of Science in Chemical Engineering from the University of Missouri on December 2016, he continued pursuing the Ph.D. During his three years in the Ph.D. study, he published five peer-review journal papers and three papers to be submitted all as a first author, and he is a co-inventor in a patent, and coauthored at least four journal papers. He presented his work in several chemical engineering conferences such as AICHE, ACS and others.

He received the 2020 award of outstanding Ph.D. as well as 2016 award of outstanding MS student from the department of Chemical Engineering / University of Missouri-Columbia. Ahmed's research has primarily focused on experimental study of metals oxides nanocoatings in electrocatalysis and potential other engineering applications. Such applications are in nano-catalysis, environmental aspects, and nanoscale ice phase transformation.